Division of Research & Innovation

Development and Validation of the Downhole Freestanding Shear Device (DFSD) for Measuring the Dynamic Properties of Clay

Final Report

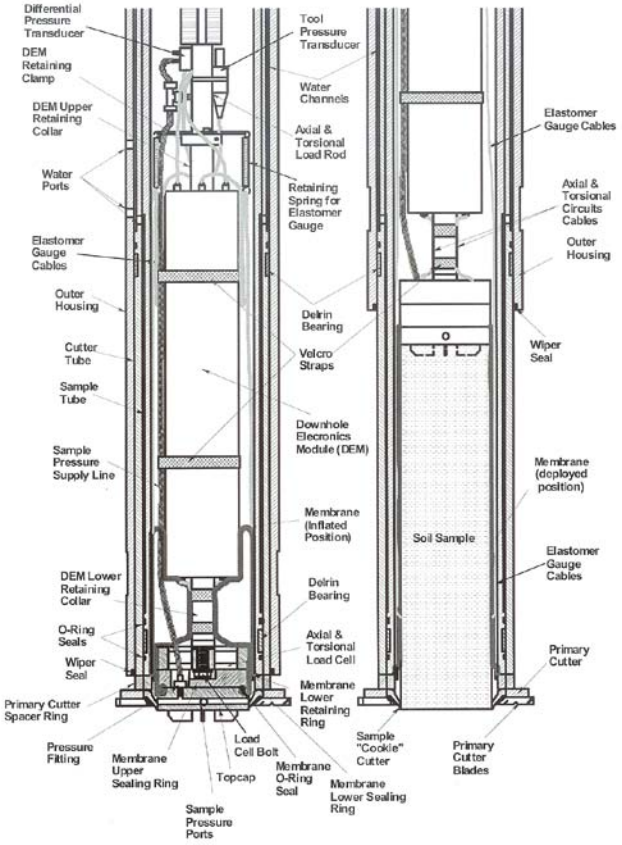

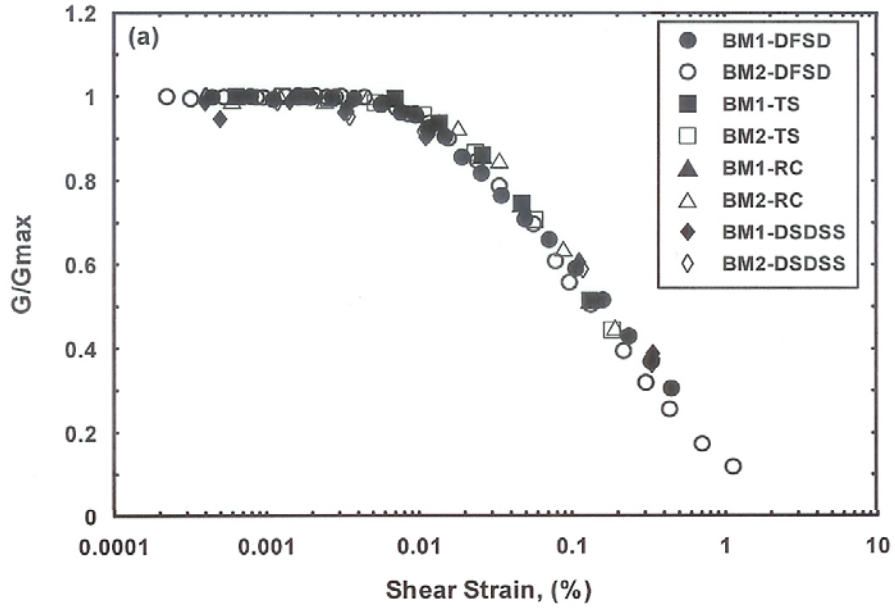

Report CA03-0024
December 2008

Development and Validation of the Downhole Freestanding Shear Device (DFSD) for Measuring the Dynamic Properties of Clay

Final Report

Report No. CA03-0024

December 2008

Prepared By:

Department of Civil and Environmental Engineering
University of California, Berkeley
Berkeley, CA 92093-0085

California Department of Transportation
Division of Research and Innovation, MS-5
5900 Folsom Blvd.
Sacramento, CA 95816

Prepared For:

California Department of Transportation
Division of Research and Innovation, MS-83
1227 O Street
Sacramento, CA 95814

DISCLAIMER STATEMENT

This document is disseminated in the interest of information exchange. The contents of this report reflect the views of the authors who are responsible for the facts and accuracy of the data presented herein. The contents do not necessarily reflect the official views or policies of the State of California or the Federal Highway Administration. This publication does not constitute a standard, specification or regulation. This report does not constitute an endorsement by the Department of any product described herein.

STATE OF CALIFORNIA DEPARTMENT OF TRANSPORTATION

TECHNICAL REPORT DOCUMENTATION PAGE

TR0003 (REV. 10/98)

1. REPORT NUMBER	2. GOVERNMENT ASSOCIATION NUMBER	3. RECIPIENT'S CATALOG NUMBER
CA03-0024		

4. TITLE AND SUBTITLE	5. REPORT DATE
Development and Validation of the Downhole Freestanding Shear Device (DFSD) for Measuring the Dynamic Properties of Clay	December, 2008
	6. PERFORMING ORGANIZATION CODE

7. AUTHOR(S)	8. PERFORMING ORGANIZATION REPORT NO.
Michael Riemer[1], Osama Safaqah[1], Carlton Grizzle[1], Clifford Roblee[2]	

9. PERFORMING ORGANIZATION NAME AND ADDRESS	10. WORK UNIT NUMBER
[1]Department of Civil and Environmental Engineering University of California at Berkeley Berkeley, CA 94720 [2]California Department of Transportation Division of Research and Innovation, MS-5 5900 Folsom Blvd. Sacramento, CA 95819	11. CONTRACT OR GRANT NUMBER DRI Research Task No. 0024 Contract No. 65A0014 Original Project ID: F97OR05

12. SPONSORING AGENCY AND ADDRESS	13. TYPE OF REPORT AND PERIOD COVERED
California Department of Transportation Division of Research and Innovation, MS-83 1227 O Street Sacramento, CA 95814	Final Report
	14. SPONSORING AGENCY CODE 913

15. SUPPLEMENTAL NOTES

.

16. ABSTRACT

The Downhole Freestanding Shear Device (DFSD) is an innovative tool developed for *in situ* measurement of dynamic properties (modulus and damping) of clay soils over a broad range of strains. The device essentially performs laboratory-quality torsional shear testing on a "freestanding" column of soil carved below the bottom of a borehole. Other shear testing modes may also be accommodated. The DFSD design and testing procedure minimizes sample disturbance by maintaining estimated values of the original *in situ* effective stress throughout the sample preparation, instrumentation, and testing processes. As a result, the sample is not significantly unloaded, and therefore does not experience the stress-relief disturbance associated with the removal and re-application of stresses.

This report documents design, development and validation work that has yielded a field-capable prototype DFSD tool that is capable of meeting or exceeding the best current laboratory testing capabilities for measurement of dynamic properties of clay soils used in earthquake site response analysis. Mechanical, pneumatic, electrical and sensor systems used to remotely create a test specimen, maintain continuous control of its anisotropic stress state, and test the specimen over a wide strain range of shear strain are described. Validation tests comparing DFSD results to state-of-the-art laboratory results are presented as well as results from a series of tests that quantify and compare reduced sample disturbance caused by the DSFD relative to conventional high-quality sampling methods.

17. KEY WORDS	18. DISTRIBUTION STATEMENT
Downhole Freestanding Shear Device (DFSD); In Situ Measurement; Dynamic Properties; Modulus; Damping; Clay Soils; Earthquake Site Response; Soil Sample Disturbance; DFSD Design and Validation;	No restrictions. This document is available to the public through the National Technical Information Service, Springfield, VA 22161

19. SECURITY CLASSIFICATION (of this report)	20. NUMBER OF PAGES	21. PRICE
Unclassified	377 Pages	

Development and Validation of the Downhole Freestanding Shear Device (DFSD) for Measuring the Dynamic Properties of Clay

Final Report

Preface:

This report tracks progress of a long-term initiative to develop new testing capabilities for *in situ* measurement of dynamic properties (modulus and damping) of clay soils over a broad range of strains. The project was initiated in 1991 in response to the recognition that soil response played a significant role in the failure of the Cypress Freeway Viaduct in Oakland during the 1989 Loma Prieta earthquake. The overarching vision was to translate state-of-the-art laboratory testing techniques for field application, thereby minimizing the poorly-understood role of soil disturbance in dynamic properties measurement.

Translating research-grade laboratory testing technologies for the rigors of the field environment was recognized to be an exceptionally challenging initiative, but one that had potential to significantly improve the fundamental understanding of soil behavior. The project scope was recognized to require development of new concepts, technologies, and systems. To manage programmatic risks, the project was pursued as a multi-phase development program with performance milestones. Technical project oversight was provided by an external advisory panel of internationally-recognized researchers, Dr Peter Robertson, Dr. Ken Stokoe, and Dr. Mladen Vucetic, each specializing in specific aspects of soil properties measurement.

Initial phases of the development program occurred under project F92TL05 extended from 1992 through 1998. That project developed the general design strategy and completed both analytical and laboratory investigations required to demonstrate the feasibility of new mechanical, electrical, control, and sensor technologies required for concept viability.

This report documents subsequent development and validation work that occurred under project F97OR05 from 1998 through 2003. This project converted the prototype component technologies developed under project F92TL05 into a more robust and integrated system capable of field deployment. It also completed a series of validation tests to demonstrate that the system was indeed capable of meeting or exceeding the best current laboratory testing capabilities. As part of the validation work, the external advisory panel 'raised the bar' substantially above the originally envisioned scope by guiding the project team through a series of unprecedented fundamental laboratory tests that demonstrated the DFSD's capabilities for minimizing soil disturbance during sample carving. At the completion of this project, the DFSD system had completed initial stages of field deployment and validation at shallow depths. It is an operational system, which in the hands of highly trained researchers, offers the potential to yield fundamental new knowledge regarding the engineering behavior of clay soils that significantly impact analyses of site response in earthquake ground motion hazard studies.

Development and Validation of the Downhole Freestanding Shear Device (DFSD) for Measuring the Dynamic Properties of Clay

Final Report

Abstract:

The Downhole Freestanding Shear Device (DFSD) is an innovative tool developed for *in situ* measurement of dynamic properties (modulus and damping) of clay soils over a broad range of strains. The device essentially performs laboratory-quality torsional shear testing on a "freestanding" column of soil carved below the bottom of a borehole. Other shear testing modes may also be accommodated. The DFSD design and testing procedure minimizes sample disturbance by maintaining estimated values of the original *in situ* effective stress throughout the sample preparation, instrumentation, and testing processes. As a result, the sample is not significantly unloaded, and therefore does not experience the stress-relief disturbance associated with the removal and re-application of stresses.

This report documents design, development and validation work that has yielded a field-capable prototype DFSD tool that is capable of meeting or exceeding the best current laboratory testing capabilities for measurement of dynamic properties of clay soils used in earthquake site response analysis. Mechanical, pneumatic, electrical and sensor systems used to remotely create a test specimen, maintain continuous control of its anisotropic stress state, and test the specimen over a wide strain range of shear strain are described. Validation tests comparing DFSD results to state-of-the-art laboratory results are presented as well as results from a series of tests that quantify and compare reduced sample disturbance caused by the DSFD relative to conventional high-quality sampling methods.

DEVELOPMENT AND VALIDATION OF THE DOWNHOLE FREESTANDING SHEAR DEVICE (DFSD) FOR MEASURING THE DYNAMIC PROPERTIES OF CLAY

[CALTRANS CONTRACT # RTA--65A0014]

A Report to

The California Department of Transportation
Division of New Technology, Materials and Research
Office of Geotechnical Engineering
Sacramento, California

Department of Civil and Environmental Engineering
University of California
Berkeley, California

June, 2003

Principal Investigator: Michael Riemer, UC Berkeley

Report Prepared by: Osama Safaqah, UCB
Michael Riemer, UCB
Carlton Grizzle, UCB
Clifford J. Roblee, Caltrans

FINAL REPORT
"Development and Validation of the Downhole Freestanding Shear Device"

Chapter 1 – Project Overview

Chapter 2 – Operational Concept of DFSD: Proving Feasibility

Chapter 3 – Design and Development of the DFSD: Making It Real

CHAPTER 1: INTRODUCTION

1.1 Research Objectives

The fundamental objective of this research effort has been to develop a new device capable of rapidly and reproducibly measuring the in situ dynamic properties of soft to medium-stiff clays over the full strain-range of interest for use in earthquake ground-response investigations. The intent is to match the measurement precision of existing laboratory methods, but in a more rapid manner through on-site measurement during the course of site exploration. Additionally, such a device can improve upon current laboratory-based approaches by minimizing the effects of soil disturbance associated with sample extraction, transportation, storage, handling, extrusion, and specimen preparation. This will permit, for the first time, a direct evaluation of conventional methods of interpreting laboratory modulus data for the field response, and provide the first field measurements of hysteretic damping at moderate and large strain levels.

The fundamental challenge of this work is to achieve the requisite level of measurement precision over a wide range of strain within the adverse operating environment which exists at the bottom of a borehole. This report describes the design and validation of the "Do□nhole Freestanding Shear Device" (DFSD), as it □as developed to meet these objectives.

1.2 Dynamic Soil Properties in Geotechnical Earthquake Engineering

To adequately model the ground response of soil deposits to earthquake shaking, analytical methods require a combination of dynamic soil parameters that capture key aspects of soil behavior under cyclic loading. This particularly includes the nonlinear hysteretic behavior of soil. One could argue that the important factors in cyclic loading which distinguish it from the more typical monotonic conditions are: (1) stress reversal, (2) rate effects, (3) energy dissipation, and (4) dynamic effects. Thus, no matter how complex or simple the method is, any combination of soil parameters used to model soil response to cyclic loading and the conditions under which they are obtained should reflect these factors. Complex analytical models need more soil parameters and involve more uncertainties in the determination of the parameters than simpler models, but would be expected to cover a wider range of material behavior and loading conditions.

Current engineering practice has settled on using relatively simple soil models that require a small number of parameters that are intended to capture only the most important factors present in cyclic loading. The most widely used dynamic soil properties are the shear modulus, *G*, and damping ratio, *D*. For example, the widely used computer program SHAKE models the soil as a one-phase viscoelastic material as described by the following equation:

$$\tau = G\gamma + \eta\dot{\gamma} = (G + j\omega\eta).\gamma = G(1 + j2D).\gamma \qquad \text{K (2.1)}$$

in which G is the shear modulus, η is a viscous coefficient, ω is the circular frequency of harmonic motion, and D is the damping ratio. Both G and D are strain dependent. Also, many complex nonlinear procedures (DESRA, SUMDES, TESS, etc.) include shear stiffness and damping in their formulation.

When a soil deposit is subjected to high levels of shaking, inertia forces, cyclic degradation of the stiffness, and the shear strength of soil may also affect the ground response. Thus, in addition to shear modulus and damping, unit weight of the soil and parameters to characterize cyclic degradation and shear failure may need to be included for realistic assessment. Complex models for strong earthquake excitation may also consider factors such as the degree of saturation of the soil and its contractive/dilative character. In all cases, however, the variation of shear modulus and damping with strain form a fundamental basis for evaluating site response. As a result, considerable attention has been given to their characterization for different soils.

1.3 Definition of Design Dynamic Soil Properties

When soil is subjected to symmetric cyclic loading, its shear stress-strain curve is typically idealized as a hysteretic loop of the type shown in Figure 1.1. This loop can be characterized by the actual path of the loop itself, as in the case of empirical non-linear models, which describe the behavior at any point during loading by the magnitude of shear strain (or shear stress), and the corresponding tangent shear modulus, G_{tan}. Since G_{tan} varies throughout each cycle of loading, a more convenient way to characterize the loop is by its general shape, i.e. its inclination and its breadth. The stiffness of the soil controls the inclination of the loop and its average value over the entire loop can be described by the secant shear modulus, G_{sec} or simply G, which is defined as the ratio of the shear stress, τ, to the shear strain, γ, on the virgin loading curve (or "backbone curve"). Because of the soil's nonlinearity, G is a function of the shear strain, γ. The breadth of the hysteresis loop depends on the energy dissipated during the cycle and can conventionally be described by the damping ratio:

$$D = \frac{1}{4\pi}\frac{W_D}{W_S} = \frac{1}{4\pi}\frac{Area\ of\ loop\ ACDEA}{Area\ of\ triangle\ OAB} \qquad \Lambda\ (2.2)$$

where W_D represents the dissipated energy, and W_S is the maximum (input) strain energy. The damping ratio is also a function of the shear strain level. When defined in this manner, G and D can be directly used in equivalent linear methods, which remain the most commonly used methods for site response analyses.

Modulus and damping are often considered separately for two ranges of strain separated by a value termed the "elastic threshold strain" ($\gamma \sim 0.001\%$). In the "low-strain range" below the elastic threshold, both modulus and damping are independent of strain amplitude and the respective values are identified as G_{max} and D_{min}. Above the elastic threshold in the "high-strain range", modulus decreases and damping increases with increasing strain amplitude.

The secant shear modulus is commonly normalized by G_{max} and presented in plots of normalized shear modulus, G/G_{max}, versus shear strain, γ. The damping ratio, D, is also presented in plots as a function of γ. Figure 1.2 shows examples of such plots on a common axis. Note that the shear strain axis is logarithmic and thus covers a very large range of values. This is consistent with the strain range of interest for sites subjected to earthquake hazard, and contributes to the difficulty of both the site response analyses, and the determination of properties to be used.

In summary, the basic parameters used in today's practice to characterize a soil's dynamic shear behavior are:

- Low-strain shear modulus, G_{max}
- The normalized modulus reduction curve, G/G_{max} vs. γ
- Damping ratio curve, D vs. γ

These are the properties which the Downhole Freestanding shear device has been developed to measure in situ.

1.4 Sensitivity of Ground Response to Dynamic Properties

The importance of accurately representing the soil dynamic properties for site response analyses is widely recognized. The NSF/EPRI Workshop on Dynamic Soil Properties and Site Characterization (CH2M HILL, 1991) pointed out that, regardless of the analytical methods used:

> **"The accuracy of those seismic response estimates is, however, controlled to a large extent by our ability to properly characterize the dynamic properties of the geological materials at the site."**

Studies have shown that relatively minor variations in soil properties can lead to large changes in the predicted site response to earthquake loading. This effect has been shown to dominate the effect of other factors, including the type of assumptions used to model the soil behavior (e.g., Roblee et. al, 1994).

The sensitivity of ground response to material properties was investigated in the early stages of this study, and the results are illustrated by the following examples. The examples involve an idealized case which is representative of a soft-clay site on the margin of San Francisco Bay. In the first study, described in greater detail by Li et al. (1993), and Roblee et al. (1994), two analytical procedures were used. The first is the popular equivalent linear program SHAKE (Idriss and Sun, 1992; Schnabel et al., 1972) and the second is the fully-nonlinear program SUMDES (Li et al., 1992). As shown in Figure 1.3, the stratigraphy consists of three soil strata having a total thickness of 90 ft (27 m) over a fractured rock layer above a bedrock half-space. The soil profile includes a surface layer of miscellaneous granular fill overlaying both soft (Young Bay Mud) and stiff (Old Bay Mud) clay layers. The values of shear-wave velocity and density assigned to each layer are considered typical and are included in Figure 1.3. For all

analyses, the "high-strain" dynamic properties of the soft clay (YBM) layer □ere varied, □hile the properties of all other layers were held constant. For the soft layer, the values of G_{max} and D_{min} were also held constant but a range of G/G_{max} vs. γ and D vs. γ curves were selected. The curves used in this study were based on the design curves presented by Vucetic and Dobry (1991) for plasticity indexes of 15%, 30% and 50% (see Figure 1.7(a)). The range of variability between the curves is well within that noted in the literature for this widely tested soil.

Three separate recorded input motions were used to represent a range of design earthquakes with different predominant frequency ranges. The motions are identified as "high", "mid", and "lo□" according to their frequency range. Figure 1.4 shows the time history and spectral content of the "mid" motion. The results of the SHAKE analyses are summarized in Figure 1.5, which shows the calculated response spectra for the soft clay layer with each of the three modulus reduction relationships. It is noticed that the differences in the design spectral amplitude are in excess of 50%, suggesting large differences in potential construction costs at such a site. This illustrates the high level of sensitivity of the response spectrum to relatively modest variation in the dynamic soil properties. On the other hand, the study also found good compatibility between the results from the equivalent linear program SHAKE and the fully non-linear program SUMDES when using the same assumed properties.

A similar study, described in greater detail by Roblee et al. (1996), was conducted to investigate the effect of the layer thickness and source-to-site distance on the sensitivity of ground response to dynamic soil properties. As shown in Figure 1.6(a), a soil profile similar to the one mentioned in the first example was used. The near-surface profiles consist of a 5 m thick fill overlaying young soft marine clay of varying thickness: 5 m for "thin", 15 m for "medium", and 30 m for "thick". A 10m-thick older clay transition layer is sandwiched between the young

clay layer and a generic stiff-soil profile to a depth of approximately 60 meters. The analyses were based on a generic Magnitude 7 strike-slip earthquake scenario where the site is located 3 km, 10 km, and 30 km away from the fault. The results were developed using a stochastically-based finite-fault model with an equivalent-linear formulation for soil behavior (Silva et al., 1990; Silva et al., 1992; Schneider et al., 1993). For each combination of soft clay layer thickness and source-to-site distance, the results were generated for three different G/G_{max} vs. γ and D vs. γ curves shown in Figure 1.6(b). These curves are also based on Vucetic and Dobry (1991) curves for plasticity indexes of 15, 30 and 50 to represent the measured range of behavior for San Francisco Young Bay Mud. Figure 1.6(c) shows the median response spectra for each combination of layer thickness, distance, and material properties. Note that the line pattern in Figures 1.6(b) and (c) correspond to one another. Again, the results clearly illustrate the strong influence of dynamic soil properties on ground response for a wide range of distances and clay-layer thicknesses.

In summary, these examples support the widely acknowledged observation that estimated ground response to earthquake excitation, when a sound analytical procedure is used, is highly dependent on the characterization of the subsurface conditions and a reasonable evaluation of the materials' dynamic properties. Moreover, the accuracy and reliability of other geotechnical dynamic analyses such as the applications of dynamic soil-structure interaction problems (e.g. seismic soil-pile-structure interaction, machine foundations, retaining structures, etc.) are also sensitive to soil properties. This provides a strong motivation to investigate and develop methods to define these properties more accurately, and to increase the confidence that measured soil properties reflect the behavior of the soil in the field, not just in the laboratory.

1.5 The Value of Field Measurements of Dynamic Soil Properties

Of the fundamental properties of interest, only the maximum shear modulus (G_{max}) is currently measured in the field in practice, using geophysical methods to measure shear wave velocity (V_S), and using the relationship between them ($G_{max} = \rho V_S^2$). In contrast, the modulus reduction curve (shear modulus vs. shear strain, G-γ) and the damping curve (D-γ) are usually either obtained from laboratory tests on samples taken from the field, or simply assumed through empirical correlations with other properties, such as the Plasticity Index (PI).

A significant problem with these approaches lies in the discrepancy between the maximum shear modulus measured in the field ($G_{max,field}$) and that measured in the laboratory ($G_{max,lab}$), with the field value nearly always being distinctly stiffer than the lab value. This common disparity suggests that the G-γ curve from laboratory testing cannot be directly used to accurately represent the G-γ behavior in the field. The difference between $G_{max,field}$ and $G_{max,lab}$ can range from 20-60%, even for the highest quality of testing, and varies according to soil type, sample depth, and the laboratory testing device and procedures. To account for this effect, $(G\text{-}\gamma)_{lab}$ is usually normalized by $G_{max,lab}$ to produce a normalized modulus reduction curve $(G/G_{max}\text{-}\gamma)_{lab}$. The $(G\text{-}\gamma)_{field}$ curve is then obtained from $(G/G_{max}\text{-}\gamma)_{lab}$ curve by scaling it by $G_{max,field}$. This approach assumes that $(G/G_{max}\text{-}\gamma)_{lab}$ is the same as $(G/G_{max}\text{-}\gamma)_{field}$, which is something that remains to be proven. Because of the large degree of disturbance associated with conventional sampling of deeper deposits, in fact, one could reasonably expect $(G/G_{max}\text{-}\gamma)_{lab}$ to be different from $(G/G_{max}\text{-}\gamma)_{field}$.

Generic curves for G/G_{max} -γ (e.g. Vucetic and Dobry, 1991) for different types of soils have also been introduced and used with $G_{max,field}$ to estimate field curves empirically. This approach capitalizes on the assumption that soils with similar properties (e.g. PI) have a similar

normalized stress-strain behavior. The problem with this approach is that natural soil deposits exhibit wide variations even in their normalized behavior. To illustrate this, Figure 1.7(b) reproduces a portion of the data from which Vucetic and Dobry (1991) derived their generic curves and data reported by other studies. The figure plots G/G_{max} versus plasticity index for a strain level of 0.1%. The data shows a large level of variability. For example, for a plasticity index of 40, G/G_{max} can vary from 0.3 to 0.7.

The dilemma with current approaches originates from the fact that the modulus reduction curve and the damping curve are not unique for a given soil but a function of many factors, including: soil structure, stress state and history, loading frequency, and the duration of time under the current confining stress. As discussed in Chapter 2, and in greater detail in Appendix C, sampling disturbance can significantly "erase" the inherent soil structure and, therefore, substantially affect the results of laboratory tests. The effects of many other factors on measured values of dynamic properties have been reported in the research literature, and are discussed in Appendix B (including detailed references), but the impact of some of these factors on current practices will be briefly summarized here.

The effect of frequency of loading on G increases directly with the plasticity index (PI) of the soil. The magnitude of shear modulus can change by 4-9% for an order of magnitude change in frequency (for a frequency level higher than 10 Hz). Since $G_{max,field}$ and $(G\text{-}\gamma)_{lab}$ are measured at different loading frequencies, scaling the latter by the former can result in an inaccurate estimation of the field curve. In addition, the loading frequency of interest during an earthquake can range form 0.1 to 25 Hz. In laboratory tests, loading frequency can range from 0.01 Hz in a simple shear test to 30-100 Hz in a resonant column test. In seismic field tests, on the other hand, the loading frequency is well above 100 Hz.

Moreover, many studies have shown that shear modulus is a time-dependent soil property. The value of shear modulus increases with increasing the time of application of the confining stress. In the field, the time-under-confinement can be in order of thousands of years while that in laboratory is usually one day or two. The impact of this difference on the measured soil properties is a function of the degree of disturbance in the laboratory samples.

In spite of these discrepancies between field and laboratory conditions, it has at least been possible to make predictions of $(G\text{-}\gamma)_{field}$. However, for damping ratio curves, because of the lack of field measurement of damping, only laboratory measurements are used to represent the field damping behavior, with no available means to assess how these curves compare to field curves.

In addition to these issues of reconciling laboratory and field behavior, the need to supplement field characterization with subsequent laboratory testing often leads to substantial delays in estimating the dynamic properties, largely because the necessary laboratory tests require special equipment and expertise that are not widely available. Valuable time and project resources could be saved if all the necessary properties could be determined in the field, and the laboratory testing phase could be eliminated or reduced to a confirmatory role. This would, of course, require a great deal of confidence in the new field methods, developed over time with experience at many sites.

1.6 History of the Downhole Freestanding Shear Device

The DFSD research project was initiated in late 1992 to address the need for a rapid means of evaluating site-specific material behavior and to examine the effects of sampling disturbance on the measured dynamic soil properties. The DFSD development has been achieved

in several phases and required the expertise of many researchers. Details of the early phases of DFSD development can be found in Li et al. (1993), Roblee et al. (1994), Roblee et al. (1996), and Wang (1997).

The development of the DFSD was very challenging and went through many stages that required the efforts of many researchers. This study presents the progress that was achieved since 1997 when the DFSD project was moved to the University of California at Berkeley. The objectives were first to continue developing the tool to make it fully functional and second to validate the tool performance through full-scale laboratory and field tests. In the past five years a lot of progress has been achieved including the improvement of the cutter module design, development of the load module, the electronic module, the instrumented membrane and its deployment system, transducers for load, deformation and pressure measurements including the elastomer gauge, development of the software and hardware of the data acquisition and control systems, integration and tuning of the different tool components, development of the benchtop version of the device and the "smart consolidometer" for laboratory validation tests, and the development of the DFSD field transportation and deployment equipment and accessories. The DFSD has been completed and for the first time is able to conduct all the various steps of a downhole test including sample creation under air confinement, remote membrane deployment, downhole cyclic torsional shear testing, and the ability to measure stress and deformation time histories over a wide strain range.

Full-scale DFSD laboratory validation tests have been conducted on two reconstituted cohesive soils in a setup that simulates field tests. The results from these tests were compared with the results from independent laboratory tests conducted at the University of Texas at Austin

and the University of California at Los Angeles as well as with shear wave velocity measurements made on DFSD samples. Moreover, the DFSD was deployed for field testing at the Richmond Field Station site using the newly developed field equipment. The results from DFSD field tests were compared with the results from shear wave velocity measurements made at the site. All these tests have indicated a successful performance of the device. The DFSD sample creation process has been proven to have minimal effects on the dynamic soil properties and the air confinement concept for maintaining the original in situ effective stresses during all test phases was validated. Most importantly, shear modulus, damping ratio and the soil non-linear behavior were fairly accurately obtained at a wide strain range from 0.0005% to 1%.

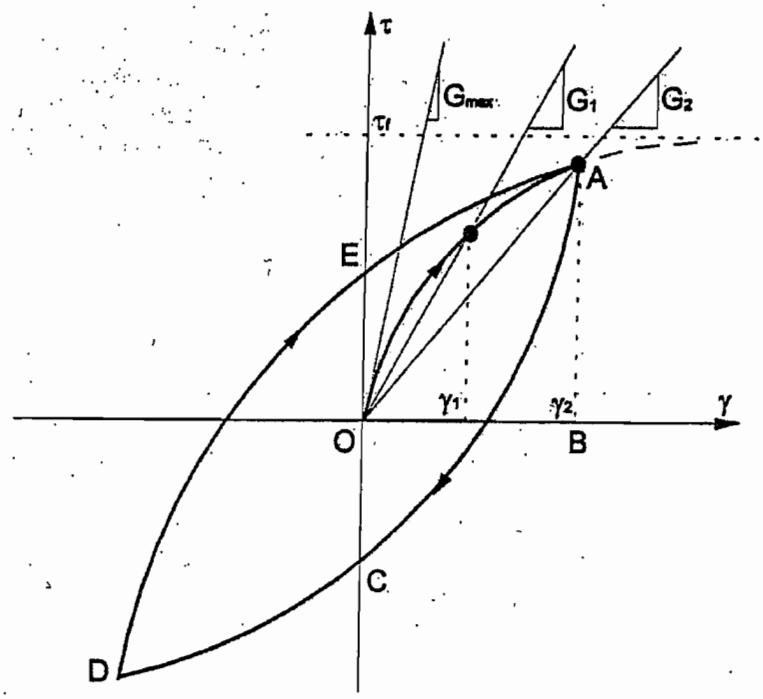

Figure 1.1 A typical hysteretic loop

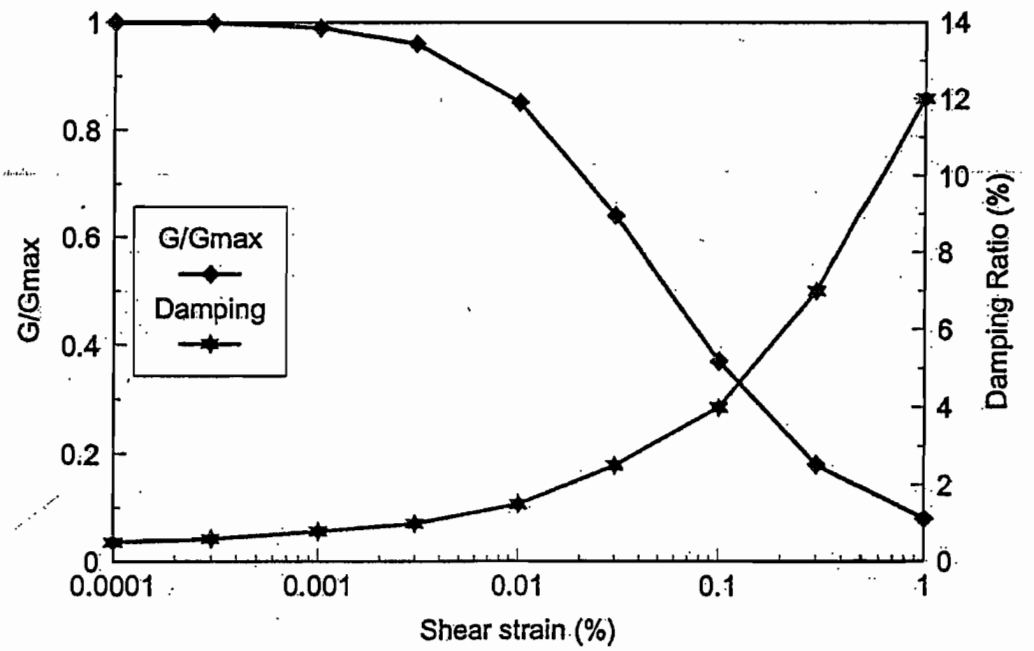

Figure 1.2 Typical modulus and damping ratio curves

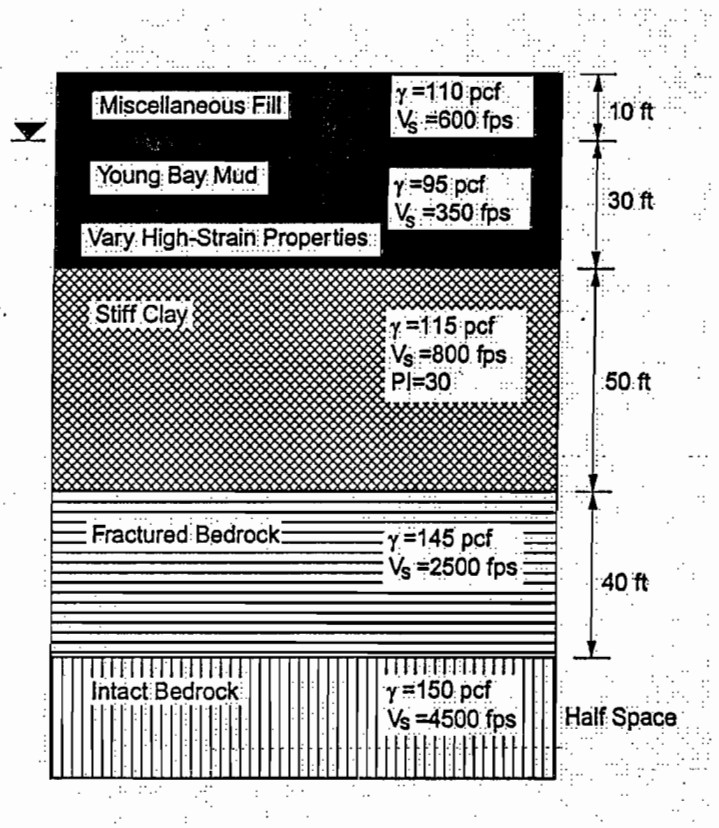

Figure 1.3 Soil profile illustrative example (after Li et al., 1993)

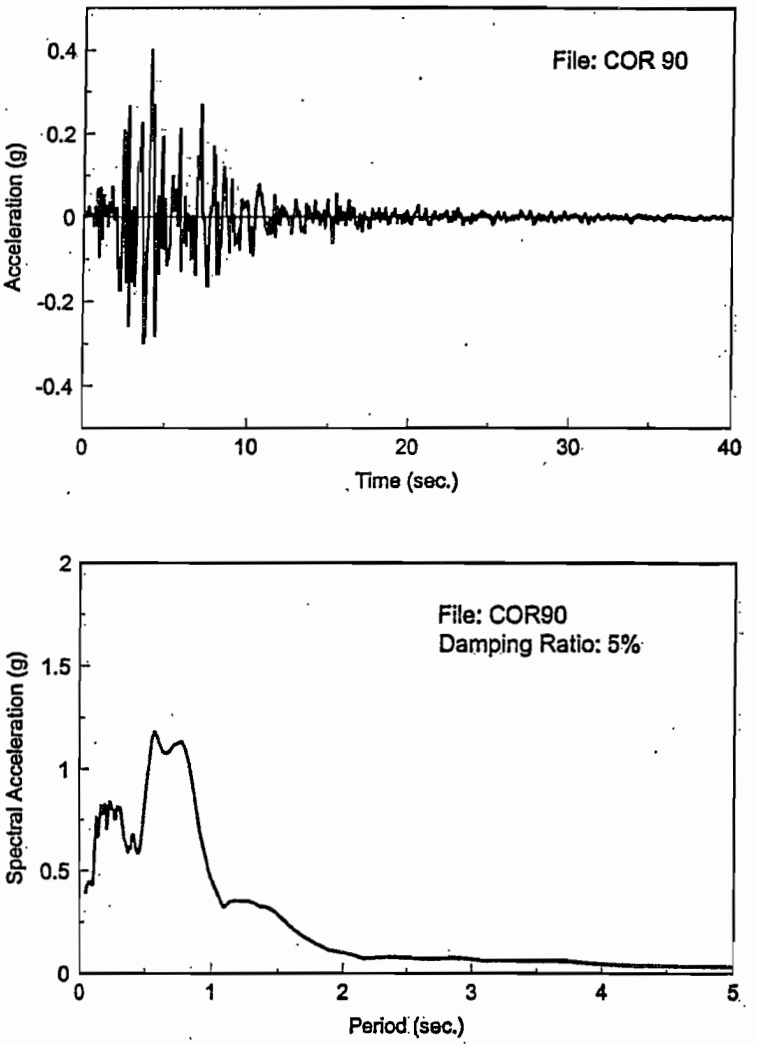

Figure 1.4 Acceleration time history and spectral acceleration of input motion (Li et al., 1993)

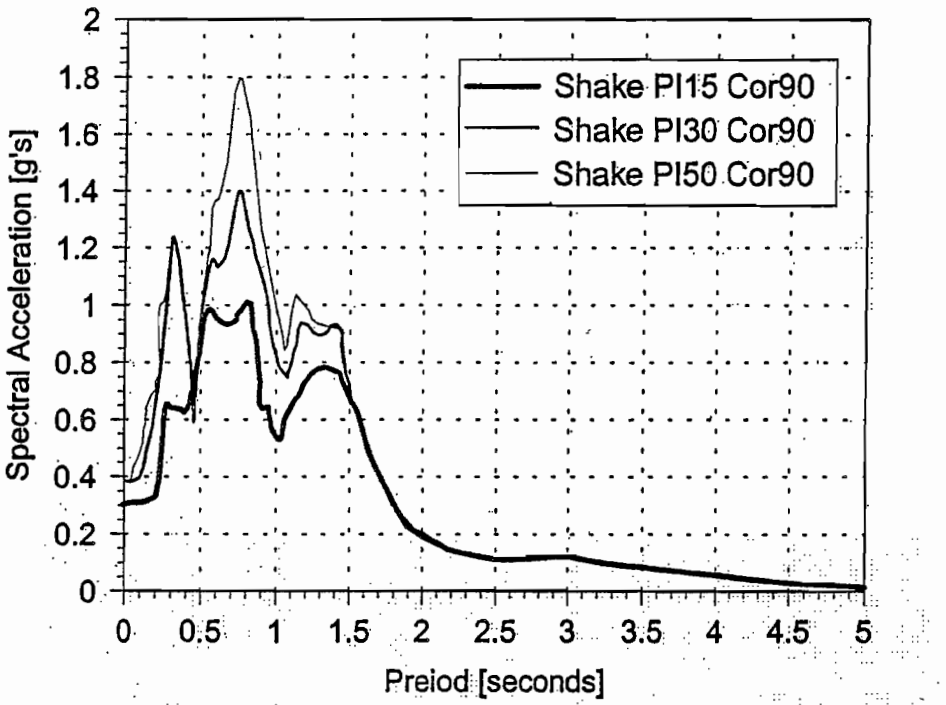

Figure 1.5 Influence of dynamic soil properties predicted by SHAKE (Li et al., 1993)

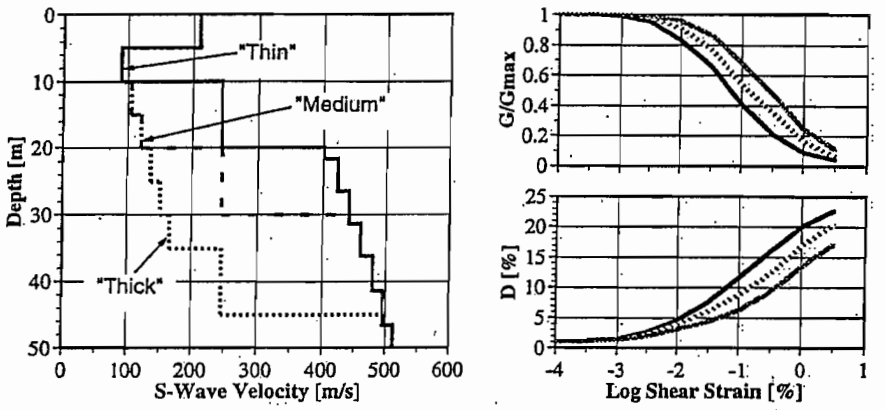

a) Velocity Profiles b) Non-Linear Properties

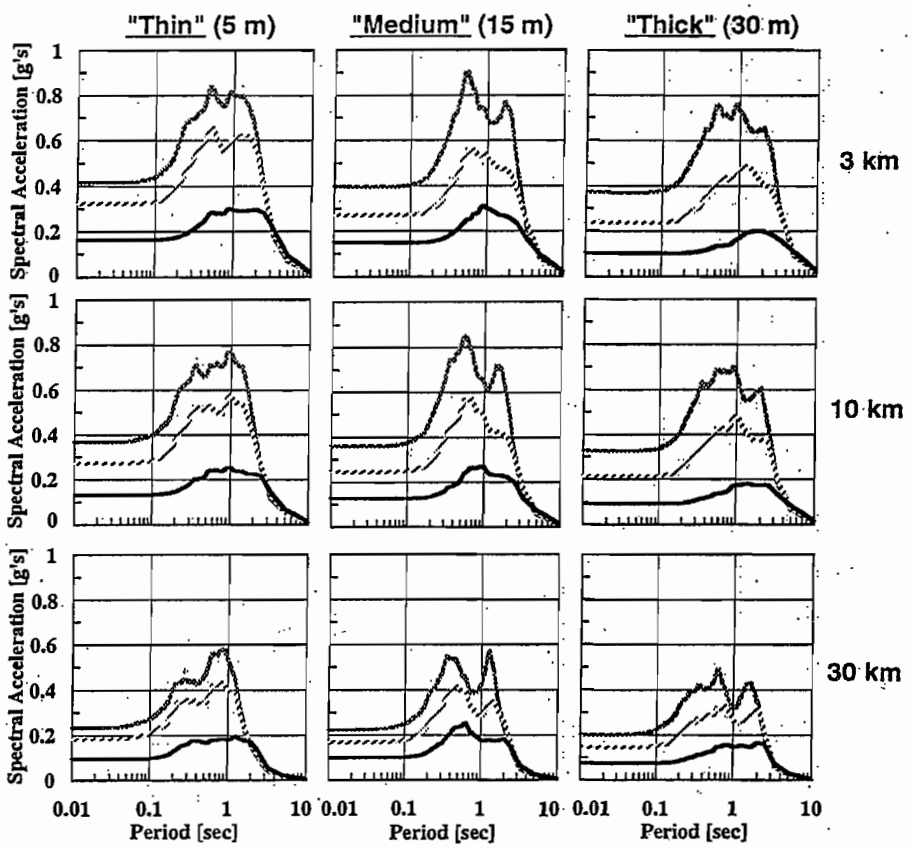

c) Results for different source-site distances and thicknesses of soft clay.

Figure 1.6 Sensitivity of site response to variations in dynamic soil properties for sites with different soft layer thickness and distance-to-source (Roblee et al., 1996)

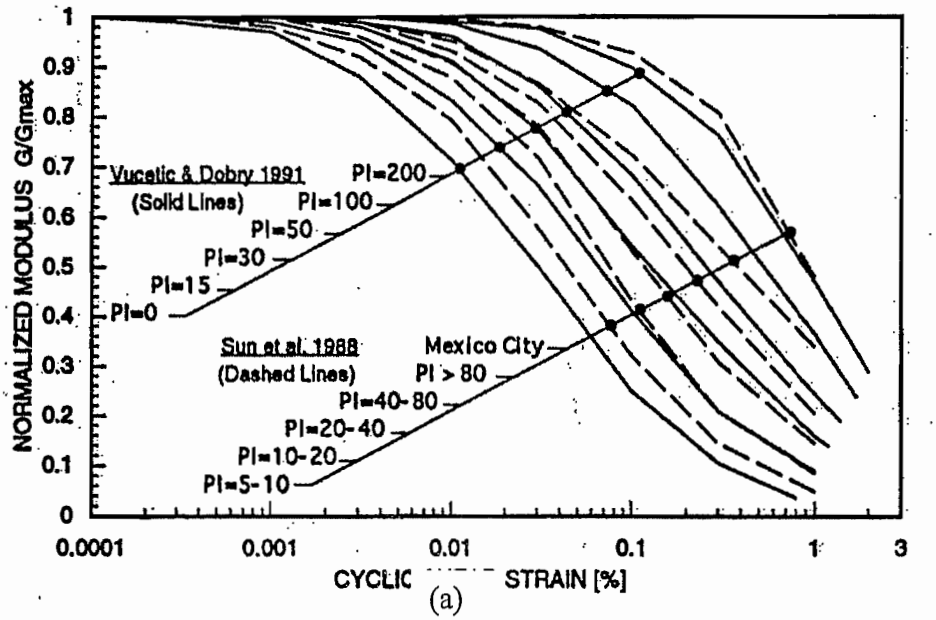

(a)

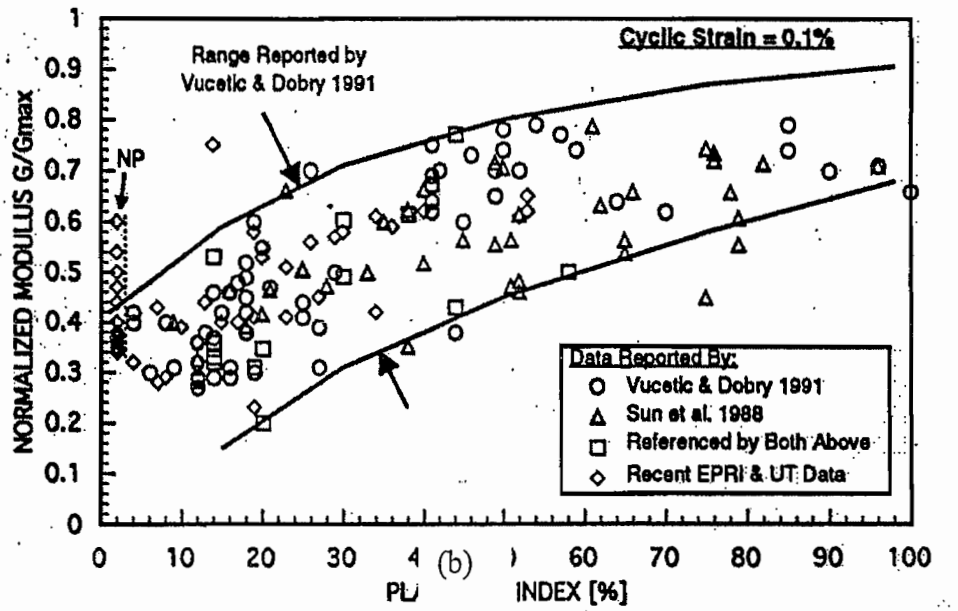

(b)

Figure 1.7 (a) Design Curves based on correlations to plasticity index, (b) range in normalized modulus for cyclic strain of 0.1% as a function of PI (Roblee et al., 1994)

CHAPTER 2

Operational Concept of the DFSD: Proving Feasibility

2.1 Introduction

The Downhole Freestanding Shear Device (DFSD) is an innovative geotechnical tool for rapid measurement of the dynamic properties (stiffness and damping characteristics) of fine-grained soils in situ. The device is designed to perform essentially laboratory-quality cyclic torsional shear testing, over a broad range of strains, on a freestanding column of soil beneath the bottom of a borehole. The dynamic properties obtained will provide important parameters for accurate prediction of seismic site response, particularly at sites with deep deposits of clay soils. The in-situ approach circumvents the limitations of existing testing methodologies for determining material properties by maintaining the original effective stress state throughout the specimen preparation and testing processes. The device will also be the first available tool to measure damping of the soil in the field, and will do so over a wide range of strains.

At the outset of the project, however, the researchers faced a wide array of questions regarding the approach that should be pursued to meet the testing objectives. These questions ranged from general choices among available options, to fundamental questions about what methods might really prove to be possible. Some of the key questions included:

- Should the test operate on an isolated element of soil, or the unbounded material?
- How can a specimen be prepared, in situ, under suitably undisturbed conditions?
- What type of loading should be applied?
- How can sufficiently accurate measurements of load and deformation be obtained?
- Can the properties be measured over the full strain range desired?

Successfully addressing these challenges required that technologies and procedures be identified or developed to surmount a number of feasibility issues, many of which were complicated by the remote nature of the downhole testing environment. While a number of these feasibility issues have been addressed in the earlier reports of this project (Li et al., 1993), this chapter provides an overview of the key developments that make the DFSD possible.

2.2 Downhole Freestanding Torsional Shear Concept

Since one of the primary objectives of the DFSD is to obtain intermediate-to-large strain properties of soil deposits at different depths, it was clear that the test could not succeed as a simple extension of conventional geophysical testing from the ground surface, but must instead operate from a borehole. One key issue that needed to be addressed early in the life of the project, however, was whether the test should be conducted on the unbounded region surrounding the bottom of the borehole, or on a discrete soil sample. Although easier to implement, the lack of clearly defined boundaries would make it difficult to precisely interpret test data, and would thereby introduce a significant level of uncertainty in the test results. In addition, experience with current field devices which employ this technique (e.g. the pressuremeter test) shows the significant detrimental effect the disturbed zone (at the boundaries of borehole) can have on test measurements, and the difficulties in bypassing this zone, particularly for small strain properties. Therefore, to obtain sufficiently accurate measurements, it was decided that developing a test on a discrete soil sample would be pursued. This requires the creation of a "freestanding" soil sample at the bottom of a borehole, which immediately raises the challenge of creating such a specimen with minimal disturbance to the fabric and structure of the soil.

The second issue that needed to be addressed is the type of loading mechanism to be applied. The alternatives considered included, among others; simple shear, triaxial shear, and torsional shear. Figure 2.1 shows the different design concepts considered during the early stages of the DFSD project. Although it has some attractive features, a simple shear test is difficult to implement in a borehole environment. The concept utilizing a downhole rectangular shear box, while directly representing the loading mechanism of vertically propagating shear waves, would have led to very complex tool design, and would result in a small attainable sample size, limited measurement range, and many unresolved design problems. On the other hand, cyclic triaxial and cyclic torsional shear tests on a freestanding solid cylindrical sample offer more practical design alternatives. A downhole triaxial test would have similar pros and cons to that of laboratory triaxial devices. It would utilize an axial motion with good control of the initial stress state, but it would suffer from the limitations of an inclined shear plane, lack of principle stress rotation, and the need for additional assumptions for data interpretation. Of additional concern in situ would be the effect of the disturbed zone immediately below the borehole, which would constitute the top of the triaxial specimen, and introduce compliance to the overall specimen response.

Accordingly, the freestanding torsional shear method, shown in Figure 2.2, was identified as the method with the most promising features for a downhole test. First, it accurately simulates the predominant earthquake motion in terms of orientation of shear planes and rotation of principle stresses. Second, its cylindrical shape offers good control of the stress state, including the ability to apply isotropic and anisotropic stresses, while maintaining a constant normal stress during the shearing process. Third, it could provide an opportunity to bypass the disturbed zone immediately below the bottom of the borehole. Finally, measurements over the full strain range

could potentially be attained. One of the main inherent limitations of torsional shear tests on solid cylindrical samples could stem from the non-uniform strain field across the radius of the specimen, and this required further investigation. Finally, even though cyclic torsional shear is intended to be the primary loading mechanism, a cyclic triaxial test could be conducted using the DFSD since it requires simple modifications.

2.3 Minimizing Effects of Disturbance on Measured Soil Properties

As mentioned previously, laboratory tests on soil samples usually underestimate the in-situ soil stiffness. This is primarily attributed to disturbance of the soil structure caused by the drilling, sampling, transportation, storage, extrusion, and sample preparation processes. The potential impact of disturbance on measured soil properties has been recognized for a long time. Hvorslev (1949) suggested that disturbance is caused by five mechanisms; change in stress condition, change in soil structure, change in water content/void ratio distribution, chemical changes, and mixing and segregation of soil constituents. More recent studies have suggested that among these mechanisms, changes in the stress condition (and the resulting deformations caused by stress release), and mechanical disturbance are the main two factors affecting the behavior of soil samples obtained by conventional sampling methods.

Mechanical disturbance is caused by the process of drilling, the insertion of a sampling tube, and suction during the retrieval of the sampling tube. Accordingly, one would expect that portions of the soil sample near the top (bottom of borehole) and near the cut surfaces would be disturbed the most. Mechanical disturbance can often be reduced by using improved procedures and equipment, for example by cleaning the borehole before sampling and by using a more appropriate sampler design. Stress changes include those caused by drilling, through the

removal of overburden pressure, and sampling-induced stress change caused by tube penetration and sample extrusion. Beneath the bottom of the borehole, stress changes during drilling can be minimized through the use of bentonite slurry while advancing the borehole. In contrast, the stress release experienced by a sample extruded at the ground surface, relative to its in situ stress at depth, is an inherent consequence of the process of sampling and is unavoidable. In contrast to the shearing of mechanical disturbance, stress release has a more uniform "global" effect on the sample.

Many researchers use the term "perfect sampling disturbance" to refer to a sampling process where disturbance is caused only by stress release, while the term "ideal sampling disturbance" is used when both disturbance mechanisms, i.e. stress release and structural disturbance caused mainly by tube penetration, are considered. Notice that disturbances caused by other processes, e.g. transportation and handling, are not included in either definition because they are very variable and difficult to model. Nevertheless, they are also easier to reduce if proper precautions are taken. Therefore, this chapter will only address disturbance caused by stress release and tube penetration. In addition, since the DFSD is designed to test fine grained soils, only the effect of sampling disturbance on these soils will be discussed here. Cohesionless soils are difficult to sample without a significant change to their structure.

Despite the important impact sampling and drilling disturbance has on measured soil properties, it was not until the last two decades that researchers started to evaluate disturbance quantitatively rather than qualitatively. This trend was especially encouraged by the introduction of the Strain Path Method (Baligh, 1985). However, the phenomenon is still not fully understood and more studies are needed. Moreover, most of the available studies address the impact of disturbance on high-strain soil parameters (e.g., shear strength or strain at failure). Relative to

these parameters, dynamic soil properties occur at rather smaller strains and therefore one should be cautious when extrapolating the results of these studies.

2.3.1 Disturbance Due to Drilling

Drilling is another potential source of soil disturbance that should be addressed in the context of the sampling process, and for in-situ tests which involve drilling a borehole. As part of the DFSD project, two studies have been performed to numerically model the influence of the drilling process on the in-situ state of stresses and strains around the borehole. In addition, such studies enable one to identify zones of soil that are most disturbed so that they can be avoided and zones of least disturbance which can be targeted for testing. The first study (described in greater detail by Li et al., 1993) used the SAC2 finite element code (Hermann and Mish, 1983, and Hermann and Kaliakin, 1987) to evaluate a twenty-foot deep borehole in soils of various permeabilities and Overconsolidation Ratio (OCR) along with certain assumptions to model the drilling process. The study assumed the soil is homogeneous and the model parameters used in the analyses are those for a "typical" soft clay.

A more recent study (Li et al., 1997) used the more advanced ABAQUS finite element code (ABAQUS, 1994) to refine the assumptions made in the previous study and to further evaluate the effect of depth and clay properties on the borehole modeling. The Cam-Clay model was used in the analyses and the soil was assumed to have an OCR of one. Three sets of analyses were performed in this study. To establish confidence in the repeatability of the numerical modeling, the first case was a direct comparison with one case from the earlier SAC2 study. The effects of depth and clay parameters were evaluated in the second and third set. To compare the results of the two models, the changes in stress state induced at four different depths below the

center of the borehole (shown in Figure 2.3 as elements A, B, C and D) were compiled for the two analyses. As shown in Figure 2.4, the resulting stress paths for elements B, C, and D are remarkably similar from the SAC2 and ABAQUS analyses. For element A, because of the assumptions made regarding the removal of vertical stress and distribution of lateral stress in the SAC2 analysis, the stress path from the two studies are different, however, the start and end points are very similar. This gives a high degree of confidence in at least the qualitative implications of these simulations.

The results from all cases show that the zone of soil influenced by the drilling process extends to depths approximately three diameters (3d) below the bottom of the borehole. The zone immediately below the borehole (element A) is the most disturbed and has undergone a reversal in the major principal stress from vertical to horizontal. However, the soil approximately one diameter below the borehole (e.g., between elements C and D) has experienced a small reduction in the stress ratio and mean effective stress and appears to be stable with the passage of time, therefore, it can be considered tolerably unaffected by the drilling process. This zone represents a "target" zone for either sampling or conducting a downhole in-situ testing. The amount of deviatoric strain experienced by soil in this zone is on the order of 0.1%. Since this strain is mainly due to unloading and follows a path within the yield boundary, it can be considered to be largely elastic, and therefore recoverable upon the re-establishment of in-situ stresses. Moreover, the analyses assumed that the in-situ soil is normally-consolidated which means that its state is right on the yield surface, when in fact most natural clays, particularly at depth, exist somewhat within their limit state boundary, and thus the analyses may have over-predicted the degree of disturbance.

The ABAQUS model was used to study the effect of borehole depth on the degree of disturbance. Borehole depths of 10, 20, and 40 feet were analyzed. The deviatoric and mean stresses are normalized to allow comparison of stress paths of points at different absolute depths but which are at the same distance from the bottom of the borehole. The results clearly show that the depth of the borehole has little influence on the degree of disturbance resulting from the drilling process, based on the similarity of stress paths. The study also investigated the effect of different soil parameters (i.e., different soil behavior) to evaluate the sensitivity of the results on the material properties. With a fixed borehole depth of 40 ft, three different cases were analyzed. Again, little influence of these variations was observed on the degree of stress change below the borehole, with the case simulating Bay Mud parameters resulting in slightly less deviatoric strains in the target zone. The stresses within the target zone remain anisotropic, with a stress ratio of 0.5-0.7.

2.3.2 Disturbance from Creating the Specimen

One of the challenging tasks in the DFSD was the design of a mechanism to carve a freestanding soil column at the bottom of a borehole. The mission was complicated by the desire to maintain the in-situ stresses throughout the carving process. The simplest option is to utilize the standard tube-sampling techniques, which would involve a pushed-tube located at the bottom of the borehole, but with a geometry that would allow for free space around the carved sample to accommodate an instrumented membrane and through which a controllable confining air pressured can be applied. However, this would require a substantial area ratio of the sampler, and the soil disturbance generated by this method would be large enough to cause significant impact on the measurements. A more elegant option, and the one pursued for the DFSD, involves a

self-boring mechanism in which the soil around the sample is removed rather than simply displaced. This could be achieved by a rotating cutting tool slowly advanced into the soil. Even though it is substantially more complex in operation, it is the only feasible option to sufficiently minimize disturbance during sample creation and facilitate other operations (such as the membrane deployment and air confinement) that need to take place around the specimen during the carving process. Moreover, the method provides the DFSD with a big advantage (as a sampling as well as a testing device) over many current sampling techniques. This approach was also encouraged by numerical and experimental studies that addressed this issue. For instance, Baligh's (1985) work using the strain path method shows that when a sharp tool is inserted into the soil such that it cuts through the soil rather than displacing it, the resulting strains are much smaller than when the tool was blunt enough to simply displace the soil. Also, experimental studies (e.g., La Rochelle et al. (1981)) done on samplers which utilize some sort of self-boring technique showed that sample quality can be as good as those obtained from a block sample in terms of subsequent consolidation and shearing behavior.

2.3.3 Disturbance Cause by Stress Release

This section focuses on the soil response to undrained shear stress release from the initial anisotropic in situ stress state to the final condition after the sample is created – which for a laboratory sample of clay is typically an isotropic effective stress from the pore water tension after extrusion. All other disturbance mechanisms are neglected (hence, the name "perfect sampling"). The effect of in situ stress release can be seen in two areas. First, the potential reduction in effective stress inside the sample, which will affect the measured soil properties if the in situ effective stresses are not re-established (which is particularly important for *in situ* tests

on soil samples). Second, whether the stress change will put the soil outside the limit state boundary (either stress- or strain-wise), thus, causing significant changes in the soil structure.

One issue that is not often discussed in the context of sampling disturbance, but which is especially important for dynamic soil properties, is the effect of time under confinement. The limit state boundary concept suggests that, assuming perfect sampling conditions, if during stress relief the stress/strain state does not exceed the limit state, time effect should still be preserved and reflected in the way soil particles are structured. Therefore, the in situ soil behavior should be retained from the soil sample once the in situ stresses are reapplied. However, if the limit state is exceeded (e.g., with deep tube samples of saturated clay), significant changes in soil structure take place which indicates that the effect of time under confinement is lost (at least partially) and re-applying in situ stresses will not be enough to retain the in situ soil structure. Perfect sampling is practically impossible to achieve because of the inevitable mechanical distortion introduced at least by sampling tube insertion. Even in the case of block sampling, a thin layer of remolded clay at the surface of the sample is created during the carving process.

2.4 Maintaining Stresses Using Air Confinement

As mentioned above, the inherent soil structure and the effect of time under confinement can be preserved if the limit state boundary is not exceeded. One of the strategies employed in the DFSD to minimize stress change during carving of the freestanding sample is the temporary application of air pressure directly to the sample's vertical surface. This pressure is intended to serve as a temporary substitute for the total lateral stress that had been acting on the sample, until the carving process is completed and the latex membrane can be applied. This concept relies on the capillary menisci which form over interparticle voids of saturated, fine soils to serve as an air

entry barrier much like a membrane. This is, of course, provided that the applied air confining pressure does not exceed the air entry pressure of the soil. For soils with extremely small particles like clays, the air entry pressure can be on the order of several atmospheres.

This concept was initially evaluated in a special laboratory investigation (Wang, 1997) and has subsequently been verified by many tests conducted by the DFSD, as shown in the Chapter 4. The laboratory testing was conducted using a conventional triaxial apparatus, though the base and top caps were modified to use small, central porous stones. Also, to provide for the application of air pressure within the membrane, an additional port and pressure line was added to the top cap, as shown in Figure 2.5(a). To conduct the test, a sample of Yolo Loam (a silty clay native to the Davis area) was first consolidated within a membrane in a conventional water-filled chamber to a certain isotropic stress and then, with the drainage ports closed, a deviatoric stress equal to 80% of the shear strength of the soil was applied to the specimen, which was then allowed to stabilize. To simulate the air confinement concept, first the water was drained from the triaxial cell and then an air pressure slightly higher than the cell pressure was applied inside the membrane. This "switch over" causes the membrane to inflate away from the specimen, and the air pressure to be directly applied against the surface of the soil.

A failure of the air confinement would result in a loss of the effective lateral stress within the soil, which should be measured by the devices transducers, but which would also lead to large axial deformations or even failure of the specimen under these large deviatoric stresses. Figure 2.5 shows the results of one such test (from a series of four at different consolidation stresses) in the form of the effective stresses and vertical strains over time, with the air confinement "switch over" occurring at approximately 450 minutes after applying the deviatoric stress. While the soil continues to stabilize under the anisotropic stresses, there is little or no

effect of the replacement of the membrane by the direct application of air pressure on the soil surface for the 1000 minutes the test was continued. Eventually, of course, applying this air pressure would tend to dry out and alter the surface of the specimen, so the air confinement is only intended to maintain the stress state for the 20 to 30 minutes needed to complete carving of the specimen. In the course of the lab feasibility investigation, none of the specimens showed excessive vertical strains that would be associated with failure of the menisci, which suggested that at least for clays, this could be a viable method of maintaining the anisotropic stress state on the soil in the target zone, while the DFSD was carving the freestanding specimen.

2.5 Load and Deformation Measurement Approach

To characterize the response of a cylinder tested in torsion, the applied torque and the torsional deformation are the key quantities to be measured. For the freestanding soil column created at the bottom of a borehole, there are complex top and bottom boundary conditions. At the top, the soil is largely disturbed by the drilling process. The finite element studies summarized in Section 2.3.1 indicated that substantial disturbance from drilling effects are likely to extend at least 4 to 6 inches (10 to 15 cm) below the bottom of the borehole. At the same time, the soil column is still connected to the surrounding soil at the base, thus creating a complex situation for data interpretation at the lower end as well. While the applied torque can be most easily measured at the top cap, with confidence that all horizontal sections of the specimen must be experiencing the same torque, the situation is more complicated for the strain measurements.

Both specimen end conditions work against a conventional top-of-specimen, global measurement of the strain. Such measurements across the entire sample would be largely affected by the disturbed zone of soil and, for a torsional shear test, requires a fixed sample

bottom as a reference, which is not the case here. It is likely that the bottom of a DFSD sample would act like a "soil pedestal" that undergoes a certain degree of rotation during a torsional test. For both of these reasons, mid-specimen local strain measurement emerged as the most feasible remedy for these boundary conditions. Moreover, this strategy also addresses another general limitation present in most soil testing. It is widely recognized that, when compared with local strain measurement, strains measured globally over the sample often yield a softer soil response because of the effects of compliance, end restraints, and bending which are not accounted for in many global strain-measurement regimes. Experimental data from static and dynamic tests have consistently shown the significance of this difference.

Although theoretically very desirable, the mid-specimen instrumentation strategy raises significant problems. It requires a special breed of strain gauges with exceptional versatility so that they can be deployed in a downhole environment. They need to be flexible enough to bond to a latex membrane which was expanded away from the soil, then pressurized against the surface of a freestanding sample for on-sample strain measurements. Moreover, these gauges should fulfill one of the main challenging tasks in the DFSD objectives, that is, the ability to measure four orders of magnitude of strain in a suite of tests in a single tool deployment. Unfortunately, no such gauges were commercially available for use in any of the current soil testing methods. The DFSD team had to go through a long process of search and research to develop and obtain gauges capable of meeting the necessary criteria.

2.6 Deformation Gauge Alternatives

Several local deformation transducer concepts were initially identified as potential approaches for evaluation, including a conductive rubber gauge, a mercury gauge, a magnetic

gauge and two types of "flex gauge", all illustrated schematically in Figure 2.6 (a-e), respectively. The features and perceived advantages of these gauges are discussed below.

The Conductive Rubber gauge and Mercury/salted water gauge are both based on the theory that the change of geometry of the gauge creates a change in its electric resistance, in same manner that foil strain gauges operate. If an electric conducting element has a uniform cross sectional area A, an initial length l, and the resistivity associated with this particular material ρ, the electric resistance R of this element is

$$R = \rho \frac{l}{A} \qquad (2\text{-}1)$$

It can be shown that the change of resistance R can be rewritten as

$$dR = K_s \frac{dl}{l} \qquad (2\text{-}2)$$

Where K_s is the sensitivity coefficient of the material. K_s is a function of the Poisson's ratio, the material's electrical characteristics, and manufacturing procedures. It can be constant for some materials but variable for others.

Conductive Rubber Gauge

The rubber gauge is an electric conducting rubber strip, cut from a sheet stock. The strip is made to a dimension of 0.25 × 1.75 × 0.05 inch (as shown in

Figure (a)). The nominal resistance of the rubber strip is a function of its length and cross sectional area. When the strip changes its cross sectional area or length when stretched or shortened, the resistance changes accordingly. To be useful as a gauge, the relation between the resistance change and the deformation causing it must be reliable and stable, so that a dependable

calibration can be achieved. Unfortunately, the conductive rubber material exhibits significant creep under constant load meaning no constant calibration value could be determined.

Mercury Gauge

The proposed Mercury gauge consists of a very stretchable plastic tubing with a 1/8 inch inside diameter and 0.012 inch wall thickness (shown in Figure 2.6(b)). The tube is filled with mercury and sealed at both ends with electric conducting leads attached. The tube should be free of air, or erroneous measurement will be made. When lengthened or shortened, the mercury in the plastic tube changes its cross sectional area and its length. Through calibration, the change in resistance can be correlated to the change in length. Mercury was proposed for this gauge because it is a liquid metal at ambient temperatures, and is highly conductive. Unfortunately, there were many disadvantages identified when first investigated, including: mercury is a toxic material, raising safety issues; it has a high surface tension which makes it difficult to fill the tubing; the tubing tended to deteriorate over time (requiring frequent re-calibration); the sensitivity of the gauge was not sufficient to measure small strains; and the deformation of the tubing when attached to the membrane was unpredictable.

Attempts to address some of these problems involved replacing the mercury with 1.0 % salted water (by weight) in the plastic tube. At room temperature, however, the salt tends to precipitate out when the concentration is high enough to provide the needed sensitivity. Another disadvantage of using salted water is that during use, air bubbles come out the solution (possibly due to electrolysis). If the gauge is connected to the measurement circuit for long enough, tiny air bubbles will form a large enough bubble to break the electrical continuity of the solution in the tube, making the gauge inoperable.

Magnetic Gauge

The magnetic gauge is composed of a latex case filled with ferromagnetic powder. The case is made of latex membrane 0.012 inch in thickness. Typical dimensions of the case are 0.5 × 1.5 × 0.1 inch, as shown in Figure 2.6(c). The operating principle behind the magnetic gauge is that changes of the geometry of a magnetic element results in change of magnetic field. The relationship between deformation of a gauge and change of magnetic field could conceivably be identified by calibration.

The advantages of using the magnetic gauge are that the gauge's case is made of the same latex material as the membrane sleeve so that deformation characteristics of both are compatible, that the gauge has a very low stiffness, thereby imposing no restriction on sample deformation at the location where gauges are mounted, and that the gauge is very stretchable such that the deformation measurement covers both low and high strain range.

The problem with the magnetic gauge centers on the ferromagnetic powder's lack of consistent form. Consequently any change of geometry of the gauge or even change of orientation of the gauge causes abrupt change of magnetic field, and that even though calibration can be made to characterize the deformation of the gauge and the change in the detected magnetic field, no single mathematic relation between these two can be established, it is difficult, if not impossible, to predict every possible geometrical change of the gauge during a test. Compared to gauges that are based on changes in electrical resistance, these gauges would require more complex equipment to monitor and record strains downhole.

Flex Gauges

Two types of flex gauges were examined, the *flex flat gauge* and the *flex coil gauge*. These gauges are made of enamel-insulated, four mil diameter number 38 transformer wire, arranged in unique shapes and then encased in latex rubber to preserve their geometrical configurations.

These gauges are inductor type transducers. When subject to an axial deformation, the inductance of the gauges change in response, which can then be measured directly, or though changes in the electrical impedance, or the phase angle (ϕ) between the voltage and current in an oscillating circuit.

Of the ideas originally identified, the Flex Coil Gauge was developed most aggressively for several years, as working prototypes and eventually specialty fabricators were located to produce small batches of them. These gauges had reasonably good sensitivity, they could be mounted directly to the membranes for specimen testing, and while the electronics needed to run them were relatively complex, secondary data interpretation hardware was developed to convert the measured shift in phase angle to a DC voltage that computers could record. Flex gauges were used evaluated in triaxial testing, comparing the implied strains with those measured with conventional LVDTs, and preliminary results were relatively promising for these types of laboratory tests. Li (1996) has used them in a variety of laboratory testing studies, and describes them in detail.

Unfortunately, the Flex gauges also exhibited some troubling features, particularly for their use in the DFSD. These included a tendency for the readings to shift suddenly if the gauge was pressed, or expanded away from a specimen and then reapplied, and a significant lag, or delay in registering deformations of the specimen, as compared to the other sensors. This would not be a problem in static testing, but was not acceptable for strain measurements in dynamic testing. It was also unclear how the necessary circuitry for powering, conditioning and interpreting the gauges would be incorporated downhole within the DFSD.

Although it required a significant delay in the overall development, it was decided to pursue another type of gauge as an alternative. This involved returning to the general concept of

the mercury gauge, but with different materials and a very different fabrication process. Based on a short-lived product developed in the 1970's, the Elastomer gauge consists of a fine capillary filled with a liquid metal alloy, which operates on a simple change in electrical resistance principle. Because these gauges were no longer commercially available, our research team learned to fabricate them in house, and to vary the design to achieve a range of different properties and sensitivities. The Elastomer gauges have proven to be more responsive to applied strains, less subject to drift when held constant, and much easier to drive and record data from. A detailed discussion of the Elastomer gauge concept and its implementation is presented in Appendix E.

With the Elastomer gauges mounted diagonally on the membrane, with respect to the axis of the sample, the shear strain can be easily obtained from the strains in the individual gauges. A set of multiple gauges at the same elevation enhances the accuracy of the strain measurement and minimize the effect of bending, electrical drift, and noise in the system. Therefore, with the torque being applied through a vaned top cap, a DFSD test will yield stress and strain time histories from which shear modulus and damping values can be obtained.

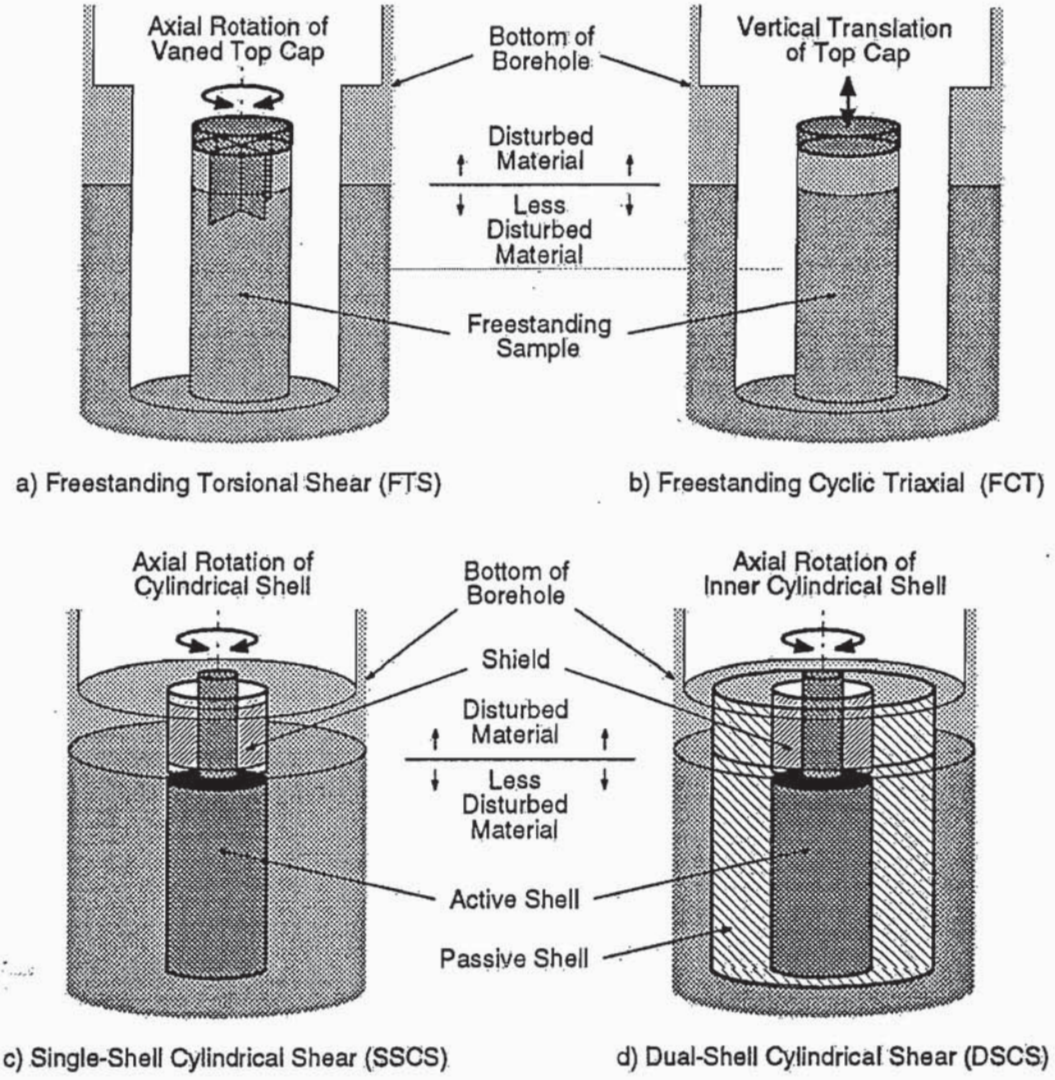

Figure 2.1: Different downhole testing schemes considered at the early stages of DFSD development (Li et al., 1993)

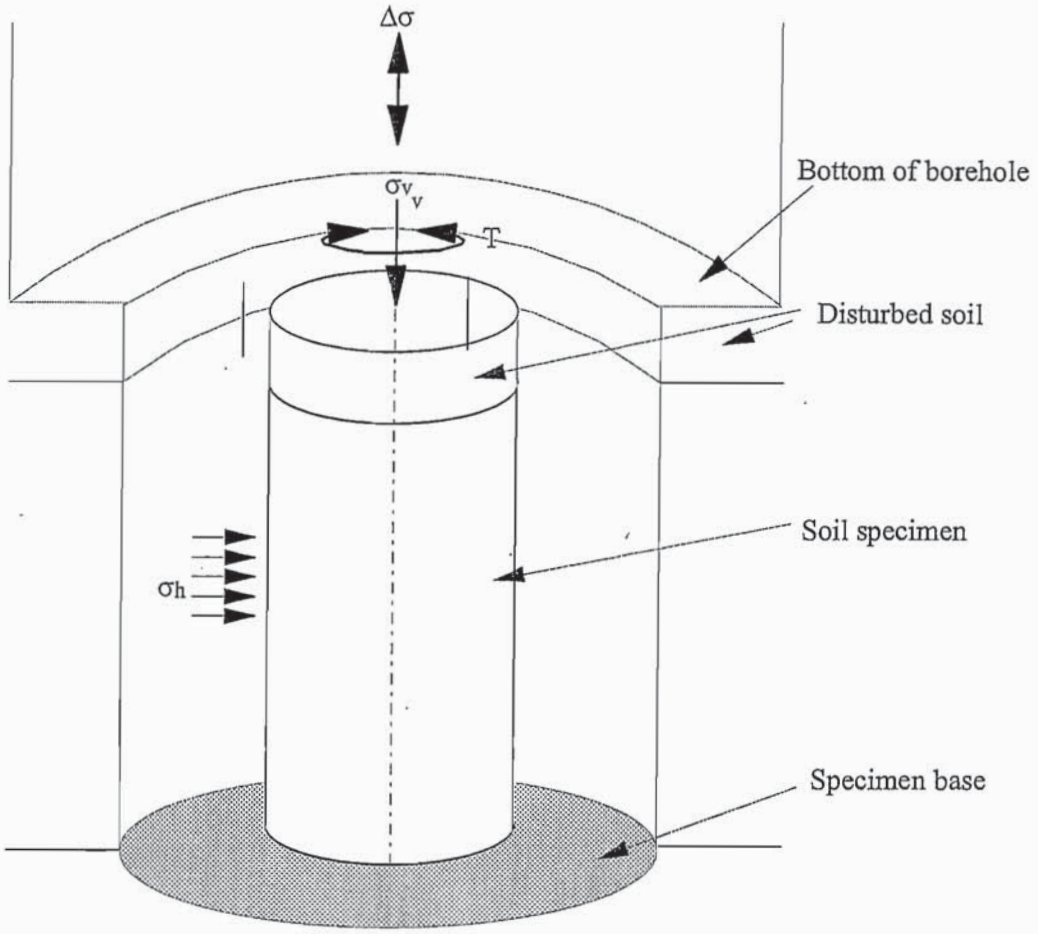

Figure 2.2: Schematic diagram showing the downhole torsional shear concept (Wang, 1997)

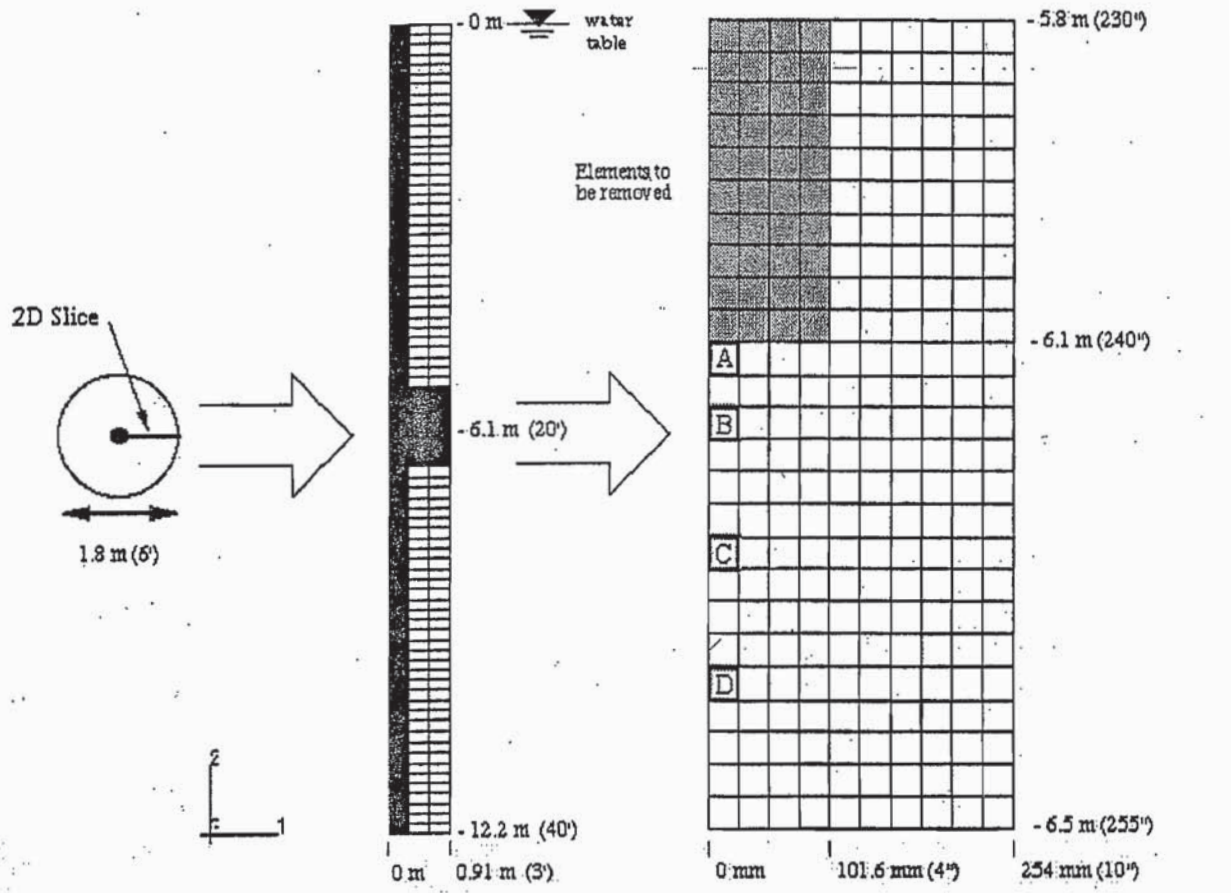

Figure 2.3: ABAQUS finite element model and the locations of elements selected for stress-path plotting (Li et al., 1997)

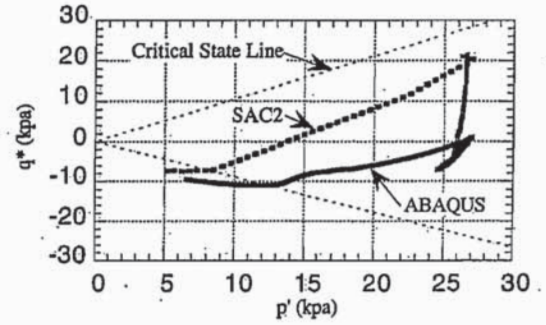

Figure 5.15a Stress path comparison for element A

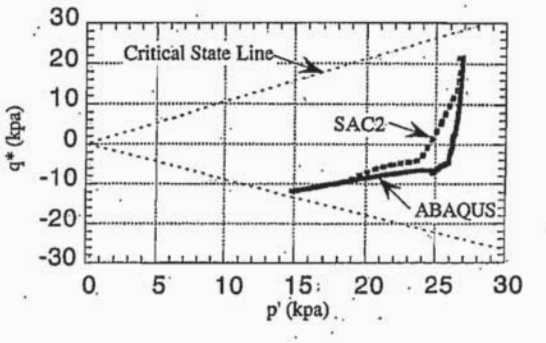

Figure 5.15b Stress path comparison for element B

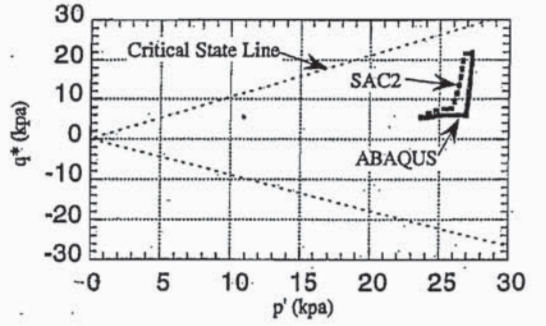

Figure 5.15c Stress path comparison for element C

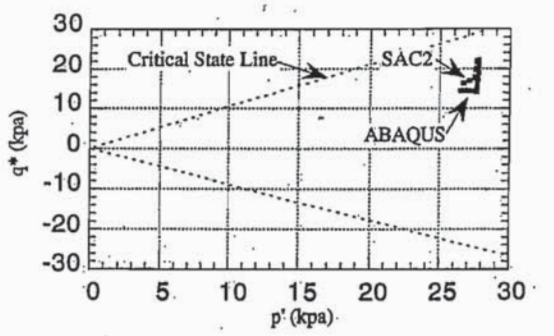

Figure 5.15d Stress path comparison for element D

Figure 2.4: Comparison of results from the SAC2 and ABAQUS models (Li et al., 1997)

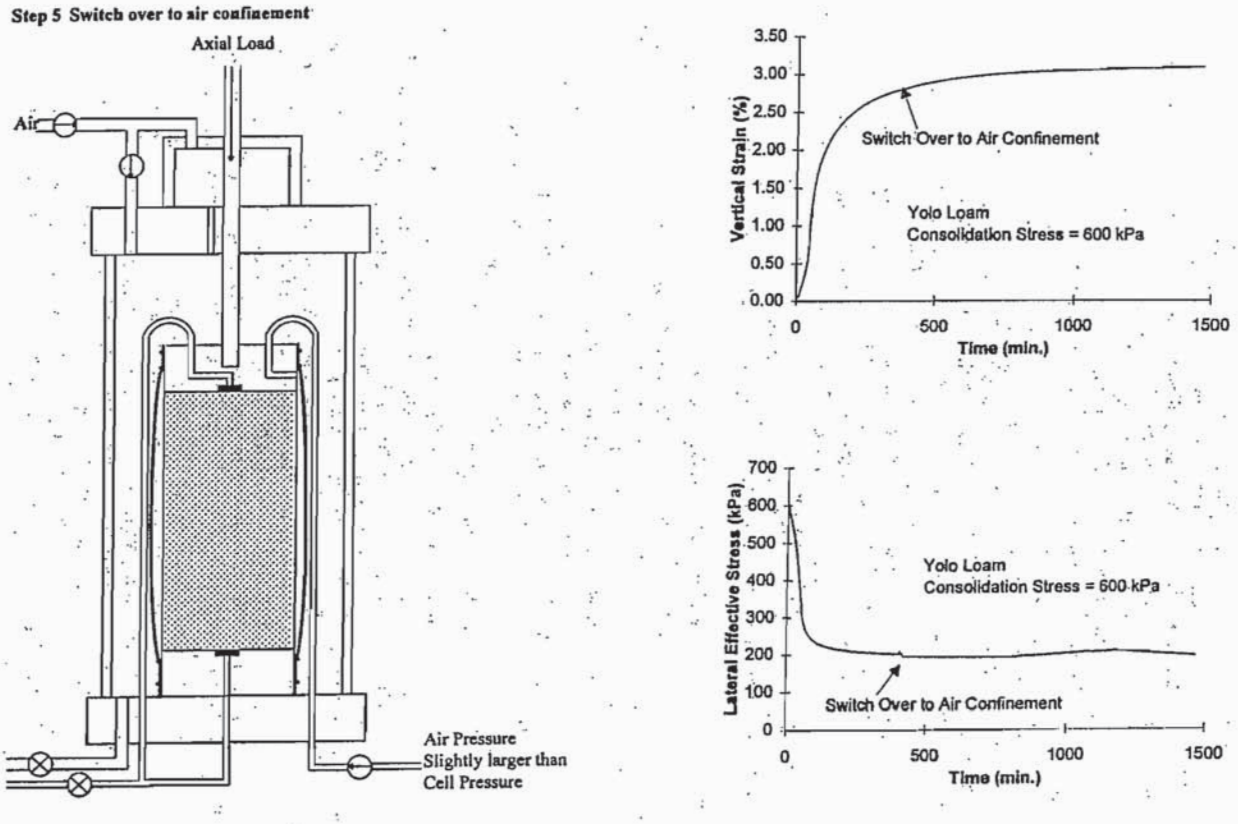

a) Testing configuration at switchover to air confinement

b) Results for successful air confinement

Figure 2.5: Proof-of-concept testing for air confinement technique (Wang, 1997)

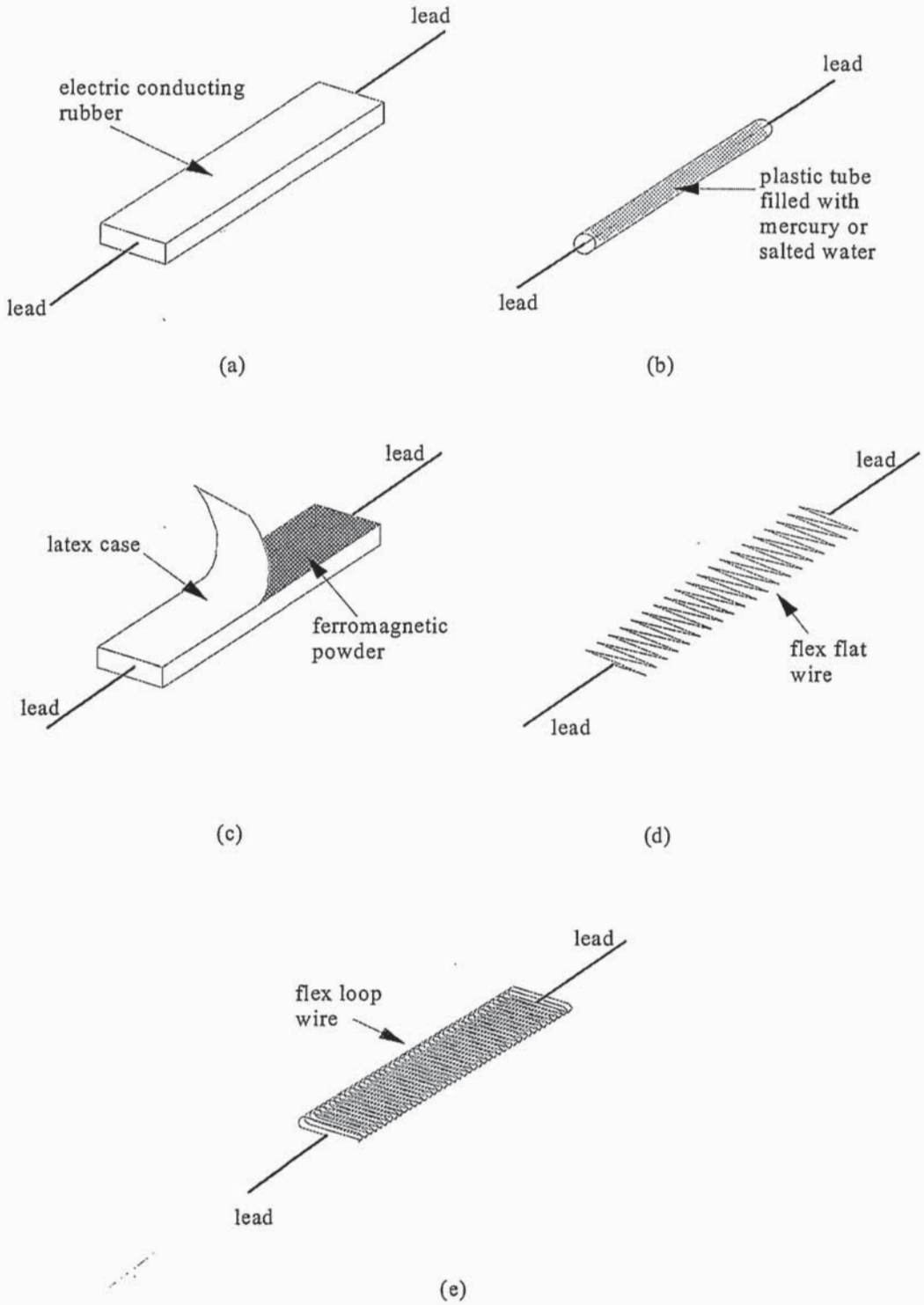

Figure 2.6: Local displacement transducer concepts (a) rubber gauge; (b) mercury/salted water gauge; (c) magnetic gauge; (d) flat flex gauge; and (e) flex loop gauge.

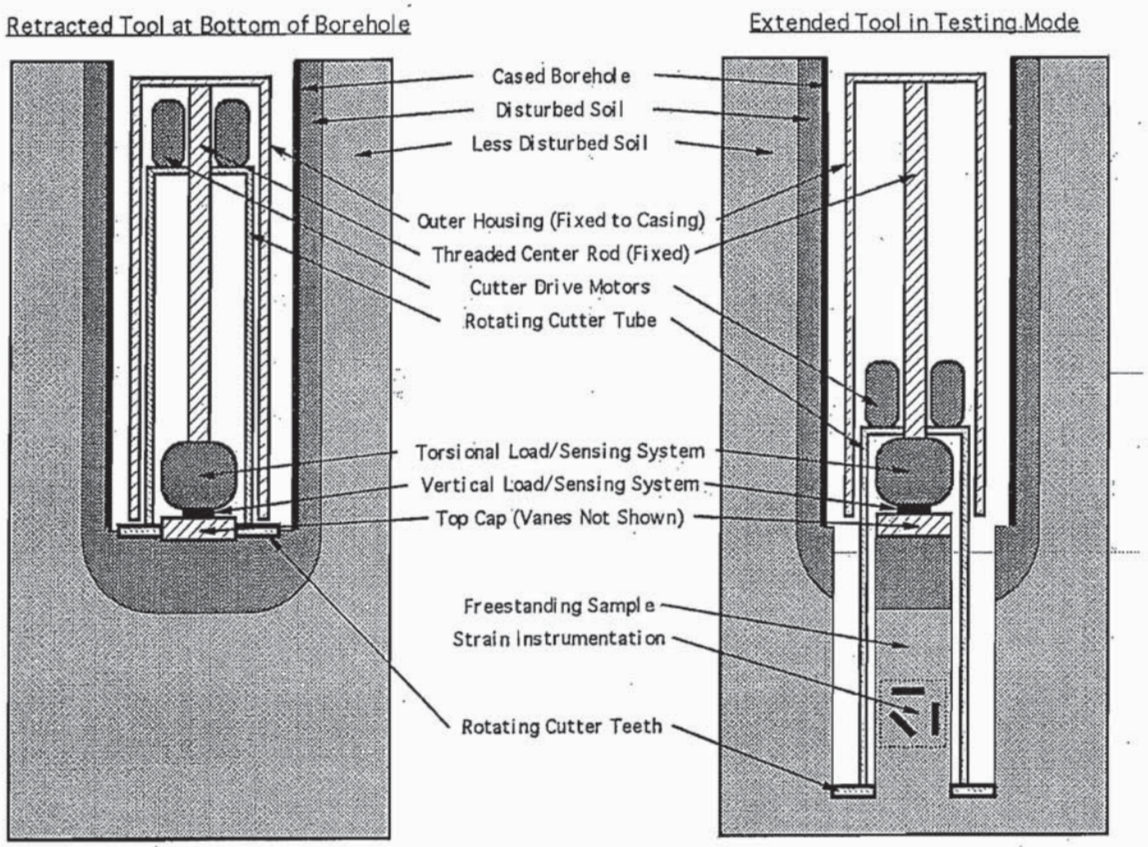

Figure 2.7: A schematic diagram showing the design concept of the cutter module and sample creation process (Roblee et al., 1994)

CHAPTER 3

Design and Development of the DFSD: Making it Real

3.1 Mechanical Design and General Operation

The overall design of the DSFD is shown in Figure 3.1. The complete device has a cylindrical shape, 3.2 m long and 17 cm in diameter and weighs approximately 3.6 kN. It can be, operationally and mechanically, divided into two main segments, or "modules", connected by a central block as shown in Figure 3.1. The lower segment (when suspended vertically, ready for operation) is called the "Cutter module" which, as the name indicates, houses the elements which carries out the carving of the soil column and the membrane deployment system and their associated accessories. The upper segment of the tool is called the "Load module" and houses the elements for application and control of the torsional and axial loads. The upper end of the load module is capped by another block, the Upper bulkhead, through which all signal, power, and air pressure lines pass to the outside of the tool. Passing through the load module, the connector block, and the cutter module is a hollow central loading shaft which transmits the axial and torsional loads down to the top of the soil column through a vaned-top cap/load-cell assembly. The load shaft also serves as a venue through which signal-carrying wires and air-pressure tubes pass between the cutter and load module through the connector block.

The DFSD is designed to operate in a 20-cm (8-in) cased borehole filled with (bentonite) slurry with a height and density such that it exerts a pressure (at the bottom of the borehole) roughly equal to the estimated total lateral stress in the field. This serves two purposes: first, the drilling slurry compensates for some of the vertical overburden pressure applied by the

excavated soil, therefore, reducing the amount of unloading experienced by the soil at the bottom of the borehole and second, and more importantly, the slurry column provides the pressure against which air pressure can be applied within the device to provide the estimated total lateral stress on the soil column during the carving process, as described in the previous chapter. During all phases of a DFSD test, the inside of the tool is always pneumatically pressurized. This "tool pressure" is adjusted such that it provides protection against any slurry leaking into the device, helps in the membrane inflation and deployment processes, and serves as a long-term confining pressure.

Once the borehole is drilled to the required depth and its bottom is cleaned and leveled, the DFSD can be then lowered and pneumatically locked against the casing for reaction. At this point, as shown by the numerical study presented in the previous chapter, the "target" soil has experienced an acceptably small amount of unloading. Similarly, before the soil column is carved, the estimated total vertical stress and the stress anisotropy can be re-established, without significant effect on the target soil, by applying an axial load at the bottom of the borehole through the top cap of the device. After that, the carving process proceeds with the instrumented membrane inflated away from the forming sample by a differential air pressure (called the "sample pressure") which serves as the temporary confining pressure and which simultaneously compensates for the total lateral stress previously exerted by the surrounding soil. Throughout the carving process, the vertical stress on the sample is measured by a load cell positioned above the top cap while the vertical deformation is monitored by a potentiometer connected to the load shaft.

The DFSD can create a freestanding soil column 10-cm (4-inch) in diameter and up to 40-cm (16-inch) long. Upon completion of sample carving, the instrumented membrane is

deployed against the sample for conventional long-term confinement. Finally, a suite of downhole laboratory-quality cyclic torsional shear tests is conducted on the freestanding sample. The torque is measured at the top of the sample via the 2-axis load cell while the deformation is measured locally by the elastomer gauges mounted on the membrane. The following sections present more details of the different components of the DFSD and their functions. A list and drawings of the DFSD components are shown in the Appendix A.

3.2 Design and Operation of the Cutter Module

The cutter module is configured as three concentric cylinders surrounding the central loading shaft and the top cap. Figure 3.2 shows the details of the lower segment of the cutter module and its main components. The cutter module is around 1.8 m (6 feet) tall and weighs about 1.8 kN (400 lb). All the tubes are made of stainless steel to resist rust and provide the required stiffness. Once the vaned-top cap is inserted into the soil at the bottom of the borehole and the in-situ stress-state is re-established, the carving process starts by advancing the inner two cylinders into the soil while keeping the outer (housing) cylinder stationary.

The innermost cylinder, called the "sample tube", is 20.5 cm (52.1 inch) long with 0.94 cm (0.37 inch) wall thickness (Figure A-18). It has a sharp removable cutting edge, called the sample "cookie" cutter, attached to its end with a 2% sampling area ratio (refer to Figure). The sample tube can move up or down but it is not allowed to rotate, to minimize potential disturbance. It has an inside diameter of 4.5 inches (11.43 cm), thus, providing 0.25-inch (0.64 cm) clearance around the sample to accommodate the membrane and allow for air confinement. The inside diameter of the "cookie cutter" smoothly changes from 4.5 inches where it connects to the sample tube to 4.0 inch (10 cm) at its tip. This helps to form a limited seal at the tip of the

cutting edge which facilitates maintaining the sample confining pressure and isolate the sample from the slurry outside the sample tube.

Figure and 3.4 show the bottom details of the cutter module and the cookie cutter. On the outside of the tube near the bottom, a 17.5-inch long and 0.1-inch wide annular recess provides a gap between the sample tube and cutter tube for water passage. Beside the soil column, the tube encloses the top cap/load cell assembly, the instrumented membrane system, air pressure gauges, and the electronic module.

The middle cylinder, called the "cutter tube", is 53.4 inch long (135.6 cm) with a 6.0 inch O.D. and 0.35 inch wall thickness as shown in Figure A-6. Its outside surface engages with the outer housing via two slightly over-sized Delrin bearings at its top. It has an annular 21.5-inch-long recess on the outside to form a gap with the inside surface of the outer housing for water passage. The inside surface contacts the sample tube in two 1-inch-long zones near their ends via two Delrin bearings fixed on the sample tube.

The cutter tube has flat stainless steel cutting teeth/blades at its base with steep angle-of-attack both vertically and radially. The four cutting blades are mounted on a removable stainless steel ring which is bolted to the bottom of the cutter tube as shown in Figure 3.5. To minimize soil displacement, the tips of the cutting teeth are positioned very near and slightly (0.125 inch) behind the "cookie cutter". Also, the inside side of the blades has the same circular contour of the cookie cutter. The cutter tube simultaneously rotates while it is being advanced into (or retracted from) the soil, thus, creating an annular space to separate the freestanding soil column from the surrounding soil.

To retrieve the sample after testing, four arc-shaped "slicer" blades, with the same curvature as the cutting tube, are used to sever the sample from its base and hold it during withdrawal as shown in Figure . Each slicer blade is connected to the outer side of one cutting blade from one end while the other end is tucked beneath the next cutting blade. Each slicer blade sweeps a quarter of a circle. The last 1 inch of the blade is bent downward as shown in Figure 3.6. During the carving process, the slicers are nearly horizontal and trailing behind the cutting teeth. After testing is completed and the sample is to be retrieved, the cutter tube rotation is reversed and the soil pushes the bent tips of the slicers, causing them to swing 90° downward around the mounting screws and cut off the base of the sample in the process. Now in the deployed position, the slicers form a cage which holds a roughly hemi-spherical ball of soil below the tested sample while the tool and sample are retrieved.

The outer housing tube is around 6 ft (182.9 cm) tall and has a 3/8 inch (0.95 cm) wall thickness. Its main function is to protect the inner tubes and other tool components and provide reaction during tool operation. The tube geometry is shown in Figure A-1. The tube has a groove on the inside surface of its lower end to house a wiper seal which serves to wipe/scrap soil and drilling mud from the surface of the cutter tube, especially during retraction of the tool. The range of movements between and within the tubes is achieved through two key components within the cutter module; an electric gear-motor drive system and a central threaded rod. Figures 3.7 and 3.8 show the details of this system. The central threaded rod, shown in Figure A-8, is a hollow steel pipe attached to the connector block and which passes through central tapped holes in the top plates of both the cutter tube and sample tube. The rod is 46 inch tall and has 1.75 inch OD, except the upper 2.2 inch which has 1.5 OD, with male threads along the lower 27.5 inch. With 1.75-12UN-3A threads, the resulting vertical movement is one inch for every 12 turns. The

change in the OD of the upper portion is to prevent the rod from moving upward into the connector block while a snap ring placed in a groove on the upper end of the rod prevents downward movement. The rod also carries the weights of the inner tubes and the driving system and transfers it to the outer housing tube.

The electric drive system has four DC permanent-magnet planetary gear-motors that can be operated by up to 27 volts (according to the desired speed and torque) with a maximum deliverable continuous torque of 46 oz-in and a backlash of less than 3°. For the motors to work as a unit, their flanges are mounted onto the flanges of a stainless steel support bracket that smoothly slides over the central threaded rod. The motor-support bracket is also engaged with the threaded rod by two shear keys (Figure A.14) to provide reaction for the motors and transfer any deformation and torque to the rod. The motor's action is transferred from its carbon-steel shaft to hardened-steel spur gears, called pinion gears, and then to a 5.25-inch-OD porous bronze internal ring gear (Figure A-9). With the pinion gears and the internal gear ring, the speed of the cutter drive system is around 8-10 rpm without any load. The properties of the gears were selected according to the desired speed and torque, the motor's properties, and the available space. To transfer its rotational motion to the cutter tube, the internal ring gear is mounted on the top surface of a short stainless steel cylinder, called the gear-support ring (Figure A-10), which is mounted on the top surface of the cutter tube's top plate. To avoid separation between the pinion gears and the internal ring gear during tool movement, an arc-shaped bronze block, called the motor-pull block (Figure A-15) serves to keep a constant distance between the motors, and between the motors and the cutter tube. The 8-foot long shielded cable of the cutting motors pass through a sealed hole in the outer housing's top plate to the load module through the connector block.

To determine how far the tool is advancing (retracting), a proximity sensor (shown in Figure 3.8) is mounted on the motor-support bracket and is used to record the number of passages of the stems of eight screws mounted on top of the gear-support ring. Accordingly, the rotation of the cutter tube can be determined down to 1/8 turn or 1/96 inch vertical movement given the 1/12-inch pitch on the threaded rod.

The cutter tube rotates around the threaded rod by means of a threaded reaction nut (Figure A-7) made from porous bronze, which is mounted on the top plate of the tube. It is by this nut that the rotational motion of the cutter tube is transformed to the up and down movement along the threaded rod. The cutter tube's movement is transferred to the sample tube by L-shaped upper and lower thrust bearing rings (Figure A-11) as shown in Figure 3.7. The lower thrust bearing ring is mounted on the top plate of the sample tube and its top surface is in contact with the bottom surface of the cutter tube. Therefore, when the cutter tube moves down it pushes on the lower thrust bearing causing the sample tube to move down with it. On the other hand, the upper thrust bearing is mounted on the inside surface of the cutter tube's top plate. Its function is to pull upward on the lower thrust bearing's shoulder, thus causing the sample tube to move upward during retraction of the tool. The sample tube is prevented from rotation by means of two shear keys accommodated in keyways both in the threaded rod and the top plate of the sample tube.

This arrangement causes the cutter tube to rotate around the sample tube while both tubes are being advanced at the same rate. The housing tube, when locked against the casing, provides guidance and a reaction frame to transfer the driving motors' torque and vertical load. These functions require a close tolerance on the tubes' centers and surfaces so that the cookie cutter does not precess during cutting. To reduce friction between the tubes during relative motion,

Delrin rings placed in grooves on the outside surfaces of the sample tube and cutter tube are used.

To help facilitate the carving process, pressurized water is circulated through the tool and jetted onto the cutting blades to flush the cuttings toward the surface. Supplied by a 5/8 hose, the water flow can reach up to 7 gallon per minutes. The water is delivered to the tool through three hoses 0.5-inch in diameter connected to the outer housing tube via 90° water elbows. Flushing water is transported through a gap between the outer housing tube and the cutter tube and then through water ports in the cutter tube to a gap between the sample tube and cutter tube. The water in these gaps is confined by two quad-rings placed in two grooves at the top and bottom of the outside surface of the sample tube and cutter tube. The length of the gaps and the location of the connecting holes are such that an overlap is always maintained regardless of the relative positions of the tubes. The water flows from the lower gap into four pairs of 0.25-inch water ducts inside the cutter tube and then through water ports in the blade mounting ring down onto the cutting blade to flush the soil cuttings.

During the carving and testing processes, it is essential that the tool is tightly locked in place. The tool pneumatic locking system consists of three equally-spaced fire hoses running longitudinally along the length of the tool. The hoses are connected to an air pressure source with a regulator. The lower ends of the hoses are tightly clamped in a circular recess on the outside surface of the outer housing. When the tool is lowered into the borehole, no pressure is supplied and the hoses are flat. Once the tool reaches its intended position, pressure is supplied and the hoses inflate and tightly lock the tool against the casing. The hoses are interconnected at the top of the tool to assure an even pressure in the hoses, and therefore, even inflation which helps keep the tool vertical. A picture of the assembled Cutter Module is shown from the lower end in

Figure 3.9, while a general layout of the module in both retracted and extended positions is shown in Figure 3.10.

3.3 Design and Operation of the Load Module and Load Application System

A cross-section of the DFSD Load Module showing its main components is illustrated in Figure 3.11. The load module consists of a rigid mounting frame and a thin outer housing. The mounting frame actually consists of two half-hollow-cylinders connected by three metal shelves as shown in Figure 3.12. The shelves are included for mounting the torque motor and the air piston. This arrangement provides easy access to the load module's components during mounting and assembly phases. The load module is sealed from the surrounding downhole environment by the outer housing, which is a thin-walled stainless steel shell that slides over the mounting frame. Both the mounting frame and the outer housing are connected to the upper bulkhead and connector block by mounting screws. Sealing of the two ends of the outer housing is achieved via two O-rings placed in grooves on the two end blocks. It is inside the load module where vertical and torsional loads are generated independently and coupled via the load shaft.

Mounted on a shelf above the torque motor, a pneumatic piston generates the vertical load used in DFSD tests by maintaining a pressure difference across the piston. The vertical load is applied once the tool is locked in place just before the carving process to re-establish the in-situ stress anisotropy. This load is usually kept constant through out the test. The air pressure in the piston is adjusted manually by a regulator rated for up to 200 psi (1378 kPa). The diameter of the bearing surface inside the piston is approximately 4.0 inch. The compressed air supplied by the compressor has a maximum pressure of 100 psi (689 kPa). The piston can, therefore, generate axial loads up to 1200 lb (5 kN).

The torsional load is produced by the Dynaserv DR-1060B-115 servo-actuator made by Compumotor Division of Parker-Hannifin Corporation. The servo-actuator is a closed loop system consisting of a direct-drive motor, a controller, and a driver (a drive and feedback device). Of these components, only the direct-drive torque motor, shown in Figure , is placed inside the load module, mounted to a shelf connected to the mounting frame. The motor communicates with other components of the system on the ground surface via signal-carrying wires. The system allows for an advanced motion control environment. The direct drive motor is of the outer-rotor typ, with a brushless resolver feedback. It has an outer diameter of 6 inches and can create a torque up to 60 N-m (528 lb-in) with compression loads up to 8900 lb.

The torsional and axial loads generated in the load module are carried to the sample through the load shaft. Running nearly the length of the tool, the load shaft is a hollow steel tube with a 7/8 inch outside diameter and 1/2 inch inside diameter. The load shaft passes and moves freely inside the 1 inch hollow space of the threaded rod. However, to provide support for the long load shaft, two press-fit porous bronze bushings with 7/8-inch ID are placed at the two ends of the hollow space of the threaded rod. The hollow space of the shaft serves as a venue through which wires and pressure tubes pass between the cutter module and the load module.

The load shaft couples, at its top end, with the piston rod via a thrust bearing to transmit the vertical load. The purpose of the thrust bearing is twofold; to attach the piston rod to the load shaft, and to isolate the piston from the twist caused by the torsional load on the load shaft. Isolating the piston removes any rotational piston friction from the system. The thrust bearing, shown in Figure 3.11, consists of a roller bearing mounted on the lower end of the piston rod and enclosed in a cage that is attached to the top end of the load shaft. The roller bearing reduces rotational friction in both compression and extension. An approximately ½ inch diameter hole

was drilled through the cage of the thrust bearing to provide an outlet for the cables and tubes coming from the hollow space inside the load shaft.

The torsional load is transmitted to the load shaft by means of the spline assembly shown in Figure 3.13. It consists of a spline shaft and a matching spline nut. The spline shaft, shown in Figure A.24, is hollow and has three track projections 120° apart which run the length of the shaft along its outer surface. The hollow space has the same diameter as the outside surface of the load shaft. This allows the spline shaft to slide over the load shaft during the assembly process. To transfer torque, the spline shaft is bolted to the load shaft via three mounting screws. The spline nut is fastened to the torque motor and has three raceways that fit the track projections of the spine shaft. The raceways have rows of ball bearings to provide a smooth rolling movement of the spline shaft. This arrangement enables the spline assembly to transmit the torque from the motor, via the spline nut, to the load shaft while permitting vertical displacement.

The loads are transmitted from the load shaft to the sample by means of the top cap-load cell assembly. The vaned-top cap and the wheel-shaped load cell are connected via the membrane upper sealing ring and the whole assembly is mounted to the end of the load shaft by a bolt which passes through the hub of the load cell and screws into the threaded inside of the shaft. The top cap is made of stainless steel and has 4.0-inch outside diameter to match the diameter of the carved sample (Figure 3.14). To transfer the torque to the sample, four vanes are half-embedded into the bottom surface of the top cap and protrude ½ inch outward. The stainless steel vanes are 0.075 inch thick, which should be enough to withstand the bending moments while minimizing disturbance to the soil they are inserted into. Made of 7075 aluminum, the load cell is a 1-inch-long hollow cylinder with four equally-spaced spokes connected to a central

threaded hub as shown in Figure 3.15. It is through the load cell's hub that the top-cap/load cell assembly is connected to the end of the load shaft. The spokes of the load cell have a rectangular cross-section, and are instrumented for load measurement as will be discussed later in the chapter.

3.4 The Connector Block, the Upper Bulkhead, and the Shock Absorber

The connector block is a cylindrical stainless steel block that physically separates the tool's two primary modules. This separation helps in many ways. First, it facilitates the assembly and maintenance of the tool and its various components, second, the block serves as an end cap on which various parts can be connected to for reaction, and last, it functionally separates the tool which allows, for example, using the cutter module as a high-quality sampler. As shown in Figure 3.16, the block has various diameters and connects to the outer housings of the cutter module and load module and the mounting frame of the load module via mounting screws. Two O-rings placed in two grooves at the ends of the block help seal the inside air pressure and prevents water from entering the tool. The connector block has a central stepped hole with keyways to accommodate the threaded rod. It also has smaller vertical holes for the passage of the electrical wires of the cutter motors (and proximity sensor) and the tool air pressure.

The upper bulkhead is also a cylindrical stainless steel block with an annular recess at its bottom segment as shown in Figure 3.17. It caps the upper end of the load module and provides a mounting surface for its mounting frame and outer housing. The upper end of the mounting frame is placed on the annular recess of the upper bulkhead. The outer surface of the mounting frame is flush with the surface of the upper segment of the bulkhead which allows the outer housing shell to slide over both of them. Mounting screws are used to connect the mounting frame and the outer housing to the upper bulkhead, while a properly sized O-ring placed in a

groove near the top end of the bulkhead is used to seal the space between the surface of the bulkhead and the inside surface of the outer housing shell.

The upper bulkhead also serves as a hub where power and signal cables and pressure lines from the ground surface are connected to the tool. Two stainless-steel water-proof plugs with 32 and 16 pins are mounted into two threaded holes through the upper bulkhead to connect power and signal lines coming to and from the tool. The two custom-made male plugs mate with two water-proof female plugs at the ends of two shielded cables. The upper bulkhead also has five smaller threaded holes into which fittings are mounted on both sides to connect air pressure (and vent) lines coming from the ground surface to utlility lines inside the DFSD.

Figure 3.18 (also refer to A.2, A.3, and A.4) shows the shock absorber used in the DFSD. It consists of two heavy-duty pre-compressed springs separated by a piston and housed in a rigid frame. The shock absorber has two functions. First, it provides a "soft" interface through which the tool can be hooked to a crane or a drill rig for lifting, to minimize shocks to the DFSD that might be caused by sudden movements of the rig. Second, it provides a location for the tool's umbilicals (electrical cables, pneumatic and water lines) to be tied down above the top of the tool, which is important for downhole deployment. Two D-shaped links are fixed to the upper and lower plates of the shock absorber to connect with the hook of a crane (or a drill rig) at one end and to another D-shaped link fixed on top of the upper bulkhead at the other end.

3.5 Air Pressure System

Air pressure is important to the operation of the DFSD. It is used during all the phases of operation, from lowering the tool into the borehole to lifting it after testing is conducted. There are four separately controlled air pressures; three of them are applied inside the tool, namely; the "tool pressure", the "sample pressure", and the "axial pressure". The fire hoses' air pressure,

which is used to pneumatically lock the tool in place, does not pass through the tool and was already discussed above. The inside pressures are all supplied to the tool through pressure lines that connect to fittings on the upper exterior end of the upper bulkhead.

The axial pressure, as the name indicates, is only supplied to the piston cylinder through a tube that connects to a fitting on the top of the piston. The pressure is used to apply the axial load which is carried from the piston rod to the load shaft and then to the top of the sample through the top cap.

The tool pressure is applied throughout the inside of the tool. It enters the tool through the upper bulkhead and from there it is released into the inside of the load module. Through holes in the connector block, this pressure is also applied in the inside of the sample tube of the cutter module. The membrane and its seals are the only barriers to this pressure near the bottom of the sample tube. Therefore, this pressure is applied behind the membrane and acts to collapse it toward the center of the sample tube.

The sample pressure, on the other hand, is applied inside the membrane and, therefore, acts to inflate the membrane away from the center of the sample tube and toward the walls. Hence, it is the membrane that separates the domains of the tool pressure and the sample pressure. There is no seal at the bottom of the tool for the sample pressure, which is instead balanced by the water/slurry column, and eventually the soil seal at the base of the specimen. The sample pressure is carried inside the tool from the upper bulkhead through a tube that passes through the inside hollow space of the load shaft. The tube connects at one end to a fitting on the inside bottom of the upper bulkhead and at the other end to a fitting on the upper surface of the top cap. The tube enters the inside of the load shaft at its upper end through an opening in the thrust bearing cage, and exits the shaft through a hole just below the top plate of the sample tube.

This fitting on the top cap is connected to two perpendicular and intersecting "airways" made on a horizontal plane inside the body of the cap as shown in Figure 3.14. The airways span the width of the top cap and serve to release the air pressure from four equally-spaced ports on the side of the top cap just below the membrane upper sealing ring.

At this point in its development, all the pressures used in the DFSD are manually controlled. The main air pressure supply line is connected to a pressure control panel through which it is used to supply four lines, each of which has its own pressure regulator. Vent lines are used to facilitate the control of the fire hoses' pressure and the axial pressure. Because the air pressure coming out from the regulator on the ground surface travels a long route, with possible leaks, the regulators' readings may not necessarily reflect what is being delivered to the downhole sample. Therefore, two electronic pressure gauges were mounted on the load shaft inside the sample tube (just above the DEM) as shown in Figure 3.2. One gauge, a model PX202, measures the absolute pressure inside the sample tube, i.e. the tool pressure, while the other gauge is connected to the sample pressure line and measures the difference between the tool pressure and the sample pressure, and hence is called the differential pressure. Accordingly, the regulators on the pressure control panel are used to roughly estimate the amount of pressure needed to supply to the tool, but it's the readings of the pressure gauges inside the tool that are reported and used for accurate pressure control. As will be shown later, the applied axial load is measured by the load cell just above the top cap, therefore, it is not necessary to precisely measure the actual pressure delivered to the piston. Also, the pressure inside the fire hoses are not measured since it was found that a pressure reading of 30 psi on the control panel's regulator is sufficient to inflate the hoses and adequately lock the tool.

3.6 Membrane System and Membrane Deployment

Housed inside the sample tube, the membrane system consists of an instrumented latex membrane and upper and lower membrane seal mechanisms. The latex membrane is 3.8 inch in diameter and 24 inch long. It has 0.025 inch thickness for durability and multiple usages. A picture of a typical DFSD instrumented membrane is shown in Figure 3.21. The diameter of the membrane was chosen based on the diameter of the sample to eliminate the formation of wrinkles (when applied against the sample) and to keep membrane-induced confinement to insignificant levels. The membrane size also provides the Elastomer gauges with a beneficial pre-stretching when applied against the surface of the sample. The length of the membrane is selected such that it can enclose a 16-inch-long soil column and the top cap assembly, and allow extra length at the ends for sealing and multiple usages. As will be shown later, the membrane is folded inside the sample tube, therefore, its length can vary, as long as it exceeds 17 inches. Because of its unusual characteristics, the DFSD membrane is custom made by 3-D Polymers, a manufacturer of membrane products.

The lower membrane seal mechanism is formed by an O-ring placed in a groove on a floating ring, called the lower membrane seal ring, and then jammed against the groove formed by a bevel on the inside surface of the bottom edge of the sample tube and the edge of the cookie cutter spacing ring as shown in Figure 3.3. Because the lower membrane seal travels with the end of the sample tube and its cookie cutter, it is always located at the bottom of the soil column. This implies that the location of the membrane gauges should always be referenced to the end of the membrane sealed by the lower membrane seal. As mentioned before, the local gauges should be located far enough from the top and bottom zones of the soil column where disturbance and complex boundary conditions are unlikely to affect the measurements. The gauges are usually

attached approximately 4 inches from the bottom end of the membrane. This was proven sufficient given the range of soil column heights carved by the tool to date.

The upper membrane seal mechanism involves the top cap, an upper membrane seal ring and an O-ring. The top cap has a stepped cross section near its top. The upper end of the top cap has a smaller diameter to fit into the hollow space inside the upper membrane seal ring. To form the seal, the upper membrane ring is first mounted onto the load cell. The upper end of the membrane is sandwiched between a groove on the smaller section of the top cap and a properly-sized O-ring. The top cap is then connected to the upper membrane seal ring by four bolts. When the bolts are tightened, the ring is drawn closer to the top cap and the stepped section starts to disappear inside the upper membrane ring, squeezing the O-ring between them as shown in Figure 3.3.

In the DFSD, the membrane is used for two primary purposes; conventional long-term control of the confining pressure during testing, and as a medium onto which the strain gauges are attached and deployed onto the surface of the sample. Both of these functions of the membrane are only needed after carving of the soil column is completed. However, the membrane also serves as a physical barrier between the top cap and the inside of the sample tube, thereby preventing slurry from leaking inside the sample tube in case equipment failure leads to a loss of tool pressure. This sealing feature is also used to deploy the membrane toward and away from the sample via the tool and sample pressures.

When the DFSD is assembled and ready for deployment, the membrane is folded inside the sample tube and resting against the top cap/load cell assembly, the load shaft, and part of the electronic module as shown in Figure 3.2. When the tool is lowered into the slurry-filled borehole, the tool and sample pressures are supplied to the tool to offset the slurry pressure at the

bottom of the sample tube. Once the tool is locked in place, axial pressure is applied to re-establish the stress anisotropy and to firmly insert the vanes of top cap into the soil at the bottom of the borehole. At this point, the tool pressure and the slurry pressure should be close to the estimated total lateral stress and the top cap is protruding slightly ahead of the cookie cutter. Just before the start of the carving process, the sample pressure is increased and its level is adjusted such that it is slightly larger than the tool pressure. At first, most of this pressure will escape through the space between the top cap and the cookie cutter. However, shortly after the start of the carving process, a "soil seal" starts to form between the tip of the cookie cutter and the surface of the soil sample. This allows a positive differential pressure to build up between the membrane and the surface of the sample. This pressure provides temporary air confinement that compensates for the removal of the surrounding soil and acts to inflate the membrane away from the sample and toward the wall of the sample tube.

As the lower membrane seal travels downward with the cookie cutter, the membrane unfolds inside the sample tube. During the carving process, the advancement of the two inner tubes (and, therefore, the height of the soil column) is monitored through the "bolt counter" which, as explained earlier, counts the number of times the stems of eight bolts on top of the cutter tube pass in front of a proximity sensor. Once the intended sample height is reached, the sample pressure is lowered below the tool pressure, thus, allowing the tool pressure to deploy the membrane against the surface of the sample and to provide a long-term confining stress as shown on the right side of Figure 3.2. The specimen preparation is then complete and a suite of cyclic torsional shear tests can be conducted.

If it is decided to abandon the soil sample after testing, the slicers won't be attached to the cutting teeth. In this case, after testing is completed, the sample pressure is re-applied to

inflate the membrane as the inner tubes are being retracted into the outer housing of the cutter module. If the sample is to be retrieved, as would usually be the case, the cutter tube is reversed half a turn to deploy the slicers and sever the bottom of the sample. To preserve the sample, the inner tubes are not retracted, but the whole tool is lifted out of the borehole in the extended position. Therefore, it is not necessary to inflate the membrane during this process, but instead, the tool pressure can be lowered as the tool is being withdrawn.

One of the useful features of the instrumented membrane is that its movements during carving and deployment can be monitored through the readings of the elastomer gauges. Inflation will elongate the gauges while membrane collapse will shorten them. This provides an important confirmation, beside the pressure gauges' readings, that the membrane deployment downhole is being carried out properly.

3.7 Load Measurement

The torsional and vertical loads applied to the sample are measured by the 2-axis load cell, shown in Figure 3.15. The load cell is mounted on top of the top-cap assembly, and therefore provides an accurate representation of the loads applied to the sample and eliminates the need to account for compliance effects and friction along the length of the loading system. Connected to the end of the load shaft, the central hub of the load cell rotates the same amount as the shaft. This motion is transferred from the hub through the spokes to the outer cylinder of the load cell and then through the vaned-top cap to the soil sample. However, since this movement is resisted by the soil, there will be a relative motion between the hub and the outer cylinder of the load cell. This will cause the spokes of the load cell to deform in the horizontal plane. The same process occurs when a vertical load is applied, but this time, the spokes of the load cell will

deform in the vertical plane. Accordingly, the applied torque and vertical loads can be correlated to the deformations of the spokes.

To achieve this, the spokes of the load cell are instrumented with sixteen strain gauges to form four 4-element transducers. The strain gauges in each transducer are wired into a Wheatstone bridge circuit. Four strain gauges, two at each side, are mounted on each spoke of the 2-axis load cell, so that each spoke acts as an independent transducer. Two of the transducers, located on the same axis, measure vertical strain with the strain gauges mounted on the top and bottom of the two spokes. The remaining two transducers have the strain gauges mounted on the sides of the spokes to measure torsional load.

Before the load cell is used in the DFSD, the output voltage of its axial load transducers (ALTs) and torsional load transducers (TLTs) has to be correlated with the applied torque and vertical loads. This can be achieved through a calibration procedure. The torsional load transducers are calibrated using the apparatus shown in Figure 3.19, which is designed to slide down the threaded rods of a standard triaxial testing support frame. The Dynaserv motor can be used to apply a torque to the load cell which is bolted to the apparatus. The load cell reacts against two calibrated force transducers located in the arms of the calibration apparatus. The voltages produced from the TLTs are then correlated to the applied torque. Figure 3.20 shows typical calibration curves of TLTs. The axial load transducers (ALTs) are calibrated simply by recording their output under varying dead loads. Each of the four load cells is wired and calibrated as an independent load cell, thus providing redundancy in the measurement system, and a measure of the uniformity of loading through the top cap.

It is essential for the operation of the load cell that its deformation remains in the linear elastic range under the anticipated loads. This was proven by the linear relationship between the

output voltage of the load cell, which is a function of its deformation, and the applied load. In addition, calibration tests done so far showed that torsional and vertical deformation of the cell is fully reversible, with no detectable hysteretic effects. It was also shown that the axial load does not affect the ability of the TLTs to accurately measure the torsional load (e.g., the loads are not coupled). The load cell is designed to measure axial loads up to 5.0 kN (1100 lb) and torques up to 68 N-m (600 in-lb). The sensitivity of the TLT is around 4.0 N-m/volt when excited by 5V, which is sufficient to provide useful measurement at very small torsional stresses on the 10 cm diameter soil sample.

3.8 Deformation Measurement Systems

In the DFSD, shear strains are measured locally by the newly developed Elastomer Gauges, which are attached to the membrane as shown in Figure 3.21. The Elastomer Gauge consists of a tiny capillary filled with liquid metal alloy, which is encapsulated in a supple polyurethane gauge body. The sensitivity of the gauge depends on the diameter and the length of the capillary. A detailed discussion of the properties and development of the Elastomer Gauge as a part of this project are provided in Appendix E.

The elastomer gauges are attached to the inside of a latex membrane at an angle of 45° from horizontal. At this orientation, it can easily be shown that the shear strain of the soil cylinder is twice the gauge strain. For orientations other than 45°, the shear strain can be obtained from the gauge strain using the following equations:

$$\gamma = \left[\varepsilon_g + 1\right]\frac{\cos\phi}{\sin\alpha} - \cot\alpha \qquad \text{K (6.1)}$$

$$\phi = Sin^{-1}\left(\frac{Sin\alpha}{1+\varepsilon_g}\right) \qquad \text{K (6.2)}$$

where γ, ε_g, and α are the shear strain, the gauge strain, and the orientation angle of the gauge, respectively. The gauge strain is simply its deformation over its length. For orientation angles between 40 to 50°, the ratio between the shear strain to the gauge strain remains very close to two.

To date, four gauges are used on a membrane and are distributed uniformly around the inside circumference of the membrane, one at each quarter point. Two of the gauges have a capillary length of 2.5 inches and a diameter of 0.75 mil, and are especially useful for measuring strains as low as 0.0005%. The other two gauges have a capillary length of 2.0 inches and a diameter of 1.0 mil and are used for measuring strains up to 1%. The gauge sensitivity is also controlled by the excitation voltage. At an excitation voltage of 1.0 volt, the sensitivity of the gauge is around 40 volts/mm, and can thus be used for small strain measurement, while at 0.125 volts, the sensitivity of the gauge is around 5 volts/mm, which is appropriate for large strain measurement. The combination of gauges with different capillary dimensions and excitation voltages allows measurement a wide range of shear strains from 0.0005% to 1% with a maximum overlap between the gauges in the mid-strain range.

In testing performed thus far, the approach has been to attach two gauges with the same characteristics opposite to each other and with a 90° difference in orientation. At any moment during the cyclic test, when one gauge is stretched, the opposing one is compressed. This means that the output of the gauges will have 90° phase difference. This is beneficial in many ways. When the outputs of the gauges are averaged, it helps eliminate errors due to electrical drift and noise, especially at small strains, where the noise-to-signal ratio is significant. It also helps to remove any bias in the gauges' behavior, if there is any, with respect to stretching and

compression. Detailed description and implementation of the elastomer gauges is presented in Appendix E.

Vertical deformation is measured by a potentiometer, Rayelco model MP-10, mounted on a shelf above the air piston in the load module. The output voltage of the potentiometer changes according to the position of its spring loaded wire as it is extended or retracted out of the potentiometer's body. The tip of the wire is connected to the top end of the piston rod and, therefore, tracks any vertical movement of the entire load shaft and the top cap assembly connected to it. Monitoring vertical deformation is important during all phases of the DFSD test, especially during the carving process, where limited vertical deformations indicate a successful sample creation with minimal disturbance. During cyclic torsional tests, it is also useful to know how much the sample settles under the cyclic shear stress. In its current configuration, the sensitivity of the potentiometer is approximately 18 mm/volt, though there are more sources of potential compliance with this measurement than with the shear deformations.

3.9 The Downhole Electronic Module (DEM)

The downhole electronic module is mounted on a segment of the load shaft inside the sample tube as shown in Figures 3.1 and 3.2. It encloses the circuit boards which carry the components for analog signal conditioning. The current design of the DEM can fit three circuit boards. As shown in Figure 3.22, the frame of the DEM is made of a central thin hollow tube capped with two disks at its ends. Approximately 1.5 inches from each end, a triangular shelf with a hollow center is attached to the tube. The sides of the shelves provide a surface onto which the boards are mounted. Each end cap has threaded holes to fit connector plugs for electronic signals. A thin-walled cylinder, which slides over the two end caps, serves as an outer

housing of the DEM. To protect the electronics in case of accidental flooding, the whole assembly is sealed with two O-rings placed in grooves around the perimeter of the two caps.

The inside diameter of the central hollow tube is slightly larger than the outside diameter of the load shaft. Therefore, the DEM can slide freely over the load shaft. It is held just above the top cap/load cell assembly by two hollow spacers that slide over the load shaft. The upper spacer reacts against a circular shelf clamped to the load shaft and prevents the DEM from moving upward. The lower spacer reacts against the hub of the load cell and restricts the downward movement of the DEM.

The downhole signal conditioning strategy has many advantages. With the DEM being close to the sensors (load cell transducers, elastomer gauges, pressure gauges), the signals only travel a short distance before they are filtered and amplified inside the DEM. This reduces the noise-to-signal ratio and the conditioned signals become much less vulnerable to electric contamination as they travel the long distance before being acquired at the ground surface. This is crucial especially at very small strains with the low-magnitude outputs of the sensors. This strategy also provides a physical separation between the actuators (torque motor and air piston) and the DEM which helps preserve the fidelity of the signals. In particular, the torque motor and its auxiliary electronics have a relatively strong electromagnetic field which could easily distort sensors' signals if the DEM were placed inside the load module.

For a compact and robust configuration, a 32x5 cm board was designed to house eight channels of signal conditioning. The board is manufactured commercially and then the components are added "in-house". Each circuit has an amplifier with controllable gain, a voltage divider and a low-pass filter with 30 Hz cutoff frequency. The elastomer gauges' channels also have bridge completion circuits with the gauge incorporated in one arm of the bridge and a

balancing potentiometer at another arm. Figure 3.23 shows a blue print of the board and a typical circuit layout. Because of the number of sensors used in the DFSD, so far only two of the three boards are used. One board houses the circuits for the four elastomer gauges and the four load cell transducers and the other board houses the circuits of the two pressure transducers.

Each board is supplied with two DC voltages of +15 and -15 volts to power the chips. Sensors are excited with adjustable voltages from 0.125 to 10 volts by changing the locations of three jumpers. The excitation voltage of the elastomer gauges can be 0.125, 0.25, 0.5 or 1.0 volts according to the type of the gauge and the required sensitivity. Load cell transducers and pressure gauges are usually powered with 5 and 2.5 volts, respectively. An instrumentation amplifier, BB INA125, is used to provide four reference voltages (1.25V, 2.5V, 5.0V, and 10V) for bridge excitation and precision differential amplification with adjustable gain from 4 to 10,000, all using a single 16-pin chip and external resistors. A gain between 500 and 4000 is usually used in the DEM depending on the type of the sensor. A voltage divider made with a regular op amp, LM358, along with external resistors and capacitors is used to divide the four reference voltages, supplied by the BB INA125, by ten to obtain another four reference voltages (0.125V, 0.25V, 0.5V, and 1.0V). After the input signal is amplified, it is filtered using the BB UAF42 universal active filter. The 14-pin chip is configured to provide an analog Butterworth-type non-inverting low-pass filter with 30 Hz cutoff frequency.

Each board in the DEM has two 26-pin connectors to provide two-way communication with the sensors and the electronic equipment at the ground surface. With one connector, which is totally devoted for the sensors, input signals are received for conditioning and voltage lines are sent for sensor excitation. Each one of the four elastomer gauges needs four input/output lines (a total of 16 lines) while each load cell and pressure gauge needs two lines. The other connector is

devoted to communication with the outside and, therefore, it receives power and analog ground lines, sends conditioned output signals, and connects balancing potentiometers (for the elastomer gauges) at the surface to their corresponding bridges on the board. Because the elastomer gauges are very sensitive, there is no guarantee that they will be in-range when they are applied against the sample. Therefore, a remote zeroing capability is needed at the surface. This was achieved by removing the balancing potentiometers from the DEM and placing them at the surface where their resistance can be adjusted to bring the gauges into range and zeroed for optimal cycling data performance.

The wires of the elastomer gauges are connected to two cables, one at each side of the membrane. These 4-wire shielded cables have a common female plug which mates with a male plug at the upper end cap of the DEM. The "membrane cable" is long enough to allow the membrane to travel with the sample tube during the carving process and is supported by retaining springs attached to the load shaft just below the threaded rod. The wires of the pressure gauges are also connected to a female plug which mates with another male plug at the upper end cap of the DEM. The load cell transducers are connected to two shielded cables each having its own plug such that ALT1 and TLT1 are on the same plug and ALT2 and TLT2 are on the same plug. These plugs mate with two male plugs at the lower end cap of the DEM. The plugs mounted on the end caps of the DEM are connected to flat ribbon cables which eventually connect to the 26-pin flat ribbon connector on the board to transfer the sensors' signals. Another 26-wire flat ribbon cable carries the conditioned output signals from the board to a 26-pin male plug mounted on the upper end cap of the DEM.

3.10 Data Acquisition and System Control

Data acquisition and the control of cyclic torsional load are totally automated in the DFSD. These processes can be physically and functionally divided into four layers/levels as shown in Figure 3.24. The first layer includes the sensors and the actuators which are all located inside the tool, followed by the analog signal processing layer and the interfacing layer. The last layer is for digital processing and includes the A/D or D/A signal conversion, acquisition (or outputting), and digital display/control which all happen via a computer. The computer supports and interfaces two important components: the data acquisition card (hardware) which does the A/D and D/A conversion, and the data acquisition and control program (software) which provides digital display, control, and data logging. The analog signal processing layer includes the DEM for the sensors, which is inside the tool, and the servo/driver for torque motor control which is at the surface. This layer is interfaced with the last layer through an "interfacing box" which serves as a hub where all signals are received, sorted, processed (if necessary), and then sent to their destinations. Moreover, through this box, DC power is supplied to the system and the control loop is switched on or off. In addition, the four elastomer gauges' balancing potentiometers are mounted on the box to remotely adjust the output of the gauges and bring them back in range before the test.

The DAQ board used in the DFSD is AT-MIO-16XE-50 (DAQCARD-AI-16EX-50 for the laptop PC used for field testing) from National Instruments. It is a 16-bit Plug-and-Play multifunction analog, digital, and timing I/O board. It has 16 single-ended analog input channels with successive approximation A/D conversion, a maximum sampling rate of 20 kHz, and ±10V input range. The two analog output channels have the same voltage range. The board also has 8 programmable digital input/output channels and two 24-bit counter/timer I/O channels. All the

signals and channels on the board are available via a 68-pin male connector. Cabling accessories sold by National Instruments are used to connect the DAQ card inside the computer to the interfacing box.

The data acquisition and control software used for the DFSD has been developed in-house using the *LabView* platform, available from National Instruments. It uses a graphical programming environment in which a hierarchy of application programs, called VIs (virtual instruments) and their subroutines, called sub-VIs, are nested together to perform a sequence of multiple tasks that constitute data acquisition and control. Any program within LabView has two interfaces, one called the front panel and the other is called the block diagram. The front panel is the user interface through which test parameters can be specified using "controls" (knobs, dials, buttons, and switches) and test outputs displayed using "indicators" (charts, meters, lamps, etc.). The block diagram is the interface in which the program is constructed using the graphical language and elements are wired to specify data flow and dependency. Two programs have been developed in LabView environment to be used in a DFSD test. The first program is used for real-time monitoring (and logging) of the outputs of all sensors, except the proximity transducer, in the DFSD. The second program is used to input test parameters (shape, amplitude, frequency, and number of cycles of the strain-time history) and to run the cyclic torsional load test. Moreover, the program simultaneously acquires sensors' outputs during the cyclic test. LabView also has a DAQ "channel wizard", which is used to configure AI channels and to perform a quick test to view the output of any channel in real time.

As discussed previously, the DEM provides analog signal conditioning for the elastomer gauges, load cell transducers and air pressure gauges, all inside the cutter module. The output signal lines from the DEM pass through the inside of the load shaft and exit from its top into the

load module. On the other hand, the cutting motors power lines and the signal and power lines of the proximity sensor pass through holes in the connector block to the load module. All signal and power lines inside the load module, including those for the torque motor and the potentiometer, are connected to the pins of the two waterproof male plugs mounted on the upper bulkhead. Two waterproof heavy duty shielded cables transport the signals and power lines from the upper bulkhead to the surface. One cable has 16 shielded pairs of twisted wires (a total of 32 lines) and carries the signal and power lines of all sensors, the balancing EGs potentiometer lines, and the torque motor data lines. The second cable has 8 shielded twisted pair wires (a total of 16 lines) and carries the power lines for the cutting motors and the torque motor and the signal lines of the proximity transducer.

At the surface, all the sensors' lines (except the proximity transducer) are directly connected to the interfacing box. Since the sensors' signals are already conditioned in the DEM (except the vertical position potentiometer signal which does not need further conditioning) they are only sorted and connected to their corresponding AI channels on the DAQ board. The sensors' power (and ground) lines, on the other hand, are connected to DC power source lines in a switched circuit inside the box. The torque motor data and power lines are connected to the servo/driver which is directly powered by 110V AC power line. The servo has two-way communications with the PC/LabView via the indexer (controller) and its auxiliary circuits inside the interfacing box as will be discussed later.

There are two stages of data acquisition and control in a DFSD test. The first stage includes the setup of the tool inside the borehole and during the carving process, while the second is during conducting the cyclic torsional shear tests themselves. In the following sections, more details about data acquisition and system control in each phase are presented.

3.11 Signal Acquisition and System Control during the Carving Process

The cutting motors' power lines and the proximity transducer signal lines don't pass through the interfacing box but have their own separate circuits and power supply lines which are all enclosed in a separate box, called the "bolt counter box". Power to the cutting motors and the proximity sensor is controlled by a single toggle switch so that the moment the motors start to rotate, the proximity sensor starts to "count" the passage of the bolts. The direction of motors' rotation is a function of the polarity of the supplied voltage. Therefore, the bolt counter switch toggles between three positions, one to advance the cutter module down, a second to retract it up, and a third to stop it. The proximity transducer outputs a pulse each time it detects the magnetic field of a bolt head. The proximity transducer signal is only acquired into the bolt counter box and its pulses are used to increment a counter that records and visually display the number of pulses output by the proximity transducer. Each pulse represents a 1/96 inch of vertical movement.

When the tool is about to be lowered into the borehole and positioned in place, all the sensors are powered and monitored via LabView. The tool and sample pressures are manually regulated such that the "downhole" pressure gauges' signals (which serve as feedback signals) read a value close to the estimated total lateral stress. After the tool is locked against the casing and the deviatoric vertical stress is re-established, the cutting motors and the proximity sensor are powered, which starts the carving process. The progress of this process is monitored through the bolt counter's reading which indicates how far the tool is advancing and the elastomer gauges' signals which show the inflation of the membrane. Therefore, one can say that the carving process is controlled by an open loop but with feedback signals. Once the required

sample height is reached, the cutting motors' power is switched off and the carving process is stopped. Shortly after, the membrane is deployed against the sample, the elastomer gauges are brought into range, and the torque motor control loop is switched on. This ends the first stage of a DFSD test, throughout which all data are continuously saved in a single file that serves as a record for tool setup and the sample creation processes. During this stage, a 2 Hz sampling frequency is usually used.

3.12 Signal Acquisition and System Control during a Cyclic Torsional Test

The torque motor direct-drive system is at the heart of the cyclic torsional test control process. The servo-actuator can be operated either in an analog velocity or torque closed-loop, or in a digital position closed-loop. For velocity and torque control, the servo-driver accepts ±10V analog input signal representing velocity or torque command and adjusts its output according to the voltage level of this signal. For position control, the servo-driver accepts, among others, two digital input signals, one called the Step input and the other is called the Direction input. For each pulse received over the Step input, the torque motor moves one motor increment in a direction that is determined by the signal received over the Direction input. The step input signal is a square wave which uses the Transistor to Transistor Logic (TTL) to specify the voltages corresponding to signal high and signal low.

In the DFSD, position control mode is used to conduct a strain-controlled cyclic test and to provide accurate and smooth control at very small deformations. However, to interface between the servo-driver and the computer for an automated control, a higher-level controller is needed to translate the command signals (generated from a PC) to a driver-compatible signal and to simplify the control process. The DFSD uses the OEM010 indexer by the Compumotor

Division of Parker Hannifin Corporation. Mounted inside the interfacing box, the indexer is a higher-level controller that communicates with the computer through the RS-232 serial COM port and controls the motion commands sent to the driver via an interface cable. Two cables run between the torque motor and the driver. The "motor cable" is used by the driver to supply and adjust the current in the motor's circuit. The resolver cable, on the other hand, is used to carry feedback signals representing the current status (including positioning) of the motor.

The control method in the position control mode can be I-PD-type or P-type control system. I-PD position control mode uses integral feedback to measure positioning error over the entire operating time history. P operating mode uses a proportional control system that alters the motor current by a proportion of the most recent positioning error. The I-PD method was selected in the DFSD because it provides highly accurate positioning and stable control under various conditions. The characteristics of the closed-loop (frequency, wind-up, and velocity loop gain characteristics) can be adjusted using switches on the front panel of the driver.

A second LabView program was developed for the control and data acquisition processes during a DFSD cyclic test. The program performs three important tasks. First it serves as an interface through which the operator can input the test parameters and visually monitor the progress of the test. Second, it uses the test input parameters to define the characteristics of the control loop which outputs the command signals to the driver via the indexer. Third, it automatically triggers and terminates the acquisition of the outputs of selected sensors and records the data into a text file.

To start a DFSD cyclic test, the operator first has to input the desired maximum shear strain amplitude, loading frequency, number of cycles and the shape of strain-time history using the LabView program. Based on this information, three parameters are determined: acceleration,

velocity, and displacement, which are then converted to the appropriate number and frequency of TTL pulses sent to the driver via the indexer. The velocity parameter determines the uniform peak rotational velocity at which the motor moves toward the specified displacement. The angular acceleration parameter is used to speed the motor up from a rotational velocity of zero to the uniform peak velocity. As the motor closes on the specified displacement, the angular acceleration changes from zero to the opposite of the initial acceleration, thus, causing the motor to slow down until it stops at the target displacement. The direction of motor rotation is then reversed and a new movement command is issued. Depending on the magnitude of the acceleration parameter, the shape of the angular displacement versus time curve produced by the indexer can be either sinusoidal or triangular in shape.

The torque motor will move one step each time the step input signal from the indexer to the driver changes from low to high. The size of the step depends upon the resolution of the motor. The Dynaserv DR-1060B direct-drive motor can be set for one of four resolutions: 507,904 steps/rev, 253,952 steps/rev, 126,976 steps/rev, or 63,488 steps/rev. To obtain the smallest torsional deformation possible, the highest resolution is usually used. This means that for a 4-inch diameter sample that is 10 inches long, each motor step represents a shear strain of roughly 0.00025%. However, this movement is applied inside the load module and because of frictional losses and compliance effects in the loading system, only a fraction of this movement is experienced by the sample. This is useful because it allows testing at very small strains with good resolution.

The driver causes the torque motor to move by increasing the current in its circuit the moment it receives the step-input signal. Motor motion is detected by a resolver that feeds it back to the driver. Any discrepancy between the desired and actual motion is corrected for by

modifying the current in the motor circuits according to the operating mode. The driver also passes the feedback signal to the computer via the indexer. This signal is displayed in real-time via the LabView program. A cable length of up to 300 ft has been used between the driver and the torque motor without any significant effect on the quality of the control loop or the feedback signal.

References

Baligh, M.M. (1985). "Strain path method," Journal of Geotechnical Engineering, ASCE, Vol. 111, No. 9, pp. 487-501.

Connolly, P.C. (1997)," The Development of a Cyclic Torsional Shear Device For Laboratory Evaluation of Soil Modulus and Damping". M.Eng. thesis, Department of Civil and Environmental Engineering, University of California at Berkeley

La Rochelle, P., Sarrailh, J., Tavenas, F., Roy, M., and Leroueil, S. (1981), "Causes of sampling disturbance and design of a new sampler for sensitive soils," Canadian Geotechnical Journal, Vol. 18, pp. 52-66.

Li, X.S. (1996)," A Flexible Strain Gauge for Soil Testing," Geotechnical Testing Journal, American Society for Testing and Materials, September.

Li, X.S., Roblee, C.J., and Wang, G. (1993). "Development and evaluation of a prototype tool for in situ determination of high-strain properties of soft to medium-stiff clays," Report No. FHWA/CA/TL-94/05, Research Project F92TL05, Caltrans, Division of New Tech., Materials and Research, Office of Geotechnical Eng.

Roblee, C.J., Li., X.S., Chan, C.K., Idriss, I.M., Wang, G., Herrmann, L.R., and Jakura, K.A. (1994),"Feasibility of a Tool for In Situ Measurement of Materials Properties of Clays Over a Wide Strain Range," Dynamic Geotechnical Testing: Second Volume, ASTM STP 1213, Ronald J. Ebelhar, Vincent O. Drnevich, and Bruce Kutter, Eds., Am. Soc. for Test. and Mat. , Philadelphia 28 p.

Roblee, C.J., Wang, G., Chan, C.K., Li, X.S., Current, W., Riemer, M.F., Holland, T.J., Herrmann, L.R., Silva, W.J., and Idriss, I.M. (1996),"Development of an In Situ Tool to Measure Dynamic Soil Properties," Proceedings of the 4th Caltrans Seismic Workshop, Caltrans, Sacramento, CA, 19 p.

Roblee, C.J., and Riemer, M.F. (1998),"The Downhole Freestanding Shear Device Concept," Geotechnical Earthquake Engineering and Soil Dynamic III Conference. ASCE Geotechnical Special Publication No. 75, Vol. 1, pp.201-212.

Wang, G. (1997),"Development of In Situ Test Apparatus for Measurement of Dynamic Properties of Soft to Medium-Stiff Clays," Department of Civil Engineering, University of California, Davis.

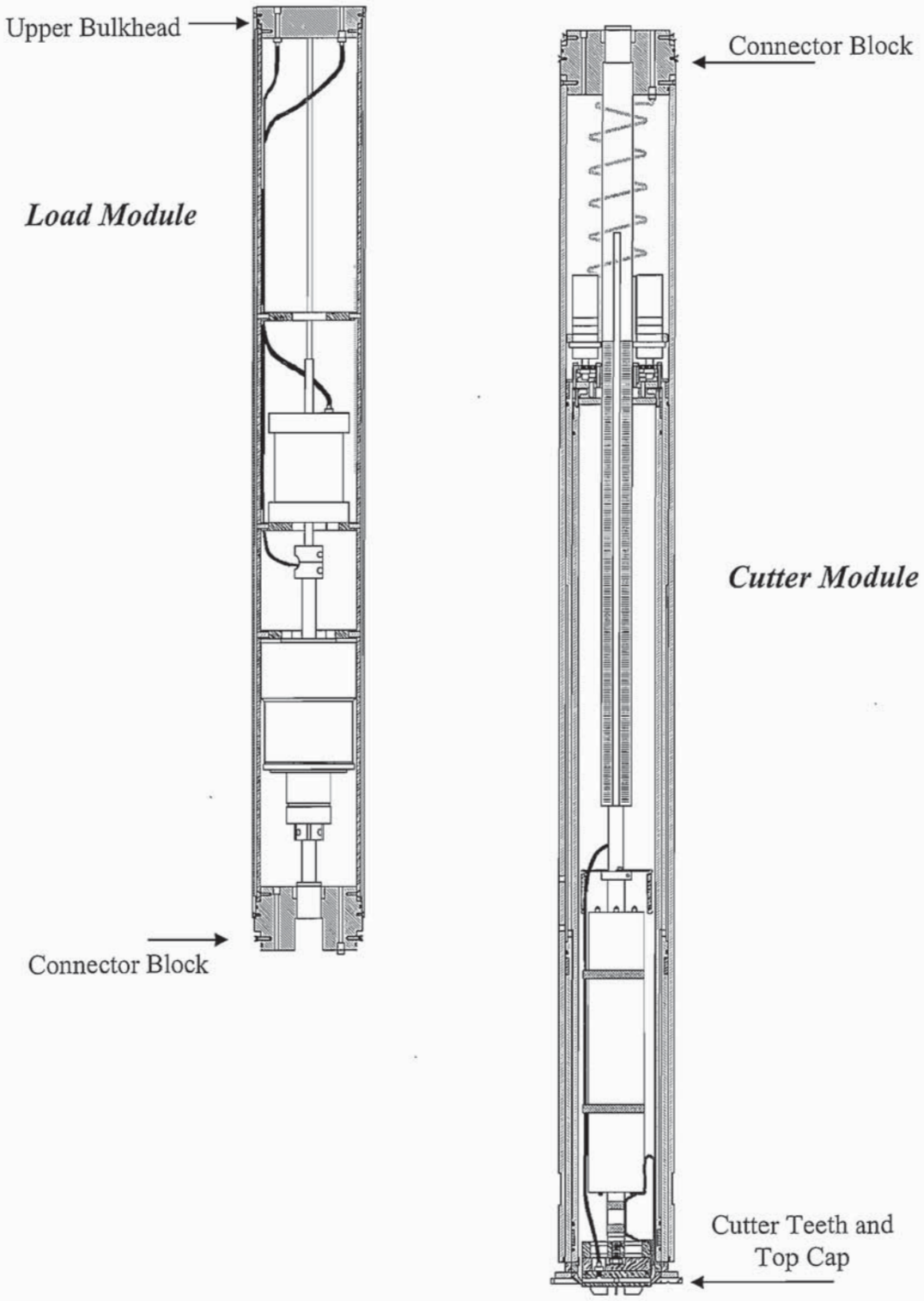

Figure 3.1 A general view of the DFSD load and cutter modules

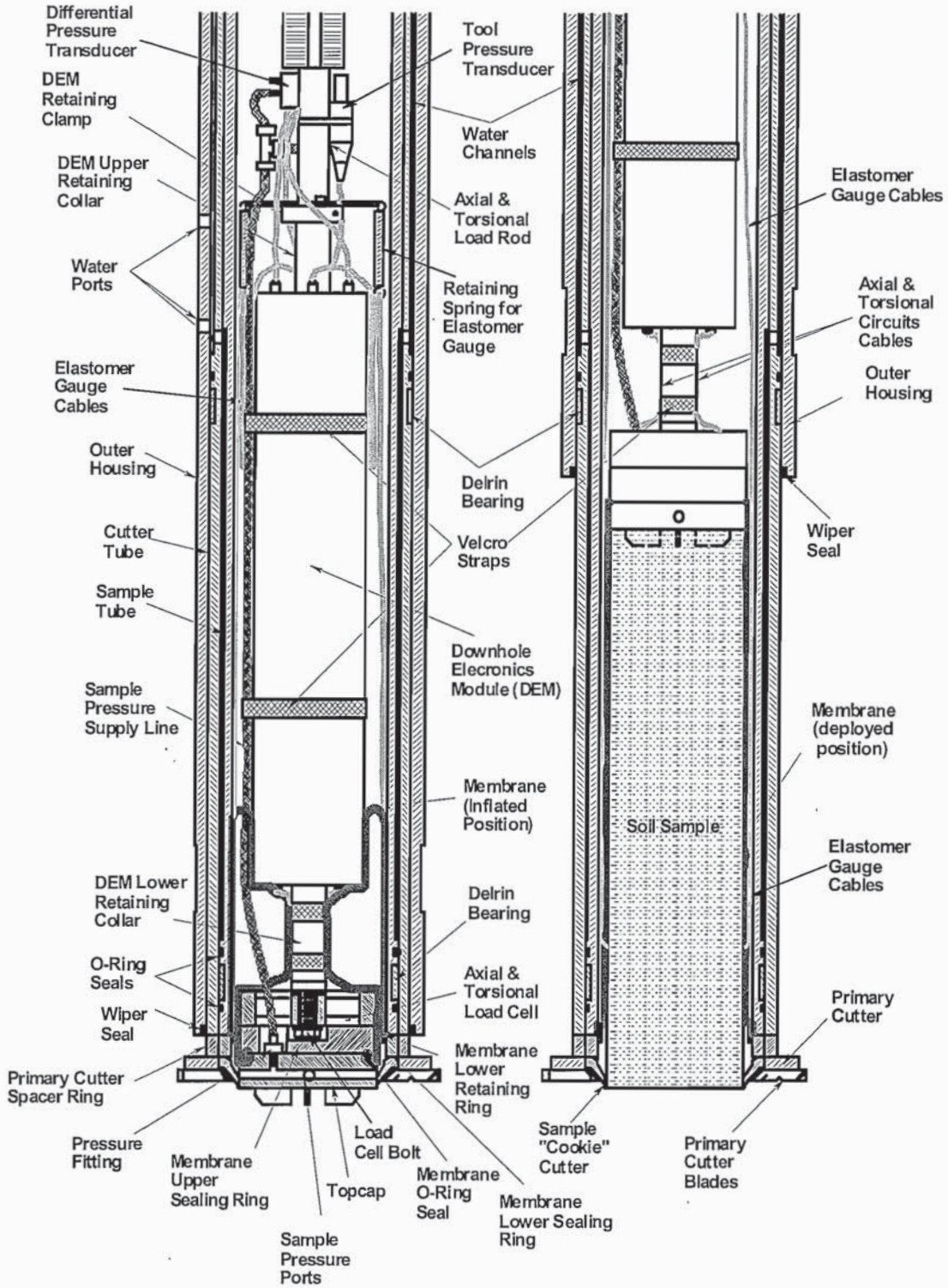

Figure 3.2: Drawings showing the lower end of the device before and after carving a specimen.

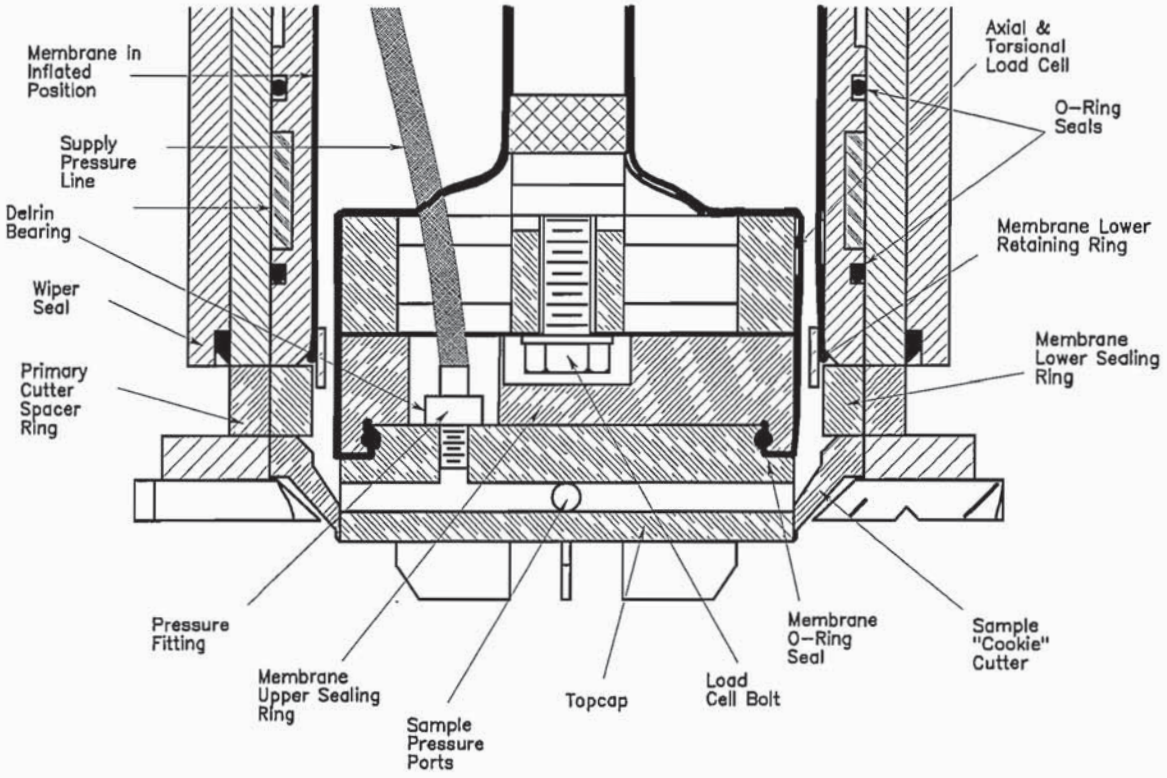

Figure 3.3: Bottom details of the cutter module

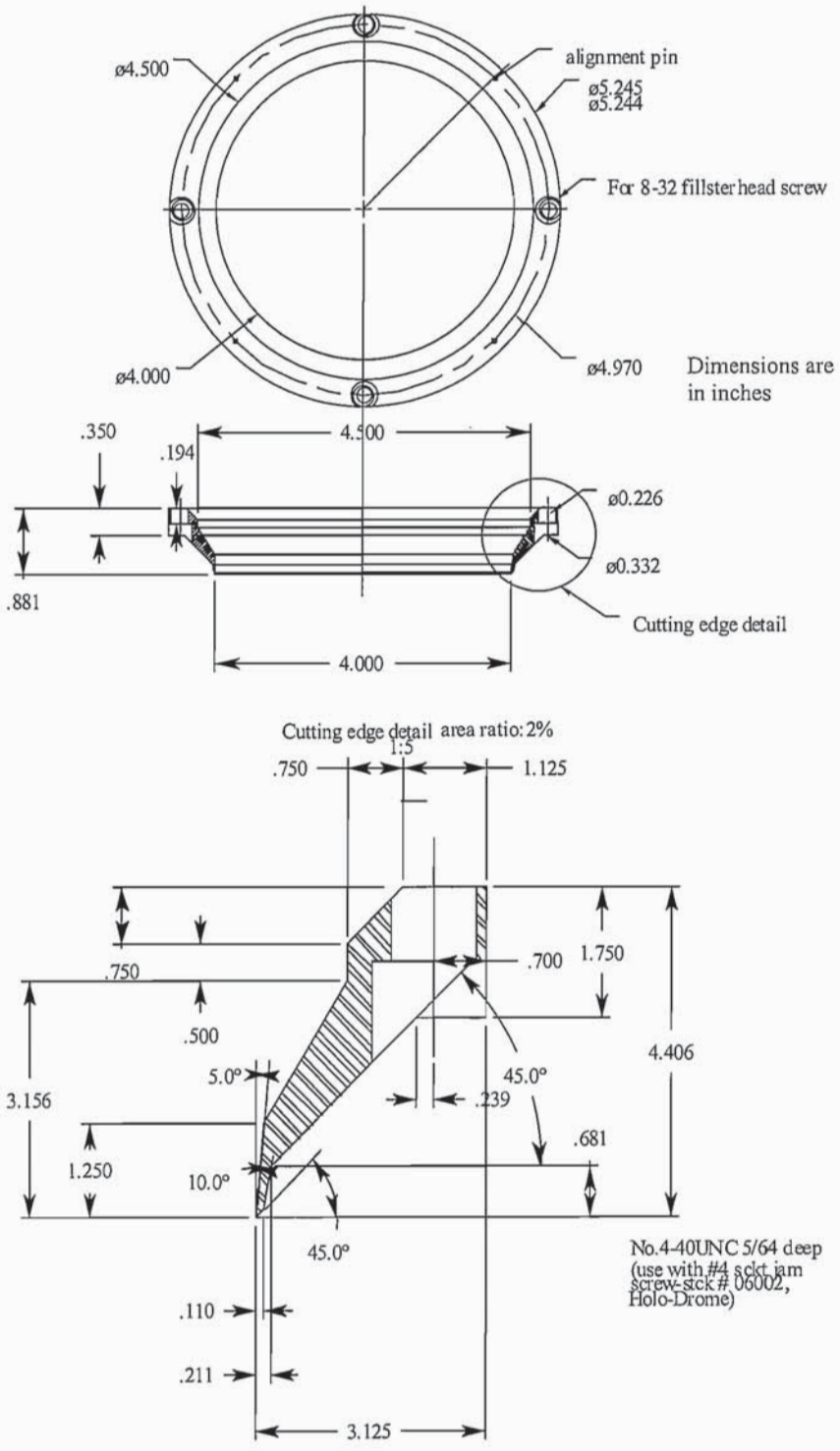

Figure 3.4: Sample "cookie" cutter design details

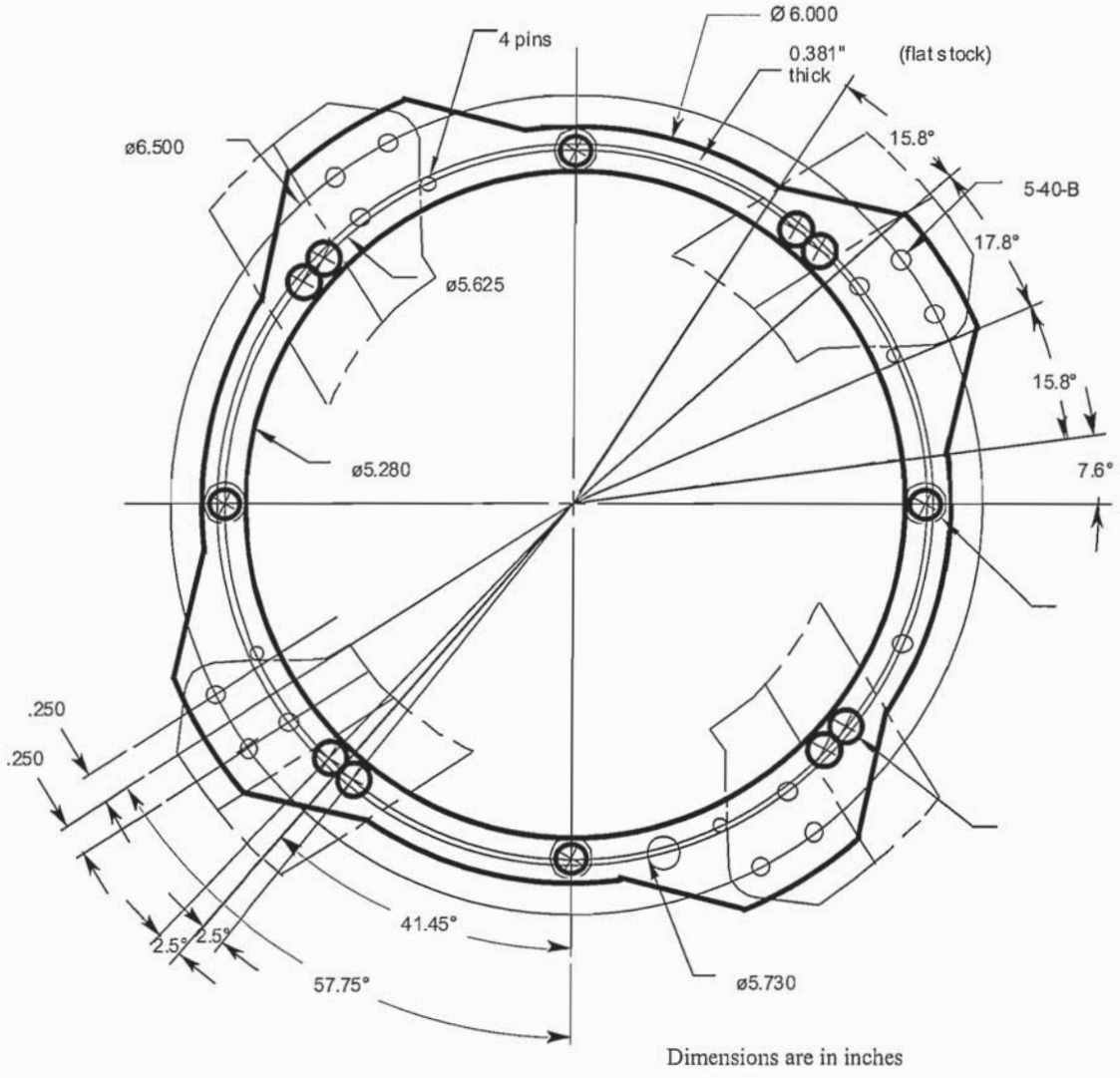

Figure 3.5: Cutting blades and cutting-blades primary mounting ring

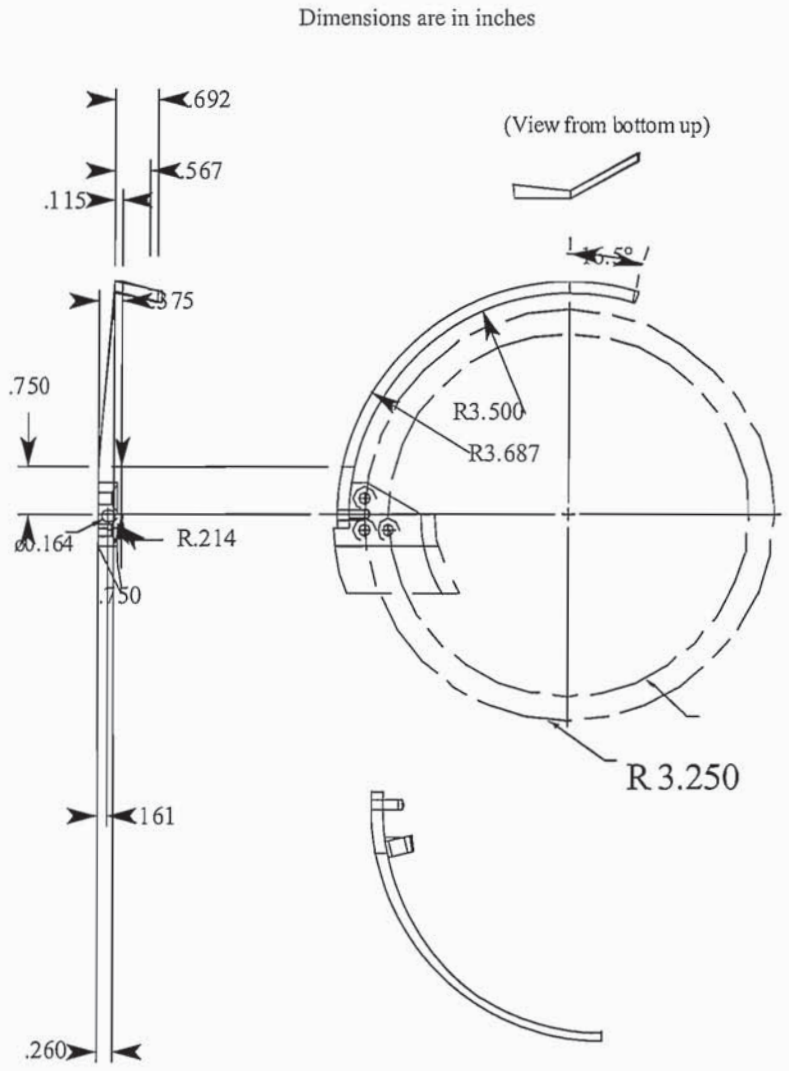

Figure 3.6: Design of the sample retrieval blades (slicer blades)

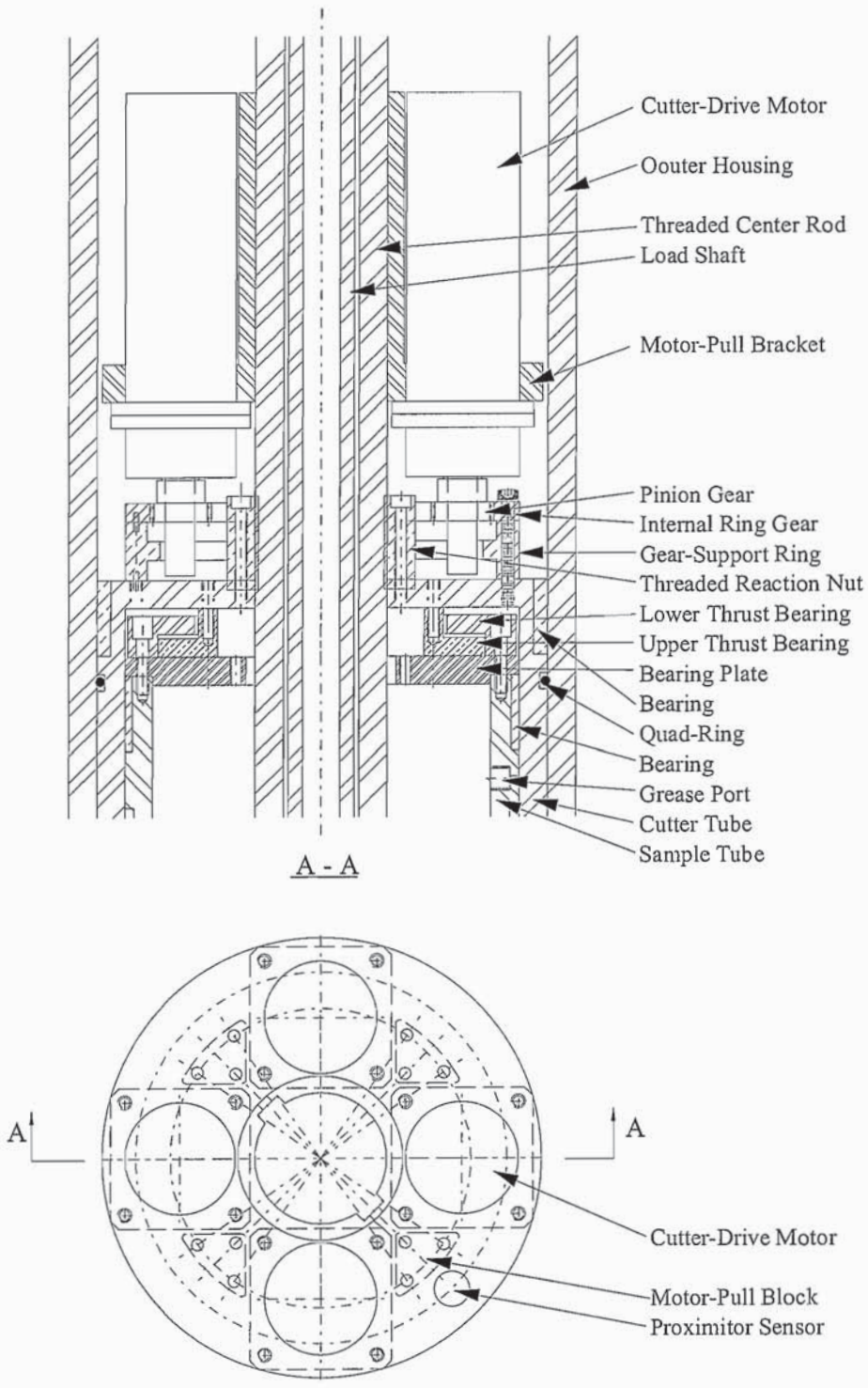

Figure 3.7: Details of the cutter-drive motor system section A-A

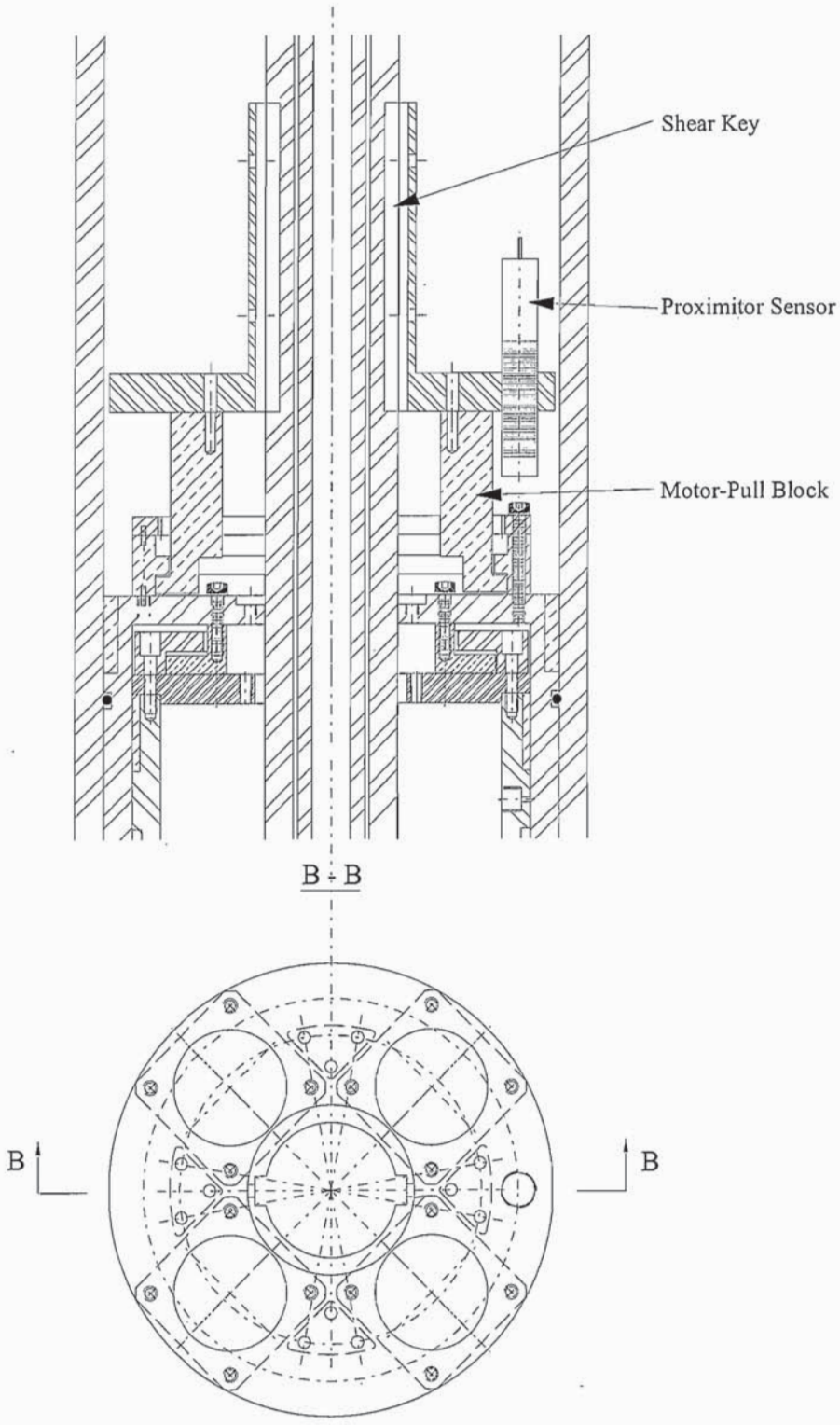

Figure 3.8: Details of the cutter-drive motor system section B-B

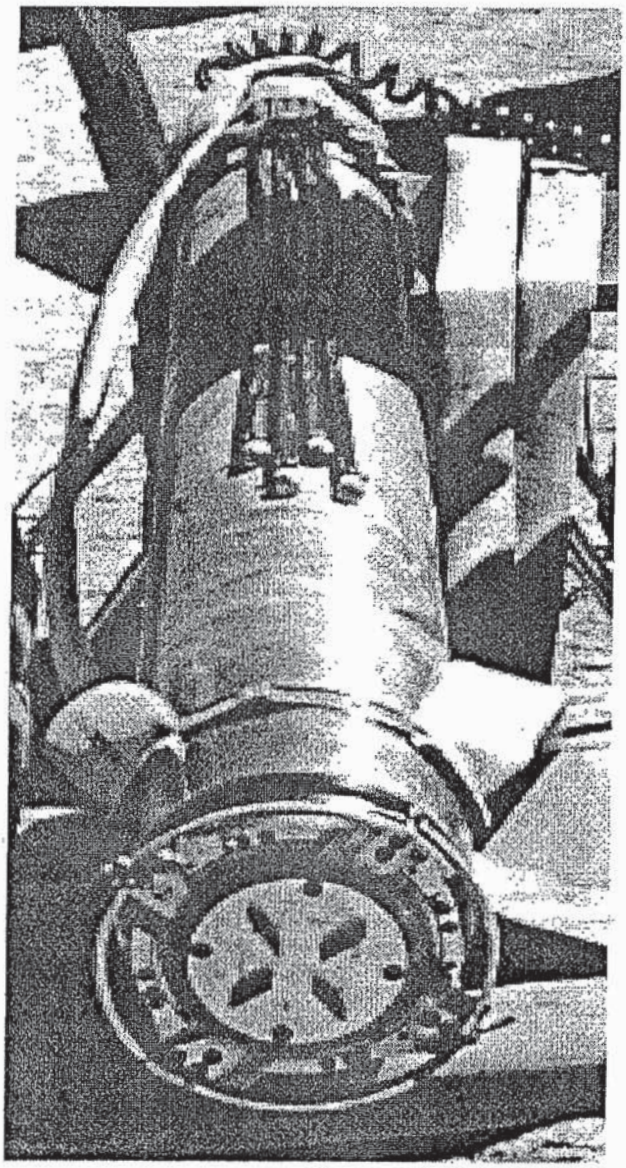

Figure 3.9: A picture showing the assembled cutter module of the DFSD

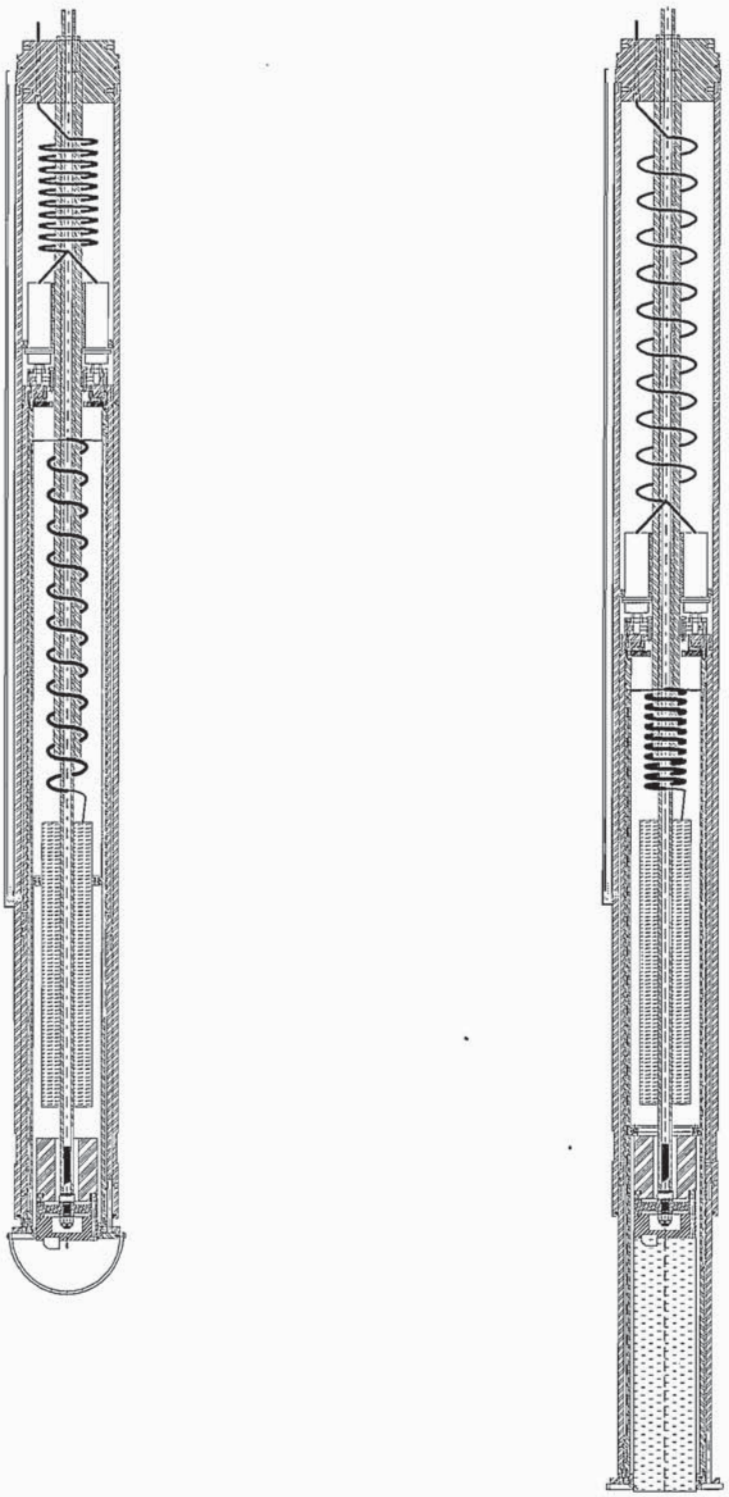

Figure 3.10: The cutter module in retracted (left) and extended/testing (right) positions

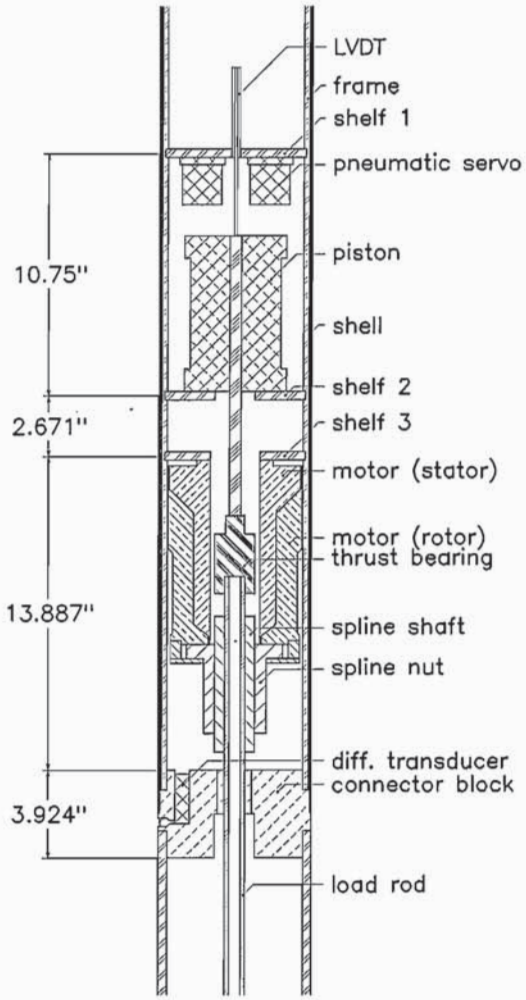

Figure 3.11: Design details of the load application system inside the Load Module

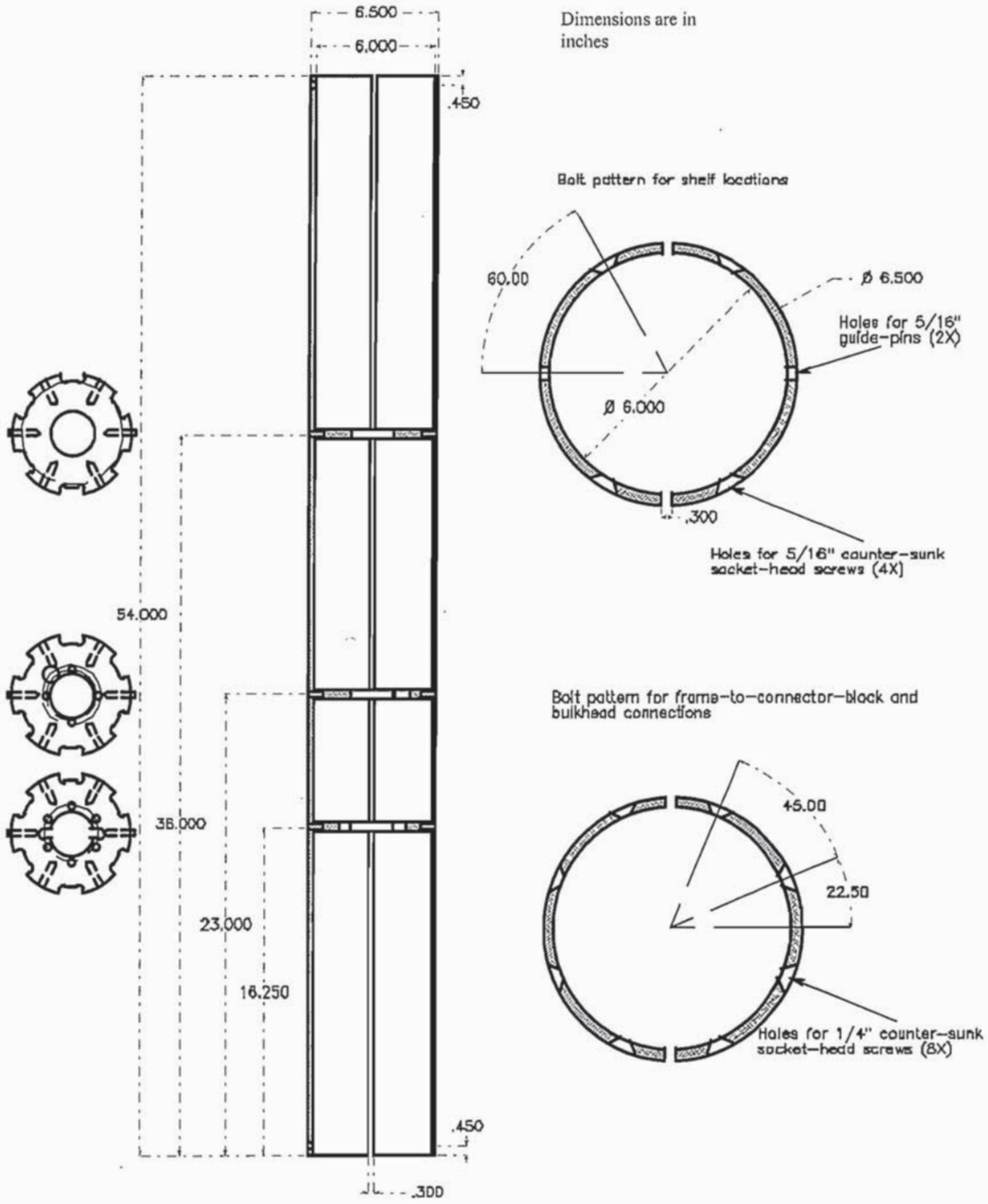

Figure 3.12: The load module frame and mounting shelves

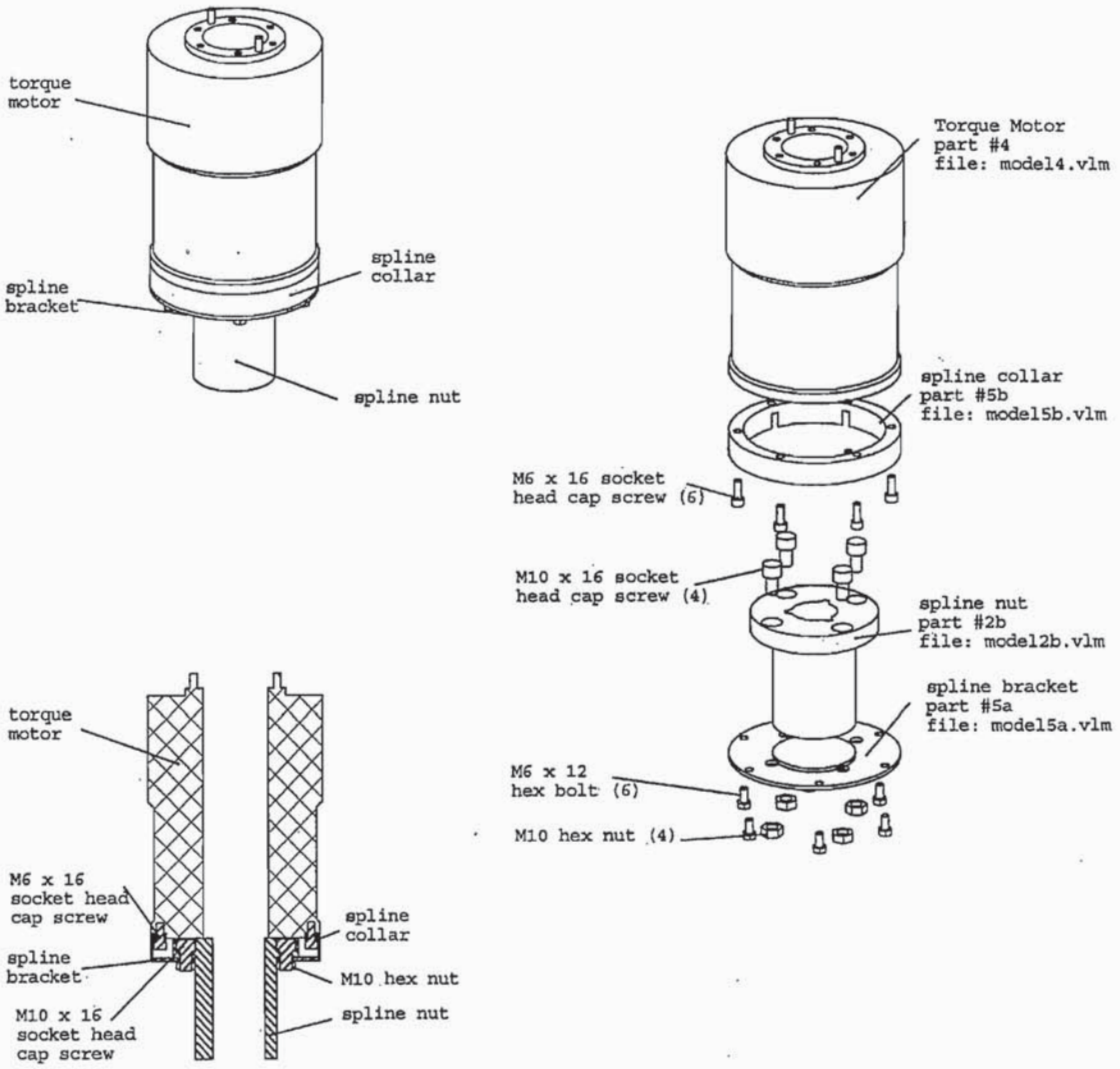

Figure 3.13: Torque motor and the spline shaft assembly

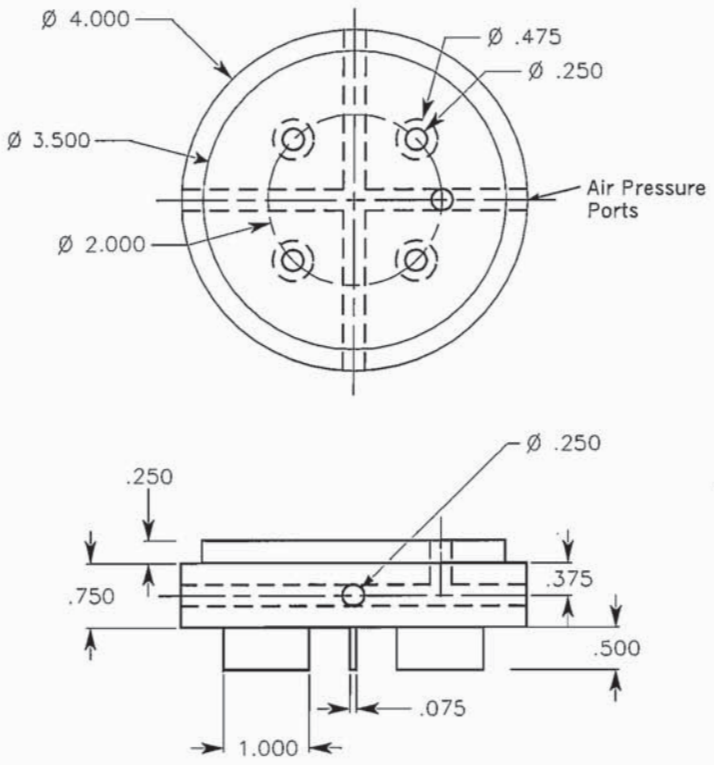

Figure 3.14: Top cap with vanes, design details

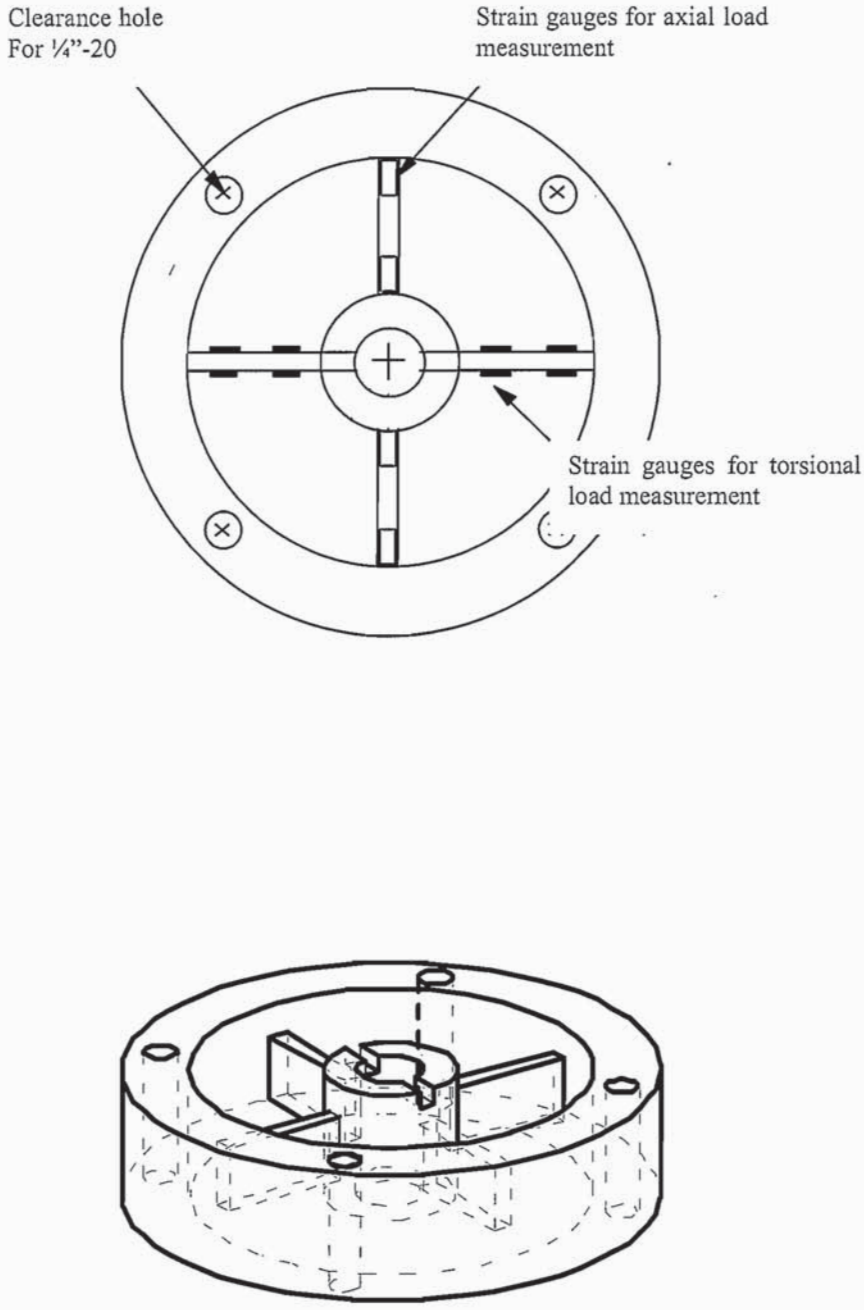

Figure 3.15: Two-axis load cell for axial and torsion loads measurement

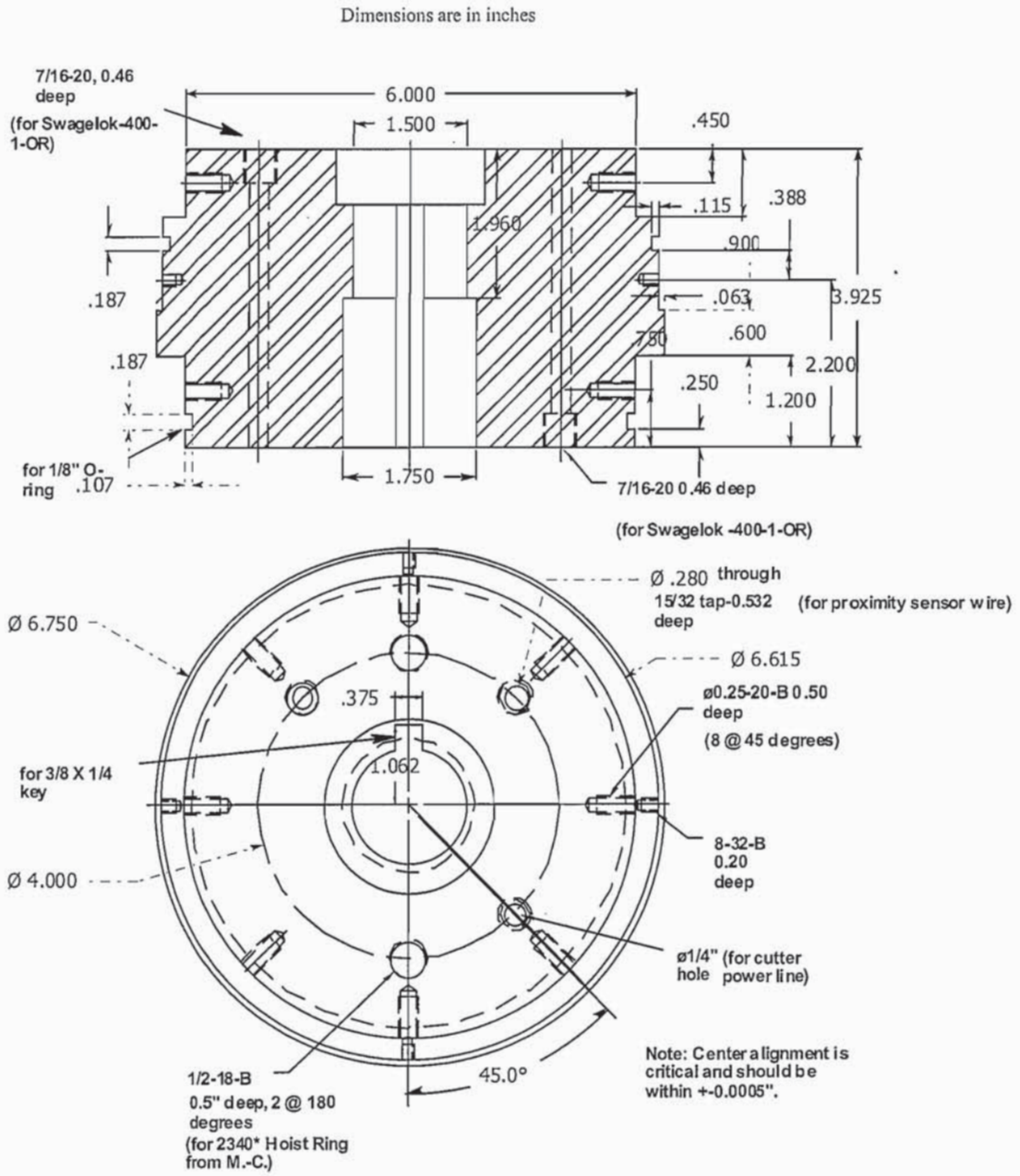

Figure 3.16: Design details of the connector block

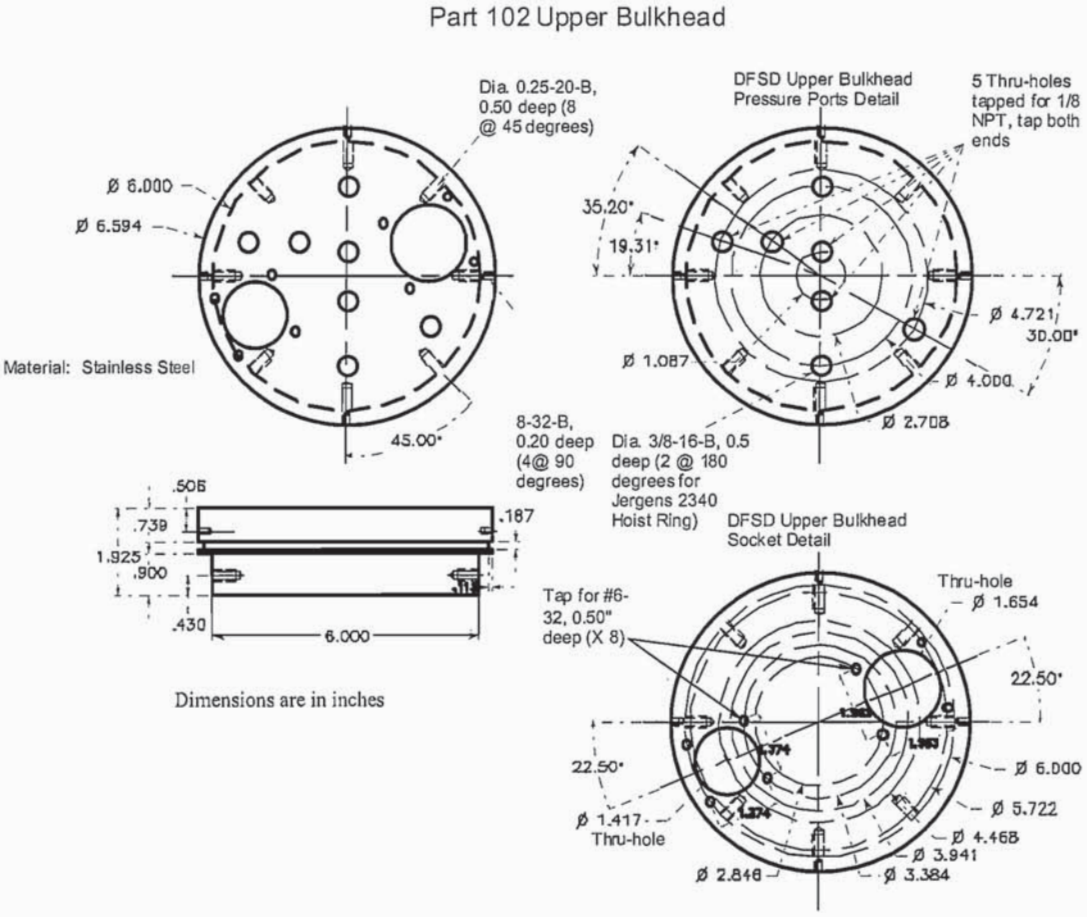

Figure 3.17: Design details of the DFSD upper bulkhead

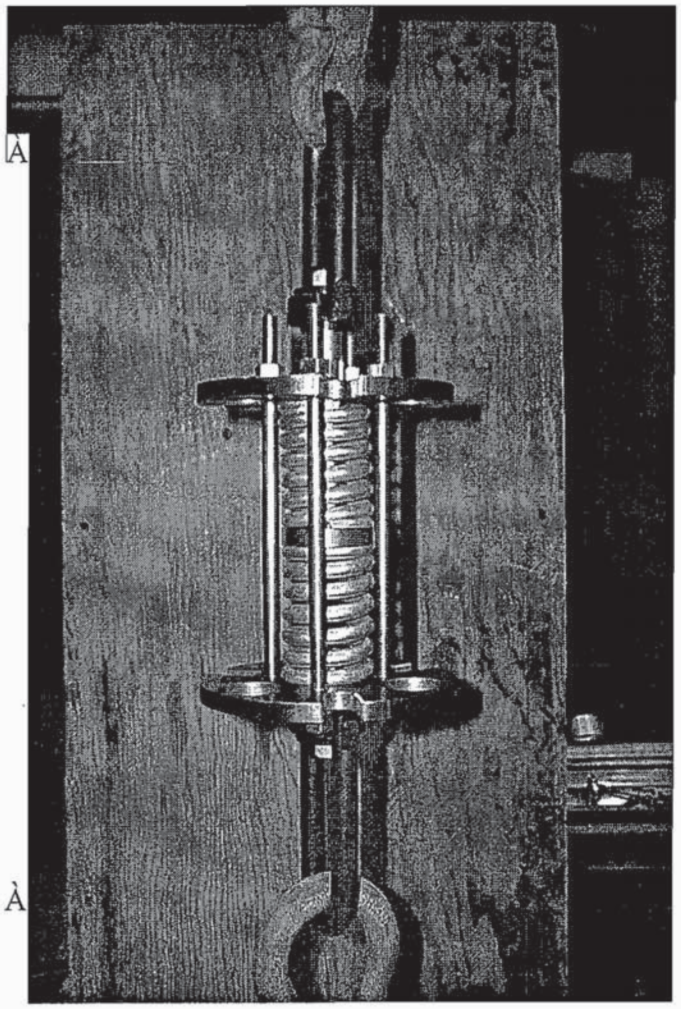

Figure 3.18: DFSD shock absorber

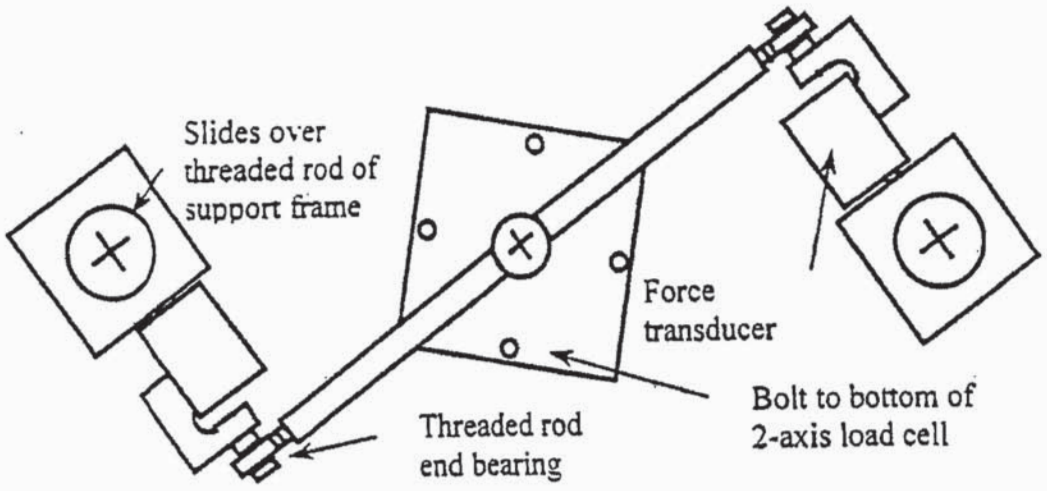

Figure 3.19: Apparatus used for calibrating the 2-axis load cell

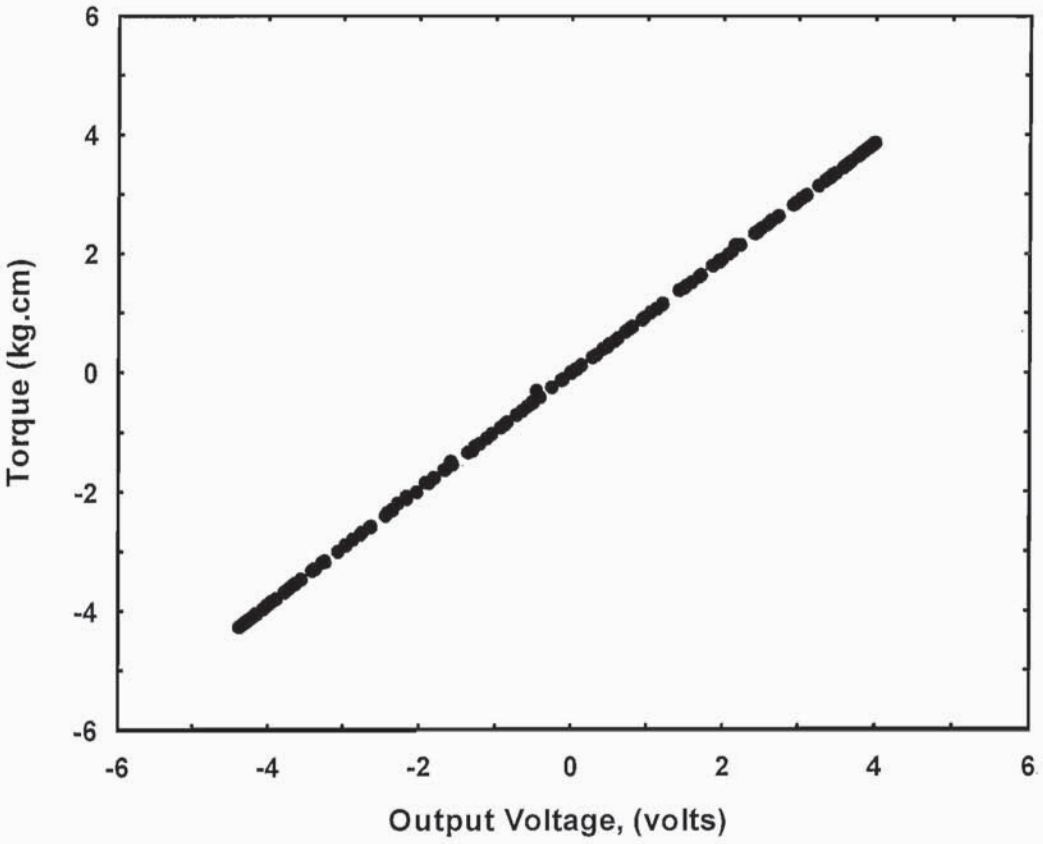

Figure 3.20: Calibration curve of the torsional load transducers of the 2-axis load cell

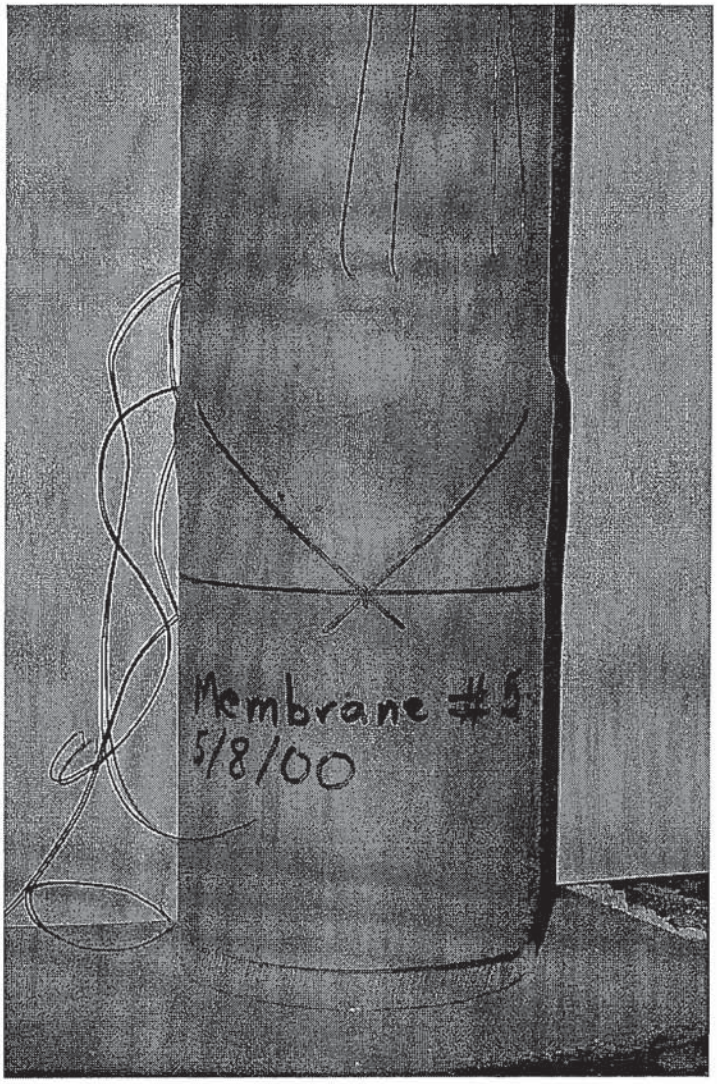

Figure 3.21: DFSD membrane instrumented with elastomer gauges

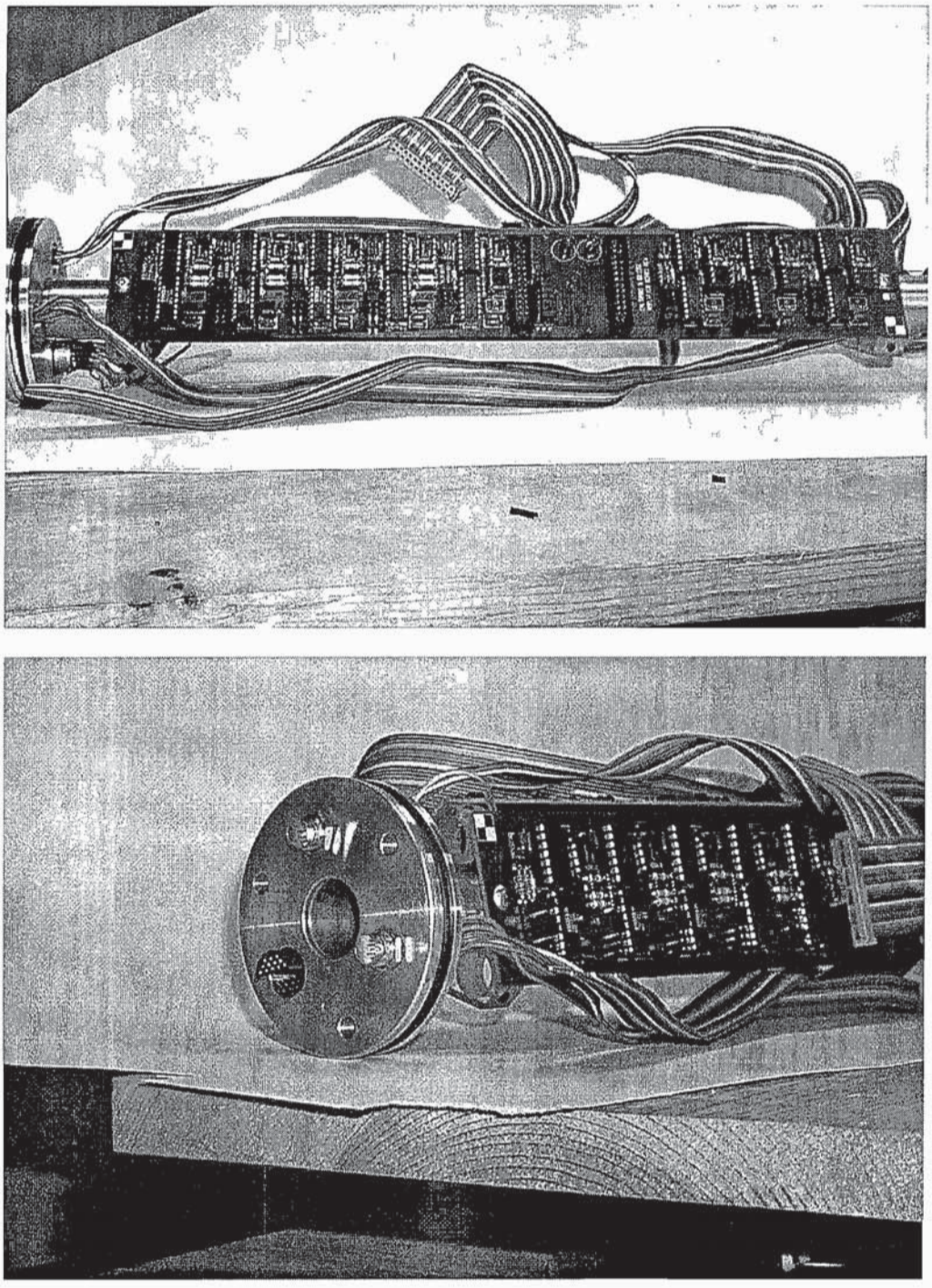

Figure 3.22: Views of the DFSD Downhole Electronic Module (DEM)

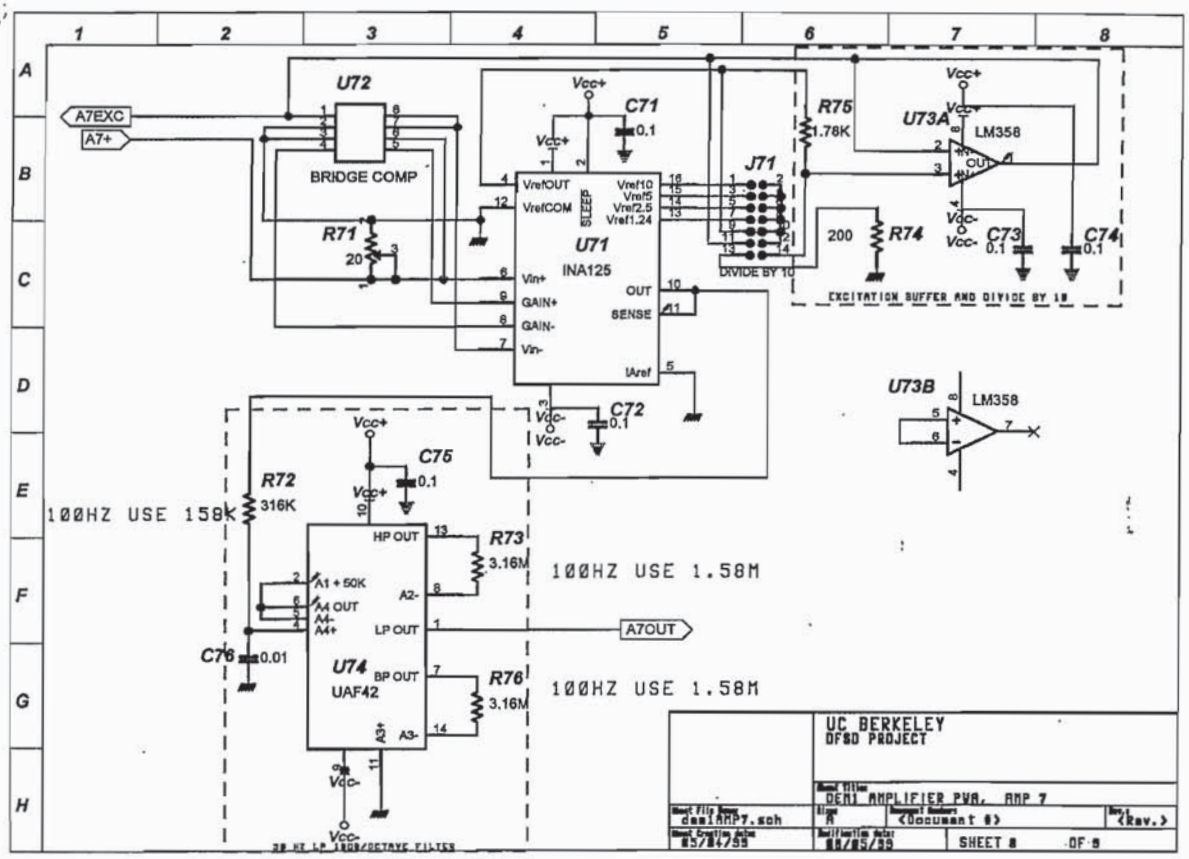

Figure 3.23: Circuit diagram for a typical signal conditioning circuit on the DEM board

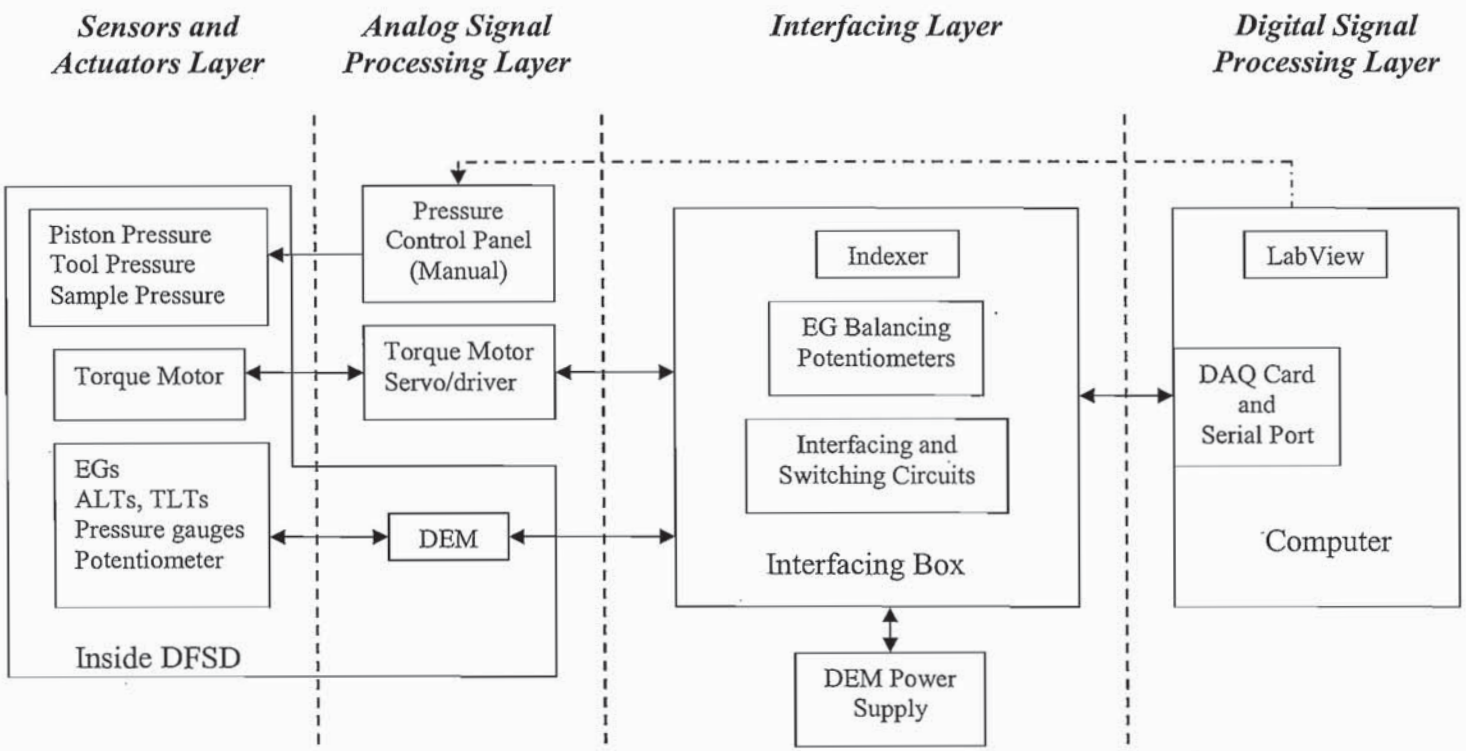

Figure 3.24: A diagram showing the data acquisition and control system employed in the DFSD during (Note: the system for the cutting motors is not shown)

CHAPTER 4:

Implementation and Validation of the DFSD

4.1 Introduction

After overcoming numerous technical challenges, the DFSD was completed and the new project focus was toward implementing the device and validating its performance. This task was carried out in several stages, starting with validating key components of the loading system using a bench top version of the DFSD and a "standard" material. Similarly, the implementation and validation of the elastomer gauge is presented in Appendix E. The second stage was aimed at implementation of the full-scale DFSD in the laboratory, testing reconstituted soils in a setup that simulates field tests. The focus in this stage was to gain experience in conducting the different phases of a DFSD test, evaluate the performance of its different components, and examine the reasonableness of the results. The objective of the third stage was to validate the DFSD in the laboratory through well-prepared tests on reconstituted soils under carefully controlled conditions. In the forth stage, the effort was directed toward field deployment and validation of the DFSD. Validation of the results from DFSD tests was achieved through comparison with the results from shear wave velocity measurements (in the laboratory as well as in the field) and/or from laboratory tests conducted independently at the University of Texas at Austin and at the University of California at Los Angles.

Ideally, validation as a concept requires comparing the shear modulus and damping obtained from the new device with the "correct" values. However, a "correct" standard for such comparison is not obvious since the DFSD is intended to improve the

measurements over conventional laboratory tests and extend the range of shear strains over which field measurements are obtained. Therefore, validation tests were conducted under conditions that would minimize the expected differences in results between DFSD tests and high-quality laboratory tests. Details of the tests conducted to validate the tool are presented in the following sections.

4.2 The Bench-Top Shear Device (BSD)

One of the strategies adopted in the implementation and validation of the DFSD is the development of a laboratory version of the device, called the Benchtop Shear Device (BSD), intended to perform high-quality laboratory torsional shear tests. The device was very useful for many objectives. First it was used to test, tune, and configure components used in the DFSD, especially its load application system and the load and deformation measurement systems both individually and as a unit. Second, it was used to calibrate and validate the performance of some DFSD elements like the load cell and the elastomer gauges. Third, it was effectively used to develop and test the software and hardware platforms of the data acquisition and control system in the DFSD. Finally, The BSD was used as part of the validation process first by testing "control" samples with known properties and second by testing retrieved soil samples to compare with the results of DFSD tests.

As with any other cyclic torsional shear device, the BSD can be used to determine shear modulus and damping ratio of soils in the laboratory. Moreover, the device has other advantages over currently available cyclic shear devices in its the ability to measure local and internal shear strains over a wide range of strains from 0.0005% to more than 1% depending on the range of interest. The device uses the same load cell assembly

employed in the DFSD to measure both axial and torsional loads experienced by the soil. The system is also capable of consolidating specimens both under isotropic and anisotropic stress paths. In the following sections, a more detailed description of the BSD and the results of the validation tests conducted on standard samples will be presented.

4.2.1 General Description of the BSD

The Benchtop Shear Device (BSD) is a torsional shear (TS) apparatus which uses the load and deformation application and measurement systems used in the DFSD. Tests are conducted by applying a cyclic angular displacement to the top of a solid cylinder of soil while fixing its bottom against rotation and translation. The sample is accommodated in a modified triaxial cell. The device components are supported by a frame with two threaded rods, 3.5-cm in diameter, supporting a crossbar which can be adjusted up and down along the threaded rods. The whole frame is mounted on a 15x18 inch steel base. A schematic of the BSD is shown in Figure 4.1.

The components and configuration of the load application system is similar to that in the DFSD. Deviatoric vertical stress is generated by a pneumatic piston, 3-inchs in diameter, mounted on top of the crossbar. The air pressure in the piston is manually regulated. With a 100 psi maximum supply pressure, the piston can generate axial loads up to 685 lb (3.05 kN). The BSD also uses a Dynaserv DR-1060B-115 servo-actuator to produce the torsional load. The direct-drive motor is mounted on a support bracket at the bottom of the crossbar. The motor has the same spline-shaft assembly used in the DFSD to provide a means to apply torsional load while allowing vertical displacement. A load rod, approximately 11.5 inch long and 0.85 inch in diameter, is used to transmit the applied loads down to the load cell/top cap assembly inside the cell. The top end of the

load rod couples with the piston rod via a thrust bearing to transmit vertical loads. Shown in Figure 8.2, the thrust bearing consists of two roller bearings mounted on an extension of the piston rod and enclosed in a cage that is attached to the load rod. The two roller bearings serve to reduce rotational friction in both compression and extension. The bottom end of the load is rigidly connected to the hub of the 2-axis load cell which is bolted to the sample top cap along the rim as shown in Figure 4.2.

To simulate a DFSD test, the apparatus has been designed for a 4-inch diameter sample with a length from 10.25 inches (26.04 cm) down to 7.25 inches (18.42 cm). The current setup allows up to 2.25 inch (5.72) of axial displacement for samples taller than 9.5 inches (24.13 cm), which decreases proportionally as the sample height decreases. The constraint on sample height and axial deformation range is a function of the height of the cell, the supporting frame and the load rod. If confining stress is not warranted, samples as tall as 11 inches (27.94 cm) and as short as 4.3 inches (10.92 cm) can be tested by leaving off the Lucite chamber.

To help transmit torsional load to the top of the sample while fixing its bottom, the top and bottom sample end caps have four 1-inch long (2.54 cm) vanes that penetrate 0.5 inch (1.27 cm) into either end of the sample. Also, the triaxial cell is clamped to the frame base plate to provide a rigid base for the sample to react against. The load rod enters the top of the triaxial cell through two linear-rotary bearings that provide guidance, smooth rotation, and linear vertical displacement of the rod. Compared to conventional triaxial cells, the linear-rotary bearings have nearly twice the number of tracks of ball bearings to reduce friction between the loading rod and its housing.

As in the DFSD, torque and axial loads are measured at the top of the sample via the load cell/top cap assembly. Deformations, on the other hand, can be measured internally at the top of the soil cylinder and locally by elastomer gauges (attached to a membrane) placed on the surface of the middle-third of the sample. Therefore, the BSD allows direct comparison between internal, global shear strains, and local shear strains and insight into the effect these have on the measured dynamic soil properties. The implementation of the elastomer gauges (number, characteristics, and orientation) in the BSD is the same as in the DFSD. Internal rotational deformations were measured by means of proximity transducers. Two types of proximity transducers made by Bently Nevada were used to cover as wide a strain range as possible. The 3000 MicroProximitor has a sensitivity of about 40 volt/mm and is used to measure small strains from about 0.0005% to 0.05% while the 7200 Proximitor has a sensitivity of 4 volts/mm and is used to measure strains form about 0.01 to 0.5%. Each proximity sensor is mounted to the outer surface of the load cell, as shown in Figure 4.3, thereby following the twisting movement of the top of the sample. The axis of the sensor is about 0.8R from the center of the sample, where R is the radius of the sample. The targets for the proximitors are 1-inch square-shaped pieces of steel, 0.25 inch thick, and are mounted on vertical posts 0.25 inches in diameter which are mounted through the top of the chamber. Thus the targets do not move during the test but they can be adjusted vertically according to the height of the sample, and rotated to remain orthogonal to the axis of the proximitor.

The confinement system employed in the BSD is the same as in any traditional triaxial apparatus, and is manually regulated. After sample setup is completed, the cell is

filled with de-aired water injected through a valve at its base. To protect the electronics of the load cell, the water level is usually brought just to the top of the sample. Isotropic confining pressure is generated through compressed air, which enters through the top of the triaxial cell. The sample is hydraulically connected to the outside through two 0.5 inch diameter porous stones at each end cap which are connected to two separate valves at the cell base by 1/8" flexible tubing. This allows for backpressure saturation and measurement of pore water pressure inside the sample. A third valve is connected to the inside of the chamber to measure the confining fluid pressure. Two pressure gauges are used, one which measures the pressure supplied to the chamber (isotropic cell pressure) and a differential pressure gauge that measures the difference between cell pressure and pore water pressure inside the sample (effective stress on the sample).

4.2.2 Implementation and Validation of the BSD

The first step toward validating the DFSD was validating its benchtop version, the BSD, using polyurethane specimens. The material was chosen for its known stiffness and handling characteristics. Samples were easy to prepare and results were less sensitive to variations in preparation procedure than for other materials. Results can be compared to documented properties from independent testing using a variety of testing methods. In this study, a two-component urethane elastomer resin specimen (Stokoe et. al. (1990)) was used. The first component consisted of dicyclochexylmethane-4,4'-diisocyanate and the second component consisted of diethyltoluene diamine. Urethane can be modeled as a linear, viscoelastic material with stiffness characteristics essentially independent of confining pressure, strain amplitude, and stress history. Urethane stiffness is, however, dependent on loading frequency and temperature. Therefore, the values of the modulus

have to be compared at the appropriate frequency and temperature. Urethane samples can be repeatedly tested as desired and are easy to construct in the appropriate sizes and hardness. Urethane stiffness is governed by the molecular structure of the prepolymer, a factor which is easily controlled during manufacture. Furthermore, the range of hardness (stiffness) is wide, enabling polyurethane to be manufactured with stiffness that is representative of different soils. Other favorable characteristics include toughness, durability, and high resistance to abrasion, weather, ozone, oxygen and radiation. However, the behavior of a polyurethane calibration specimen can be affected by time exposed to ultraviolet radiation and creep under load. Stokoe et. al. (1990) studied the effect of isotropic confining pressure, time under confinement, strain amplitude, loading frequency and temperature on calibration test results using urethane samples. The study used torsional shear, resonant column, and static compression testing on polyurethane samples having different stiffness.

The polyurethane used in this study to validate the apparatus was manufactured and calibrated in 1994 at the University of Texas. It was cast into a 4.0-inch diameter cylinder that was machined into its final 8.0-inch height. The urethane has a unit weight of 12.0 kN/m^3 (65 pcf) and a durometer hardness of 75A. Durometer hardness is a common index test for synthetic elastomers and is related to static Young's Modulus. The static Young's modulus of the urethane sample should therefore be about 15.5 MPa (2250 psi).

A series of cyclic torsional shear tests have been conducted at different strain levels. A hysteresis loop from one of these cyclic tests with shear strains obtained from the elastomer gauge measurements is shown in Figure E10. Figure 4 .4 shows the

values of shear modulus and damping ratio obtained from BSD tests based on the elastomer gauges' and the proximity transducers' strain measurements as compared with the results from the tests conducted at the University of Texas-Austin using a torsional shear device with global internal strain measurement using proximity transducers. As a linear material, the shear modulus of urethane should be independent of shear strain. This property is very useful in a "calibration" material since it shows the accuracy of measurement and the effect of any compliance in the system at very small strains. The shear modulus obtained by the BSD is essentially the same at all strain levels which indicates a negligible compliance effect and fairly accurate measurements at very small strains. In general, the shear modulus values from BSD tests and UT's TS tests are in good agreement. The higher values obtained from the elastomer gauges is due to the local rather than global nature of strain measurement in which alignment errors and end-restraint effects are largely eliminated. This observation has been noted by many studies (e.g. Hight et. al. (1983)). The minor difference between shear modulus values obtained from proximity transducer's global strain measurement in BSD tests and UT's TS tests is believed to be mainly due to aging of the sample. Moreover, the damping ratio obtained from BSD testing is also independent of strain level and is about 4%, which is similar to the value reported from UT's TS tests.

In summary, the successful implementation of the BSD indicated that the load and deformation application and measurement systems can be reliably used in the DFSD to obtain accurate results. It also shows that the hardware and instrumentation are capable, as hoped, of measuring dynamic soil properties across the entire strain range of interest for geotechnical problems. Accordingly, the next phase was to validate the full-scale

DFSD in laboratory tests that simulate field conditions. This was done in two stages. The first stage was focused toward implementation of the device. The second stage was the final laboratory validation of the device and included comparison with independent tests conducted on specimens sampled from blocks of identically prepared soil.

4.3 Laboratory Implementation of the DFSD

Before validating the device, it was necessary to gain experience conducting the various steps of a DFSD test, evaluate the performance of the different components to see if any adjustment was warranted, and to examine the reasonableness of the results. Because of the scale of the DFSD, field deployment requires special equipment and a relatively lengthy preparation procedure and, therefore, is not well-suited for preliminary implementation where multiple trials are needed. Moreover, there is less control over test and material conditions and more uncertainty regarding changes produced by the device, all of which are unfavorable conditions for a first-hand evaluation of its performance. Therefore, laboratory implementation of the full device was carried out in large blocks of reconstituted clay to simulate field tests. The clay was consolidated from thick slurry to obtain homogeneous specimens under controlled conditions. However, to fully characterize the test and material conditions and maximize the amount of information that can be gathered from DFSD tests, specially instrumented chambers were developed, as illustrated in the following section.

4.3.1 Development of the "Smart" Consolidometer

The "smart" consolidometer is an instrumented stainless steel chamber approximately 0.3 m in diameter and 0.5 m in height. The concept and the configuration

of the apparatus are shown in Figure 4.5 and Figure 4.6. The consolidation stress is generated by air pressure introduced through the bottom plate of the chamber and applied against a piston. The upward movement of the piston squeezes the soil up against a floating porous stone which reacts against the fixed upper plate of the chamber.

Because of side friction between the chamber wall and both the piston and the soil, the applied air pressure may not necessarily be the same as the consolidation stress experienced by the soil. Therefore, a load cell is placed between the upper plate of the chamber and the floating stone to measure the consolidation load. Consolidation-induced vertical displacement is measured by a wire potentiometer that is connected to the piston rod. Before filling the consolidometer with soil slurry, a small pore water pressure transducer (0.5 cm in diameter) mounted on a stainless steel stand is centered and attached to the bottom plate of the chamber. This transducer measures the pore water pressure within the soil during the consolidation process, the carving/sampling process, and the DFSD cyclic shear test. The transducer was positioned such that it is near the central axis of the carved sample, so that the tool would carve around it. The transducers' output signals are acquired by a computer via a DAQ card and instantaneously monitored and saved using a LabView program. With measurements of load, displacement and excess pore water pressure, the consolidation process, as well as the effective stress within the soil, is reasonably characterized. Figure 8.18a shows a typical consolidation curve obtained from an increment of loading using this apparatus

4.3.2 Laboratory Simulation of DFSD Tests

When the soil is fully consolidated under the desired vertical stress, the consolidometer is set up to simulate a DFSD field test. The process begins by removing

the upper plate and the porous stone from the top of the consolidomter to expose the upper surface of the consolidated soil block, which simulates the bottom of a borehole. Meanwhile, the piston is locked to prevent any downward movement of the soil block during the test. A 0.2 m diameter steel casing is then rigidly attached and sealed to the top of the chamber as shown in Figure4 .7. The 1.5 m length casing has the same functions as the casing used in a field test. The length of the casing affects the level of confining stress that could be applied by the DFSD and is limited by the clearance of the crane used in the laboratory to lift the tool and the casing. The DFSD is then lowered into the casing and onto the soil surface and pneumatically locked against the casing by inflating the fire hoses. Figure 4.8 shows this setup. With the tool secured in place, an axial load is applied, using the piston in the DFSD, to insert the vanes of the top cap into the soil surface and to re-establish the vertical stress. With this setup, the test conditions are very much the same as those present in the field. With the membrane inflated away from the soil, a freestanding column of soil is carved inside the consolidometer by the excavation of an annular ring of soil while maintaining the pre-existing stress state. Cuttings are flushed off the cutting blades and up the consolidometer by streams of water jetted onto the blades. Once the sample has been cut to the desired length, the instrumented membrane is deployed against the sample by adjusting the differential pressure across the membrane. Figure 4.9 shows the DFSD in the consolidometer after the completion of sample creation and just before torsional loading.

4.3.3 Materials Used in the DFSD Laboratory Implementation Tests

Several DFSD tests were conducted on reconstituted cohesive soils prepared from thick slurries using the "smart" consolidometer. Most of the preliminary tests were

conducted on kaolinite. The soil is a synthetic clay manufactured by Georgia Kaolin Company (The product is called Sno-Cal-50). It has a liquid limit of 29, a plastic limit of 22, and a plasticity index of 7. One of the reasons for using this material is its short consolidation time, especially given the soil quantities required for the tests. This was very appropriate during the first DFSD tests when the focus was on implementation of the DFSD.

However, as more DFSD tests were conducted, more attention was directed toward evaluating the reasonableness of the tests results, especially as preparation for laboratory validation was underway. Because it is an artificial material with predominantly silt-size particles (60%) and low plasticity, the kaolinite behavior is more sensitive to changes in stress and water content compared to natural cohesive soils and, therefore, some aspects of its behavior would be expected to resemble cohesionless soils, especially at low stresses. Consequently, another clayey soil was tested as well. This time the soil was a natural brown plastic silty clay (CH) obtained from a region called Bear Creek. It has liquid limit of 71%, a plastic limit of 34% and a plasticity index of 37%. Because it takes a long time to consolidate a batch of this soil, only one DFSD laboratory test was conducted on this material. The general objective was to test two soils with a low and a high plasticity to examine if the DFSD would predict the expected trends in dynamic soil properties as a function of soil plasticity.

4.3.4 Evaluation of DFSD Laboratory Implementation Tests Results

In the early DFSD tests on kaolinite, the focus was on performing the basic functions of the tool, which includes tool setup inside the casing, sample carving process, air confinement and stress control procedures, membrane deployment, application of

cyclic torsional load, and the data acquisition and control processes. The tests were very successful and for the first time the full-scale DFSD was implemented with all its modules and test phases. As hoped, all tool systems functioned properly and the DFSD concepts were proven to be applicable and valid. Also, during this phase, adjustments were made to address some of the concerns raised during the tests.

In the following series of DFSD tests on kaolinite, the focus shifted to assessing sample quality and disturbance, conducting high-quality "downhole" cyclic torsional shear tests, and evaluating the measured dynamic soil properties. Issues such as signal quality and noise level, measurable strain range, soil behavior during the carving and testing processes, test data interpretation and processing, sample retrieval, and post-testing evaluation of sample quality were especially important. A key challenge (and anticipation) during this phase was whether very small strain measurements (G_{max} strain level) would be attainable given the "downhole" environment. This task was further complicated by the fact that all test phases using the DFSD including the instrumented membrane deployment are remotely controlled. Accurate measurement of small strain stiffness is still not easy to obtain in conventional laboratory devices where test setup and progress are under direct control and observation. However, the successful implementation of the elastomer gauges in the bench top testing device indicated that the main obstacle in the DFSD would be the electrical noise level. Therefore, a significant effort was directed towered decreasing the noise-to-signal ratio. Obviously, this can be done by either increasing the voltage level of the output signal or by decreasing the electrical noise infiltrating the signals. Both strategies were pursued.

Increasing the sensitivity of the elastomer gauge was one of the effective remedies to improve the fidelity of the strain signal. In the first DFSD test on kaolinite (in August 1999), 0.5-inch long gauges with a 1.5 mil capillary diameter were used. Liquid latex was used to attach the gauges to the membrane. Also, at that time, the balancing potentiometers were left on the boards inside the DEM with no remote means to bring the gauges back in range. Therefore, the level of excitation voltage and, hence, the sensitivity of the gauges was limited to increase the probability that the gauges would be in-range after the sample is cut and the membrane is deployed. Data obtained from this test was noisy at moderate strain levels and damping was only observable at large strains. The elastomer gauges worked very well but were not reliably applied.

Subsequently, several measures were taken to improve the strain measurement capabilities starting by implementing the "Uphole Balancing Potentiometers" concept. The potentiometers, which constitute one arm of the elastomer gauges' bridge circuits, were moved out of the DEM to the "surface" and placed in the interfacing box, adjacent to the computer. Four high-quality potentiometers with very responsive and stable output were used, one for each gauge. This allowed remote and independent adjustment of each gauge zero point, therefore allowing very sensitive gauges to be used without risking the loss of "gauge range" prior to the test.

As discussed in Appendix E, , the sensitivity of the elastomer gauge can be increased by increasing its resistance. Gauges with capillary diameters of 1.0 and 0.75 mil and lengths of 1.0 to 2.5 inch were manufactured. This increased the potential sensitivity of the gauges up to four times compared with the early generation of gauges. After several trials, a combination of two 2.5-inch long gauges with 0.75-mil capillary

and another two 1.0-inch long gauges with 1.0-mil capillary was proven sufficient for measurement of a wide strain range. Moreover, the method of attachment of the elastomer gauges to the membrane was also improved. Urethane adhesive made from the same material as the elastomer gauge was used to provide a stronger gauge bond to the latex membrane and to seal wire penetrations. The gauges became more integrated with the membrane and the whole system became more robust, durable and reusable.

The second approach to enhance the signals' fidelity was to reduce electrical noise infiltration to and noise generation from the tool's systems. Many measures were taken to achieve this goal. First, all cable and wire shields were properly grounded along with the tool's frame. Several testing sessions (without soil testing) were conducted to try different grounding schemes. The objective was to avoid ground loops and identify the best grounding arrangement. Second, high- and low-voltage signal lines were carried in separate cables to avoid cross-contamination by the generated inductive fields. A third measure was reducing the cutoff frequency of the analog filter inside the DEM from 100 to 30 Hz. Finally, it was realized early that the torque motor drive system generates a strong magnetic field which is reflected as electrical noise and distortion in the small-magnitude signals. To address this issue, a special noise filter provided by the same manufacturer of the torque motor drive system was used. The filter is coupled with the servo/driver and functions to filter and enhance the quality of the torque motor data signals which are sent from the servo/driver to the torque motor inside the tool. Also, the driver was separately grounded and placed at a sufficient distance from the rest of the tool electronics.

The aforementioned measures were very successful in improving the quality of the signals. To gauge this improvement, a comparison between the strain signals obtained from two DFSD tests before and after these changes were made is shown in Figure 4.10. Moreover, the quality of the stress and strain measurements at different strain levels is shown in Figure 4.11 and Figure 4.12, respectively. It is evident that substantial improvements had been achieved since the first test. The measurement/system noise was reduced by orders of magnitude which enabled strain measurement below 0.001%. The quality of DFSD measurements is also demonstrated by the stress-strain loops shown in Figure 4.13. At small-strain levels, the loops show the non-degradable linear behavior of the soil. As the peak shear strain increases, the loops become gradually fatter with decreasing slope. This improvement in the tool performance was a major milestone in the DFSD development.

Once small-strain measurement was proven attainable, more tests were conducted to evaluate the quality of the measured dynamic properties. Figure 4.14 shows the G/G_{max}-γ and D-γ curves from two separate laboratory DFSD tests conducted on different batches of reconstituted kaolinite. The vertical consolidation stresses were 2 and 0.5 ksc in the first and second test, respectively, and both were tested at a vertical stress of 0.5 ksc. Examining the results from the two tests, two important observations can be made. First, dynamic soil properties were obtained over a wide strain range from about 0.0005% up to 1% in one suite of tests with a single test setup. This is a significant achievement given the fact that even with today's advanced laboratory torsional shear devices, measurable strain range is usually limited to small-to-intermediate strain levels using one test setup. The second important observation is the repeatability of test results for the

same material both for the normalized shear modulus and damping ratio. This indicates a high level of reliability in the DFSD measurements. As discussed in Appendix D, the G/G_{max}-γ and D-γ curves of cohesive soils are not significantly influenced by moderate changes in effective stresses. The shape of the normalized shear modulus curve and damping ratio curve obtained from the DFSD is typical for cohesive soils with low plasticity. The curves begin with a short plateau followed by a rapid degradation in shear modulus or increase in damping ratio. The linear cyclic threshold shear strain obtained from DFSD tests on kaolinite is about 0.0008% which is in the range reported by Vucetic (1994) for soils with similar plasticity (Figure D.2).

Another set of laboratory DFSD test were conducted on reconstituted Bear Creek clay. Figure 4.15 shows the G/G_{max}-γ and D-γ curves form two DFSD tests at mean effective stresses of 0.33 and 0.75 ksc. As expected for a high plasticity soil, the results show more linear behavior and insignificant effect of a moderate change in confining stress. The cyclic linear threshold strain is approximately 0.0045% which is again in the range predicted by Vucetic (1994). Figure 4.16 shows the G/G_{max}-γ and D-γ curves obtained from the previous tests as compared to the generic curves of Vucetic and Dobry (1991). The DFSD seems to predict the correct trend of the degradation behavior of G and D as a function of plasticity as discussed in Appendix D and modeled by the Vucetic and Dobry (1991) curves. The soil with the higher plasticity shows less degradable behavior and lower damping values at moderate-to-large strains. It should be noted, however, that the DFSD measurements of damping ratio of kaolinite (PI=7%) are higher than the Vucetic and Dobry (1991) curve for soils with PI=0%. This was not a failure of the DFSD but rather an expected behavior of the tested kaolinite. Gookin

(1998) has tested the same material under different consolidation conditions in cyclic triaxial tests. The reported damping values are similar to those measured by the DFSD under similar stress conditions.

4.4 Laboratory Validation of the DFSD

After the successful completion of the implementation phase and with the confidence gained in conducting DFSD tests, laboratory validation was carried out using the same test setup. However, to minimize the unloading effects, the final increment of consolidation was applied with the tool in place within the casing. This was achieved by using a "donut" plate to retain an annular area of the soil. The plate occupies the space between the top surface of the soil block and the bottom surface of the casing's flange (Figure 4 .9). The exposed soil surface left by the donut plate at the center of the soil block is retained by the tool's top cap and cutting blades. The DFSD 2-axis load cell was used to measure the consolidation load since the consolidometer's load cell can no longer be used with this setup. This measure has better defined the effective stress within the tested specimen.

Similar to the previous phase, DFSD laboratory validation tests have been conducted on two cohesive soils with different plasticity. Kaolinite and Young Bay Mud were used to represent a low and relatively, high plasticity cohesive soil, respectively. Kaolinite has a PI of 7 with 60% silt-size particles. Bay Mud, on the other hand, has a PI of PI of 35 (LL=65 and PL=30). DFSD tests were conducted on kaolinite and Bay Mud samples with different stress conditions. Pore pressure transducers were embedded in each sample close to the anticipated "target elevation" at which the elastomer gauges would be applied.

In parallel with each DFSD test, another batch of the same soil was consolidated under the same stress conditions and subsequently sampled with Shelby tubes. From each batch of soil, three samples of 3.0-inch O.D. and one of 4.0-inch were obtained, each with a minimum length of 8.0 inches. Figure 4.17 shows the setup and the different stages of the Shelby tube sampling process. After the completion of consolidation, the soil block is unloaded and the top plate of the consolidometer as well as the porous stone are removed and replaced with a wooden plate with four circular holes having the same size as the sampling tubes. A manual jack is used to apply the downward sampling load via another solid wooden plate that rests on top of the tubes. A load cell is sandwiched between the jack and the upper reaction plate to measure the load needed to advance the tubes. To establish the degree of uniformity of the soil block, multiple water content measurements were taken throughout the remaining soil after tube sampling.

The validation strategy was to compare the DFSD laboratory tests results with the results from samples tested in different modes and locations that included; the Double Specimen Direct Simple Shear Device (DSDSS) at the University of California at Los Angeles, the Resonant Column/Torsional Shear (RC/TS) Device at the University of Texas at Austin, and the Benchtop Shear Device (BSD) at UC Berkeley. Moreover, to establish the relationship between G_{max} and changes in effective stress, low-strain dynamic testing was performed at different consolidation stresses for each of the laboratory specimens. This was done by consolidating the specimen to a stress smaller than the target stress, measuring G_{max} and then consolidating the sample to the target stress and conducting a full suite of tests to establish the G -γ and D-γ curves. Finally, the sample was consolidated to a stress higher than the target stress and then G_{max} was

measured again. As discussed in Appendix C the slope of the $\log(G_{max})$-$\log(\sigma'_m)$ relations is sensitive to sample disturbance and can, therefore, be a useful tool to evaluate the results from DFSD tests. However, homogeneous samples of cohesive soils reconstituted and normally consolidated to low stresses should not be substantially affected by the sampling and unloading reloading processes once the original stresses are re-established. Accordingly, DFSD results should be comparable to those obtained by high-quality testing of specimens sampled from blocks of identically prepared soil. On the other hand, reconstituted overconsolidated samples are more sensitive to sampling disturbance, and therefore, are useful to evaluate the degree the DSFD tests results are affected by its sampling creation process as compared with the other tests conducted on specimens sampled by Shelby tubes. This is because sampling disturbance will affect th structure gained by overconsolidation. Moderately overconsolidated reconstituted soils have no aging-induced structure, and therefore their current stress state is close to their limit state. For tube samples of these soils, overconsolidation-induced structure can be recovered by reconsolidating the sample to the maximum past pressure and then unloading to the current stress state.

4.4.1 DFSD Laboratory Validation on Kaolinite

DFSD tests were conducted on three kaolinite samples each prepared with a different consolidation history: normally consolidated to a vertical stress of 0.5 (K1) and 2.0 ksc (K3), and an overconsolidated sample (K2) unloaded to 0.5 ksc vertical stress after consolidation to 2.0 ksc (OCR=4). These values represent the vertical stresses at which the soil block was reconstituted from slurry in the consolidometers. As possible,

the same stress level was maintained for the series of cyclic tests. Table 4.1 shows the effective stresses at which samples where tested for each testing mode/location.

It should be noted that samples tested with the RC/TS device at U-Texas were consolidated isotropically, while in the rest of the tests, K_o-conditions were targeted. For the DFSD tests, the soil block in the consolidometer is of course reconstituted under K_o-conditions. However, during carving of the sample, the horizontal confining pressure is simultaneously re-compensated by the tool pressure which is determined based on an estimated K_o value. Since this value can not be determined precisely, there is always the chance that the sample is slightly unloaded or "overloaded" after the DFSD carving process. This might cause a slight negative or positive pore water pressure in the sample. Nevertheless, as discussed in Appendix C the stiffness of undisturbed samples is less sensitive to small changes in effective stress as long as the limit stress state boundary is not exceeded. The reported magnitudes of effective stresses for laboratory DFSD tests are after the carving process and are deduced from the applied tool pressure and vertical axial load and the reading of the pore water pressure transducer. Because of the differences in stress anisotropy between the different tests, the mean effective stress may be the best basis for comparing the measured stiffness values.

Before addressing the validation test results, the DFSD carving process can be evaluated as compared with tube sampling. As mentioned before, for each validation test two consolidometers were filled with thick soil slurry from the same batch. One consolidometer is used for tube sampling while the other is used to conduct DFSD tests. The soil in the two consolidometers undergoes the same consolidation process in which vertical stress is increased in increments with the pore water pressure and piston vertical

position monitored to evaluate the progress of consolidation. Figure 4.18a shows a typical "consolidation" curve obtained from the "smart" consolidometer in which excess pore water pressure dissipates with time and reaches a value close to zero at the end of consolidation. Since unloading the soil block after the completion of consolidation is unavoidable in order to set up the DFSD, a reloading stage with the tool in place is needed to restore the stresses in the soil. This is because unloading involves changing the stress regime from the anisotropic K_o-conditions to an isotopic negative pore water pressure. As a result, shear stresses are generated which causes "loss" of effective stress reflected in the decrease of negative pore water pressure. Figure 4.18b shows the changes in water pore pressure during the second stage of consolidation with the DFSD. Note that it does not take much time to re-establish the original stress state since reloading happens much faster than virgin loading. It is also noted that the DFSD setup process did not cause any significant or permanent change in the level of negative pore water. It should also be mentioned that for a DFSD field test, the soil zone below the bottom of the borehole which is targeted for testing is, theoretically, never significantly unloaded. The vertical load applied by the DFSD in the field is mainly to prevent unloading when the soil column is separated from its surrounding soil during the carving process.

The smart consolidometer offers a unique opportunity to evaluate the sampling process using both Shelby tubes and the DFSD. The effects of sampling on the soil can be characterized through measurements of pore water pressure and mean effective stress inside the sample, changes in the loading shaft vertical position during DFSD sample carving, and the vertical load needed to insert the Shelby tubes. Figure 4.19 shows a comparison between the pore water pressure generated by the two sampling methods for

two identical soil blocks consolidated under 0.5 ksc (7.5 psi) vertical stress or about 0.35 ksc (5 psi) mean effective stress. The measurements are made at the "target zone" which is approximately at the middle of the sample. For this test, the pore water pressure generated by tube insertion is approximately an order of magnitude larger than during DFSD sample carving. Moreover, the original level of mean effective stress and pore water pressure was essentially recovered just after the end of the DFSD carving process, which indicates that most of the generated deformations were elastic. The slight residual negative pore water pressure is probably a result of slight unloading due to the underestimation of the K_o value for kaolinite. In comparison, tube insertion has caused permanent loss of a significant portion of the original negative pore water pressure. In addition, the vertical pressure needed to advance the tubes was large for a soil consolidated at a relatively low stress. Figure 4.20 shows the changes in the loading shaft vertical position during the DFSD carving process. The cumulative change is less than 1 mm which is insignificant and indicates a successful DFSD performance. These results are very encouraging especially given the fact that kaolinite is a sensitive and relatively inelastic material (mostly silt-size particles) in comparison with the materials that the DFSD is designed to test.

In the first validation test, thick kaolinite slurry was consolidated under a vertical stress of about 0.5 ksc (7.5 psi) in two consolidometers. This was proven to be a very low stress for a sensitive material like kaolinite, but it was chosen based on the maximum lateral pressure (applied by the DFSD during the carving process) that can be balanced by the height of water column inside the casing. The sample sent to UCLA collapsed during extrusion and, therefore, no tests were conducted. The DFSD, BSD and RC/TS tests were

conducted as planned but the differences in the measured G_{max} were significant. Figure 4.21 shows the modulus reduction curves and the damping curves obtained from these tests. The magnitude of G_{max} measured by the DFSD, BSD, TS, and RC were 20, 13, 31, and 34 MPa, respectively. The magnitude of G_{max} predicted by the DFSD from this test was consistent with the magnitudes predicted from previous tests conducted during the implementation phase. The higher values of G_{max} predicted by the RC/TS tests may be due to lower void ratio. The estimated void ratio in the DFSD sample was about 0.71 while that in the RC/TS sample was about 0.69. This difference is significant for kaolinite as illustrated in Figure 4.22 which shows the change in G_{max} as a function of void ratio as measured by RC tests. The reduction in void ratio in the RC/TS sample could be the result of tube sampling, transport and handling, reloading to the specified stress, and the difference in size between the DFSD/BSD sample and the RC/TS sample. Also, as discussed in Appendix C, isotropic consolidation results in a lower void ratio than in K_o-condition for the same mean consolidation stress.

The normalized modulus reduction curves and damping curves, on the other hand, are more comparable. As shown in Figure 4.21b and Figure 4.23a, the G/G_{max}-γ curves and the D-γ curves from the DFSD and TS tests are in excellent agreement. The corresponding curves from the RC devices show more linear response (less degradation in G). This trend was seen in all the tests on kaolinite, which is uncommon for the RC/TS device. Prof. Stokoe has attributed this observation to the "unusual" behavior of the tested material. The BSD test on this sample was not as successful as hoped. Air and water leakage into the sample and out of the cell were encountered. The low G_{max} value,

which may have affected the shape of the G/G_{max}-γ curve, may be the result of loss of effective stress due to the leakage problems.

Overall, given the low stiffness and plasticity and high sensitivity of the material, the results obtained from the DFSD as compared with other tests are not unexpected. The fact that the DFSD was able to successfully sample and test such material is especially important. One should note that in a DFSD test, the sample is never reconsolidated after carving. This is beneficial since it preserves the original void ratio and structure but means that minimizing sample disturbance and unloading is important. In laboratory tests, on the other hand, the sample is almost always reconsolidated to the original stresses. For "structure free" materials, as in reconstituted NC soils, stiffness is mostly dependent on the levels of effective stress and void ratio. For such materials, reconsolidation will result in a lower void ratio because of the partial rebound in void ratio after unloading. The net effect, on laboratory tests, is usually a higher stiffness level. However, for "structure rich" materials, as is the case in most field materials, the damage in structure induced by sampling disturbance will almost always overshadow the change in void ratio due to sample reconsolidation in the laboratory tests. The net effect on laboratory tests in this case would be an underestimation of stiffness. This point is re-emphasized because of its significance to the interpretation of the results of laboratory validation tests on reconstituted soils and to the general function of the DFSD.

With the lessons learned from the first validation test on kaolinite, the second and third tests, K2 and K3, were planned to provide a more useful comparison between the tests and avoid, as much as possible, the shortcomings encountered previously. This was achieved by first testing an overconsolidated specimen, K2, at the same stress level as

K1, and then, to consolidate the sample to a higher stress to bring it in the NC range. This approach has helped in many ways. First, overconsolidation increases material stiffness making it less vulnerable to a large degree of sampling disturbance at low stresses. Second, changes in void ratio due to unloading from and reloading to the reference stress are much smaller than in NC samples (swelling and recompression indices are an order of magnitude smaller than the compression index). Third, OC reconstituted soil has, to some degree, a similar behavior as the structured natural soil in that it shows less dependency on stress level and the same general behavior under disturbance. Therefore, differences in test results can be attributed to the sampling method rather than the unload-reload cycle. For the normally consolidated sample, the above procedure would minimize the differences between the samples due to preparation procedures.

For the second and third validation tests, two blocks of kaolinite were reconstituted in two consolidometers under a vertical stress of 2.0 ksc (28.5 psi). When the soil blocks were fully consolidated, the applied load was reduced to 0.5 ksc (7.5 psi) and the soil was allowed sufficient time to rebound. Later, one of the consolidometer was used for tube sampling while the other was used to conduct DFSD tests K2 and K3 with the same procedure as discussed for the K1 test.

The K2 tests were conducted under a mean effective stress of approximately 0.35 ksc (5 psi) and an OCR of 4. Figure 4.24a shows the G-γ curves from all tests. The magnitude of G_{max} measured by the DFSD, BSD, TS, RC, and DSDSS tests were 38, 32, 41, 43, and 19.5 MPa, respectively. The reported initial void ratios were similar in all tests and around 0.6. Except for the DSDSS test, the measured values of G_{max} are in good agreement given the differences in testing apparatus, procedure, and stress conditions.

The low G_{max} value predicted by the DSDSS is probably due to lack of lateral confinement which is a widely recognized observation in direct simple shear devices especially with overconsolidated soils. The D-γ curves and G/G_{max}-γ curves from all tests are shown in Figure 4.24b and Figure 4.23b. Except for RC tests results, the curves are in excellent agreement at all strain levels.

These results imply a successful validation of the DFSD since the K2 specimen was not consolidated after sampling as was the case with the other tests. To further investigate the quality of the DFSD carving process, the DFSD K2 sample was left under the same confining pressures. As discussed in Appendix C, disturbed samples show significant change in G_{max} after reconsolidation. The DFSD tests conducted 24 hours after the K2 test series showed a G_{max} value of 41 MPa. This slight increase in G_{max} (from 38 to 41 MPa) is due to the time effect, and is in the range predicted for soils with similar plasticity. In comparison, RC tests conducted on the K2 sample showed that reconsolidating the sample after extrusion has increased G_{max} from about 32 to 43 MPa, which is four times the increase observed with the DSFD. If the effect of frequency on the RC results is corrected for (40 Hz vs. 0.4 Hz) the range of G_{max} will be 29 to 39 MPa. This was based on tests conducted using the TS/RC on the K2 sample to study the effect of frequency, time under confinement, and reconsolidation under different stress levels as part of the validation tests. This clearly shows that the DFSD sample did not encounter significant mechanical disturbance or stress change during the sample creation process.

Moreover, another proof of the high quality of the DFSD sampling and testing techniques is shown in Figure 4.25 which shows, among other things, G_{max} values

obtained from DFSD, BSD and RC tests on kaolinite at a mean effective stress of approximately 0.35 ksc and OCR of 4. However, the stress path followed was different from one test to another. The DFSD test and one of the BSD tests are those obtained from the K2 tests. The second BSD test and the RC test were conducted after consolidating the K2 sample (at the end of the cyclic tests) to the maximum past stress (~1.4 ksc) and then unloading to the original stress (0.35 ksc) to "erase" the effects of sampling disturbance. Perhaps because of the similarity between the DSFD and the BSD, their tests results can be more accurately compared for the effect of tube versus DFSD sampling. It can be clearly seen that the G_{max} obtained from the first BSD test was noticeably lower than the one from the DFSD mainly because of sampling disturbance. However, the BSD and RC samples that were subjected to the reload-unload cycle have a G_{max} that is more comparable to the DFSD value (the small difference is due to the change in void ratio as a results of unloading-reloading). This clearly shows that the disturbance in the DFSD sample was not significant.

The third validation test on kaolinite, K3, was conducted by consolidating the sample from the K2 test under a mean effective stress of approximately 1.4 ksc to bring it to the normal consolidation range. This will "erase" any effect of sampling disturbance and unload-reload cycles. As a result, the test results should show the quality of the DFSD measurements and testing methodology when all other factors are equal between all testing devices. The test would also show another feature of the DFSD, i.e., the ability to consolidate a sample "downhole" in the field. Figure 4.26 shows the progress of consolidation using the DFSD as indicated by the increase in mean effective stress and changes in pore water pressure inside the sample. By all measures, the consolidation

process was very successful. The results from K3 tests are shown in Figure 4.27 and Figure 8.23c. The G_{max} values obtained by the DFSD, BSD, TS, RC, and DSDSS were 61, 62, 60, 66 (60 after adjusting for frequency effect), and 47 MPa, respectively. The similarity of the results is impressive. Although the DSDSS is still under-predicting the G_{max} value, the difference is much smaller than in the previous tests. The G-γ and D-γ curves from the DFSD, BSD, and TS tests are very close. The G-γ curve from DSDSS tests is also in good agreement with the other curves at intermediate to high strain levels. The various tests also show a similar degradation behavior as indicated by the G/G_{max}-γ curves.

In summary, the validation tests on reconstituted kaolinite samples point to a successful performance of the DFSD. The different test conditions made it possible to evaluate the different aspects of DFSD performance from sample carving to testing methodology. The quality of the measurements made by the device is impressive, and as good as the best testing devices available today. The device has been shown to provide accurate measurements of shear modulus and damping ratios at a wide strain range and to measure the correct modulus degradation behavior. This can be clearly seen in Figure 4.28 which shows the G/G_{max}-γ and D-γ curves from all tests on K2 and K3 samples. The device has also proven to show the correct trend of shear modulus with mean effective stress and OCR as illustrated by Figure 4.25, which shows the $\log G_{max}$–$\log \sigma'_m$ relation for kaolinite. What is perhaps the most valuable achievement validated through these tests is the successful DFSD sample creation process which is a key function in a DFSD test. Measurements made during the carving process as well as from subsequent cyclic tests by the DFSD and by other tests on tube samples have shown that the DFSD sample

was not subjected to significant disturbance or stress change. Moreover, DFSD samples retrieved after the test showed all the signs of a high quality sample, including uniform distribution of water content, smooth surfaces and absences of cracks. In addition, the imprints of the elastomer gauges can be clearly seen on the sample's surface. Figure 4.29 shows pictures of one of the DFSD samples after retrieval.

4.4.2 DFSD Laboratory Validation on San Francisco Bay Mud

The second series of validation tests were dedicated for testing San Francisco Bay Mud, a moderately plastic clay (PI=35%). Because of the quantities involved in consolidation, testing a clay with a higher plasticity would have required a much longer consolidation time. Moreover, SF Bay Mud is a widely known natural material, and large homogenous quantities can be obtained from nearby sites. The material used was obtained from the Port of Oakland, where large quantities of Bay Mud had been dredged for construction projects in the port. The material can be described as a greenish gray clay with fragments of white shells having variable sizes. The material was obtained as thick slurry and, therefore, there was no need for mixing or adding water. Shell fragments, especially those of moderate to large sizes, were removed before filling the consolidometers with this material.

The same validation strategy has been followed as done with kaolinite but with some modifications. Because of the higher plasticity and lower sensitivity of Bay Mud compared with kaolinite, good-quality Shelby-tube samples can be obtained at low stresses under normal consolidation conditions. Accordingly, two soil blocks were reconstituted in two consolidometers under a vertical stress of approximately 0.5 ksc. One consolidometer was used for DFSD testing while the other for Shelby tube sampling

for the other laboratory tests. Two validation tests, BM1 and BM2, were conducted on each sample under two different stress levels. For the DFSD, the first test (BM1) was conducted just after sample creation while the second test (BM2) was conducted on the same sample after it was consolidated (by the DFSD) to a higher stress. Laboratory tests using the TS/RC and the DSDSS devices were also conducted under the same stress levels as in the DFSD tests. As was the case with tests on kaolinite, the BM1 tests should reflect the effect (if any) of the sample carving process on DFSD results as compared with the effects of tube sampling and sample reconsolidation on laboratory test results. Because of the "structure-free" nature of reconstituted soils, the above effects are not expected to be large. In BM2 tests, however, the effect of these factors are "erased" and the results should reflect the accuracy of measurements made by each device. Table 4.2 shows the effective stresses under which these tests were conducted.

A major improvement has been made which allowed the measurement of shear wave velocity inside the soil in the consolidometers during the phases of consolidation, sampling, and cyclic testing. This has provided a reference G_{max} against which values from the different cyclic tests can be compared. In addition, by tracking changes in shear wave velocity during DFSD and tube sampling, more insight into the quality of samples obtained from each method can be obtained. This is an added validation of the DFSD concepts since it indicates whether the DFSD would permanently alter the dynamic properties of the soil in the process of sample creation.

Shear wave velocity measurement inside the consolidometer has been achieved by embedding an array of three accelerometers and a miniature air hammer as a wave source. The small-size accelerometers are attached to the stainless steel stand which

carries the pore water pressure transducer as shown in Figure 4.30. The accelerometers were placed at three different elevations. The top and bottom ones (A3 and A1) are approximately 8 and 2 inches (20 and 5 cm) above the bottom porous stone, respectively, with the third accelerometer (A2) at the middle. The air hammer, on the other hand, is attached to the bottom of the stand just above the porous stone. The location of the stand/sensors is determined such that it is at the center of the carved sample and in the zone targeted for cyclic testing. The accelerometers are hermetically sealed and are coated with epoxy as an added measure against water leakage. The cable of the accelerometer is water proof with three shielded wires; two for the ±3-volts input power signal and the third for the internally-conditioned output signal. The axial accelerometers are sensitive enough to easily detect deformations in the G_{max} range. The original concept of the air hammer was adopted from Arulnathan et al. (2000). As shown in Figure 4.30 and Figure 4.31, the hammer consists of 47-mm long hollow stainless steel tube with each end capped and fitted with an air port. 3-mm diameter nylon tubing connects the air ports to the outside of the consolidometer for air pressure application and venting. A 25 mm long Teflon piston fits inside the tube. Applying a small air pressure at either end of the hammer will cause the piston to fire toward the other end (i.e., a forward and a reverse hit can be generated). The impact of the piston at the end of the hammer will generate p and s-waves propagating upward inside the consolidometer. The amplitude and frequency of the waves are a function of the intensity of the applied air pressure and the relative stiffness of the piston and hammer end materials. The generated peak shear strain in the soil can be estimated by $a_o/\omega V_s$, where a_o and ω are the peak acceleration and angular frequency, respectively, obtained from the accelerometer's output.

The hammer and the accelerometers are placed with their axes parallel to one another to maximize the shear wave content in the accelerometers' output signal and to facilitate interpretation. The accelerometers output signals are connected to the input channels of a digital oscilloscope for display and data acquisition. The acquired signals are temporarily stored in the oscilloscope's memory until they are transferred to a computer through a serial port. Because of its proximity to the air hammer, accelerometer A1 is used to trigger the oscilloscope for data acquisition. Shear wave velocity measurement starts by applying air pressure at one end of the hammer (forward hit) and another time to the other end (reverse hit) and acquiring the output signals of the accelerometers in each case. The generated shear waves in the two cases will have opposite polarities, which helps to identify the difference in shear wave arrival time between any two accelerometers. With the distance between the accelerometers known, the shear wave velocity in the soil can be determined.

Figure 4.32 shows accelerometers A1 and A2 output signals at different stages of Bay Mud consolidation inside the consolidometer. A few days after the start of consolidation, there was no detectable shear wave arrival in accelerometers A2 and A3 because the soil is still largely in slurry form. Accelerometer A1, on the other hand, is close to the bottom porous stone, which means that the soil in this zone consolidates much faster than the soil in the middle, as it is evident from the appearance of shear waves in the A1 output signal early in the consolidation process. With time, more water is expelled from the soil which becomes denser and therefore the shear wave velocity increases. This is reflected in the accelerometers signals as a stronger appearance of shear waves arriving earlier in the record. Figure 4.33a shows the changes in shear wave

velocity with time during the entire consolidation phase. As reported in the literature, two phases of the increase in V_s is noticed; an initial rapid increase in V_s during most of the primary consolidation phase followed by a second phase in which V_s increases at a gradually slower rate toward the end of primary consolidation and the beginning of secondary consolidation. Figure 4.33b shows the second stage of Bay Mud consolidation during which the soil block was unloaded to set up the DFSD and then reloaded with the DFSD in place. The measurements clearly show the decrease in V_s as a result of unloading and then the recovery of the original level of V_s after the re-application of vertical stress by the DFSD.

Shear wave velocity measurements were very valuable during the DSFD sample carving and tube sampling processes. The measurements revealed, directly, the impact each sampling method had on the stiffness of the sampled soil. Figure 4.34 shows the changes in V_s and pore water pressure during Shelby tube sampling of reconstituted Young Bay Mud. Unloading of the soil block from the anisotropic K_o-condition to the isotropic negative pore water pressure has alone caused an 8% reduction in V_s (or about 14% reduction in G_{max} from 15.4 to 13.2 MPa). The corresponding change in mean effective stress, assuming a K_o value of 0.65, is approximately 14% reduction (from about 5.7 to 4.9 psi). Tubes insertion, on the other hand, has caused a dramatic change both in V_s and the effective stress inside the soil. Shear wave velocity has been reduced an additional 26% at the end of tube sampling or approximately a 45% reduction in G_{max} (from 13.2 to 7.3 MPa). The corresponding reduction in mean effective stress (negative pwp) was approximately 67%. The negative pore water pressure has changed from -4.9 psi after unloading to 2 psi during tube sampling and stabilized at -1.6 psi at the end of

sampling. Therefore, the cumulative reduction in V_s and G_{max} as a result of unloading and tubes insertion is approximately 31% and 52%, respectively. It should be noted that these measurements were obtained with the accelerometers and the pore water pressure transducer between the sampling tubes as shown in Figure 4.17. However, a test conducted on reconstituted kaolinite with the pwp transducer inside a single 4-inch sampling tube showed the same change in negative pwp as in the previous case.

Figure 4.35 shows shear wave velocity and pore water pressure measurements made during DFSD sample carving of reconstituted Bay Mud. Until about halfway into the carving period, no detectable change in V_s has been observed in the zone targeted for testing and where V_s measurement is made. As the DFSD cutting assembly approached and passed this zone, a slight reduction of about 3% was observed in V_s, probably the result of the cutting action of the blades and the compensation of soil pressure with air pressure. However, the original level of V_s was quickly recovered toward the end of the carving process. Measurements of V_s made before and after DFSD sample creation are almost the same and within the accuracy of the measurement method, as shown in Figure 4.35, Figure 4.36, and Figure 4.37. The minimal level of disturbance is also confirmed by pore water pressure measurements, which show small changes during the DFSD carving process. In addition, the cumulative change in the vertical position of the DFSD shaft was less than 0.3 mm, which indicates successful test control. These results clearly indicate that the transient changes induced by the DFSD during sample creation can be mostly elastic and have no significant effect on the dynamic properties of the sampled soil.

Figure 4.38 shows the G-γ and the D-γ curves obtained from the DFSD, RC/TS, and the DSDSS tests on BM1 as well as G_{max} obtained from V_s measurements. The G_{max}

value obtained from the DFSD, V_s, RC, TS, and DSDSS tests were 13.8, 14.5, 16.7, 15.5, and 7.4 MPa, respectively. Except for the DSDSS, the levels of G_{max} obtained from the different tests are in reasonable agreement. G_{max} obtained from the Vs measurement is slightly higher (less than 5%) than the DFSD value, possibly due to the frequency effect. On the other hand, G_{max} from TS and RC are higher (7 and 15%, respectively) than from V_s measurement. Since the level of mean effective stress is practically the same among all tests and the test frequency in V_s measurement is higher than in TS and RC tests, this indicates that the RC/TS sample had undergone some changes that lead to higher stiffness compared with the soil block.

Because of the "structure free" nature of normally consolidated reconstituted soil, the stiffness of tube samples is mainly affected by changes in effective stress and void ratio. Since the level of effective stress before sampling was re-established, the only remaining factor that had likely affected the RC/TS sample stiffness is a decrease in void ratio due to the unload-reload cycle. Also, the RC/TS sample was left for 2 days under a 2-psi isotropic confining pressure and another 2 days under a 4-psi confining pressure before the validation tests were conducted. This had also lead to a decrease in the sample average void ratio due to time effects. This result validates the argument made with kaolinite testing where the same trend in RC/TS versus DFSD results was also observed for DSFD tests conducted without tool consolidation.

In general, damping ratios obtained from DFSD tests are somewhat higher than TS and DSDSS values but closer to RC values. The agreement with the TS and DSDSS tests is good at small and large strain levels. Since there is no reference damping curve, it is hard to tell which curve is more accurate. However, it is likely that a lower void ratio in

the reconsolidated tube samples could have contributed to this since damping ratio decreases with decreasing void ratio and frequency (hence RC values are closer to DFSD values).

The second validation tests on Bay Mud, BM2, were conducted on the same samples tested in BM1 tests but after consolidation to a higher stress level that would "erase" all effects of unloading, sampling, and previous testing. Figure 4.39 shows the G-γ and the D-γ curves from all tests. As expected, the results show a better agreement than in the previous tests. G_{max} obtained from the DFSD, V_s, RC, TS, and DSDSS tests were 24, 25.2, 23.9, 22.6, and 12.6 MPa, respectively. The ratio between G_{max} from V_s and DFSD measurements is almost the same as in BM1 (V_s-based G_{max} is about 5% higher than from DFSD), which indicates a good consistency in DFSD measurements and that the effects which the DFSD sample carving process had on BM1 results were insignificant. As mentioned earlier, the lack of lateral confinement is probably the main reason that the DSDSS device underestimates the shear modulus. Damping ratios obtained from DFSD tests are also in better agreement with TS and DSDSS tests at all strain levels compared with BM1 tests. This shows the high quality of DFSD damping measurements and that the differences observed in the previous tests were mainly due to differences in the sample's conditions among the different tests.

The normalized modulus reduction curves obtained from BM1 and BM2 tests are shown in Figure 4.40 and Figure 4.41. All the tests show almost the same modulus degradation behavior which indicates that the normalized curve is much less sensitive to differences in sample conditions than the absolute values of G, at least for reconstituted cohesive soils. Figure 4.42 shows the $\log G_{max}$–$\log \sigma'_m$ relation for the Bay Mud as

obtained from all tests. The DFSD measurements seem to predict the correct relation between effective stress and soil stiffness.

In summary, laboratory validation tests on reconstituted Bay Mud showed a successful performance of the DFSD. V_s measurement, in particular, clearly showed that the DFSD sample creation process has little effect on the stiffness of the soil. As shown in Figure 4.43, the Bay Mud sample retrieved after the DFSD tests showed all the signs of a high-quality sample. Multiple-point measurements showed a uniform water content distribution across the sample. The tests also revealed the high quality of DFSD measurements of modulus and damping. The device was shown to be capable of capturing the effects of factors influencing the dynamic properties of soils including stress level, plasticity, time and frequency effects, and soil structure.

4.5 Field Deployment and Implementation of the DFSD

After a successful laboratory validation of the DFSD, efforts were directed toward making the DFSD ready for field testing. This included developing techniques for transportation and field deployment and field support equipment. After weighing several alternatives, transporting the DFSD to the test site in a trailer was selected as the most appropriate and economical option. A towing vehicle can be rented and used for field tests. The DFSD will be mounted on a transport cart and wheeled out of the trailer to the borehole location. The cart is secured inside the trailer via four straps connected to D-rings mounted onto the trailer floor. The trailer was custom made by Wells Cargo, California, based on specifications developed by the DFSD research team and CALTRANS personnel. Figure 4.44 and Figure 4.45 show the trailer and its mechanical components. The hitch-type trailer is 19 ft long, 8.5 ft wide and 8.5 ft high. The trailer

tandem axel has a payload capacity of 7,000 lbs and a gross vehicle weight rating of 10,000 lbs.

The trailer has a swing-down ramp door with extension and a 2000-lbs capacity floor-mounted winch to facilitate and control the movement of the transport cart into and out of the trailer. A 100-psi compressor housed in a special separate cabinet in front of the trailer is used to supply the DFSD with air pressure. The compressor keeps compressed air in a storage tank for a long-term control and supply of air pressure. The compressor's cabinet is insulated to reduce the amount of noise that could infiltrate to the DFSD electronics. A 10 kilowatt water-cooled "quiet" diesel generator from Onan is used to power the DFSD components, the air compressor, and the trailer auxiliary equipment (AC unit, lights). The generator and its diesel supply tanks are housed and secured in a separate compartment on the front right side of the trailer which can only be accessed from the outside. This "quiet" generator produces much smaller vibrations and noise than ordinary generators, which is important for the function of the DFSD. The 110-volt generated electricity can be accessed inside the trailer via a number of regular power outlets. Usually, a power conditioner is used to protect the DFSD electronics from any sudden electrical spikes or surges. A UPS unit with a rechargeable battery was also used as a source of clean power. The unit draws it power from the generator and its battery can be used as an alternate power source for as long as two hours in case of a generator shutdown. The trailer also has a folding table on which the interfacing box, a notebook computer, and the DFSD pressure panel can be placed. Several cabinets and shelves inside the trailer are used for equipment and tool storage.

The umbilical requirements for the DFSD include 2 multi-conductor cables for power and signal lines; one water supply hose; and five pneumatic hoses for sample, tool, axial load, and clamping pressures. The heavy duty shielded cables are waterproof and were obtained from Belden. As discussed in Chapter Six (Section 6.3.8), one cable has 16 pairs of twisted wires, which are also shielded both individually and as a pair, while the other has 8 pairs and are mainly used to carry higher-voltage signals and power. The cables connect to the DFSD upper bulkhead via waterproof electrical connectors that were custom made by ITT/Cannon. Inside the trailer, the electrical wires from the cables are connected to the interfacing box and the bolt counter box, while the pneumatic hoses are connected to the pressure panel. Since the DFSD is designed to test soils as deep as 100 ft, a substantial length of umbilical cables is needed. Therefore, a total umbilical length of 300 ft was made available to the DFSD in two 150-ft sections. The extra length is for the case where access to the site is difficult and the DSFD trailer has to be kept at some distance from the borehole. At the testing site, drillers will be hired to drill the borehole using bentonite slurry and to install the 8-inch inside diameter casing. Lifting the tool can be done by the drill rig or by a tripod and a manual winch system operated by the DFSD testing team.

Preliminary DFSD field implementation tests have been conducted at the Richmond Field Station (RFS) site. The purpose was to conduct DFSD tests using the trailer and other field support equipment and examine the quality and the reasonableness of the results using the new setup. A shallow hole, about 6-ft deep, was drilled using an 8-inch hand auger and steel casing was installed. A special tool was used to clean the bottom of the hole and make it as flat as possible. A tripod with a winch system was used

to lift the tool off the transport cart and lower it into the hole. Figure 4.46 and Figure 4.47 show the DFSD setup for field implementation tests.

Shear wave velocity measurements were also made at the site at different elevations using the cross-hole method. Two accelerometers were placed in two 3-inch diameter holes which were drilled adjacent to the testing hole. A third hole was also drilled for the wave source. Shear waves were generated by applying a torsional motion at the bottom of the "source hole" using a shear vane tool. Figure 4.48 shows a schematic diagram of the test setup and the measured shear wave velocity at different depths. Acceleration time histories from one of the cross-holes tests are shown in Figure 4.49.

At the test site, a homogenous clay layer was found at about 2 ft below the ground surface. The soil can be described as dark blue plastic silty clay with a PI of 31 (LL=61, and PL=30). A series of DFSD tests were conducted on this layer at about 4 ft below ground surface. As shown in Figure 4.50, the quality of the strain signal was as good as obtained from the DFSD laboratory tests. The G-γ curve and the D-γ as measured by the DFSD are shown in Figure 4.51. Shear modulus and damping ratio in the field were measured, for the first time, at a wide strain range from below 0.001% to more than 1%. G_{max} obtained from the DFSD was 11.4 MPa while it was between 12.14 to 13.6 MPa from shear wave velocity measurements. The agreement between the two methods is excellent given the difference in testing frequency (0.33 Hz and 100-200Hz). The modulus degradation behavior indicated by the G/ G_{max} -γ curve shown in Figure 4.52 appears reasonable as compared with Vucetic and Dobry (1991) curves for materials with similar plasticity. The damping measurements, on the other hand, are relatively higher than the corresponding generic curves, but this may be due to the very low confinement

of the soil (the tested soil is at a shallow depth). In addition, generic damping curves are not as reliable as modulus curves due to the larger scatter in the damping measurements upon which those curves were based.

References

Arulnathan, R., Boulanger, R.W., Kutter, B.L., and Sluis, W.K., (2000),"New Tool for Shear Wave Velocity Measurements in Model Tests," Geotechnical Testing Journal, GTODJ, Vol. 23, No.4, pp. 444-453.

Connolly, P.C., (1997)," The Development of a Cyclic Torsional Shear Device For Laboratory Evaluation of Soil Modulus and Damping". M.Eng. thesis, Department of Civil and Environmental Engineering, University of California at Berkeley.

Gookin, W.(1998),"Effect of Frequency of the dynamic properties of clays," Ph.D. Dissertation, Department of Civil and Environmental Engineering, University of California, Berkeley.

Hight, D.W., Gens, A., and Symes, M. J., (1983), " The Development of a New Hollow Cylindrical Apparatus for Investigating the Effects of Principle Stress Rotation in Soils", Geotechnique, Vol. 33, No. 4, pp. 355-383.

Stokoe, K.H., II, Kim, D.-S., and Andrus, R.D., (1990),"Development of Synthetic Specimens for Calibration and Evaluation of MR Equipment", Transportation Research Record, No. 1278, pp. 63-71.

Vucetic, M. (1994). "Cyclic threshold shear strains in soils," Journal of Geotechnical Eng. Div., ASCE, Vol. 120, No.12, pp. 2208-2227.

Vucetic, M., and Dobry, R. (1991). "Effect of soil plasticity on cyclic response," ASCE, Journal of Geotechnical Engineering, Vol. 117, No. 1, pp. 89-107.

Table 4.1 Tests conducted on reconstituted kaolinite samples as part of the DFSD Laboratory validation

Test Mode	Effective Stress (ksc)	K1	K2	K3
DFSD UC-Berkeley	σ'_v	0.53	0.60	2.36
	σ'_h	0.38	0.27	0.99
	σ'_m	0.43	0.38	1.45
BSD UC-Berkeley	σ'_v	0.435	0.49	2.28
	σ'_h	0.24	0.24	1.0
	σ'_m	0.31	0.32	1.43
TS/RC U-Texas	σ'_v	0.35	0.35	1.41
	σ'_h	0.35	0.35	1.41
	σ'_m	0.35	0.35	1.41
DSDSS UCLA	σ'_v	-	0.52	2.02
	σ'_h	-	0.26*	1.01*
	σ'_m	-	0.35*	1.35*

*based on the assumption K_o=0.5
** $\sigma'_m = (\sigma'_v + 2\sigma'_h)/3$

Table 4.2 Tests conducted on reconstituted San Francisco Bay Mud samples as part of the DFSD Laboratory validation

Test Mode	Effective Stress (ksc)	BM1	BM2
DFSD UC-Berkeley	σ'_v	0.38	0.83
	σ'_h	0.24	0.52
	σ'_m	0.29	0.62
Vs measurements UC-Berkeley	σ'_v	0.38	0.83
	σ'_h	0.24	0.52
	σ'_m	0.286	0.62
TS/RC U-Texas	σ'_v	0.285	0.63
	σ'_h	0.285	0.63
	σ'_m	0.285	0.63
DSDSS UCLA	σ'_v	0.385	0.80
	σ'_h	0.24*	0.50*
	σ'_m	0.29*	0.60*

*based on the assumption K_o=0.62

** $\sigma'_m = (\sigma'_v + 2\sigma'_h)/3$

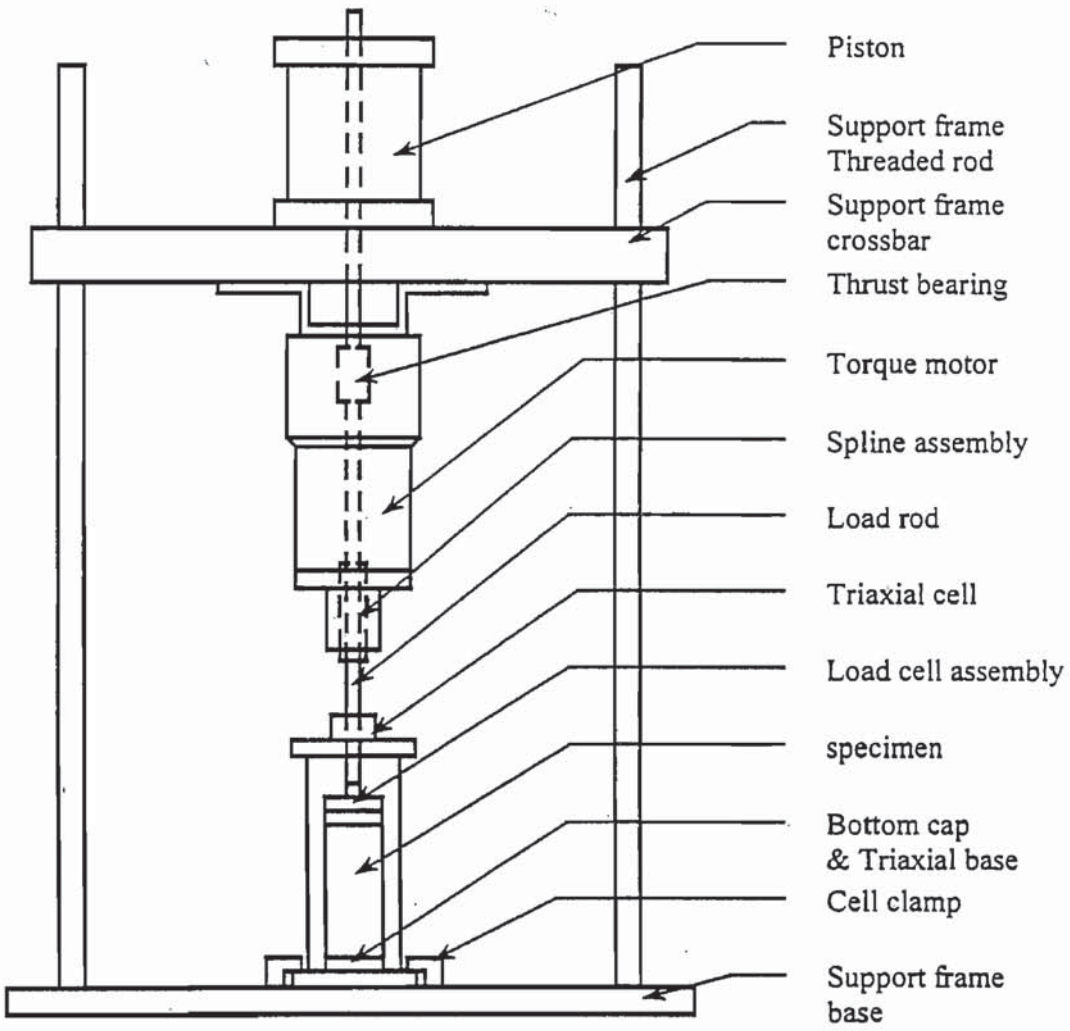

Figure 4.1 A schematic showing the configuration and the main components of the BSD

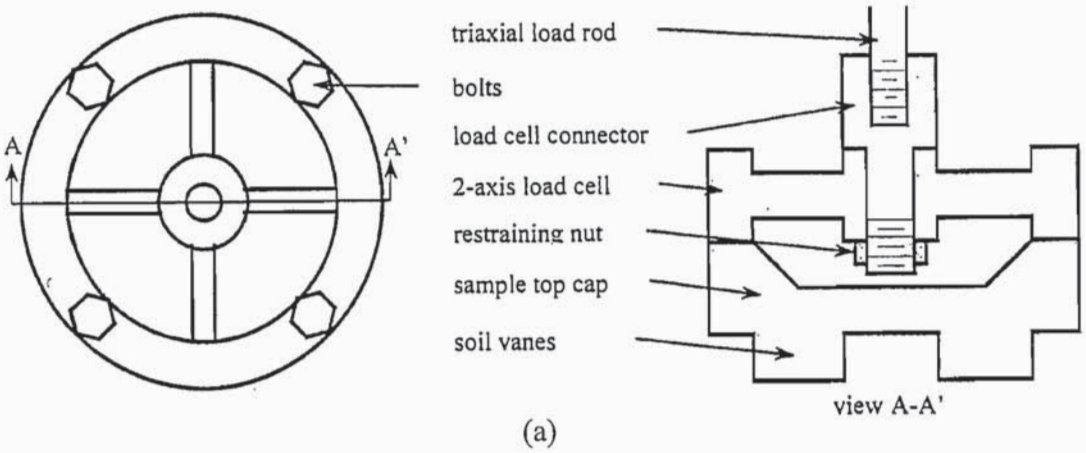

(a)

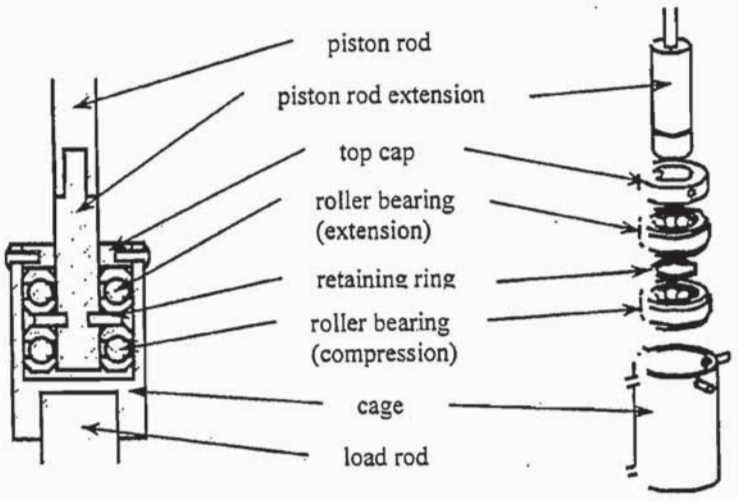

(b)

Figure 4.2 (a) The top cap-load cell assembly and (b) the thrust bearing assembly of the BSD

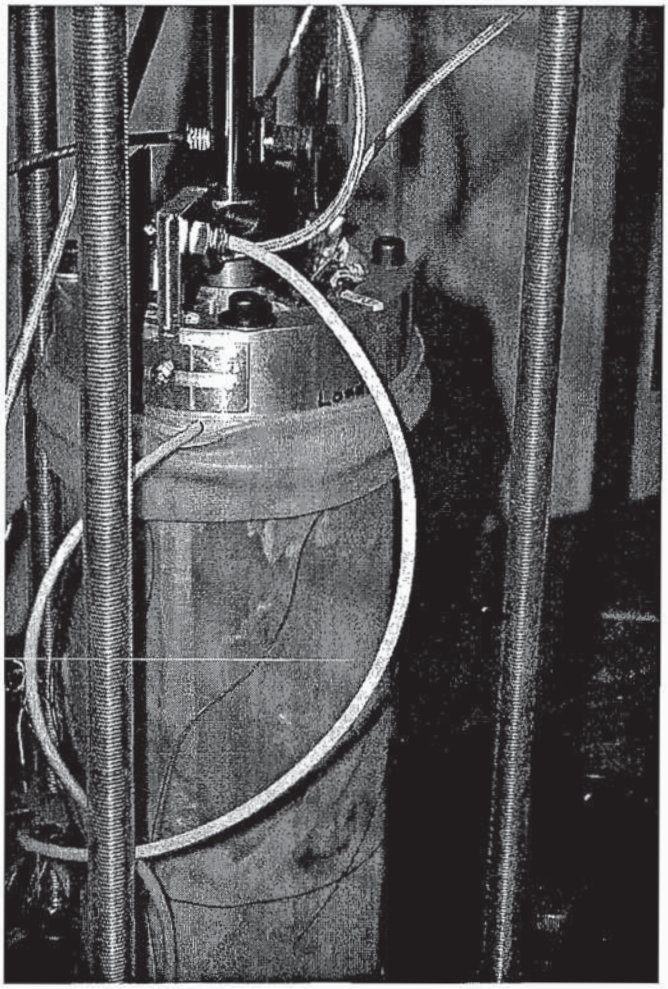

Figure 4.3 A picture showing the proximity transducers and the instrumented membrane for internal and local deformation measurement in the BSD

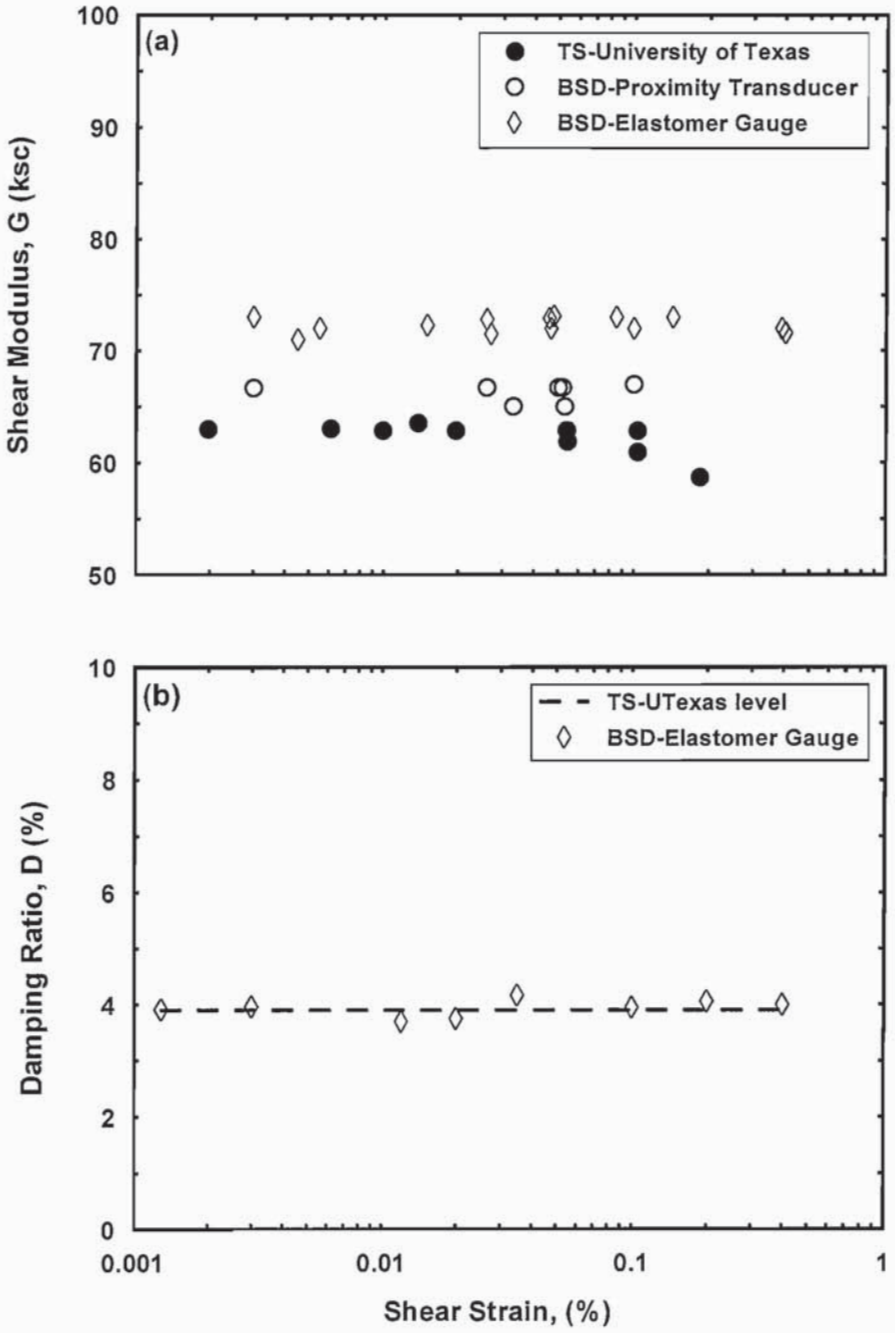

Figure 4.4 Shear modulus and damping ratio vs. shear strain of the urethane sample measured by the BSD and UT's torsional shear device

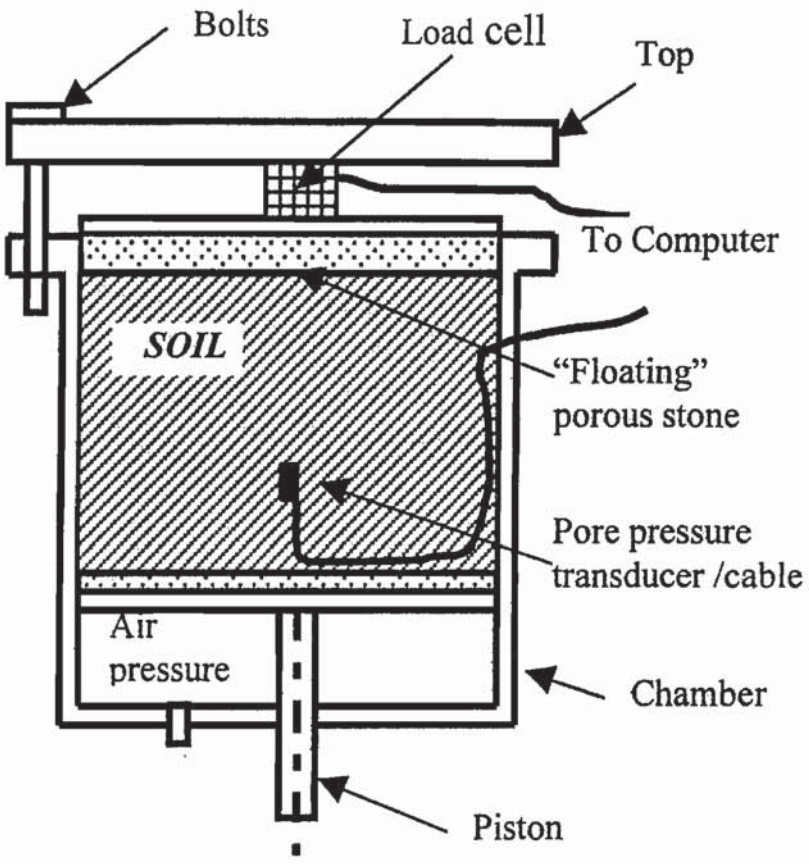

Figure 4.5 A schematic diagram showing the concept of Berkeley smart consolidometer

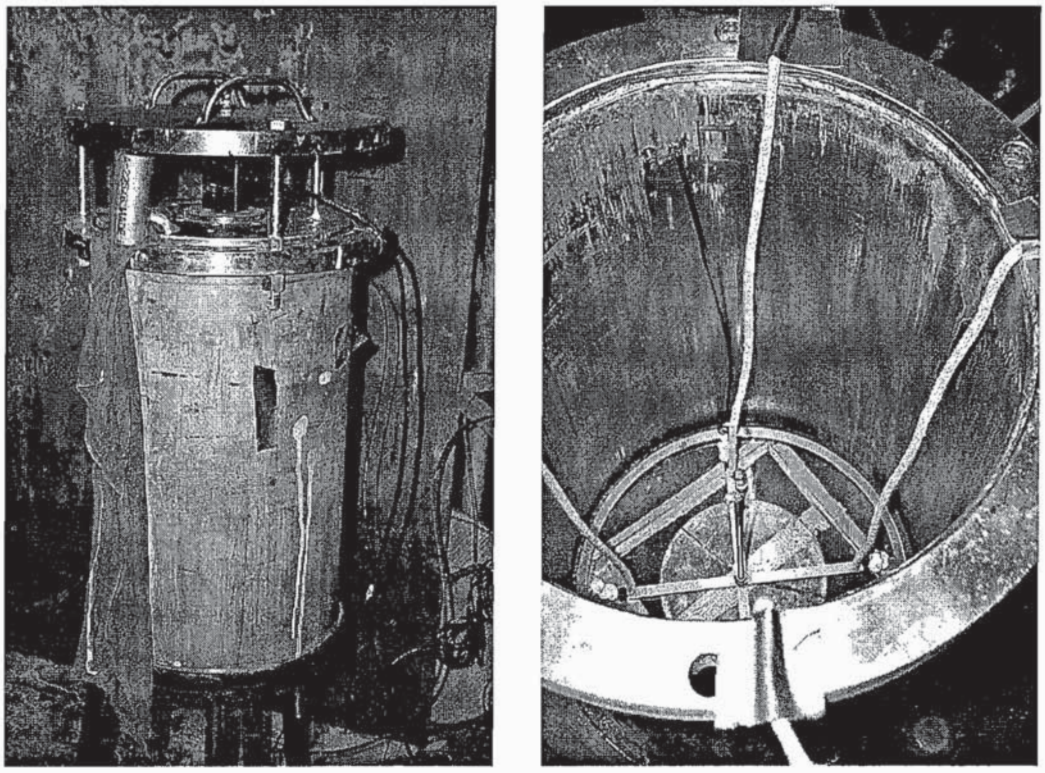

Figure 4.6 Pictures showing the outside and inside layout of the smart consolidometer

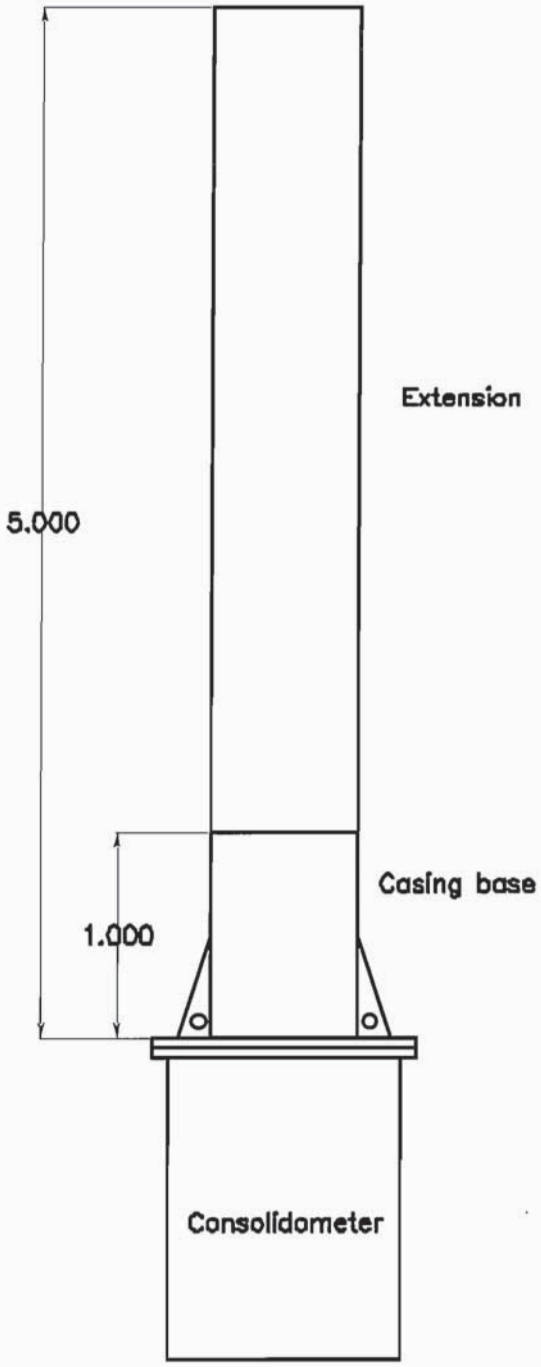

Figure 4.7 A 5-ft casing mounted on top of the smart consolidometer to simulate a DFSD field test (dimensions are in feet)

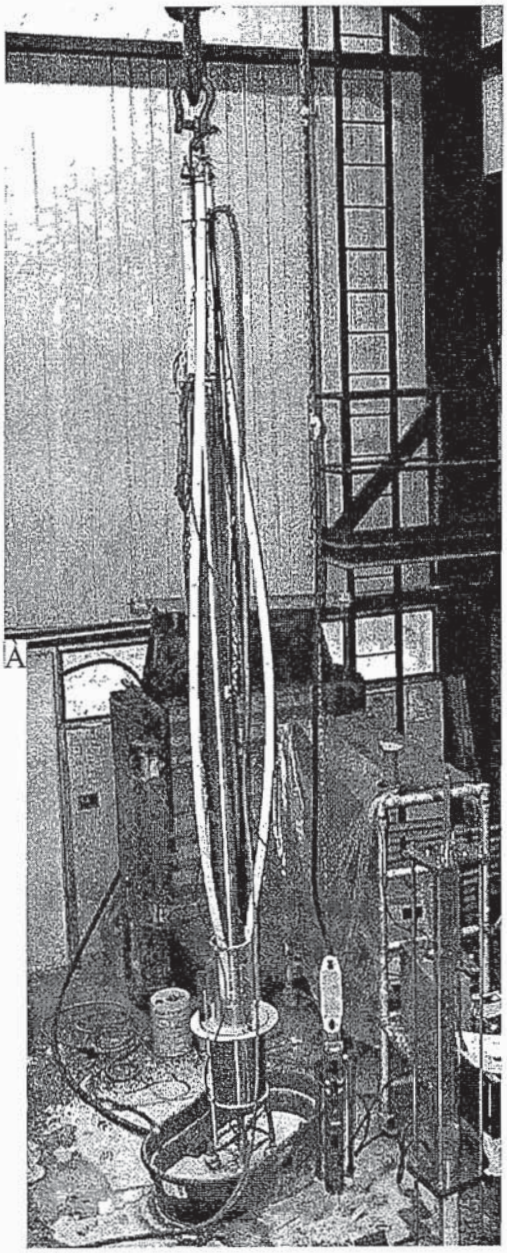

Figure 4.8 A picture showing a DFSD laboratory test setup

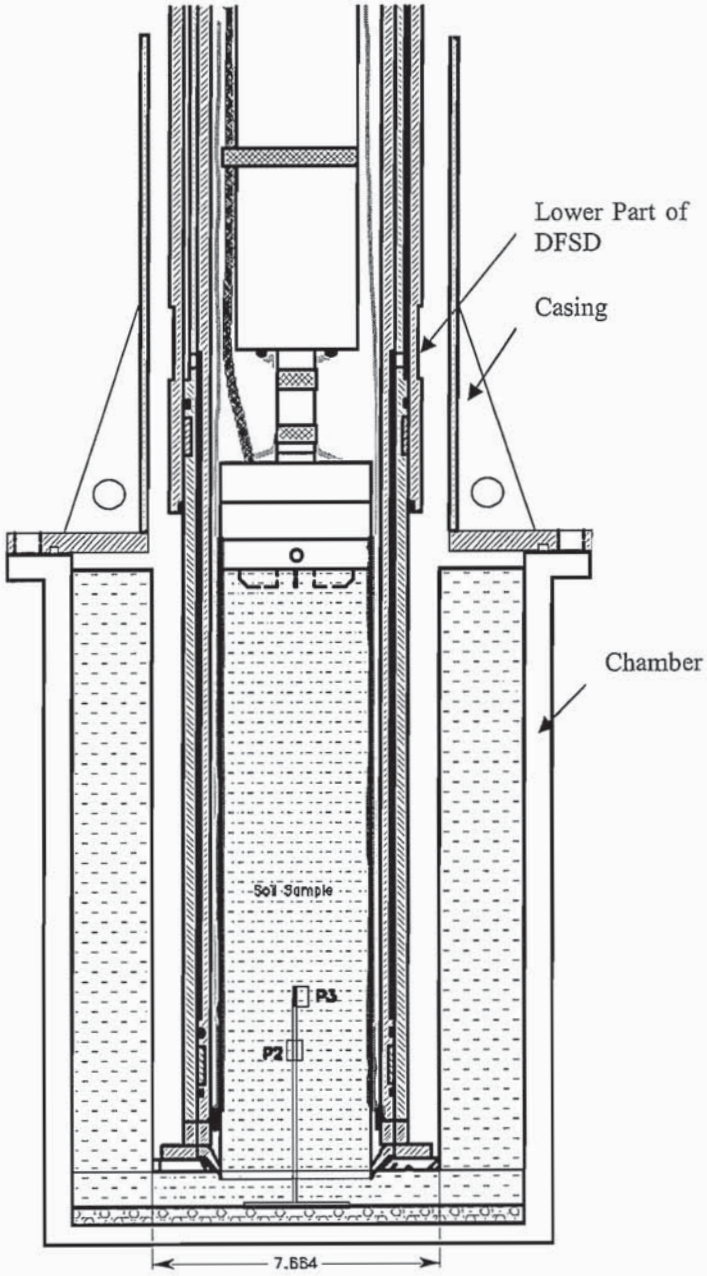

Figure 4.9 An illustration of a DFSD laboratory test setup after the end of the sample creation process (dimension in inches)

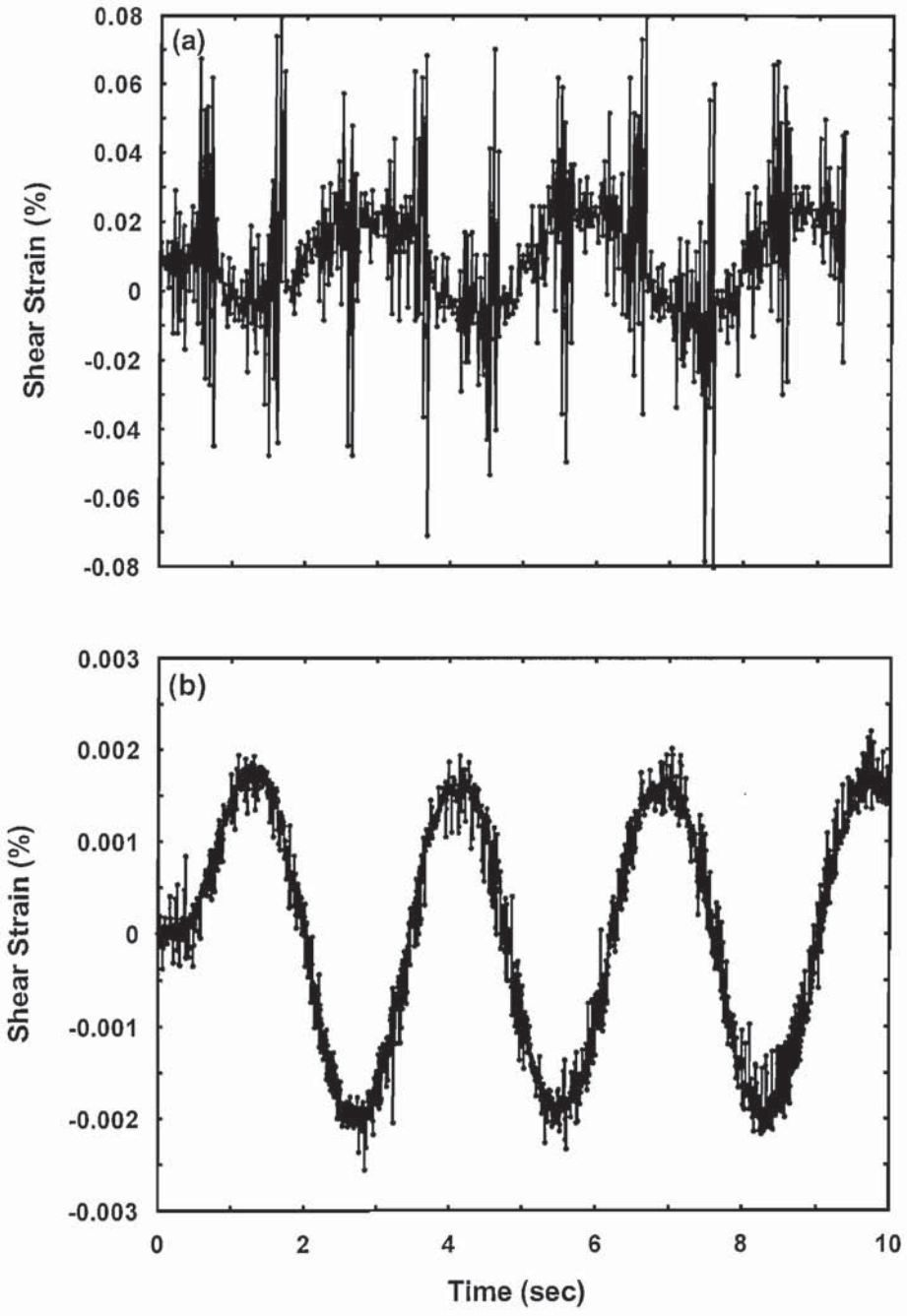

Figure 4.10 DFSD-measured strain signal from tests on reconstituted kaolinite samples (a) before and (b) after the improvement in signal-to-noise ratio

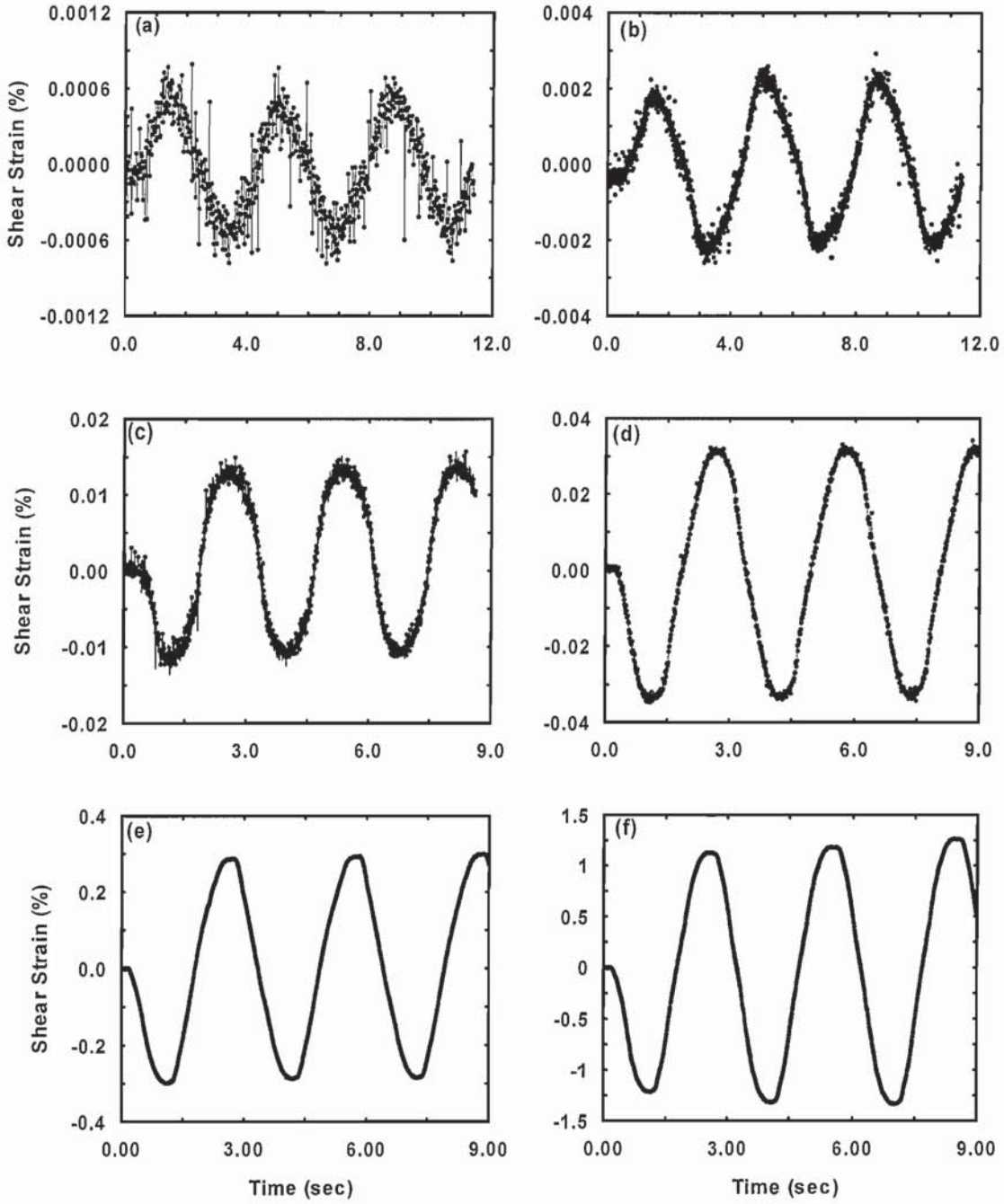

Figure 4.11 Strain time histories as measured by the DFSD from tests on reconstituted kaolinite at different peak strain levels

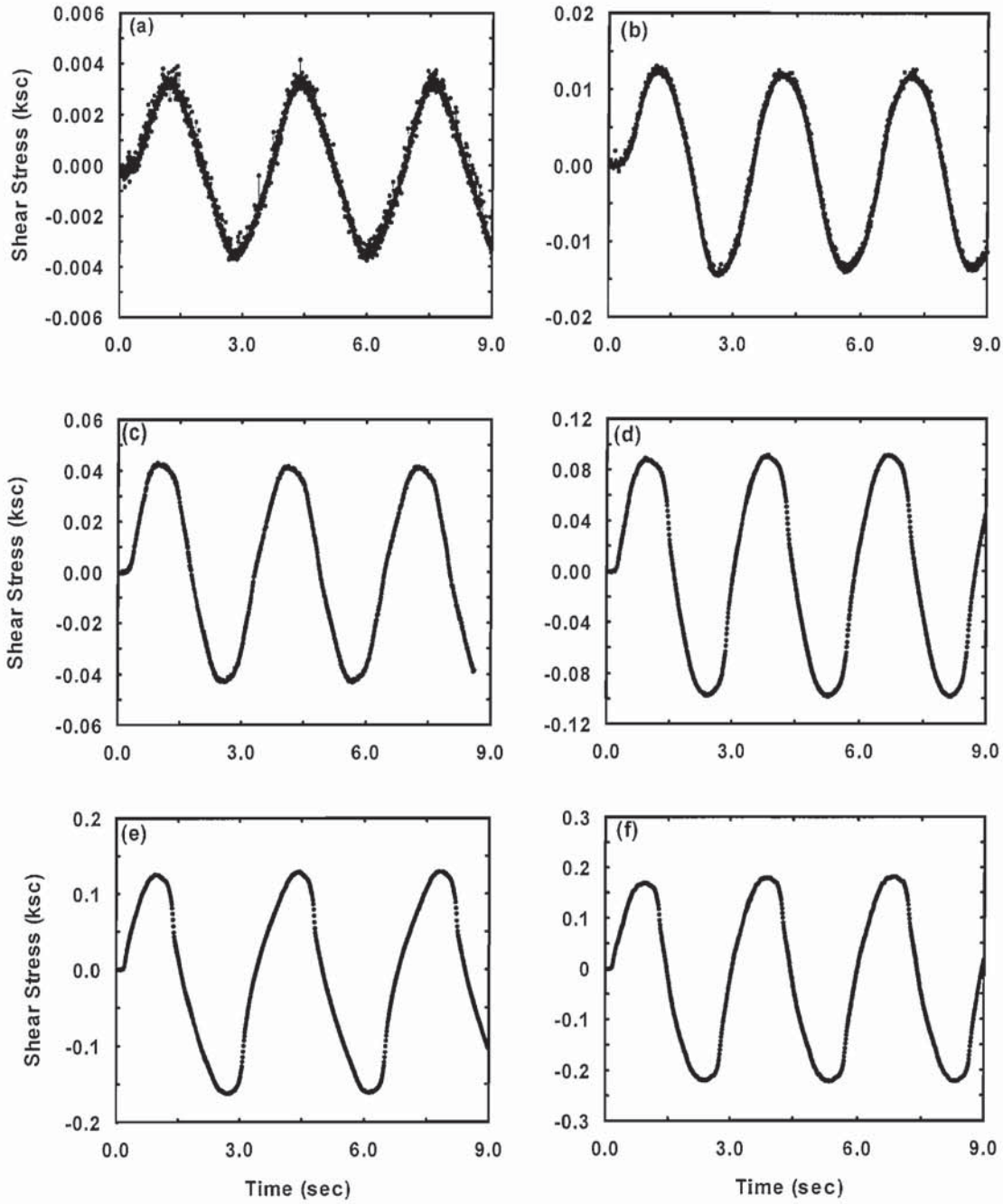

Figure 4.12 Stress time histories as measured by the DFSD from tests on reconstituted kaolinite samples at different peak strain levels

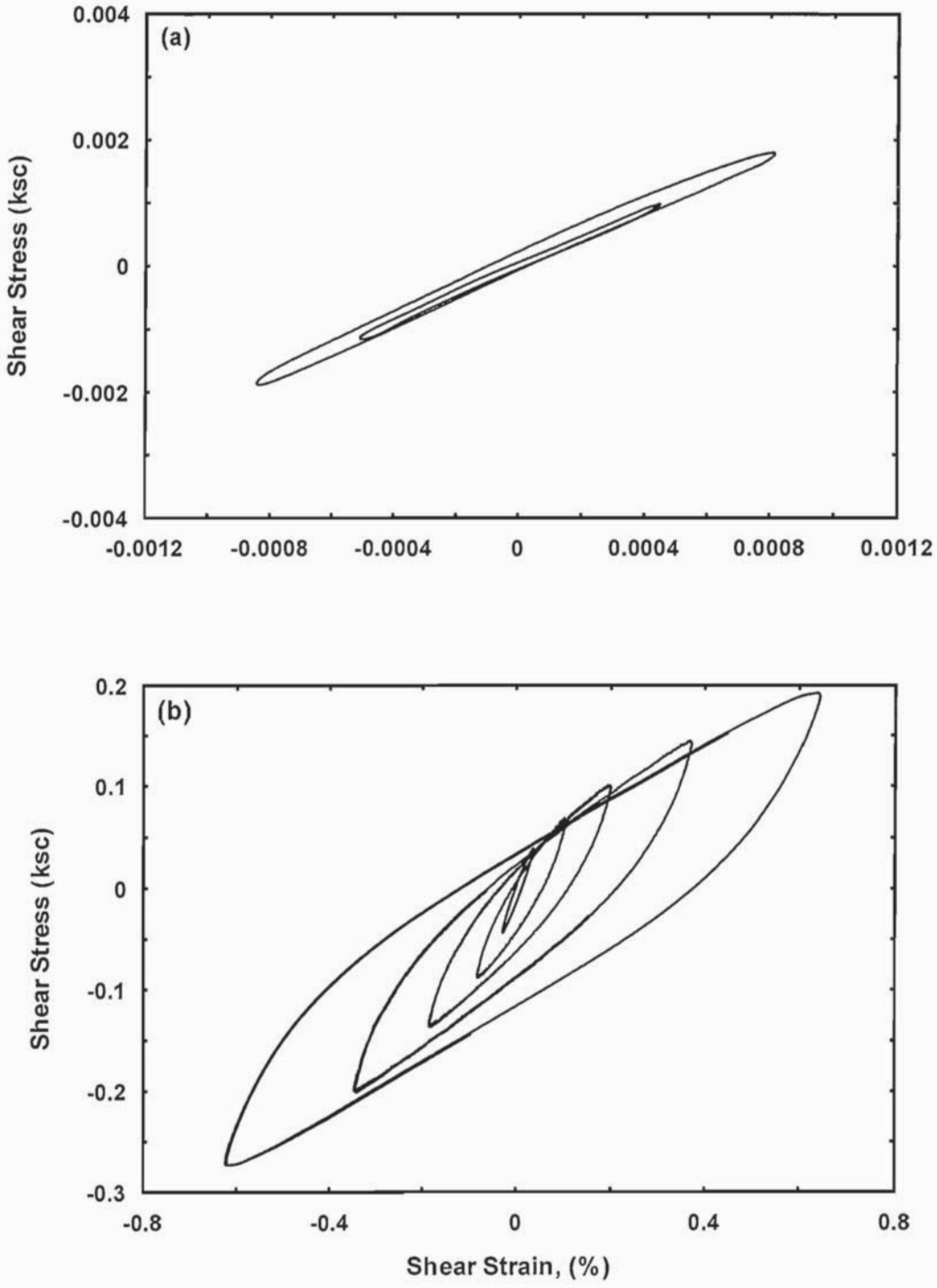

Figure 4.13 Stress-strain hysteretic loops obtained from DFSD tests on reconstituted kaolinite (a) at very small peak strain levels and (b) at intermediate-to-large peak strain levels

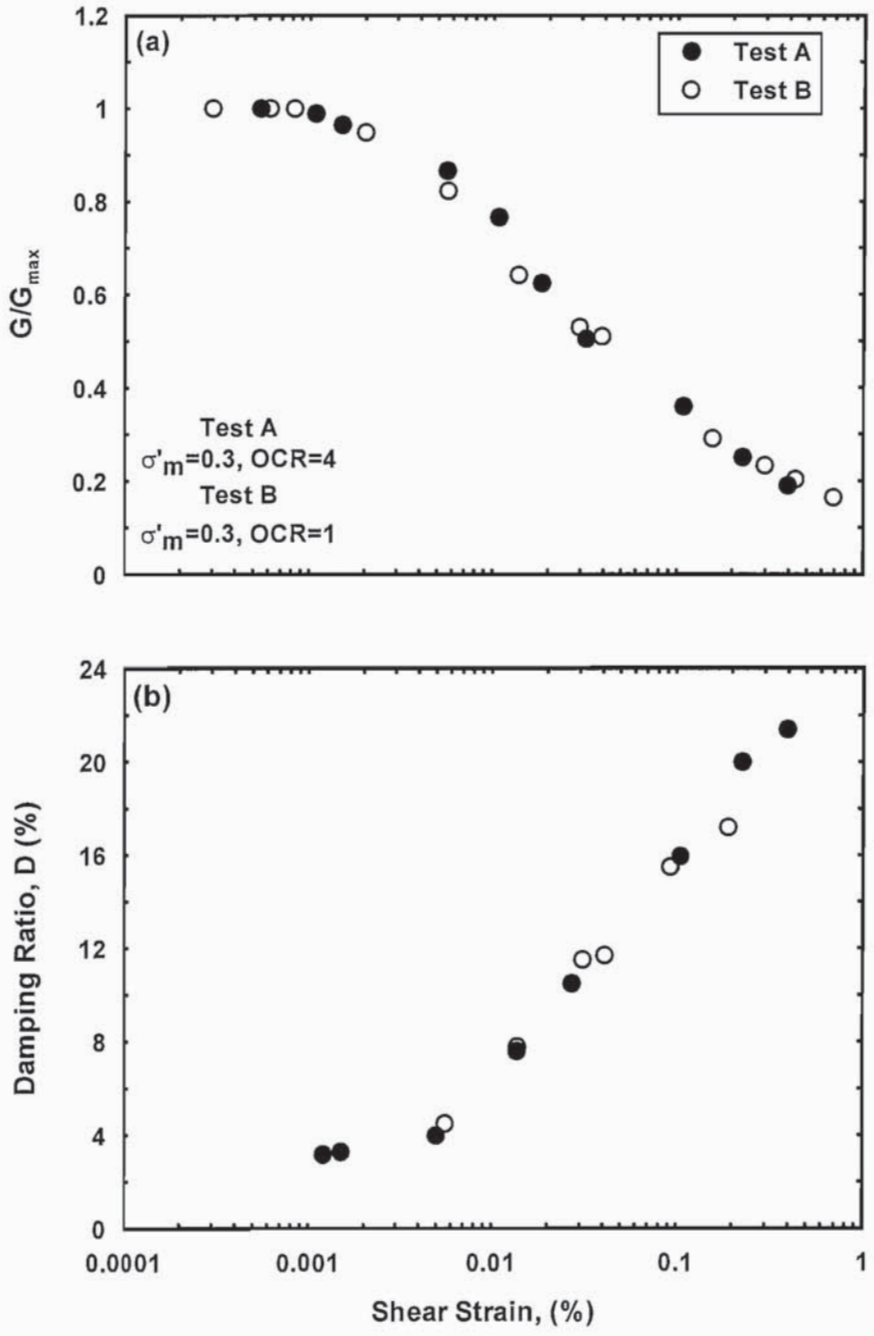

Figure 4.14 Normalized modulus reduction curve and damping curve from two separate DFSD laboratory tests on reconstituted kaolinite samples

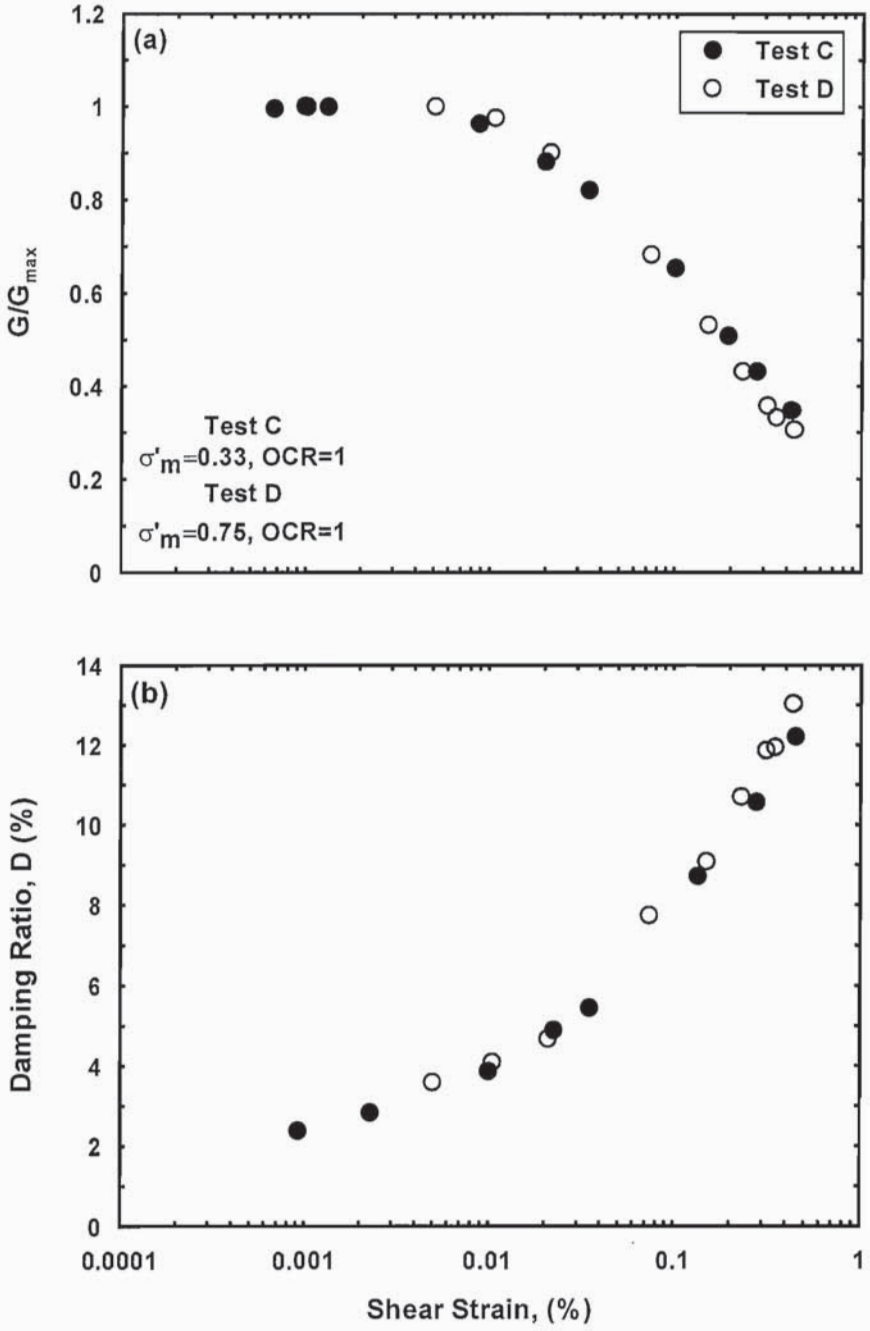

Figure 4.15 Normalized modulus reduction curve and damping curve from two separate DFSD laboratory tests on reconstituted Bear Creek soil samples

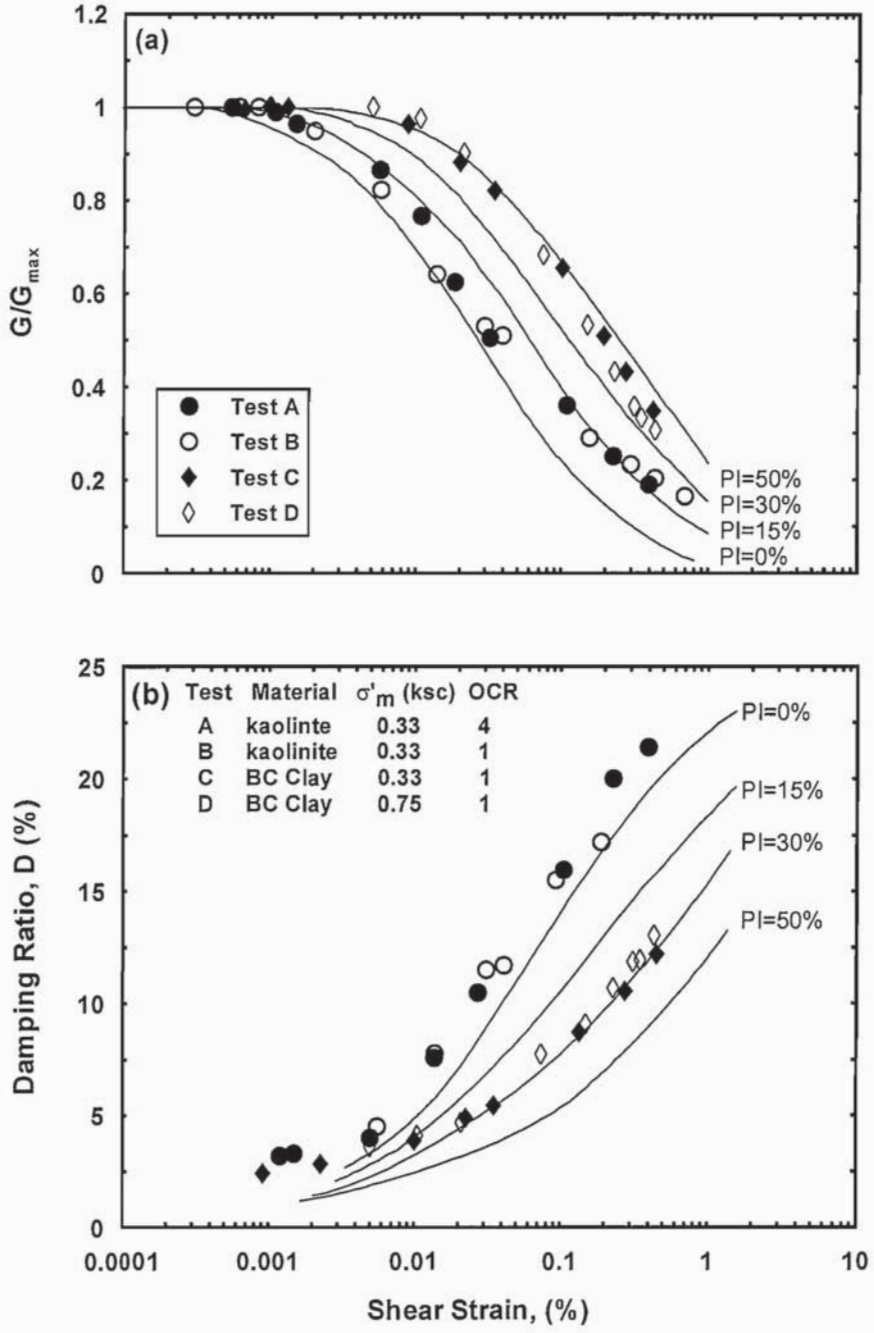

Figure 4.16 Normalized modulus reduction curves and damping curves from DFSD laboratory implementation tests as compared with Vucetic and Dobry (1991) curves

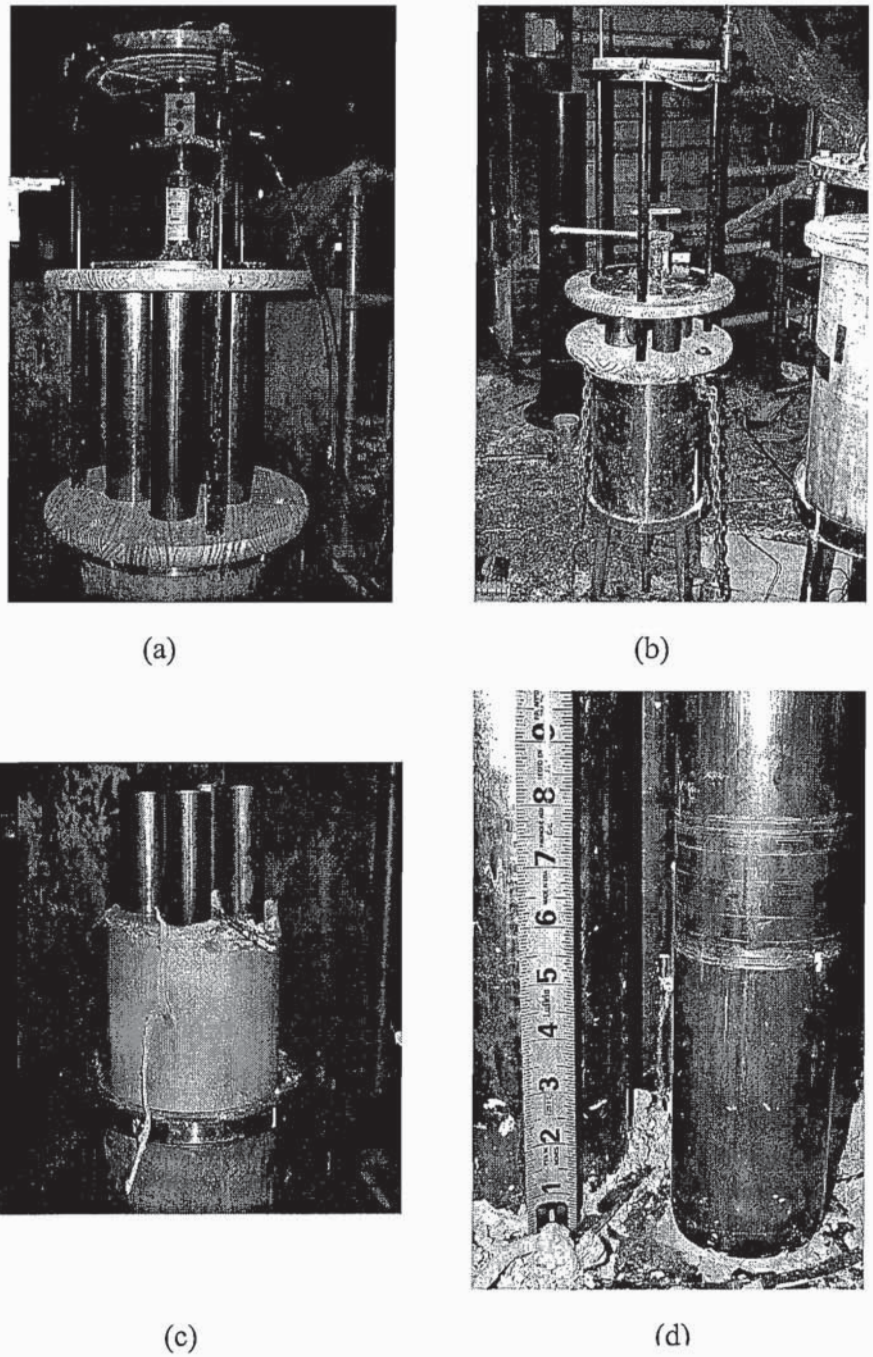

Figure4 .17 Setup and steps of the Shelby tube sampling process of four reconstituted kaolinite specimens

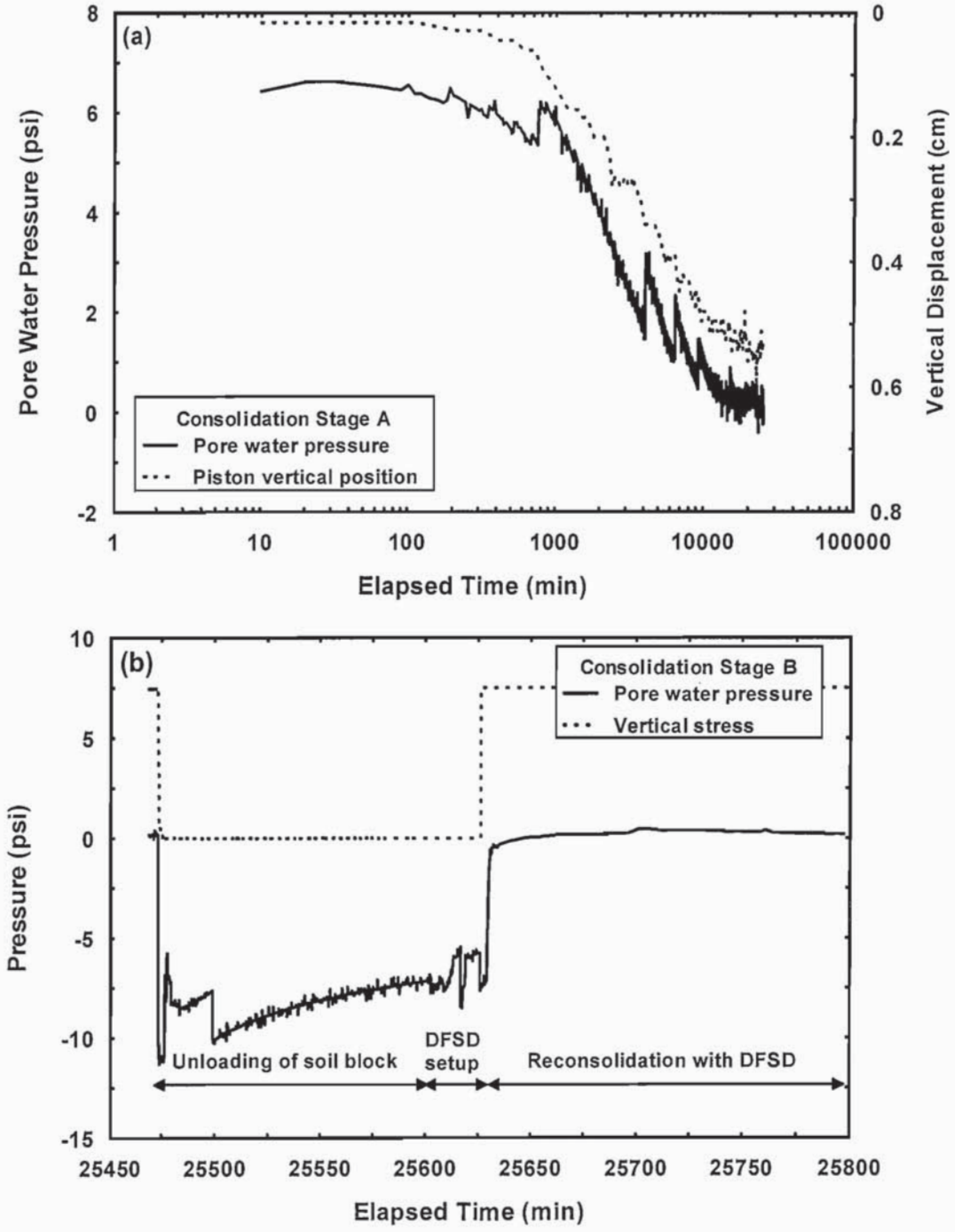

Figure4 .18 The two stages of kaolinite consolidation for DFSD validation tests; (a) typical incremental consolidation from thick slurry using the smart consolidometer (b) unloading of soil block and reconsolidation with the DFSD in-place

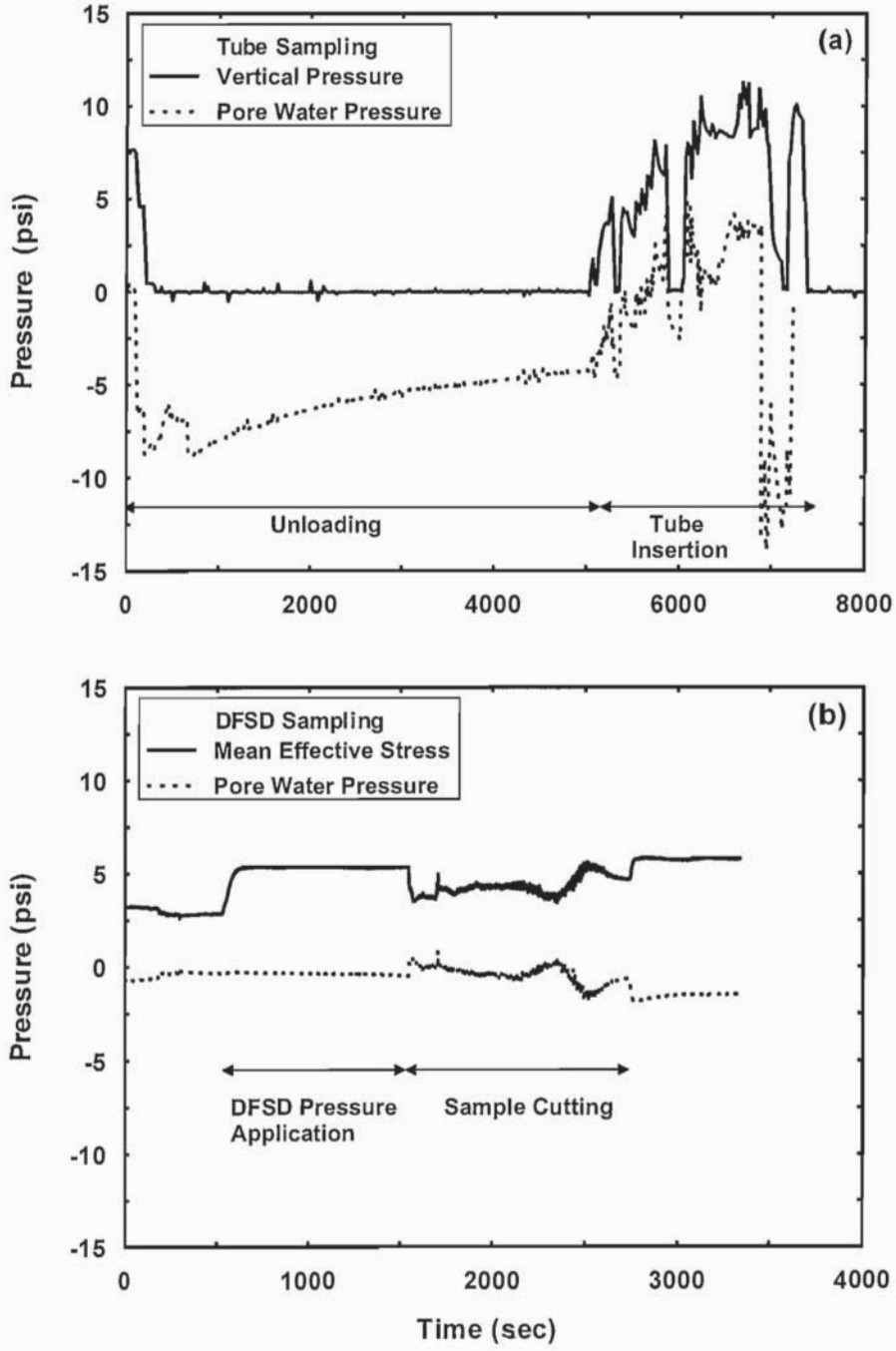

Figure 4.19 A comparison between Shelby tube sampling and DFSD sample creation process

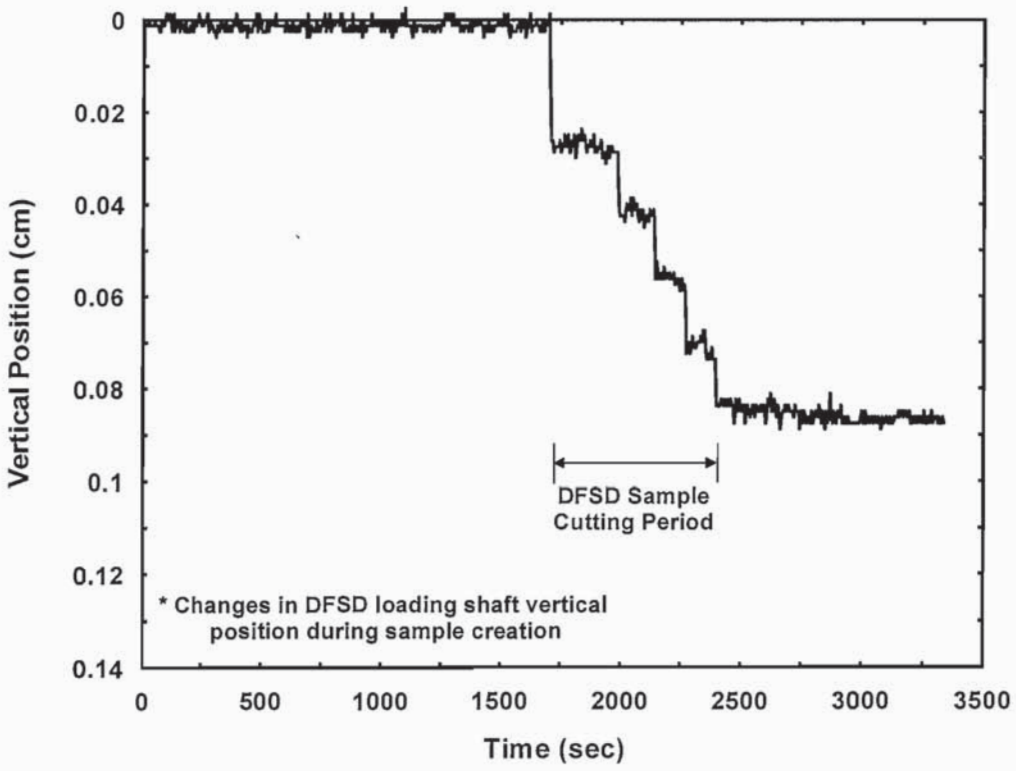

Figure 4.20 Changes in the load shaft vertical position during the DFSD kaolinite sample carving process

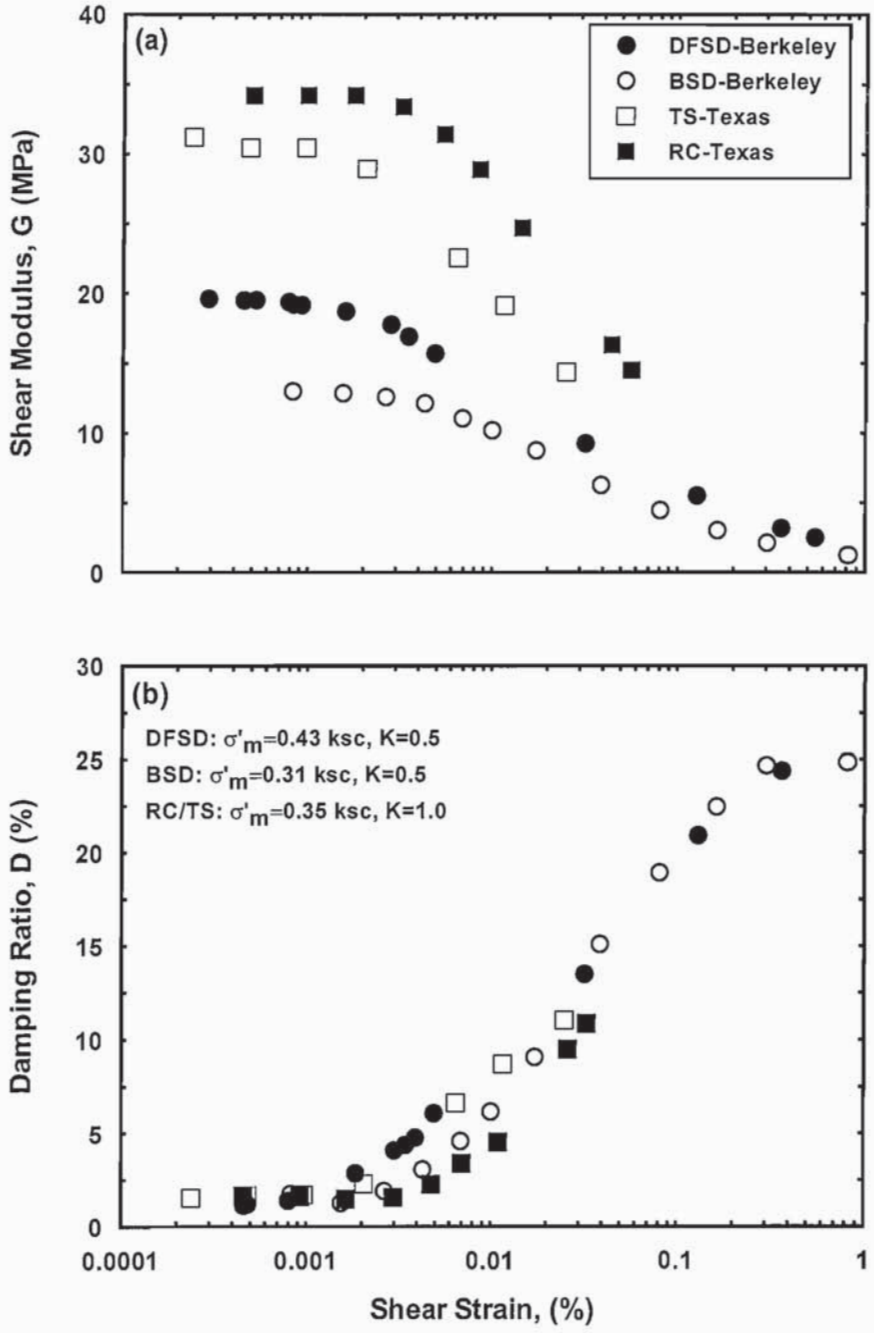

Figure 4.21 Modulus reduction curve (a) and damping curve (b) from K1 validation tests on reconstituted kaolinite samples

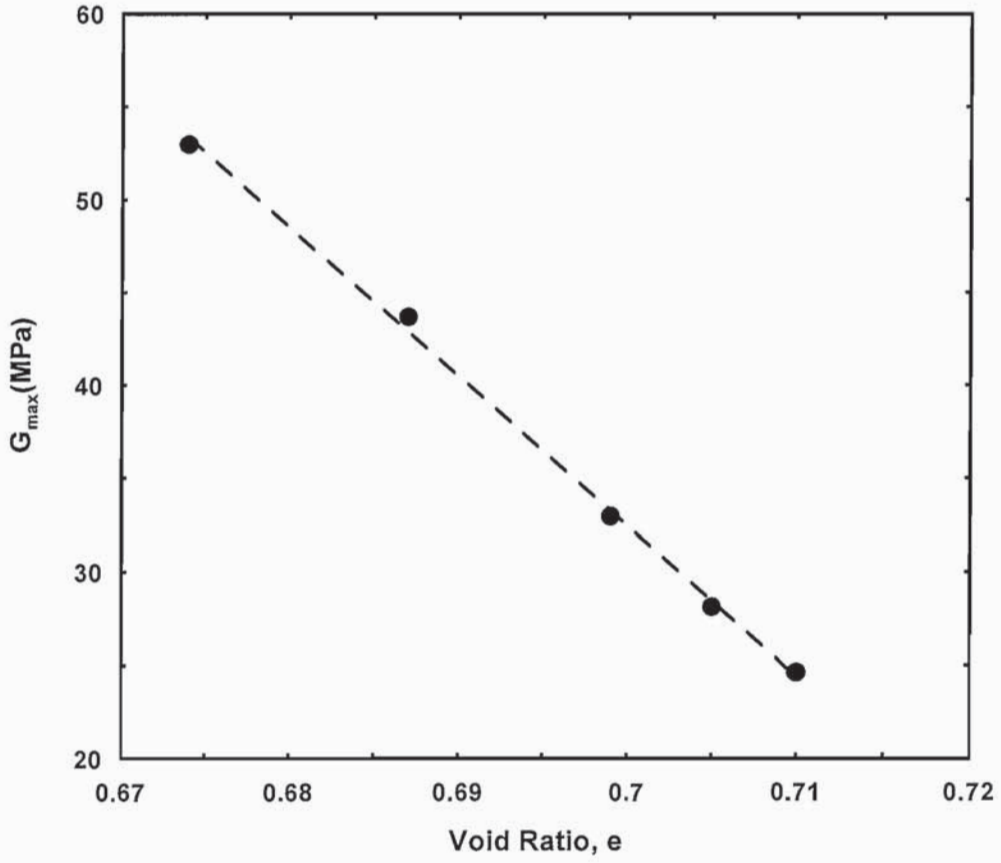

Figure 4.22 Variation in low-amplitude shear modulus, G_{max}, with void ratio as measured by RC tests on K1 kaolinite sample

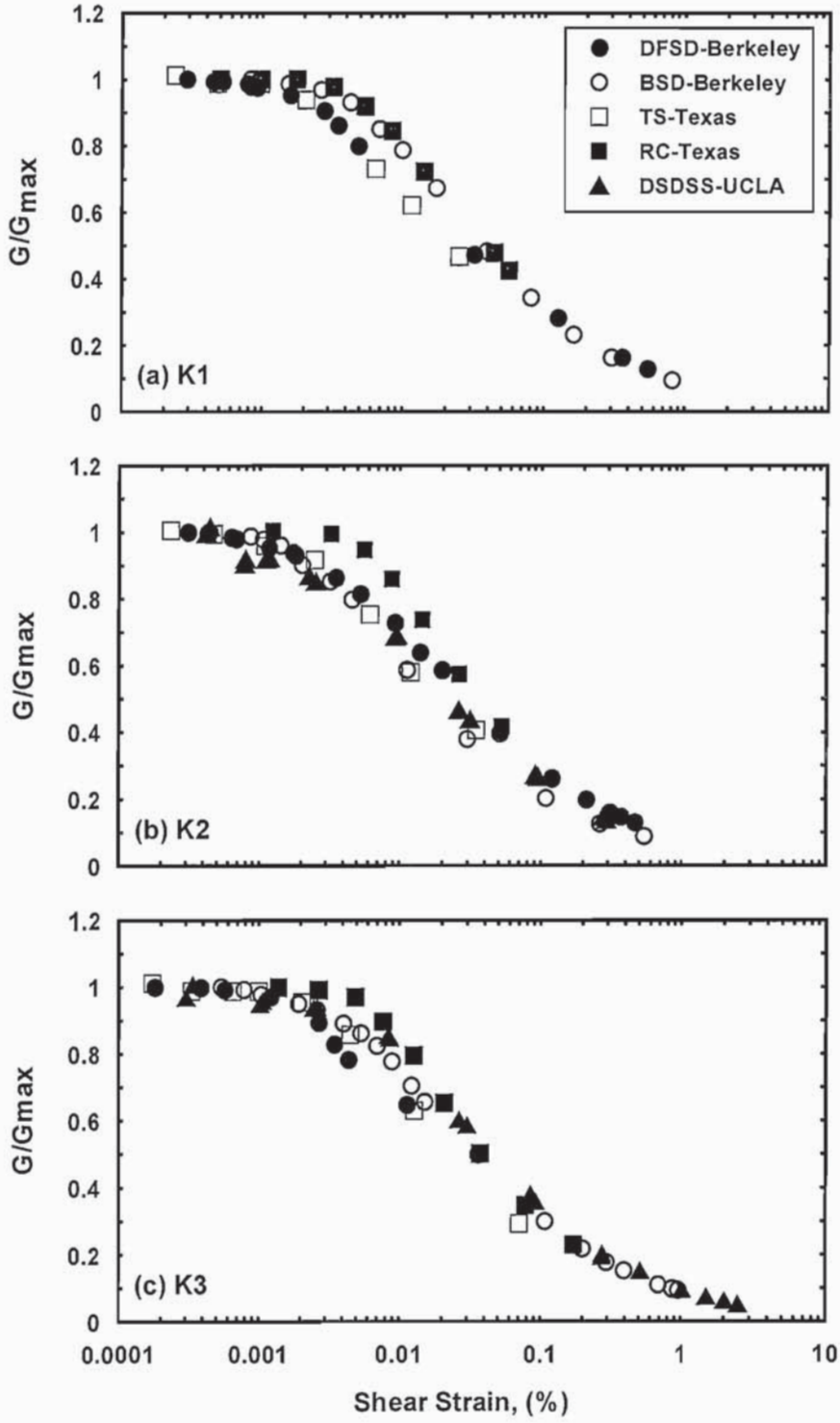

Figure4 .23 Normalized modulus reduction curve from K1 (a) K2 (b) and K3 (c) validation tests on reconstituted kaolinite samples

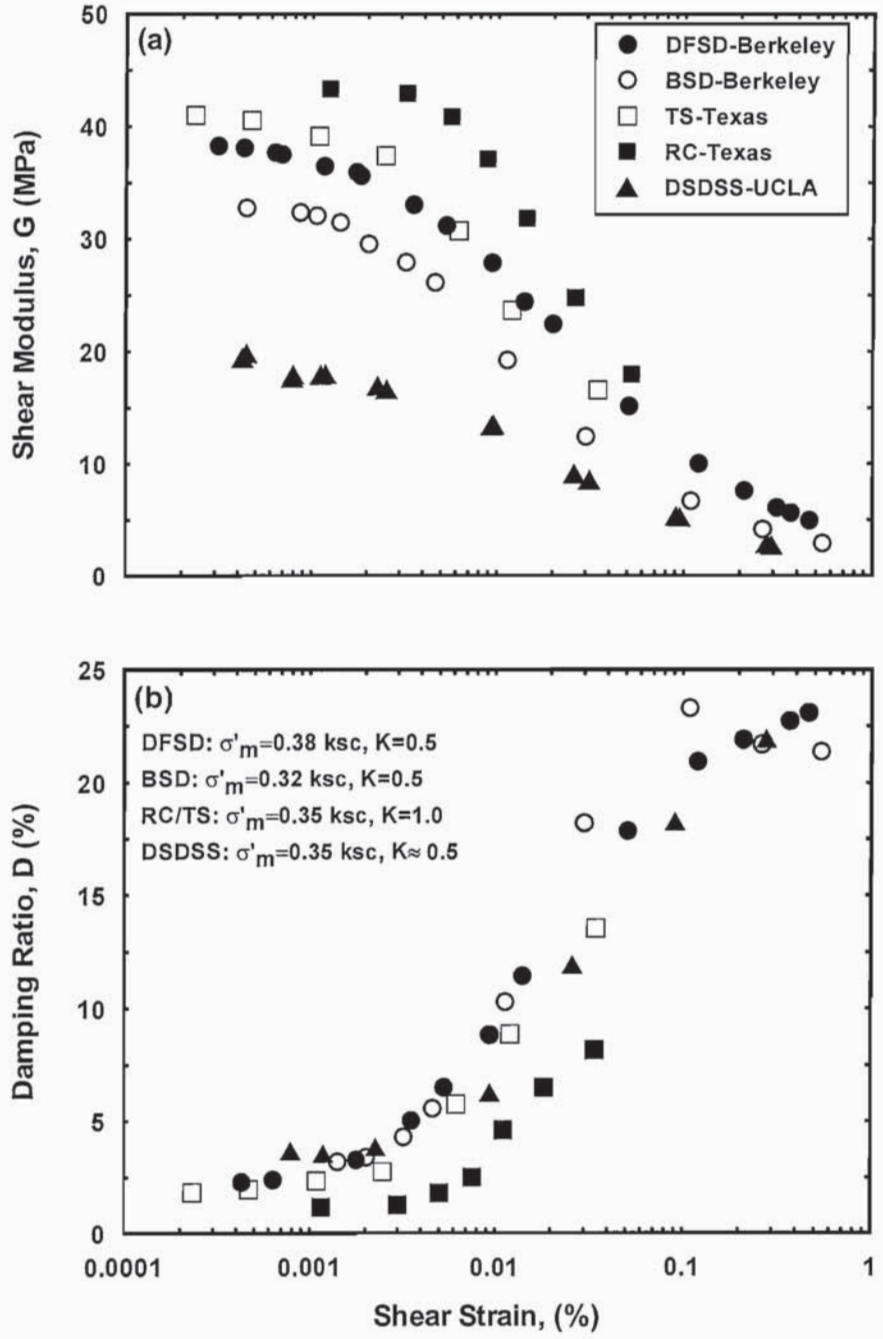

Figure 4.24 Modulus reduction curve (a) and damping curve (b) from K2 validation tests on reconstituted kaolinite samples

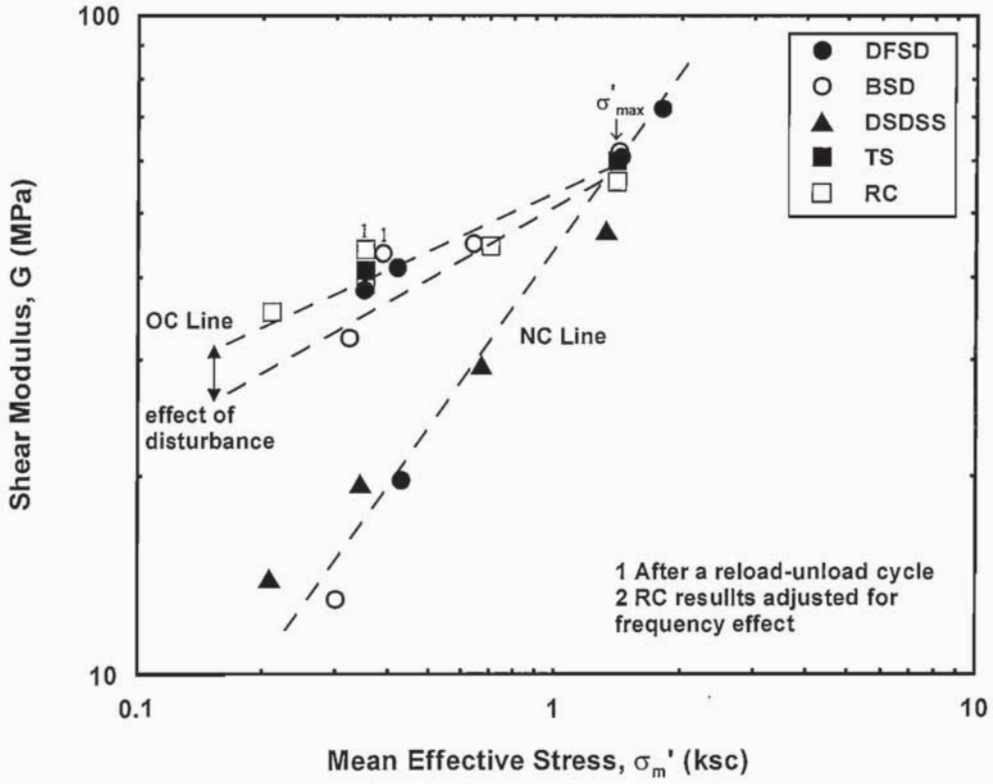

Figure 4.25 Variation in low-amplitude shear modulus, G_{max}, with mean effective confining stress from validation tests on reconstituted kaolinite samples

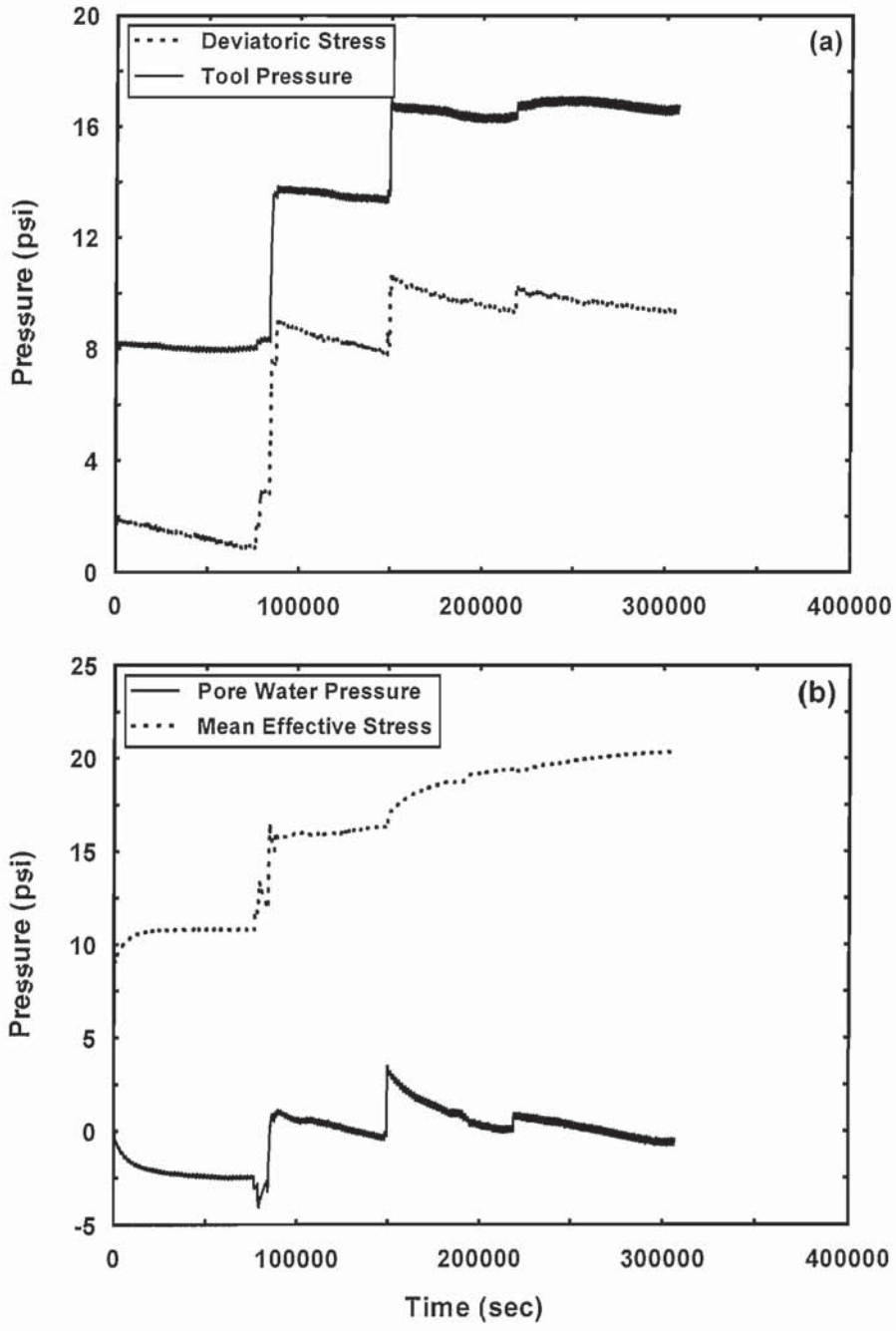

Figure 4.26 DFSD consolidation of K3 sample as indicated by (a) changes in the applied confining pressures and (b) the corresponding changes in pore water pressure and effective stress

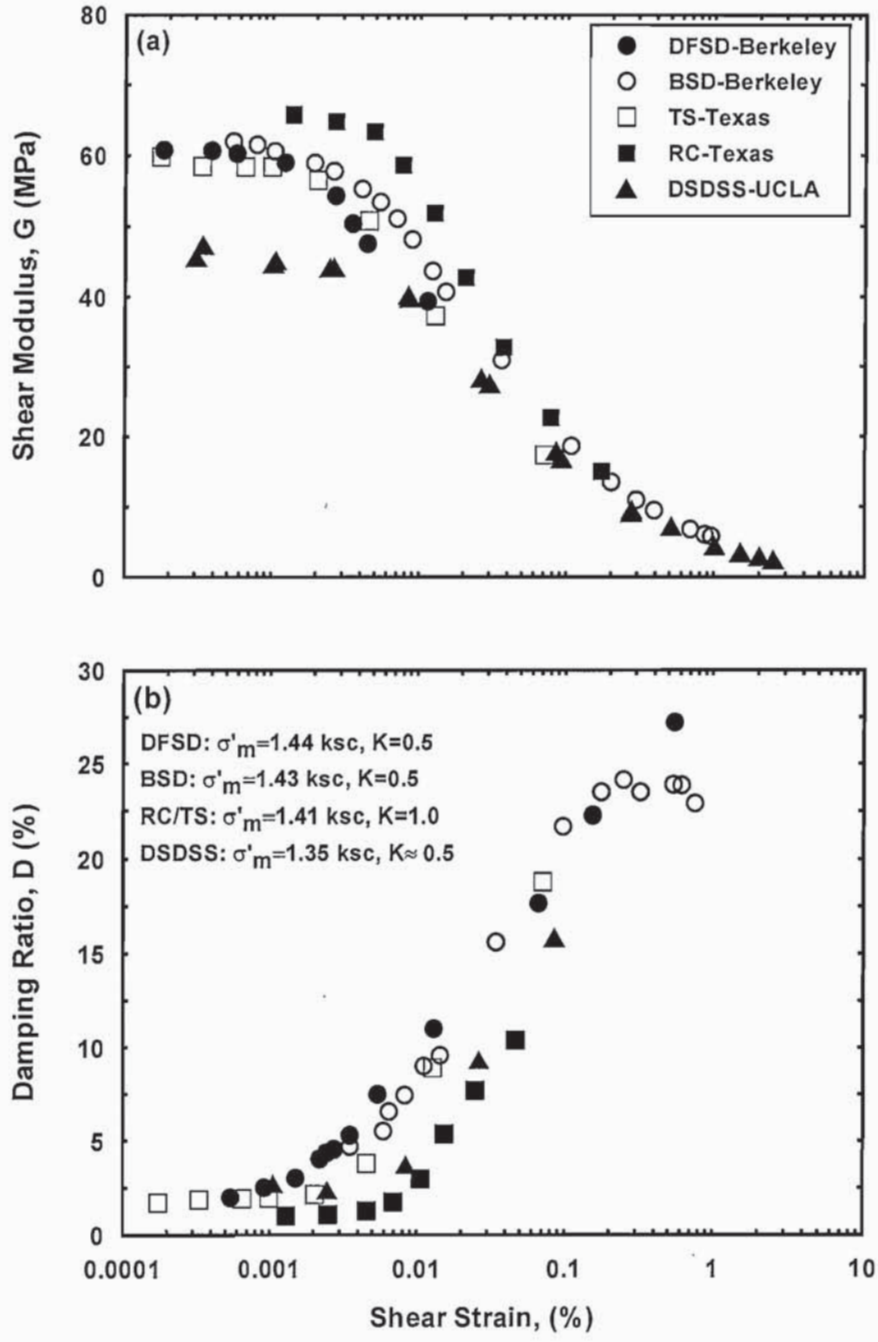

Figure 4.27 Modulus reduction curve (a) and damping curve (b) from K3 validation tests on reconstituted kaolinite samples

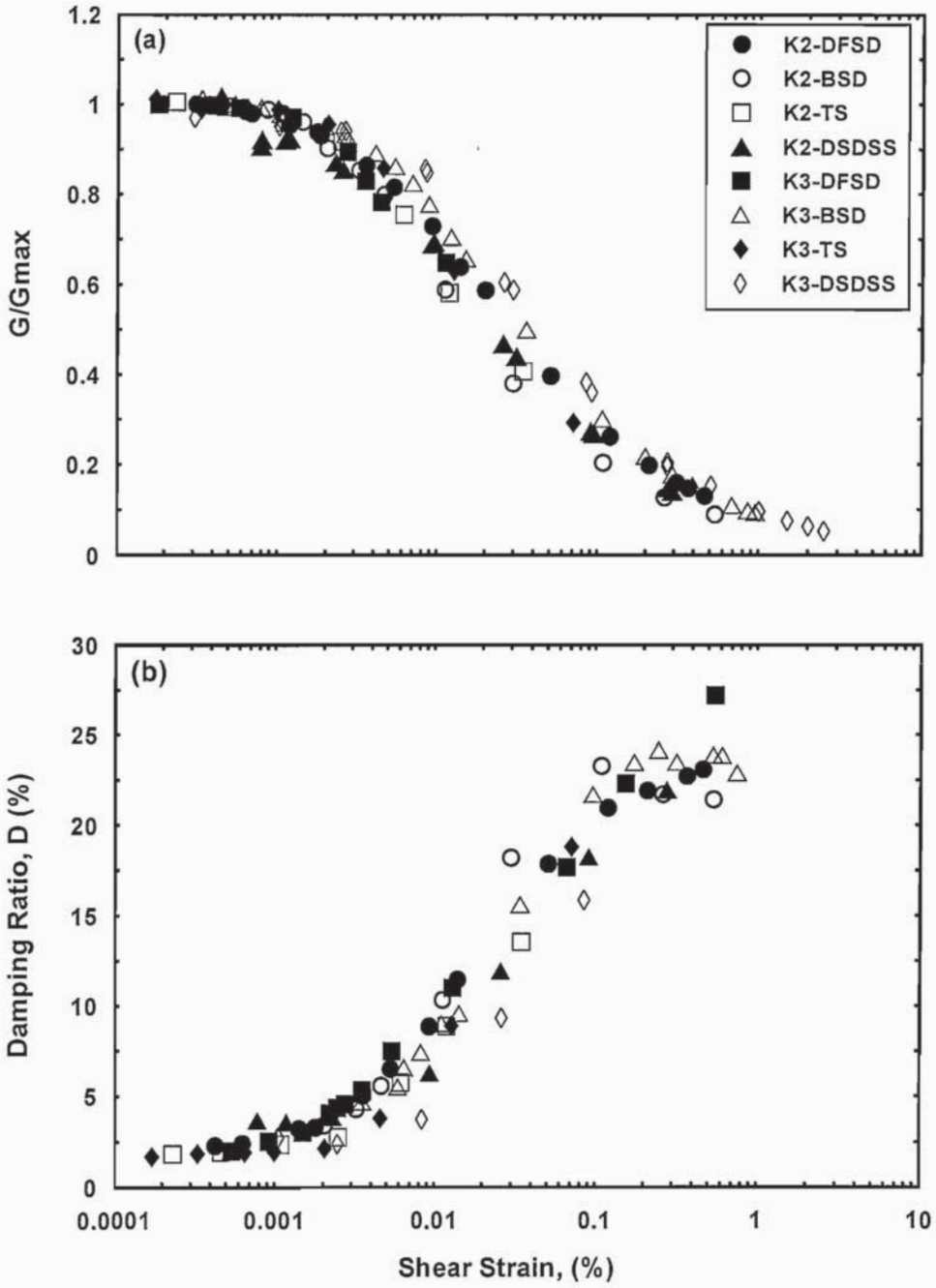

Figure 4.28 Normalized modulus reduction curve (a) and damping curve (b) from all validation tests on reconstituted kaolinite samples (excluding RC tests)

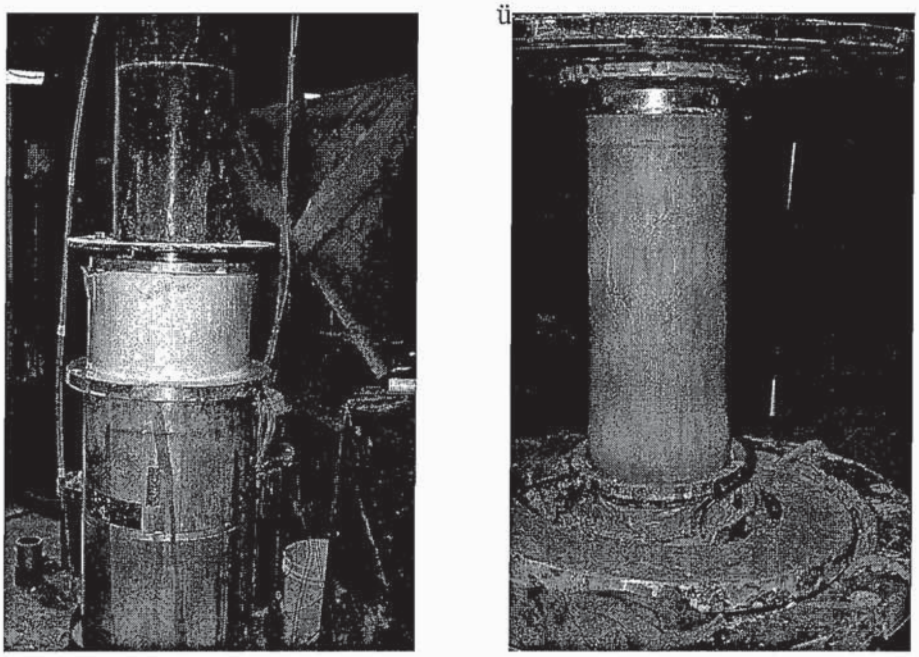

(a) (b)

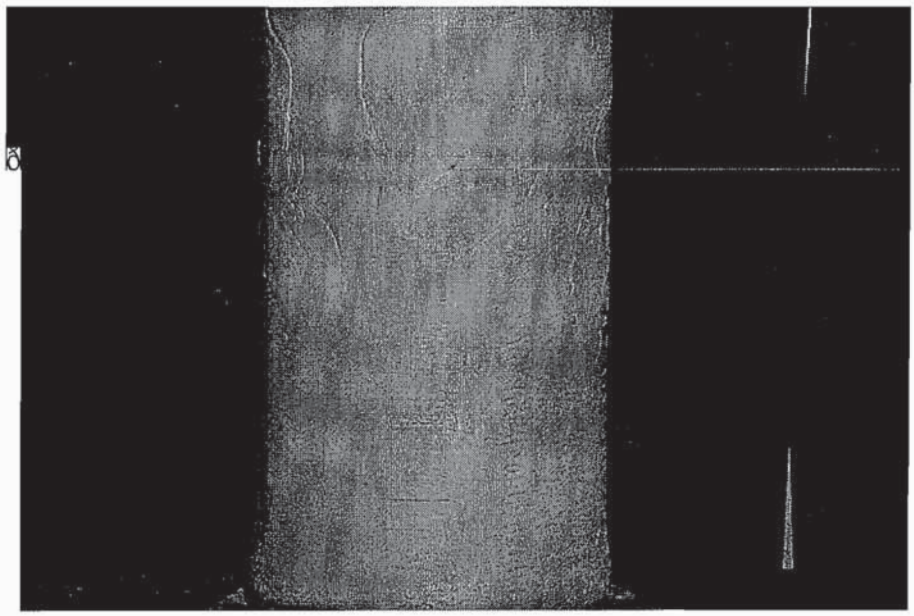

(c)

Figure 4 .29 Extraction of kaolinite sample after a laboratory DFSD test. Note the quality of the sample and the elastomer gauges imprints on its surface

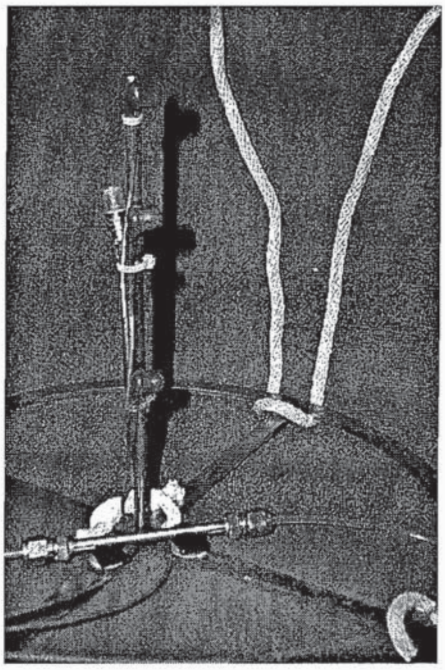

(a)

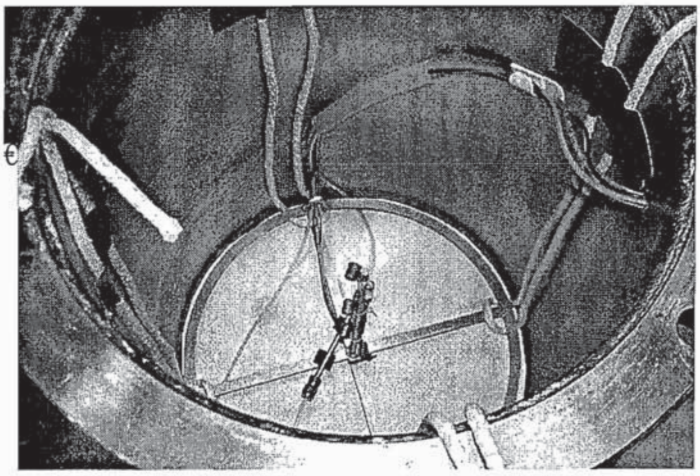

(b)

Figure 4.30 (a) The layout of three accelerometers and the mini air hammer (b) the whole assembly inside the consolidometer

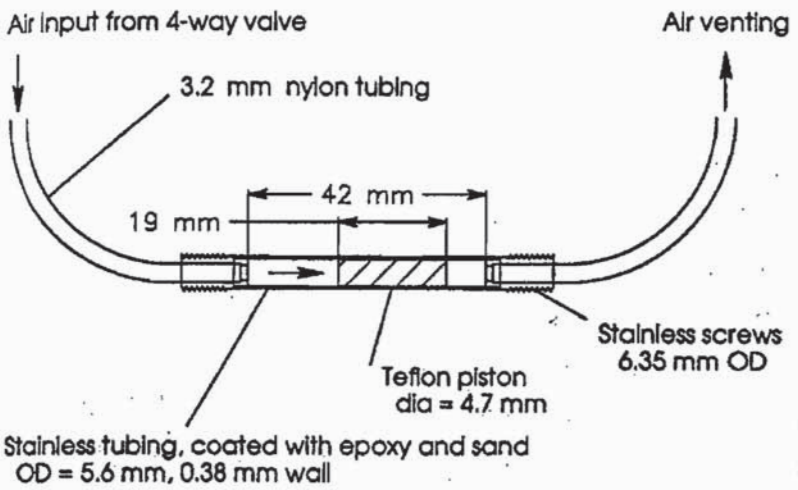

Figure 4.31 The design of the mini air hammer (after Arulnathan et. al, 2000)

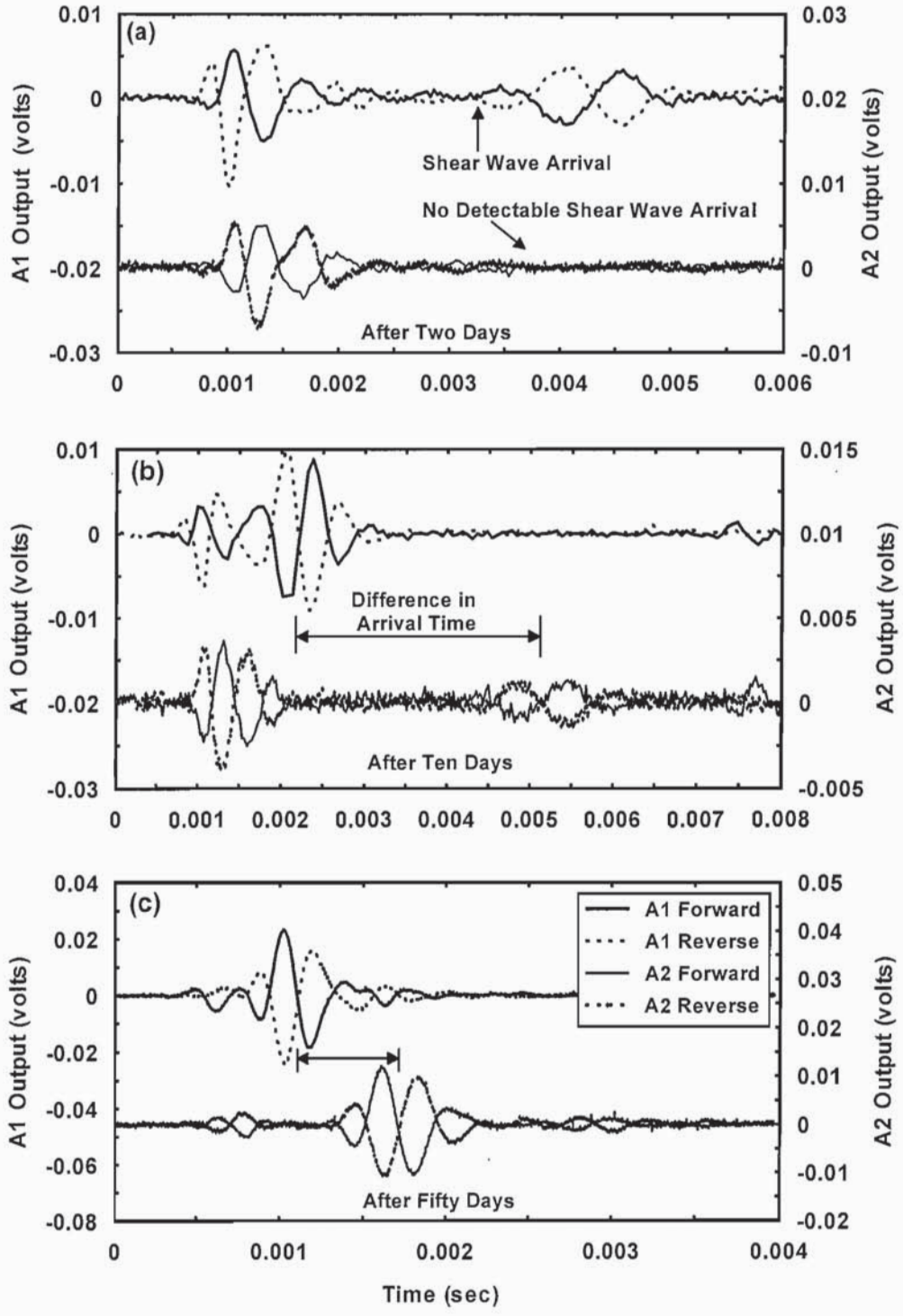

Figure 4.32 Recorded output signals of the three accelerometers at different stages of Bay Mud consolidation. Note the change in shear waves arrival time with the progress of consolidation

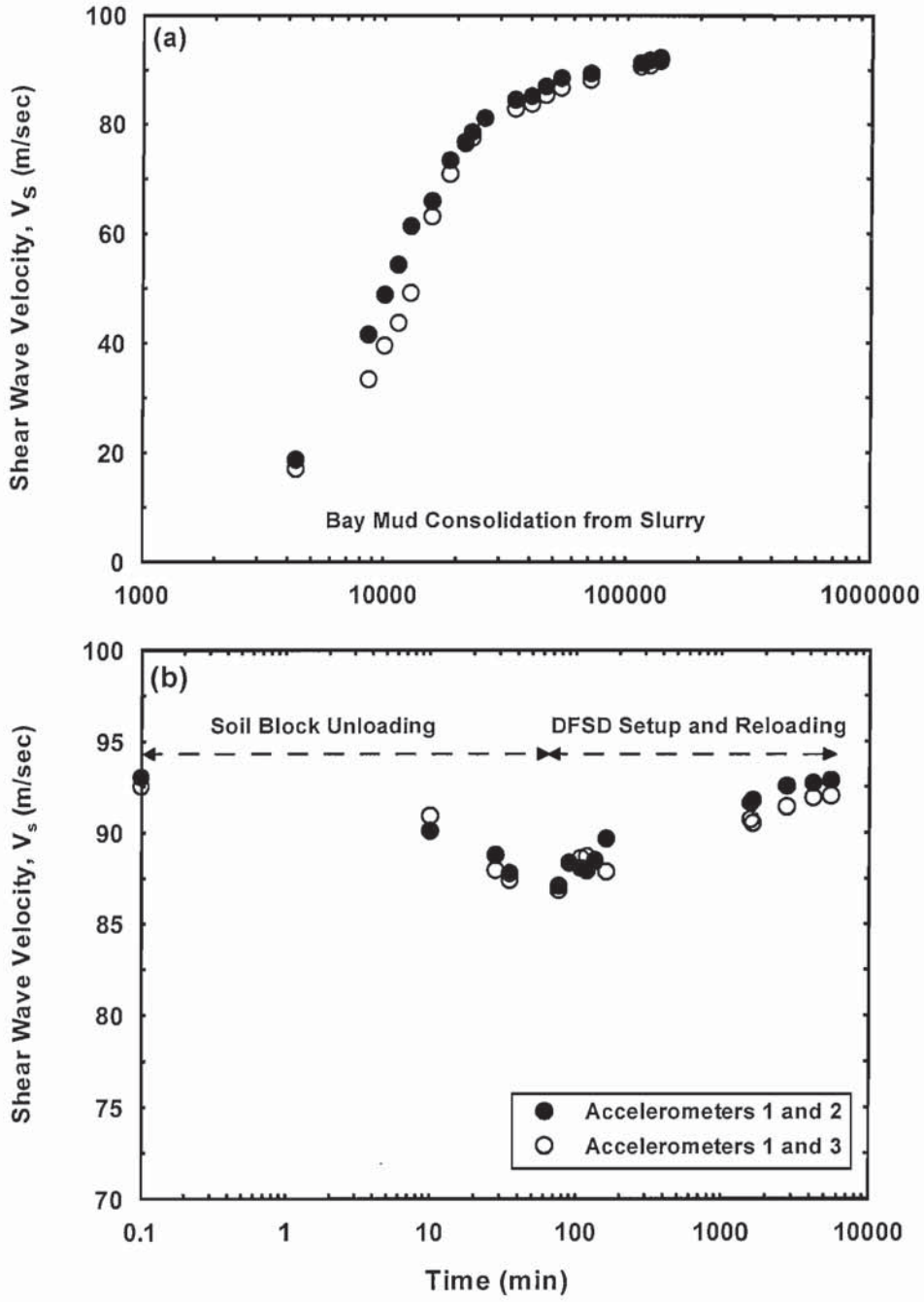

Figure 4.33 Shear wave velocity measurement made during the two stages of Bay Mud consolidation (a) first stage from slurry (b) with the DFSD in place

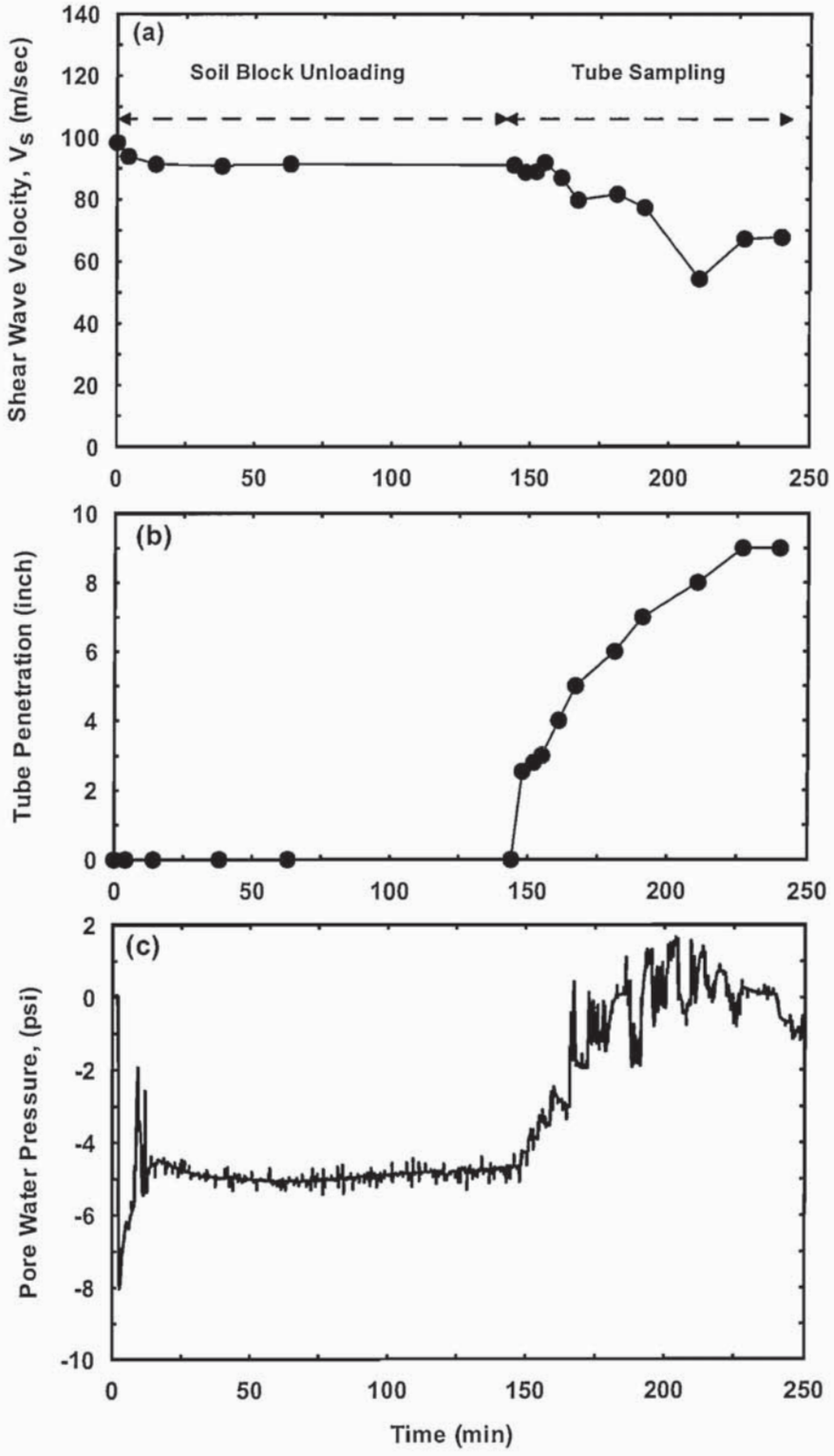

Figure 4.34 Changes in (a) V_s and (c) PWP induced during Shelby-tube sampling of reconstituted Young Bay Mud

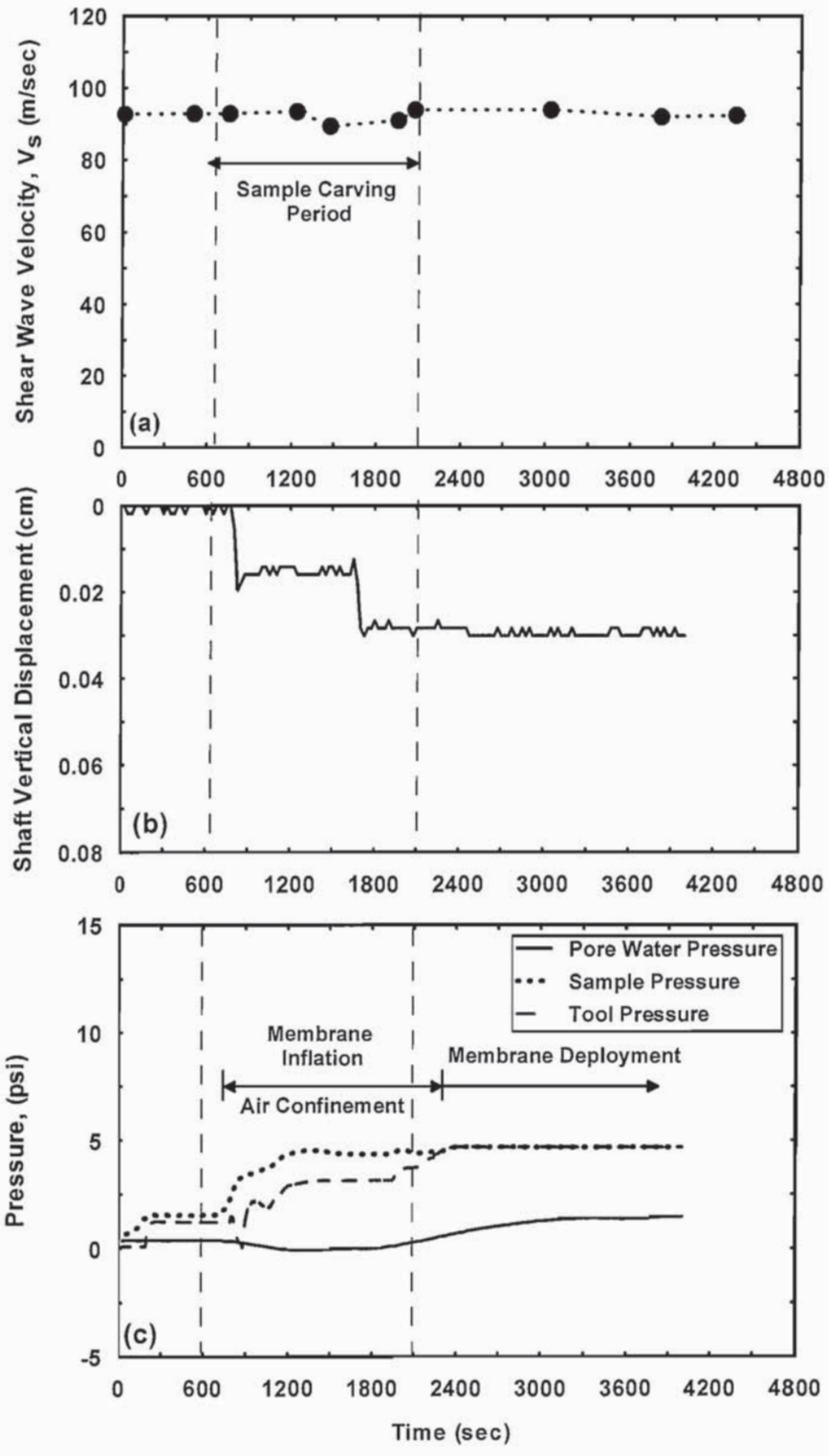

Figure 4.35 Changes in (a) V_s (b) vertical position and (c) PWP as induced by DFSD sample creation process

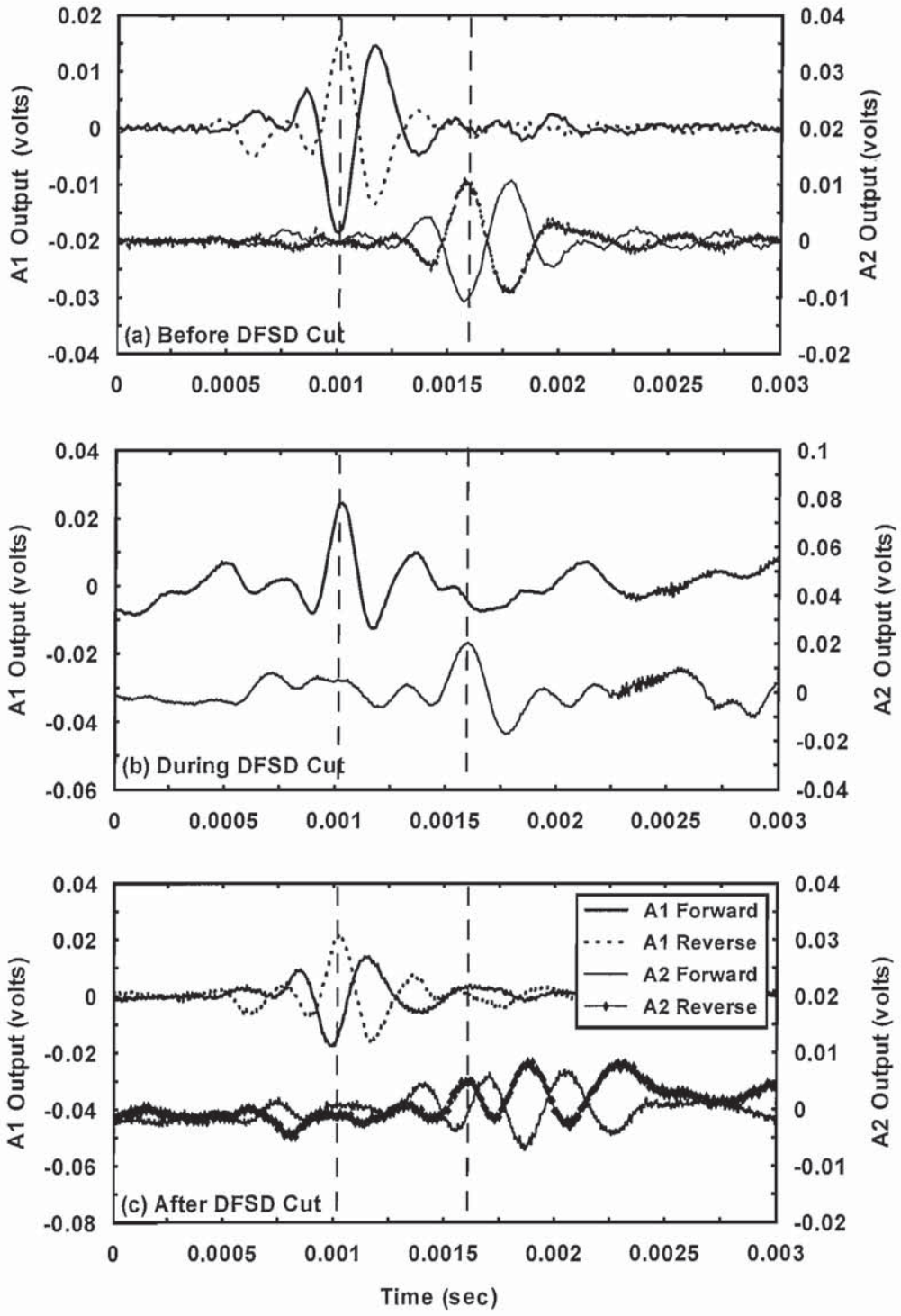

Figure 4.36 Accelerometers 1 and 2 signals as recorded (a) before (b) during and (c) after DFSD Bay Mud sample carving

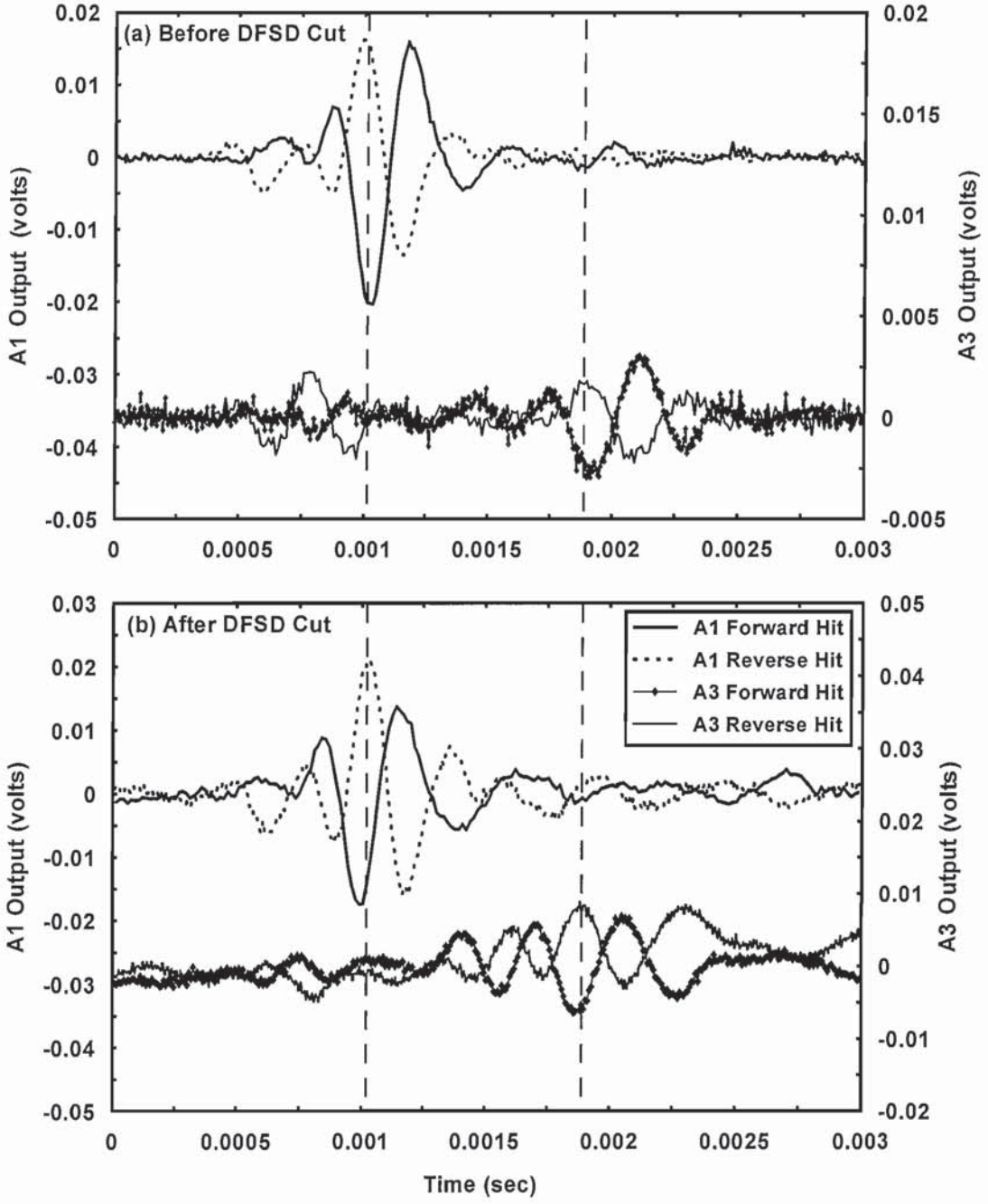

Figure 4.37 Accelerometers 1 and 3 signals as recorded (a) before and (c) after DFSD Bay Mud sample cut

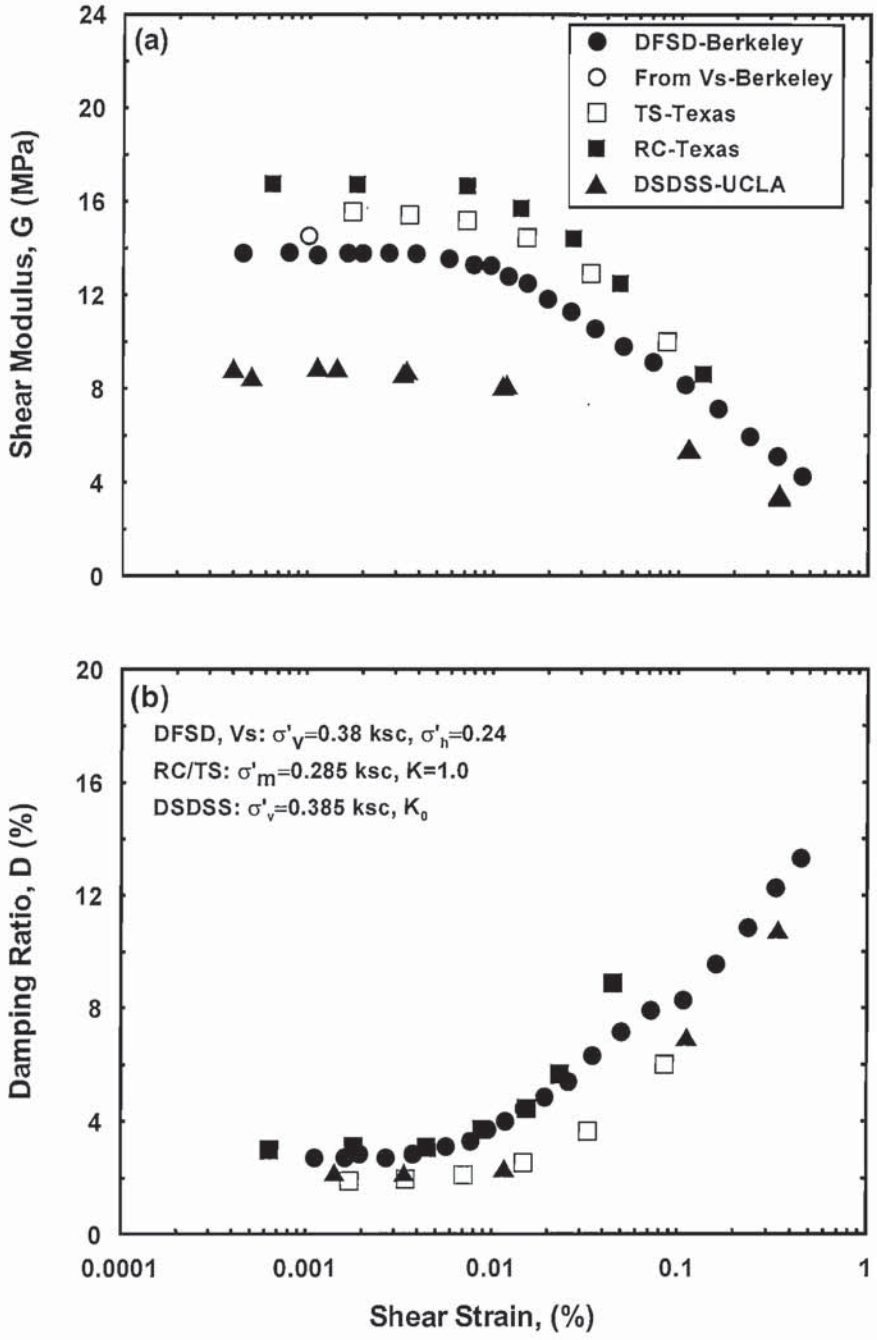

Figure 4.38 Modulus reduction curve (a) and damping curve (b) from BM1 validation tests on reconstituted Bay Mud samples

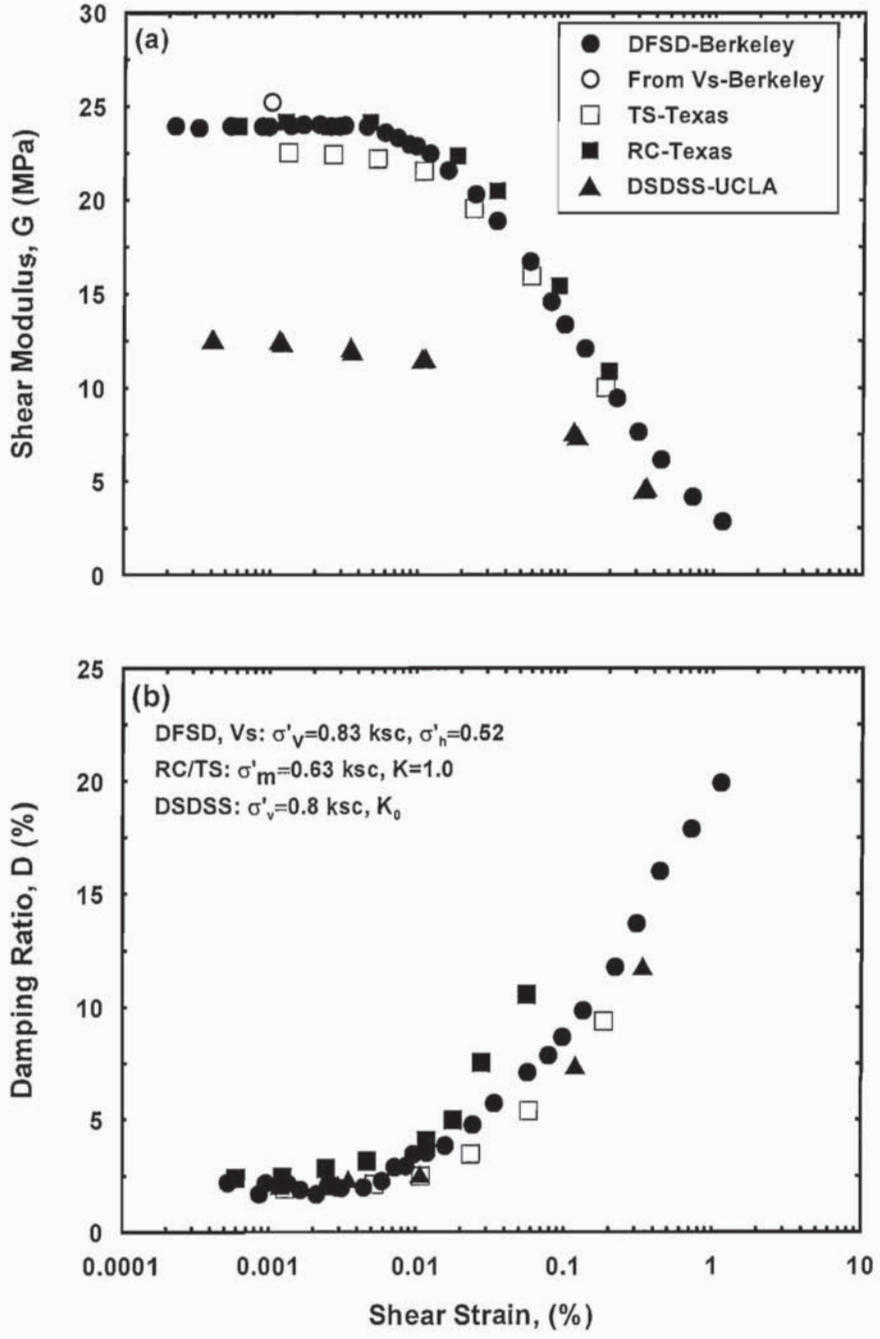

Figure 4.39 Modulus reduction curve (a) and damping curve (b) from BM2 validation tests on reconstituted Bay Mud samples

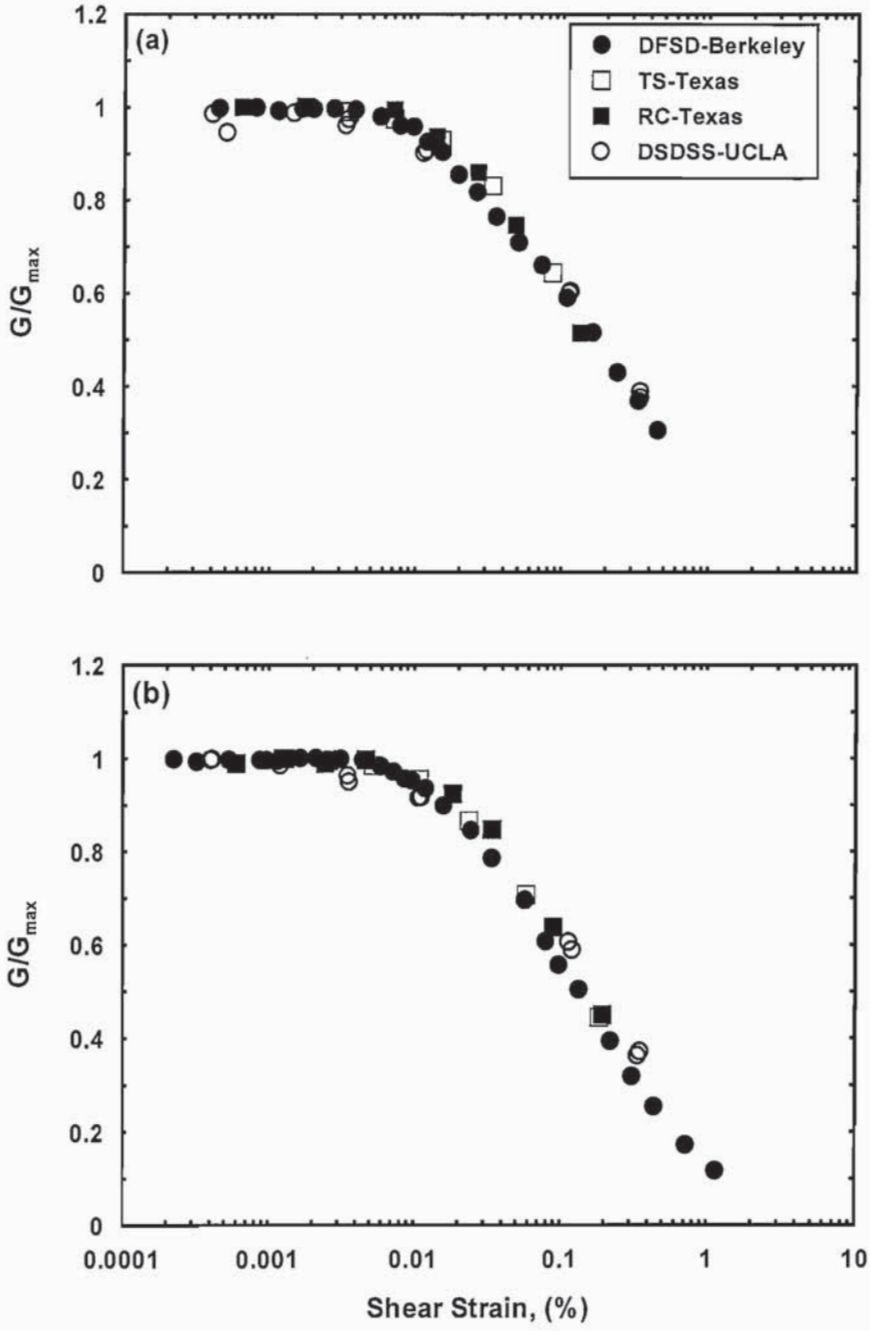

Figure 4.40 Normalized modulus reduction curve (a) from BM1 and (b) BM2 validation tests on reconstituted Bay Mud samples

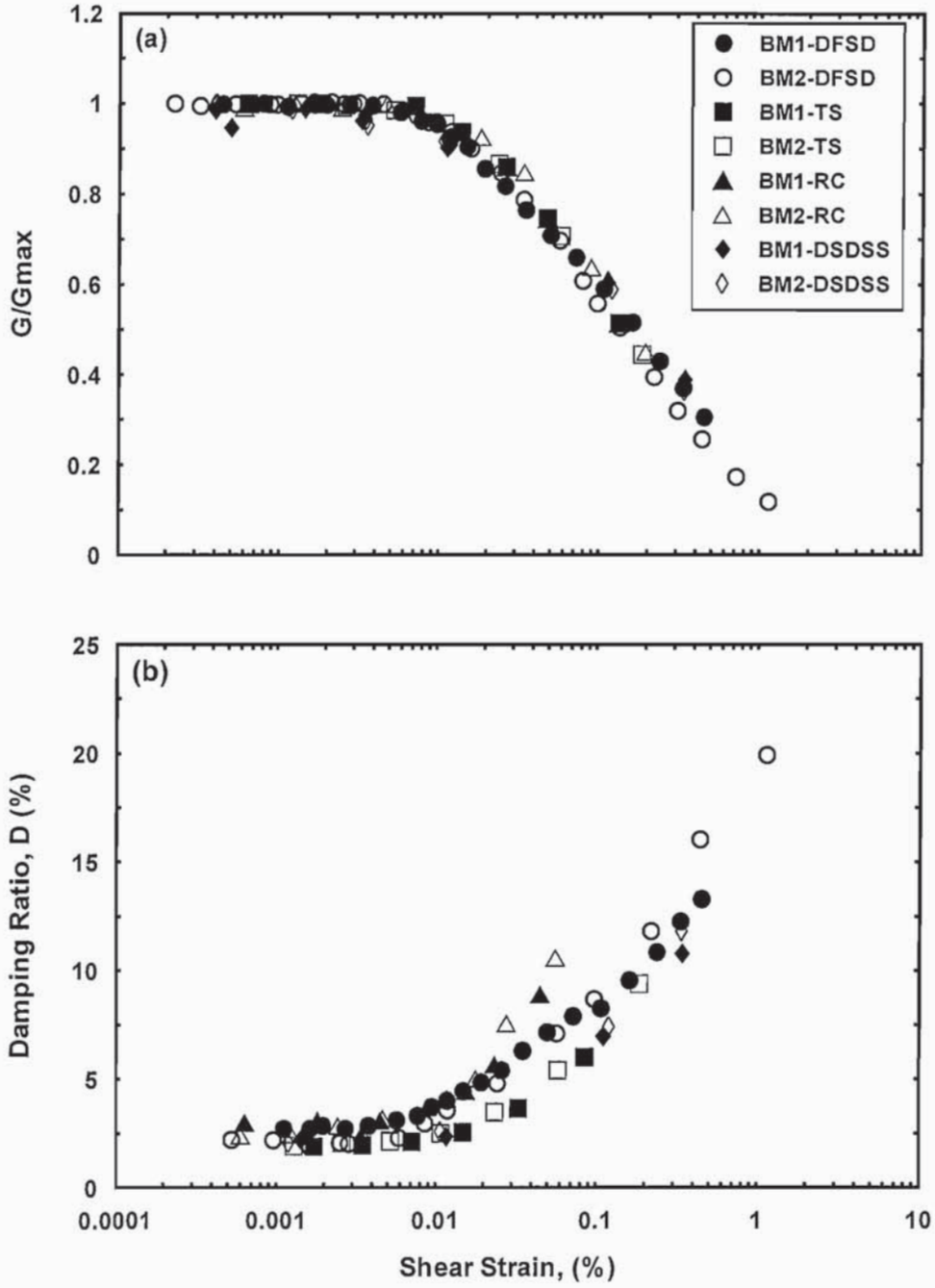

Figure 4.41 Normalized modulus reduction curve (a) and damping curve (b) from all validation tests on reconstituted Bay Mud samples

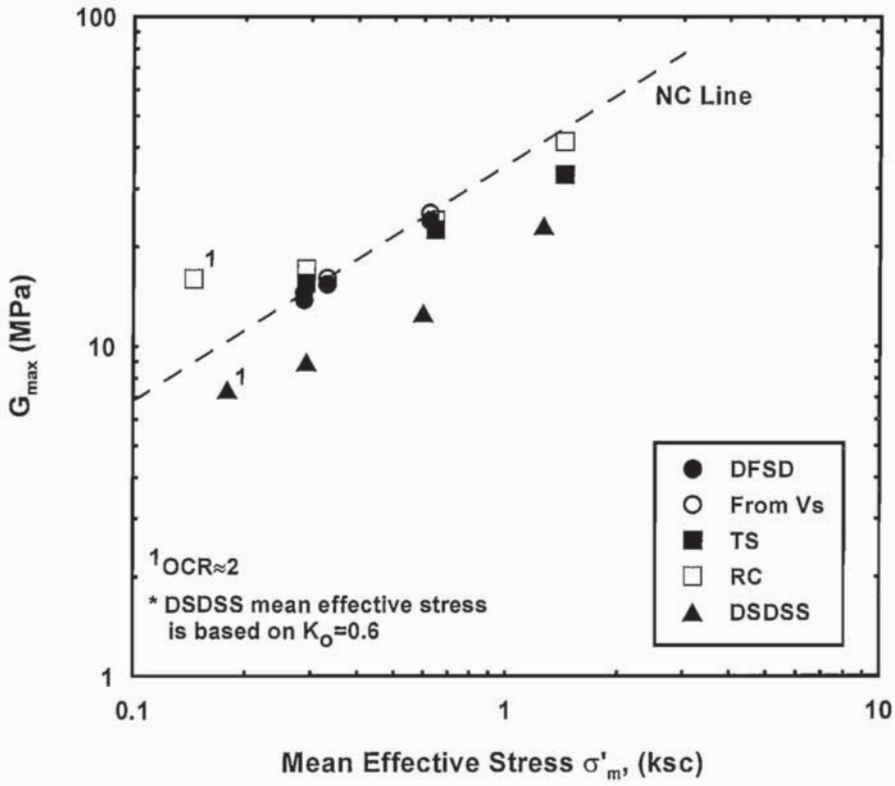

Figure 4.42 Changes in G_{max} as a function of mean effective stress for reconstituted Bay Mud

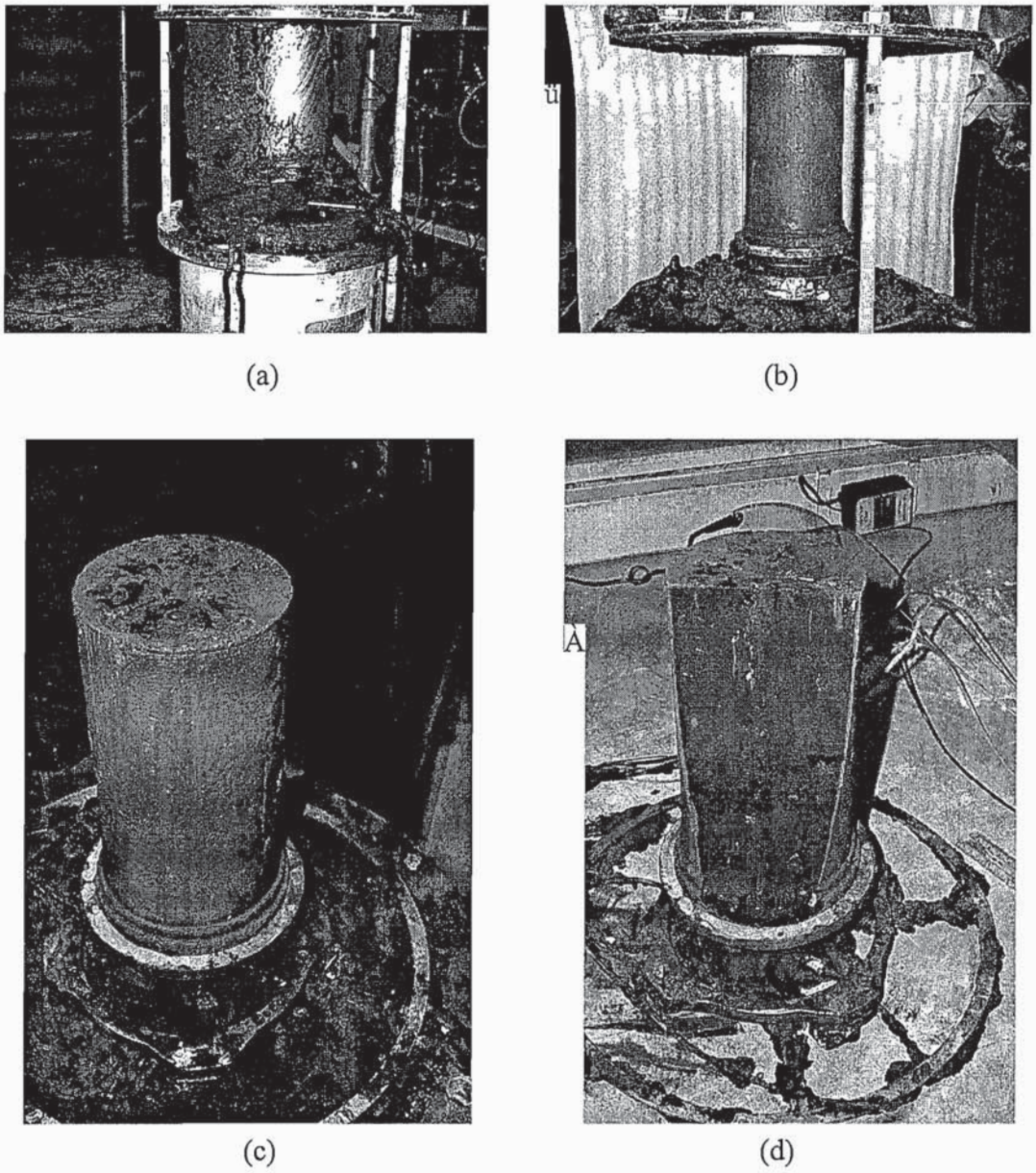

Figure 4.43 Pictures showing the retrieval and quality of the Bay Mud sample after the completion of DFSD tests

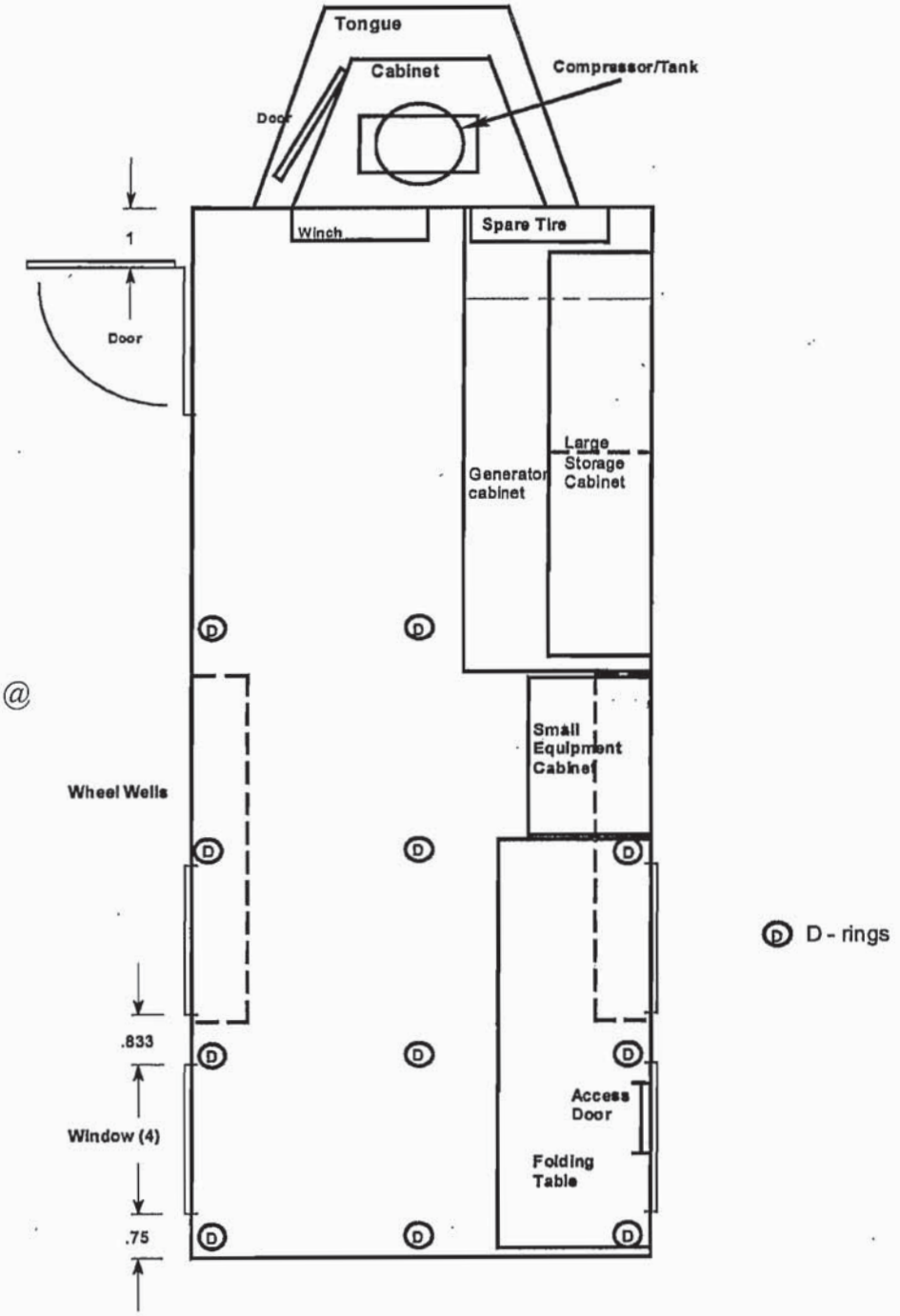

Figure 4 44 The layout and the main mechanical components of DFSD trailer

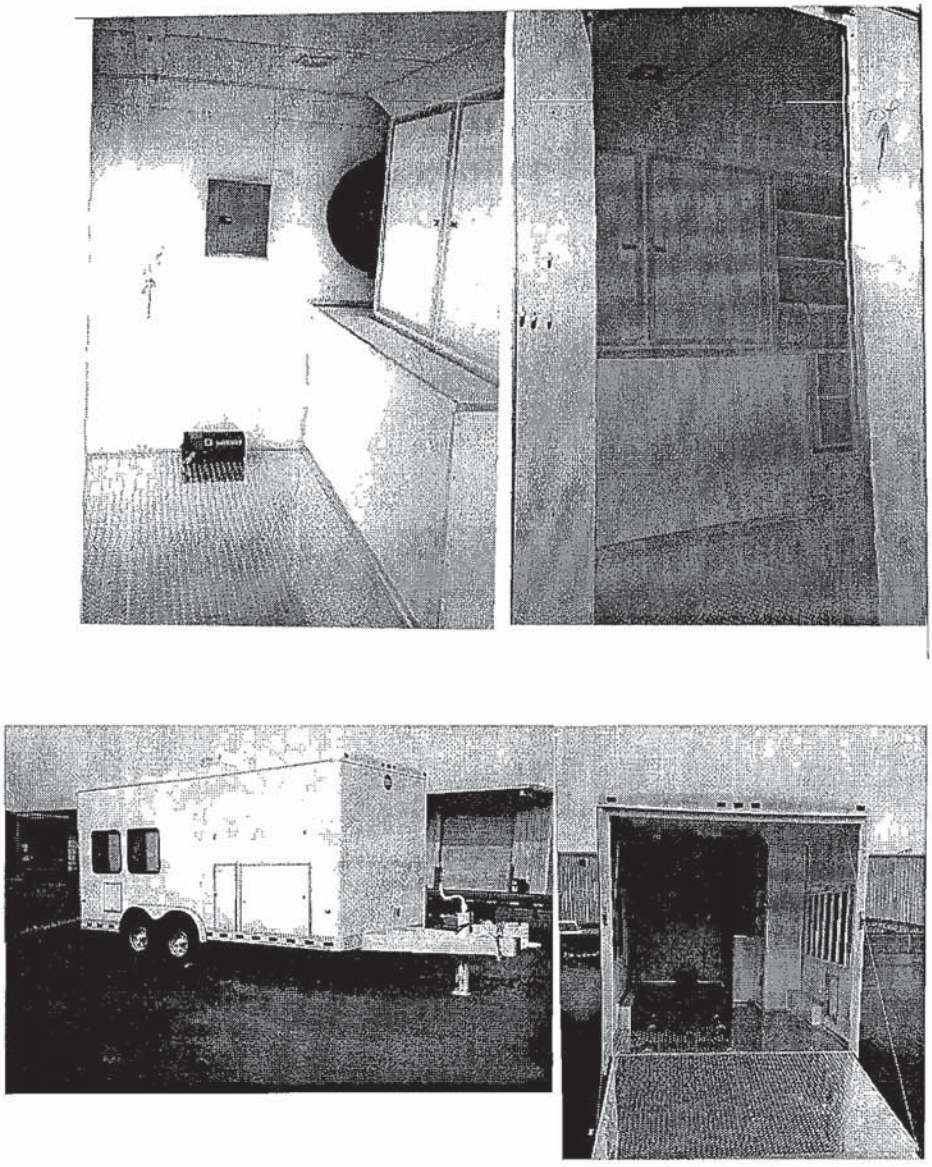

Figure 4.45 Pictures showing the outside and inside of the DFSD trailer

Figure 4.46 DFSD field setup using the trailer and a tripod

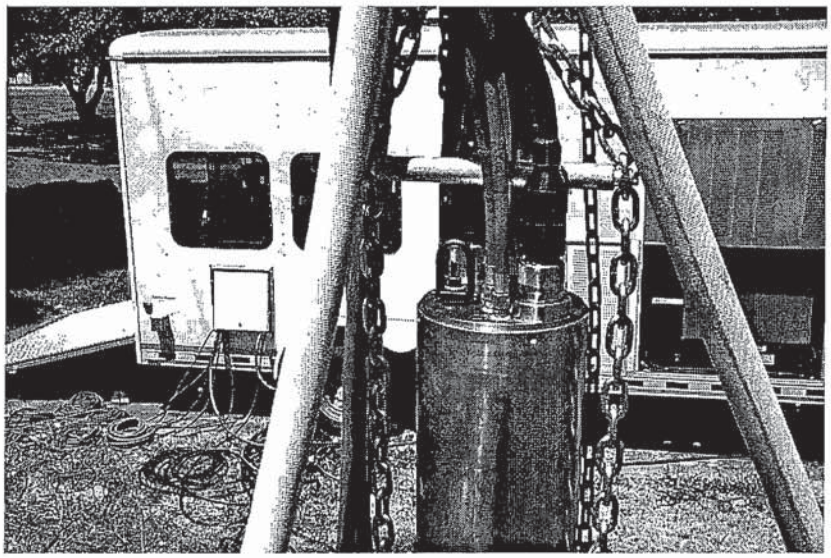

(a)

(b)

Figure 4.47 (a) Umbilical attachments to upper bulkhead of the DFSD (b) DFSD test control from inside the trailer

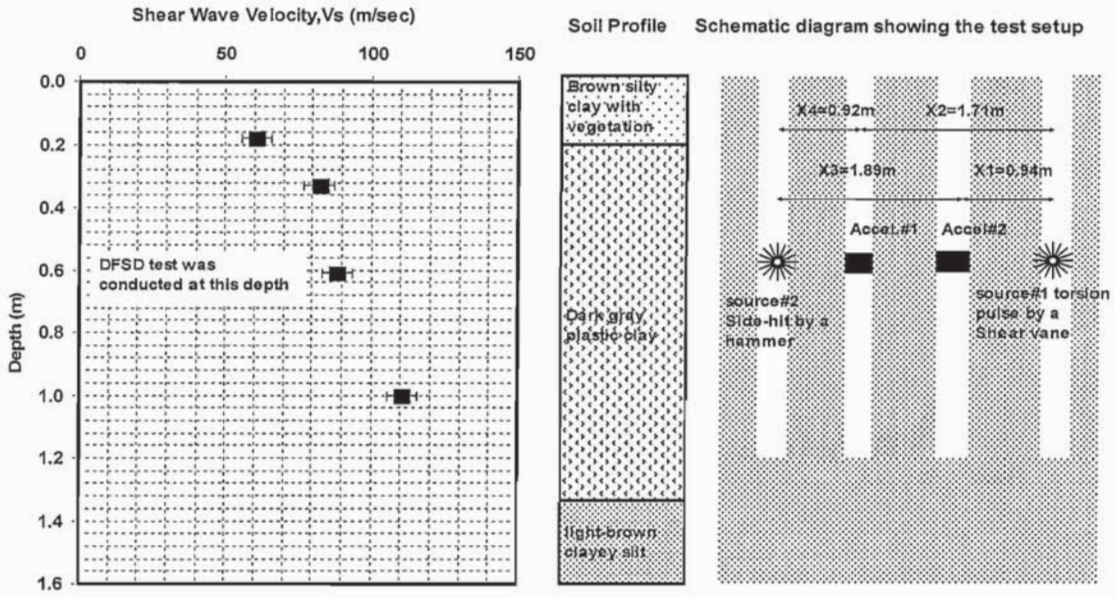

Figure 4.48 Shear wave velocity measurements at Richmond Field Station test site

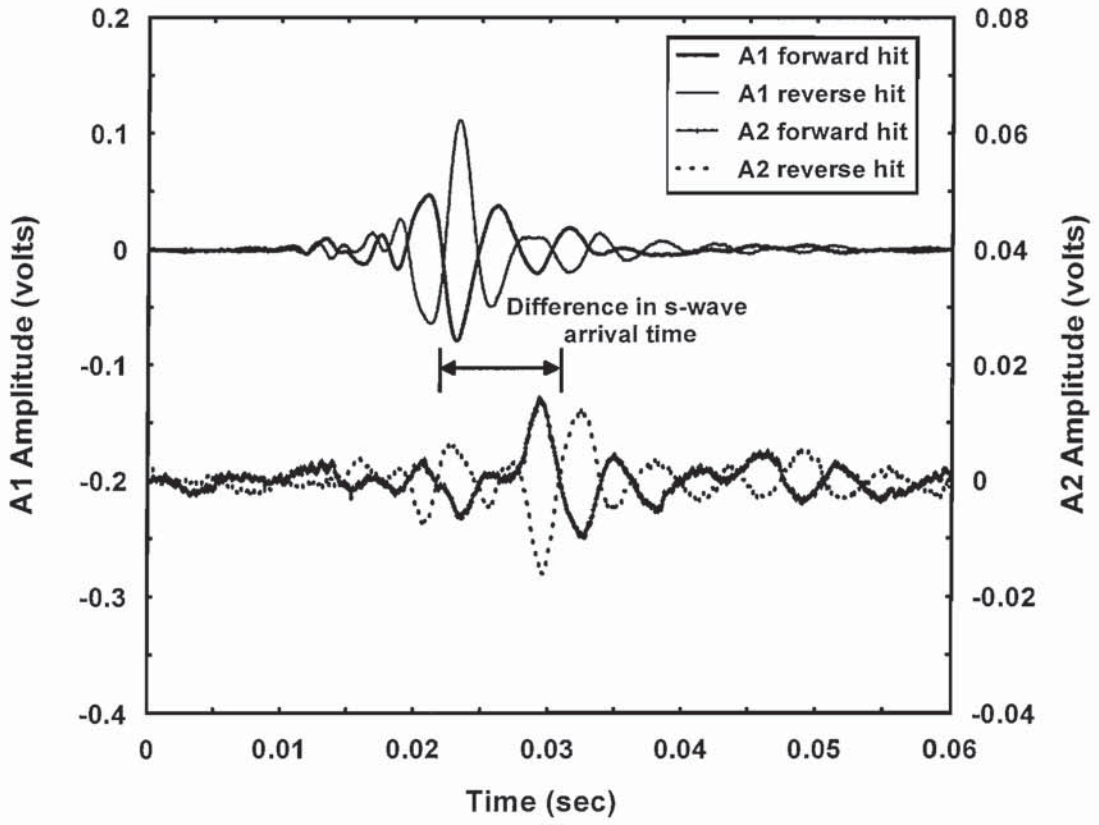

Figure 4.49: Accelerometers' signals as recorded from a cross-hole test at RFS using torsion disturbance as a shear source.

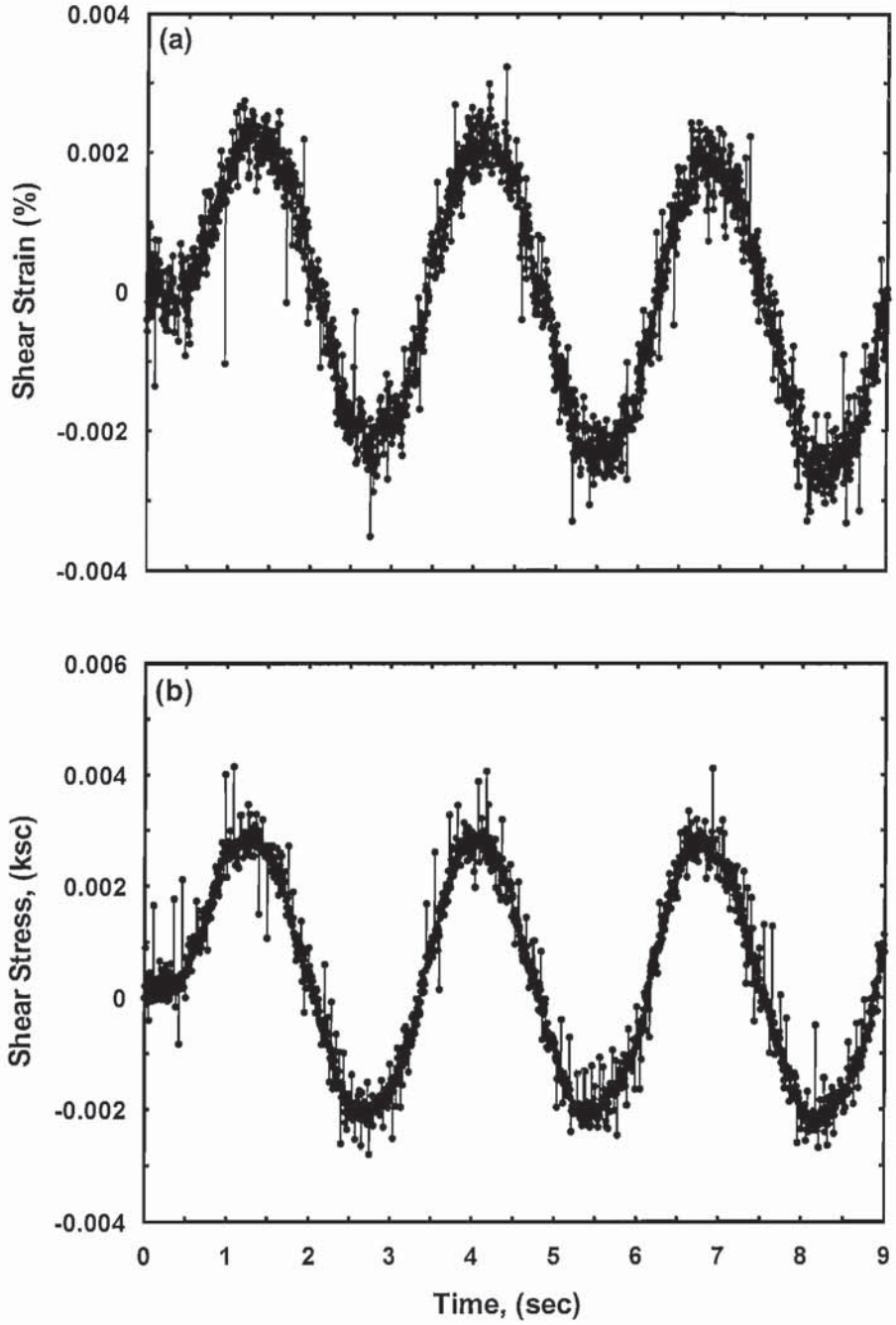

Figure 4.50: As-recorded (a) strain and (b) stress time histories from a small-strain DFSD test at RFS site

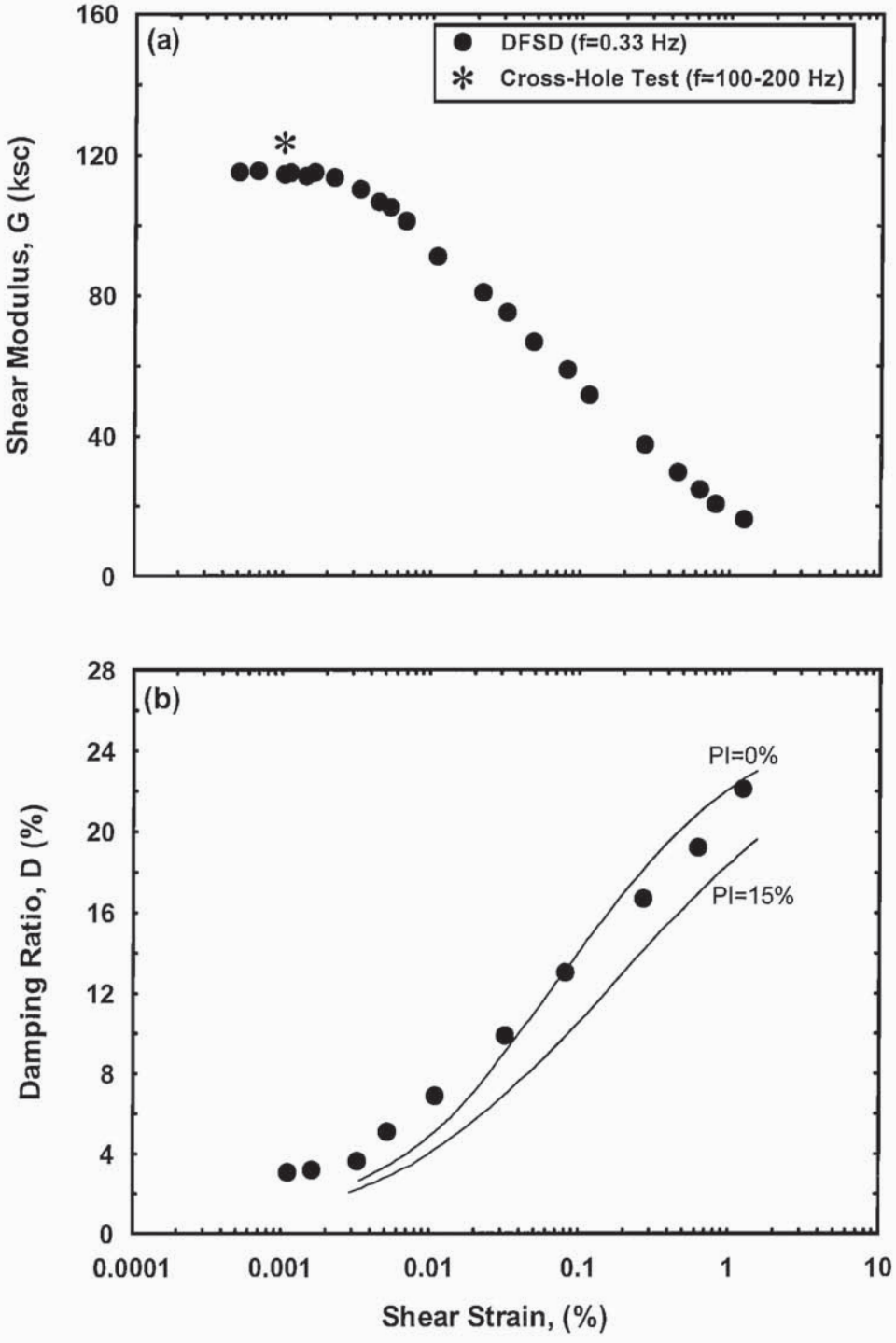

Figure 4.51 Modulus reduction curve and damping curve obtained from DFSD tests at RFS

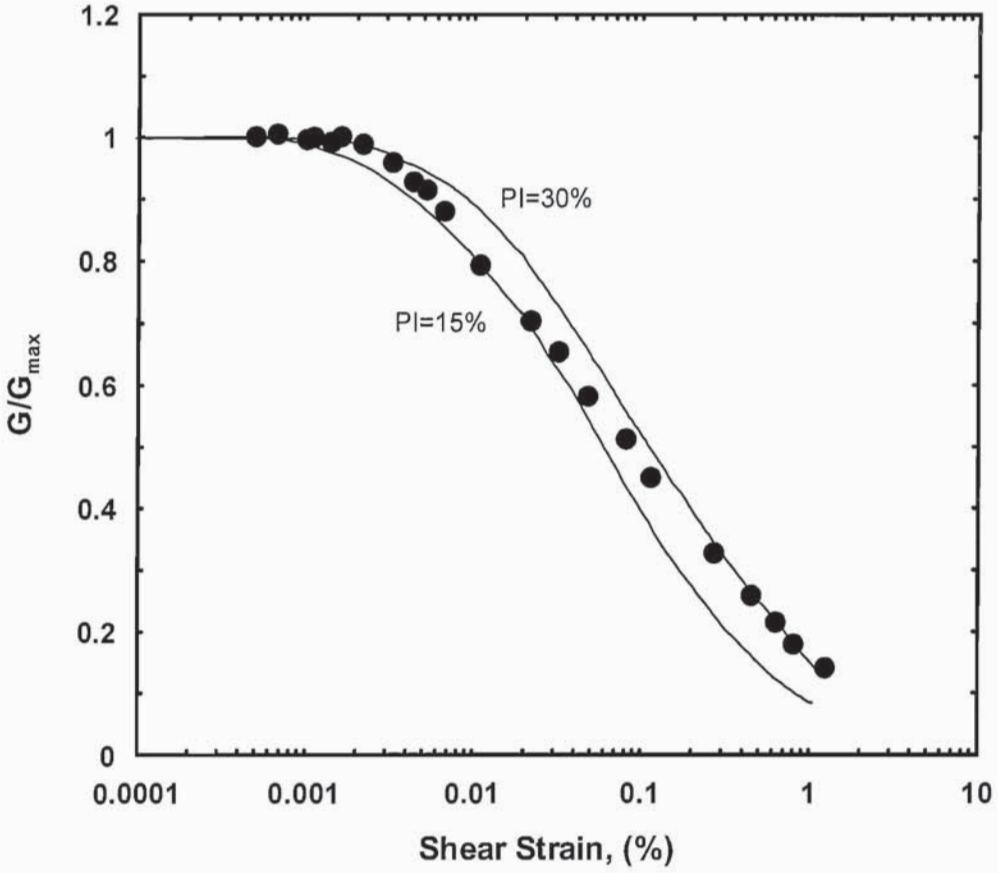

Figure 4.52: Normalized modulus reduction curves obtained from DFSD tests at RFS site at a depth of 4 ft as compared with Vucetic and Dobry (1991) curves.

CHAPTER 5:

Conclusions, and Further Work

The Downhole Freestanding Shear Device (DFSD) is an innovative geotechnical tool for field measurement of the dynamic properties of cohesive soils. The mechanical design and operational concepts of the device allow cyclic torsional shear tests to be performed on a freestanding column of soil which has not been significantly disturbed by the drilling, sampling, or unloading/reloading processes associated with conventional sampling and testing techniques. The device will provide, for the first time, high quality field measurements which will be crucial for a better understanding of the non-linear inelastic behavior of natural soil deposits and sheds more light on the reliability of current laboratory testing methods.

The development of the device was a challenging task with numerous technical obstacles. It required new methods and technologies for in-situ sample creation and remote membrane deployment with minimal mechanical disturbance and stress change. Perhaps the most difficult assignment was the desire to obtain field measurements over a wide strain range from the G_{max} level and up to 1%, a task that has never been achieved before. The DFSD development has been completed and the tool is now fully functional and capable of conducting all the phases of a DFSD test from sample creation to downhole cyclic torsional shear testing. The efforts in the last five years have succeeded in developing the DFSD load module, load application system, air confinement system,

the electronic module, the instrumented membrane and its deployment system, the load and deformation measurement system including the elastomer gauge and the 2-axis load cell for measuring local stress-strain response of the soil, the hardware and software of data acquisition and system control, the hardware for interfacing the downhole tool with its control station at the "surface", schemes for digital and analog signal processing, measures for enhancing signal quality, data interpretation methods, field deployment equipment, tuning and calibration of the different DSFD sensors and actuators, and the integration of the different units and modules for smooth and effective performance.

After its completion, the DFSD was implemented and validated through an elaborate laboratory testing program. First, a benchtop version of the device was developed to test a "calibration" urethane specimen with known properties. The shear modulus and damping ratio measured by the benchtop device were in good agreement with the values reported by independent tests conducted on the same sample at the University of Texas at Austin. In the second phase, the full-scale DFSD was implemented in laboratory tests on reconstituted soils in a setup which simulate field tests. This required the development of the "smart" consolidometer which has the ability to measure the consolidation stress, the pore water pressure inside the soil, and the vertical deformation of the soil block. Later, shear wave velocity measurement capability at the middle of the soil block was also added. All of these measurements can be made during the consolidation process, during the sample carving process, and before and after cyclic testing. This allowed valuable information to be gathered about the level of impact the DFSD has on the soil behavior and to accurately characterize the stress conditions within the soil, which was crucial for tool validation. In these tests soil blocks from different

materials were reconstituted from thick slurries inside the consolidometer. After the completion of consolidation, a special steel casing was mounted on top of the consolidometer to simulate a field borehole and to accommodate a water column.

The full-scale laboratory implementation tests were conducted on reconstituted kaolinite samples as a low-plastic cohesive material and on reconstituted Bear Creek Clay, a moderately plastic material. The results from these tests have indicated a successful performance of the DFSD. All of the tool systems and components functioned properly and no major modifications were needed. The DFSD design and operational concepts which include sample creation, air-confinement, membrane deployment, mid-specimen instrumentation and torsional testing on a freestanding sample were proven achievable. Moreover, these tests were very important to gain experience conducting and controlling the different phases of a DFSD test. The tests have also triggered a comprehensive effort to enhance the quality of the measured signals especially at small strain levels. At the end of this testing phase it was clear that the DFSD would be capable of measuring the correct modulus degradation behavior of soils with different plasticities. Most importantly, modulus and damping measurements at a strain range from 0.0005% to 1% were proven attainable.

With a successful tool performance during the implementation phase, the next logical step was to validate the device by comparing its results with measurements made by high-quality independent laboratory tests conducted on identically prepared samples. The RC/TS device at the University of Texas-Austin and the DSDSS device at the University of California-Los Angeles were part of a class-A validation of the DFSD. The same setup as in the implementation tests was used, adding "parallel" batches of

reconstituted soil blocks that were used for Shelby tube sampling for the independent tests. The smart consolidometer was effectively used to evaluate the impact that a conventional tube sampling process has on the properties of the sampled soil versus the DFSD sample creation process. Moreover, the smart consolidometer was also used to provide a much needed "correct" reference of G_{max} through shear wave velocity measurements. Batches of kaolinite and San Francisco Bay Mud were used as two materials with different modulus degradation behavior and sensitivity to sampling. With mostly silt-size particles and low plasticity, kaolinite represents an extreme case for the kind of materials the DFSD is designed to test. For each soil, two types of DFSD tests were conducted; (a) immediately after the sample creation process, and (b) after reconsolidating the sample to a higher stress. The tests would, therefore, show the effect of the DFSD sampling method and the accuracy of DFSD measurements of shear modulus and damping ratio at different strain levels.

The data from the validation tests have shown that the DFSD sample creation process does not have a significant impact on the dynamic properties of the sampled soil. Most of the induced deformations and stress changes were elastic, as shown by shear wave velocity measurement made before, during, and after the DFSD sample carving process and by the induced changes in pore water pressure. The DFSD sampling method has proven to be much less disruptive than the conventional Shelby tube sampling. For comparison, tube sampling has caused about 52% reduction in the G_{max} value of reconstituted Bay Mud as a result of unloading and tube insertion while no detectable change in G_{max} level has been noticed after DFSD sample creation process. For reconstituted kaolinite, the measured induced pore water pressure was much higher

during tube sampling than DFSD sampling. These findings were also supported by the general agreement between shear modulus and damping measurements made by the DFSD immediately following sample carving and measurements made by the independent tests. In those tests, the DFSD specimen was not reconsolidated after sampling as was the case with the other independent tests. This also indicates that whatever effect the DSFD sampling process has (on the dynamic properties of the soil sample) it was not significant. Moreover, measurements from DFSD tests made after consolidating the sample to stresses higher than the initial consolidation stresses were also in good agreement with the measurements made by the independent tests. It should be noted, however, that shear modulus measurements from the DSDSS device were always significantly smaller than from other devices. Nevertheless, the normalized modulus reduction curves and damping curves from this device were in good agreement with the other devices. In summary, the laboratory validation program has proven the following:

- The DFSD design and operational concepts have been implemented successfully.
- The DFSD is capable of fairly accurate measurements of shear modulus and damping ratio of the soil over a wide shear strain range from 0.0005% to 1%.
- The DFSD can accurately predict the modulus degradation behavior of soils with different plasticities.
- The DFSD can accurately capture the effect of effective stress level and stress history on the dynamic soil properties
- The DFSD sampling method does not have a significant impact on the properties of the sampled soil and is therefore superior to other conventional sampling methods.
- The DFSD is capable of in-situ consolidation of a downhole column of soil to study the effects of different stress paths on the dynamic properties of natural soils, though this may require substantial time downhole

After a successful laboratory validation of the DFSD, efforts were directed toward developing the necessary equipment for field transportation and deployment. All the DFSD electrical and pneumatic connections, cables, and hoses were upgraded to heavy-duty water-proof alternatives. A total umbilical length of up to 300 ft was made available to the DFSD in 150-ft sections collected on reels. A special trailer was designed and custom-made to transport the tool to the testing site and provide a control station. The trailer is equipped with a "quiet" diesel generator for clean power supply, an air compressor and a pressure control panel with regulators, a ground winch for moving the tool into and out of the trailer, floor mounting rings for securing the tool during transportation, cabinets and tables for storage and usage during tool operations and other accessories.

With the DFSD ready for field deployment, a site at Richmond Field Station was chosen to conduct preliminary DFSD field testing along with shear wave velocity measurements using the cross-hole method. All the "new" field equipment including the trailer and its generator and air compressor along with the new umbilical were used. An 8-inch hand auger was used to drill a cased hole up to 6 ft deep. A tripod and a winch system were used for lifting the tool. The quality of DFSD field measurements were as good as those obtained from laboratory tests. Shear modulus and damping measurements were made over the full strain range. The G_{max} value predicted by the tool was reasonable compared to the one interpreted from shear wave velocity measurements given the large differences in loading frequency between the two tests. Overall, the tests have indicated a

successful field application of the DFSD and its supporting equipment, and provided another proof of the high quality measurements the tool is capable of recording.

Finally, with the work done so far, the next step for the DFSD project will be a "full" field testing program to further validate and examine the performance of the tool under conventional drilling conditions. This testing would also achieve the original objective for initiating this project, i.e. to better understand the dynamic behavior of the soil in the field and the effects that sampling disturbance has on laboratory test results. In addition, despite the fact that the tool development has been completed, there is still room for improvement. This may include digitizing the signals downhole inside the DEM to further enhance their quality, adding pore water pressure measurement capability to the downhole sample, and with some modifications, make the tool capable of conducting cyclic triaxial as well as cyclic torsional shear tests.

APPENDIX A

DFSD PARTS LIST AND DRAWINGS

Table A.1 A list of DFSD parts

Part Number	Part Name	Qty	Material	Notes
100 Outer Housing and Support Equipment				
100	Outer Housing	1	304SS	
101	Connector Block	1	304SS	
102	Upper Bulkhead	1	304SS	
150	Shock Absorber Piston	1	Steel	
151	Shock Absorber Bearing Plates	2	Steel	
152	Shock Absorber Tie Rods	4	Steel	
160	6" ID Wiper Seal	1	Buna (Parker SH959-53)	
161	1/16" NPT Grease Fittings and Plugs	2	Stainless Steel	For Upper and Lower Outer Cutter Seals
162	1/8" by 6" O-Ring	1	Buna	For Outer Housing on Bottom
163	1/8" by 6.5" O-Ring	1	Buna	For Cover Shell on Top
164	1/4" x 1" Screw	8	Stainless Steel	For Outer Housing
165	1/4"-20 x ½" Allen Head Counter-sink Screws	8	Stainless Steel	For Mounting Frame
166	#8-32 x 3/8" Allen Head Counter-sink Screws	8	Stainless Steel	For Cover Shell

200 Cutter System				
201	Cutter Tube	1	304SS	
202	Threaded Reaction Nut	1	Porous Bronze	
203	Threaded Center Rod	1	304 SS	
204	Threaded Rod Flange Bushings	2	Porous Bronze	
205	Shear Key	1	Porous Bronze	
210	Internal Ring Gear	1	Porous Bronze	
211	Gear Support Ring	1	304SS	
220	Thrust Bearing-Upper	1	Porous Bronze	
221	Thrust Bearing-Lower	1	304SS	
222	Bearing Plate	1	304SS	Top of Cutter Tube
223	Shear Key	1	Porous Bronze	
231	Cutter Motors Support Bracket	1	304SS	
232	Shear Key	1	Porous Bronze	
233	Motor Pull Bracket	4	Porous Bronze	
240	Primary Cutter Ring	1	304SS	
241	Primary Cutter Space Ring	1	Aluminum	
242	Primary Cutter Blades	4	304SS	
243	Sample Retrieval Blades	4	304SS	
250	Threaded rod seal	1	Aluminum	Top of connector block
251	2" O-ring	1	Buna	Threaded rod seal (outer)
252	1 ½" O-ring	1	Buna	Threaded rod seal (inner)
253	Upper Bearing	1	Delrin	Press fit
254	Split Lower Bearing	1	Delrin	
255	1/8" by 6" Quad-Ring	2	Buna	
256	#8-32 x 1.5" Screws	4	Stainless Steel	For threaded reaction nut

257	#8-32 x 1.25" Screws	4	Stainless Steel	For gear to cutter tube
258	Bolt heads	4	Stainless Steel	Cutter Position Sensor
259	1/16" NPT Grease Fitting and Plug - Lower Cutter/Sampler Seal	1	Stainless Steel	Lower Cutter/ Sampler Seal
260	¼"-20 x 1" Screws	4	Stainless Steel	For Upper
261	#8-32 x 1" Screws	4	Stainless Steel	For Lower
262	#8-32 x 0.5" Screws	2	Stainless Steel	For Keys
263	#8-32 x 1 ¼" Screws	4	Stainless Steel	Ring to tube through space ring
265	#8-32 x 3/8" Screws	12	Stainless Steel	Teeth to Ring
266	Screws	4	Stainless Steel	Slicers to Ring
267	Cutter-Drive Motors	4	Mf Part No. M102M390	(Globe Motors, Dayton, OH)
268	Pinion Gears	4	Hardened steel	
269	#8-32 x ¾" Screws	16	Stainless Steel	Motors to Bracket
272	#-32 x 3/8" Screws	4	Stainless Steel	Keys to Bracket
274	Pull Block Spacers	4	Aluminum	
275	#8-32 x ¾" Screws	12	Bronze	To Motor-Pull Blocks
300 Sampling System				
301	Sampler Tube	1	304SS	
302	Sample Cutter Space Ring	1	Aluminum	
303	Sample Cutter	1	Aluminum	"Cookie Cutter"
310	Upper Bearing	1	Delrin Press-fit	
311	Split Lower Bearing	1	Delrin	
312	1/8" by 5.25" Quad-Ring	2	Buna	
313	1/16" NPT Grease Fitting	1	Stainless Steel	Upper Cutter/ Sampler Seal

314	#8-32 x 1" Screws	2	Stainless Steel	Through cookie cutter and lower membrane seal ring
315	#8-32 x 5/8" Screws	2	Stainless Steel	Through lower membrane seal ring
316	Lower Membrane Retaining Ring	1	304SS	Inserts inside membrane
317	4" O-ring	1	Buna	Holds membrane to retaining ring
400 Loading System				
401	Load Module Frame	1	Aluminum	2 pieces
402a,b,&c	Load Frame Shelves	1	Aluminum	3 pieces
406	Load Rod Alignment Ring	1	HDPE	
410	Top Cap	1	Aluminum	Part of membrane retaining system
411	Membrane Retaining Ring	1	Aluminum	
413	Two Axis Load Cell	2	7075 Aluminum	
421	Spline Shaft	1	Hardened Steel	
430	4" Diameter, 24" Long Membrane	1	Latex Rubber	
431	O-ring	1	Buna	Seals membrane to top cap
432	NPT fitting	1	Brass	
433	¼"-20 x 1 ¼" Screws	4	Stainless Steel	Top cap to upper membrane seal ring
434	Wire pot	1		To measure load rod vertical displacement
435	Load module protective shell	1	304SS	Provides water resistant seal around load module
436	½"-13 x 1 ½" Bolt	1		To Load Shaft
437	0.9" OD x 0.5" ID Washer	1		
438	Load Shaft	1	304SS	Hollow
439	Lower DEM Retaining Collar	1	Aluminum	
440	Upper DEM Retaining Collar	1	Aluminum	

441	Upper DEM Clamp	1	Aluminum	
442	Upper DEM Clamp Screw	1		
443	Spline Nut	1	304SS	
444	Adaptor Plate	1	304SS	Spline Nut to Rotor
445	523 in-lb (peak) Servo Motor - Parker Motion & Controls Compumotor Division Parker Hannifin Corporation	1	Dynaserv DR-1060B	
600 Laboratory Consolidation System				
601	Consolidometer	3	Stainless Steel	For laboratory consolidation of samples
602	Casing Base	1	Steel	
603	Casing Extension	1	Steel	
604	Consolidometer Bearing Plates	3	Stainless Steel	
605	Consolidometer Load Cell Bearing Plates	4	Stainless Steel	
606	Porous Stone Frame for Consolidometer	3	Stainless Steel	
610	Consolidometer Sampling Alignment Template	1	Wood	

Part 100 Outer Housing

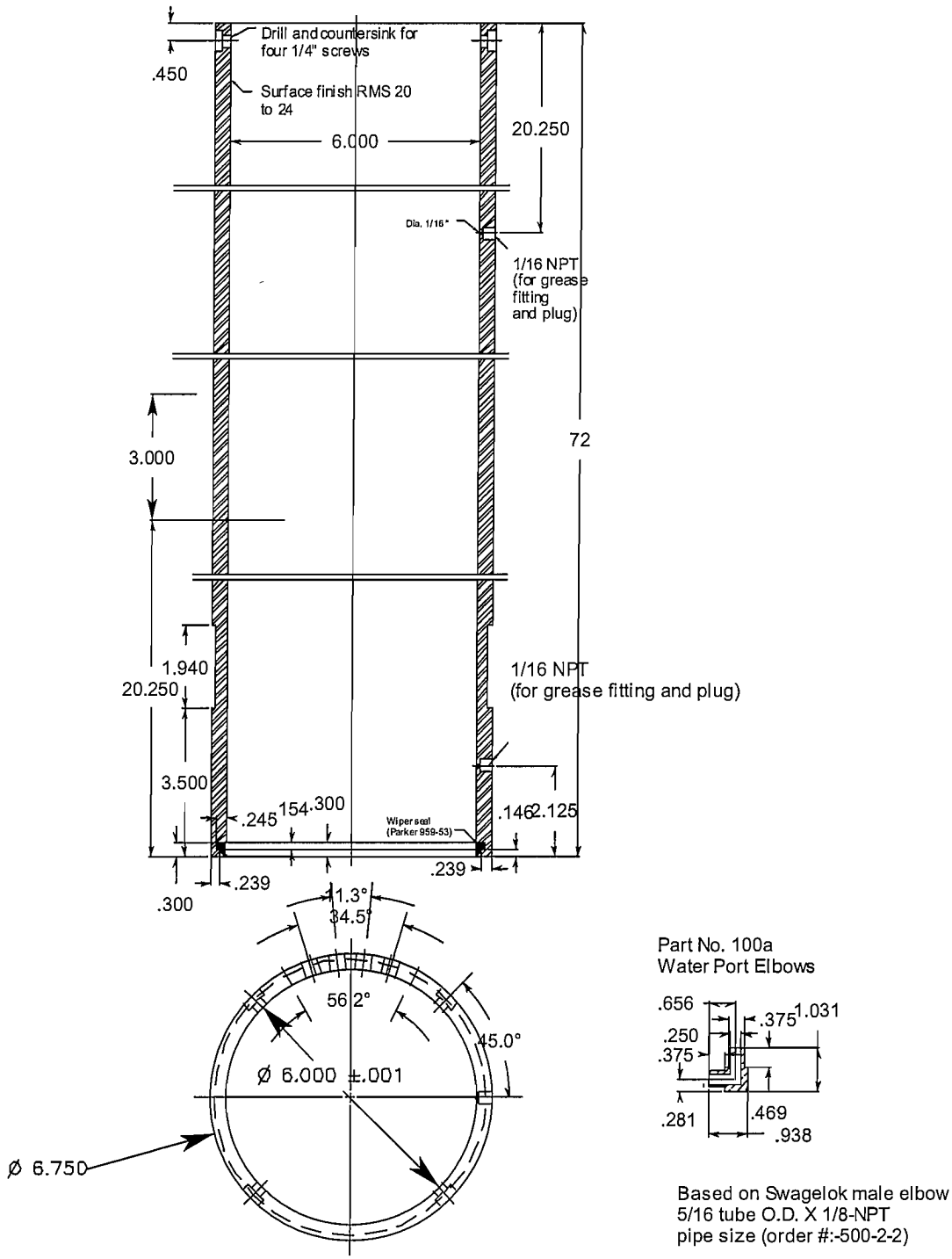

Figure A.1 Cutter module's outer housing

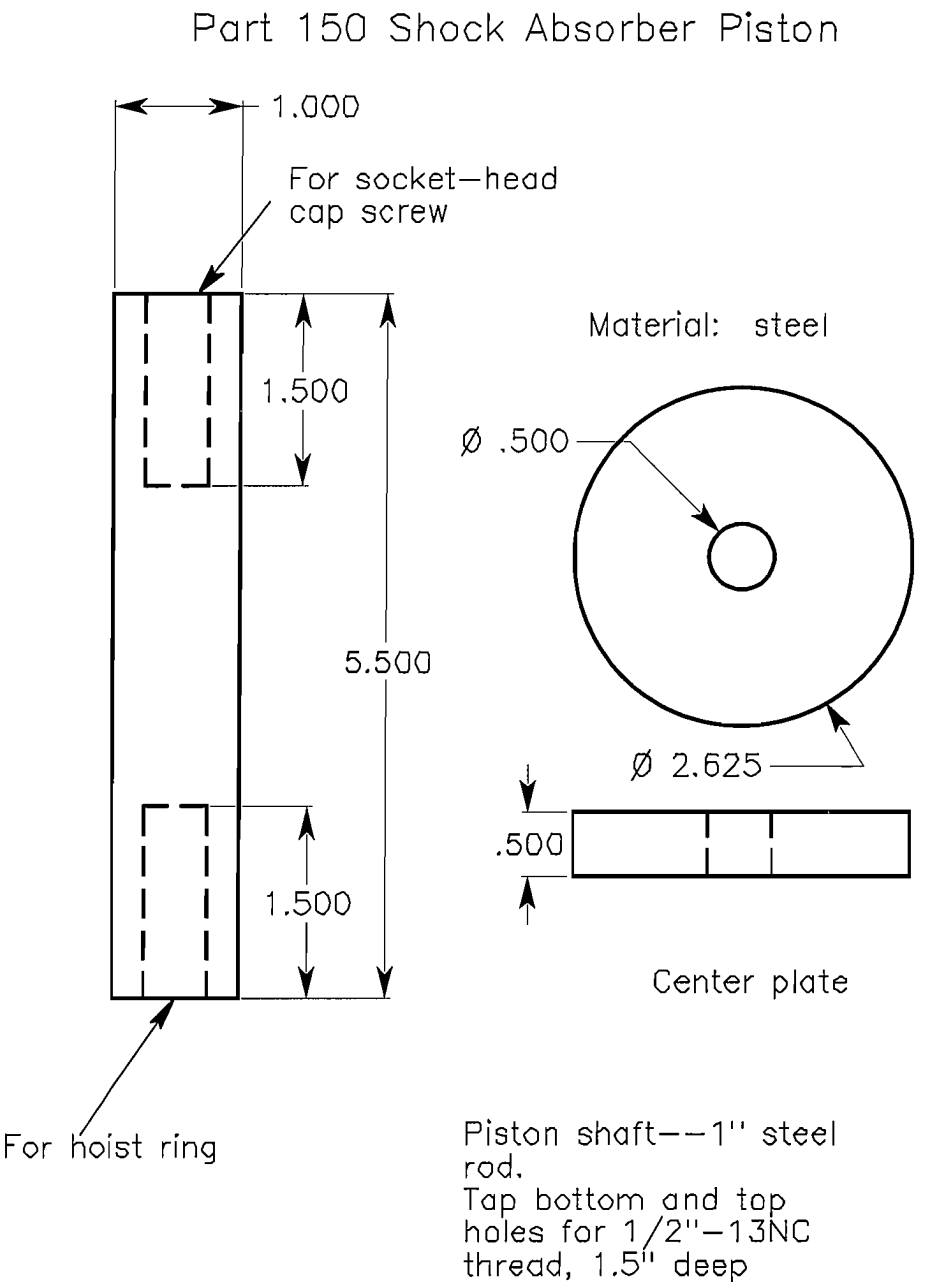

Figure A.2 Design details of the shock absorber piston

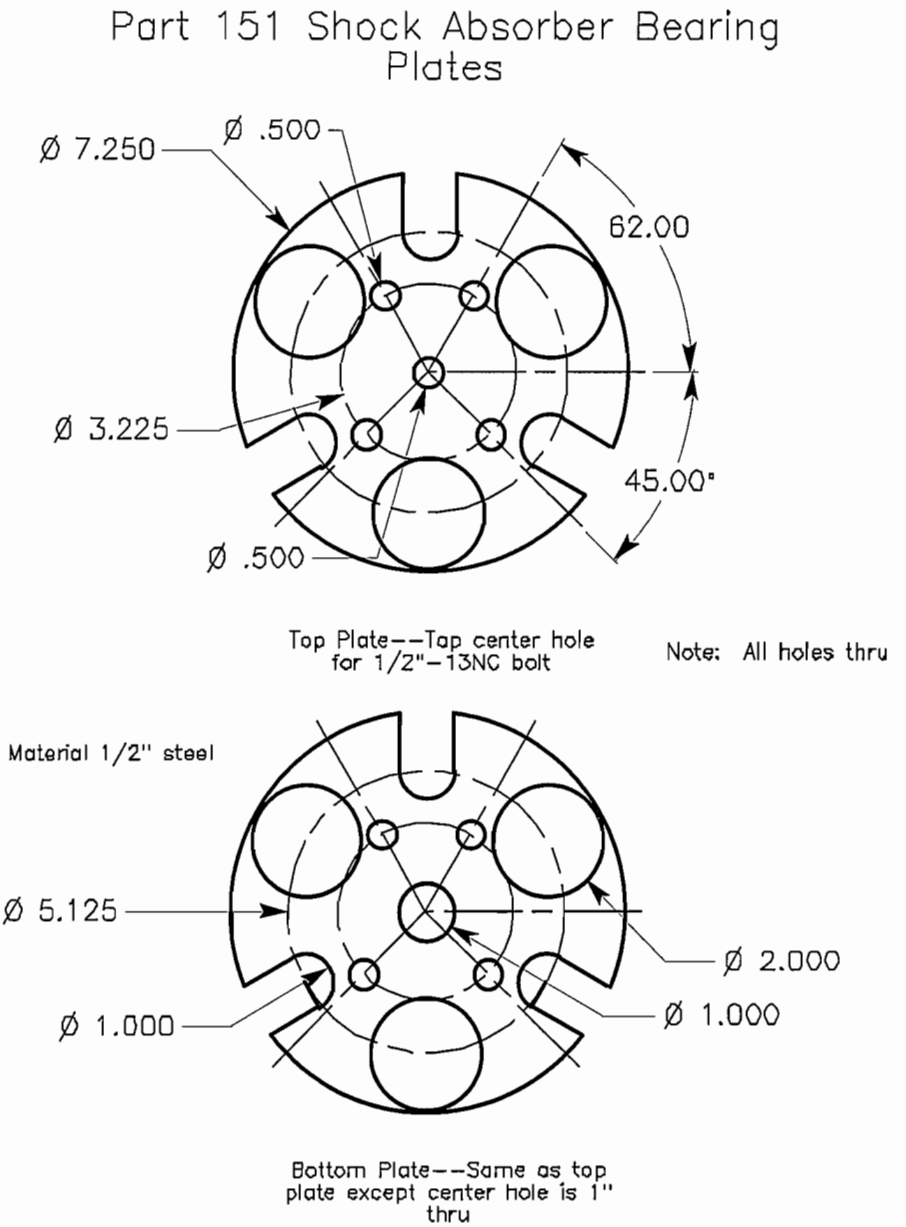

Figure A.3 Shock absorber bearing plates

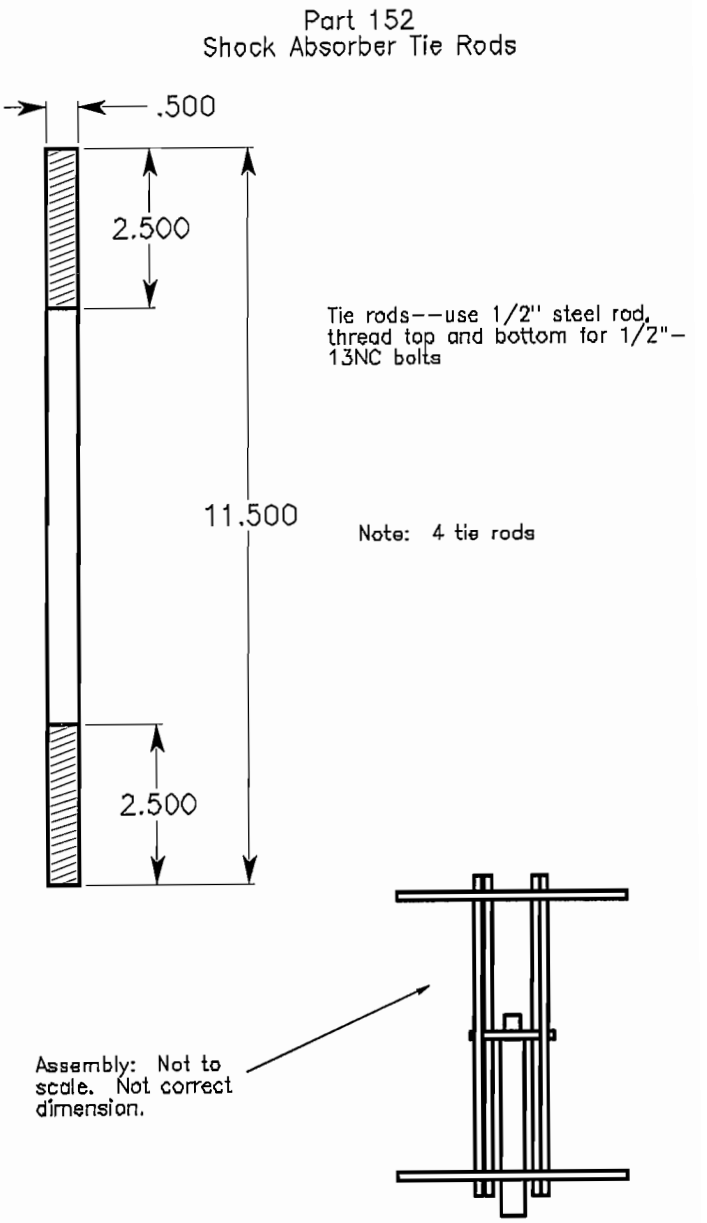

Figure A.4 Shock absorber tie rods

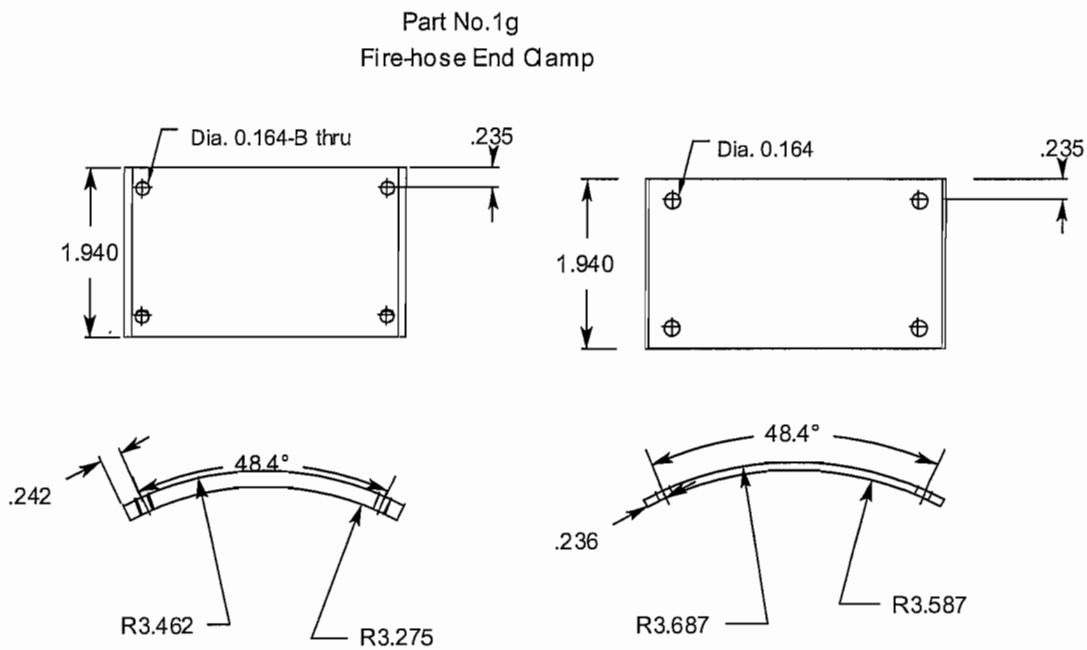

Figure A.5 Fire house end clamp

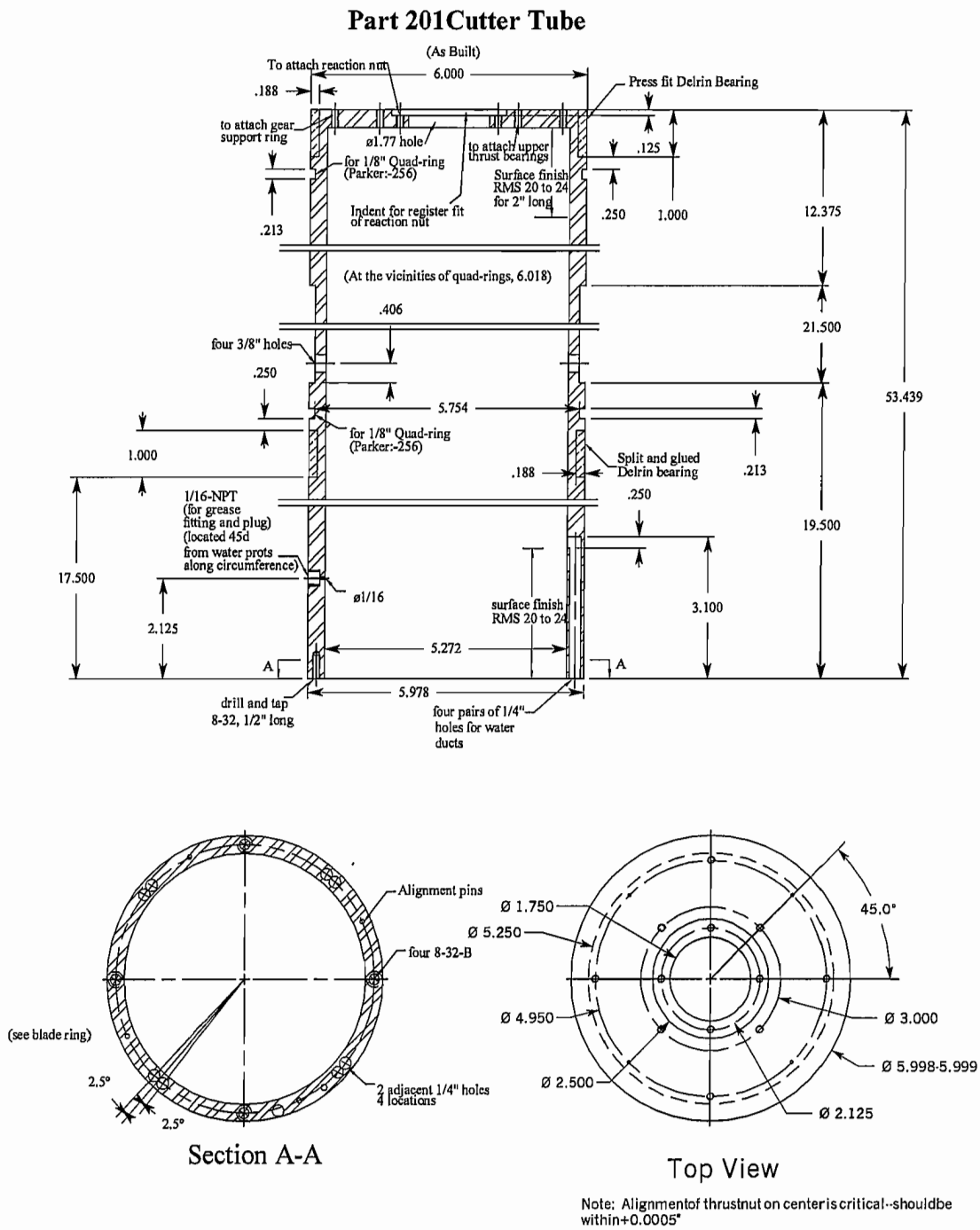

Figure A.6 Design details of the cutter tube

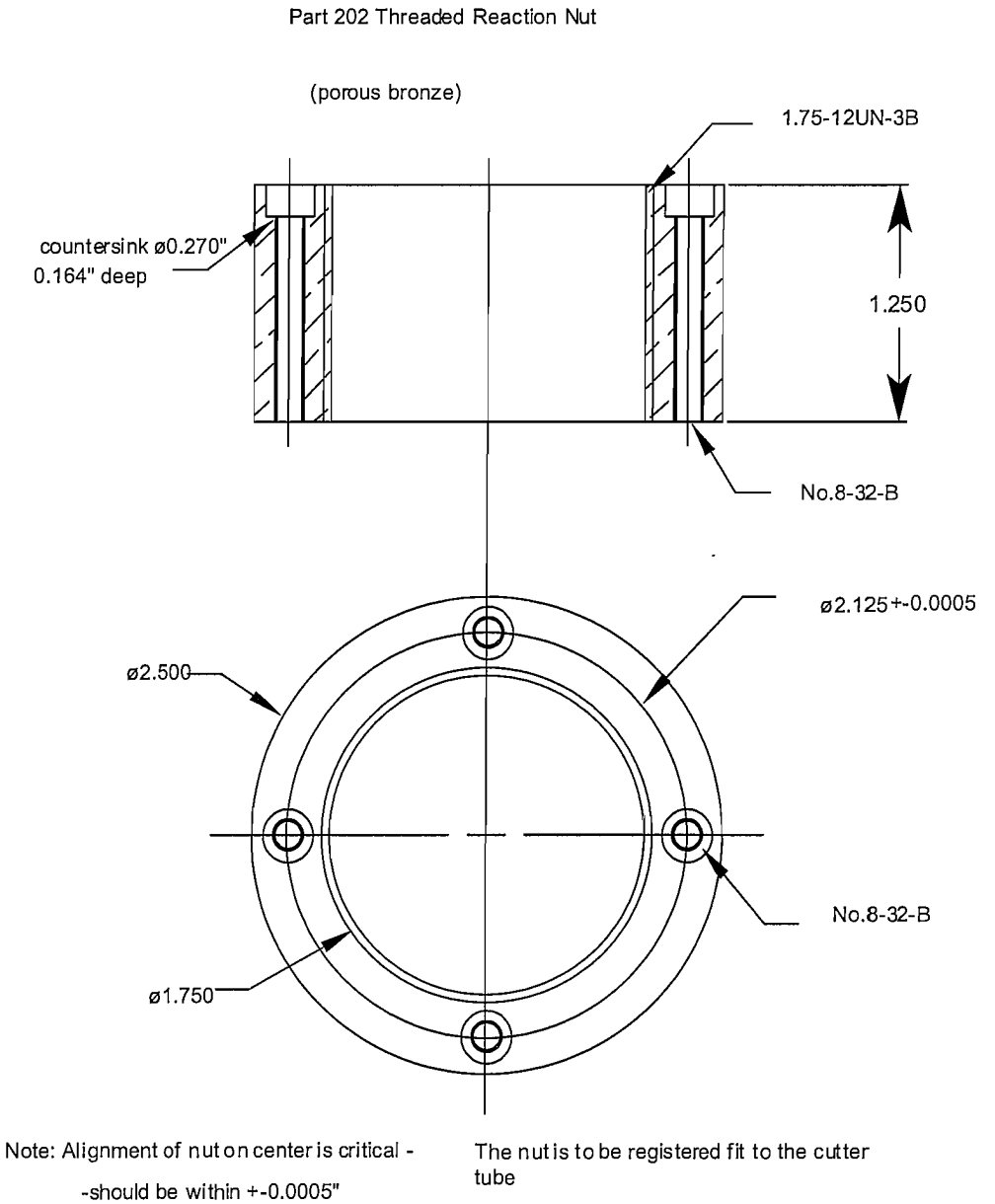

Figure A.7 Threaded reaction nut of the cutter-motor drive system

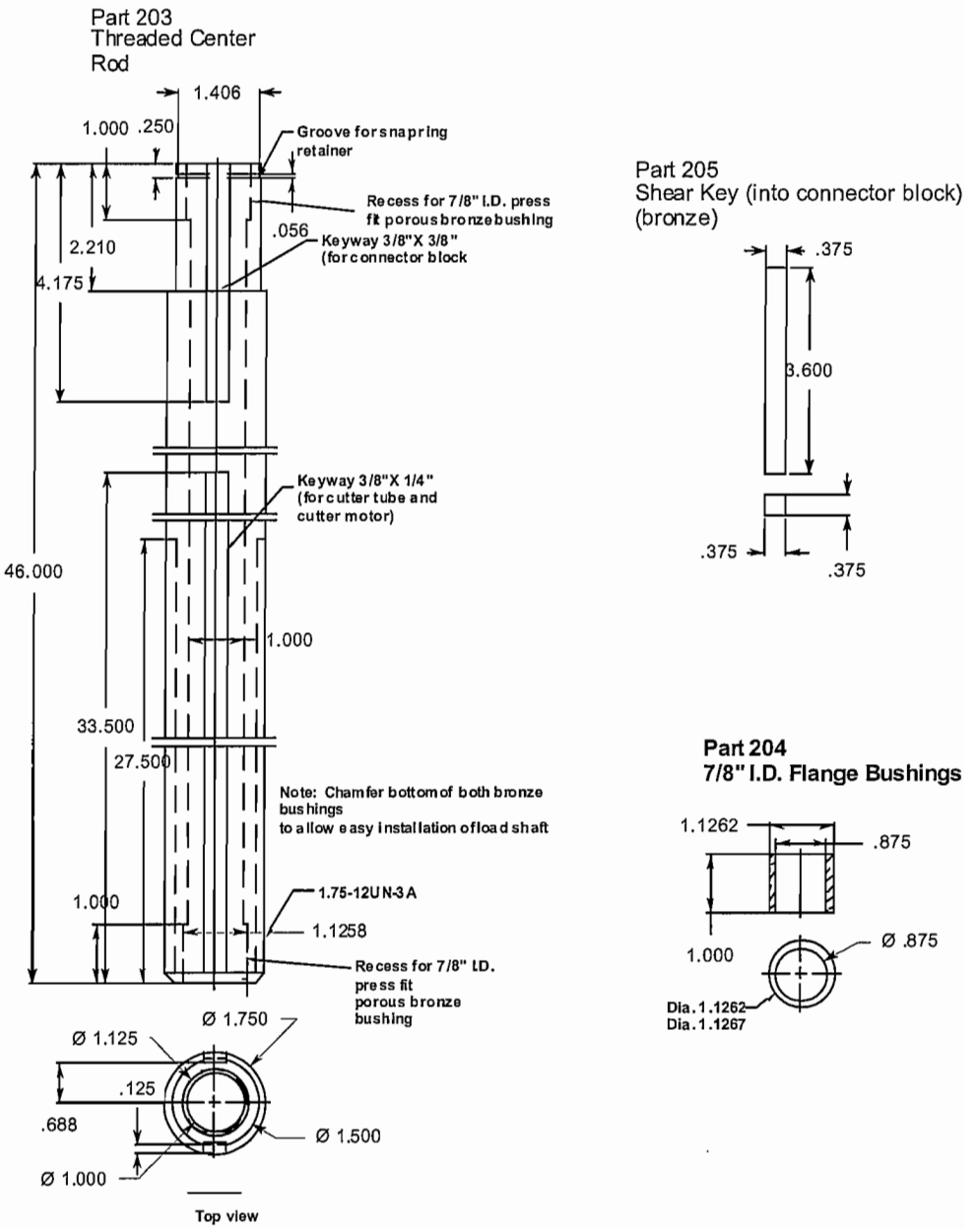

Figure A.8 Threaded center and its shear keys

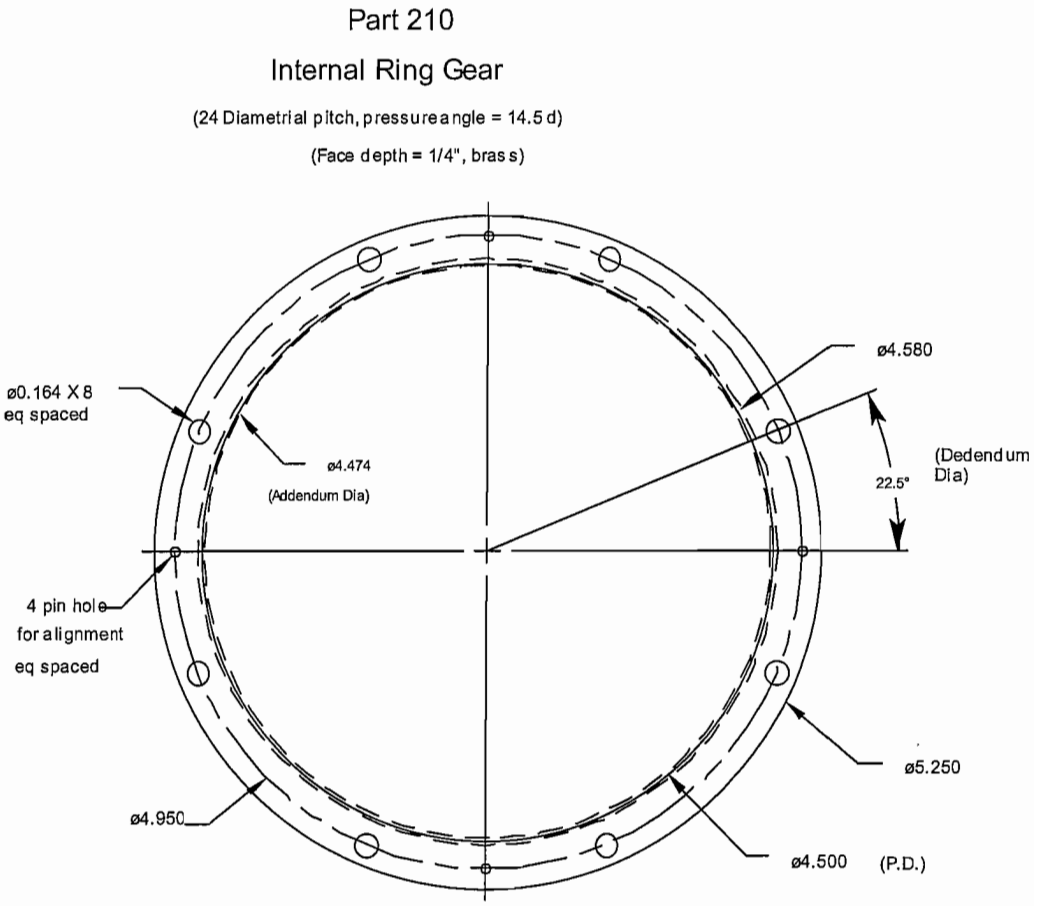

Figure A.9 Internal ring gear of the cutter-motor drive system

Part No. 211

Gear-Support Ring

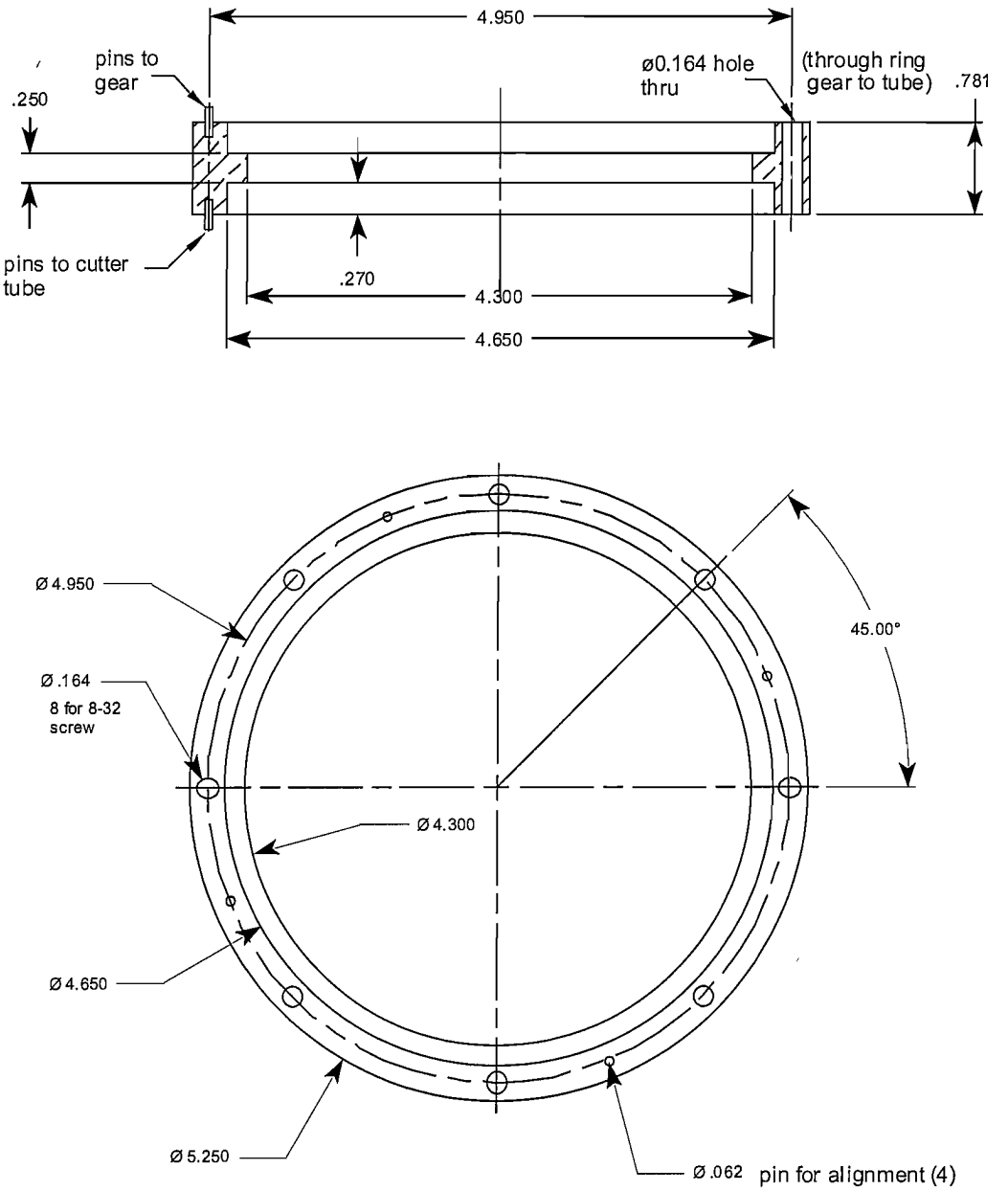

Figure A.10 Gear-support ring of the cutter-motor drive system

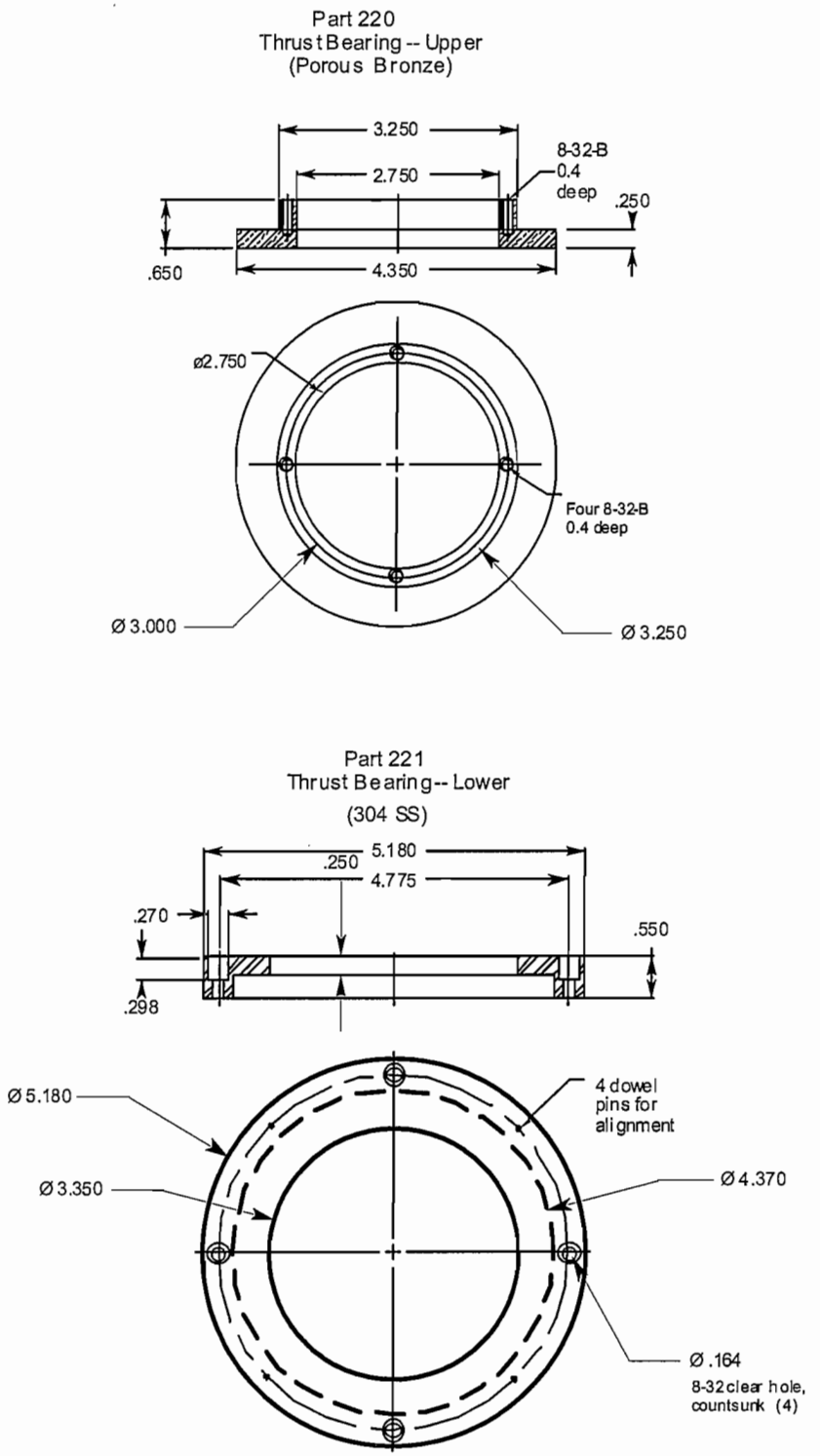

Figure A.11 Upper and lower thrust bearing rings of the cutter-motor drive system

Part 222
Bearing Plate (top of Cutter Tube)

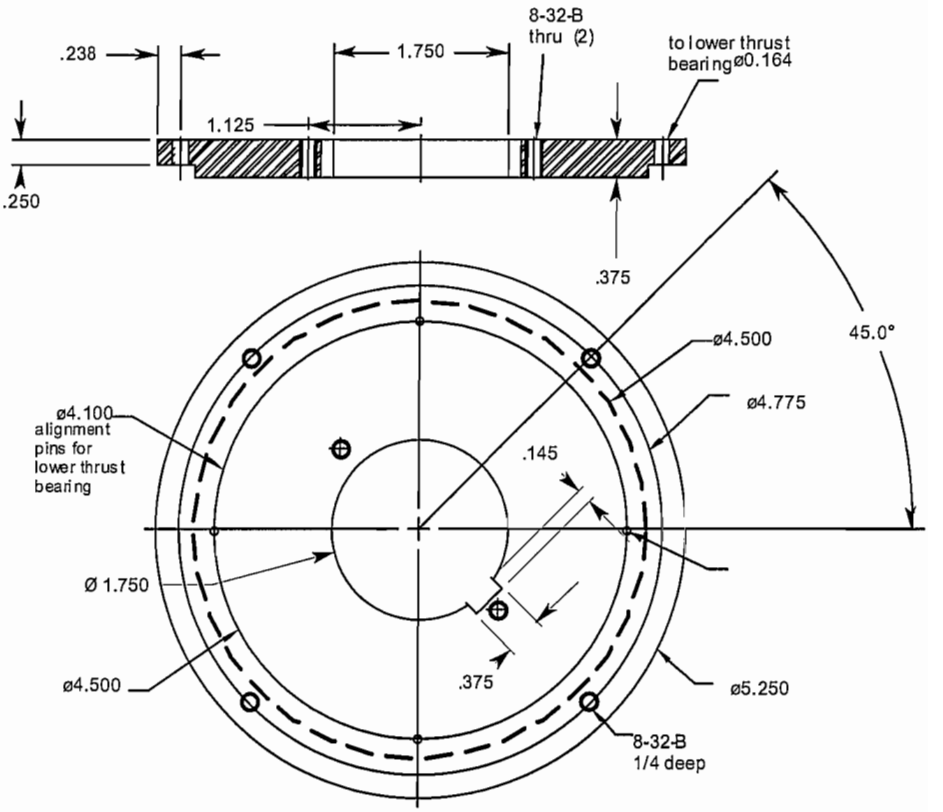

Part 223
Shear Key
(Porous Bronze)

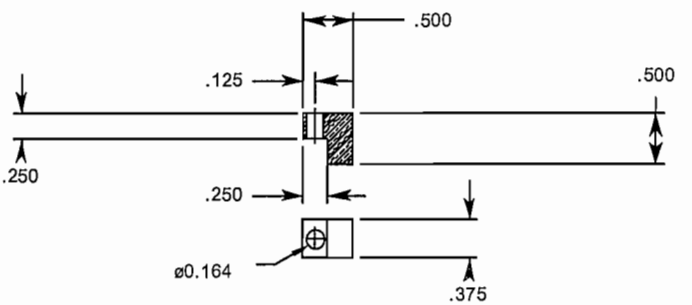

Figure A.12 Cutter tube top bearing plate and its shear key

Part 231
Cutter Motors Support Bracket

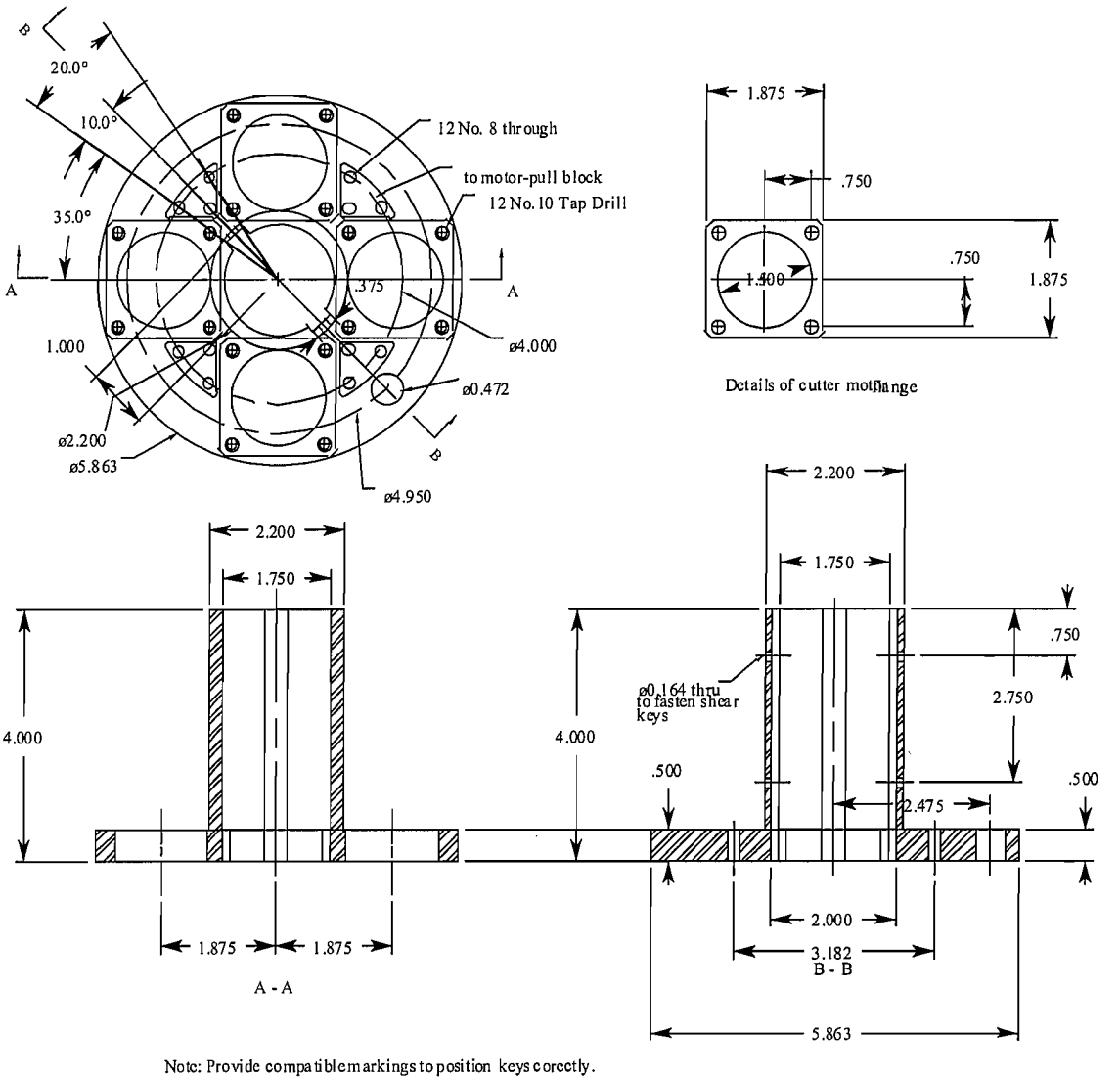

Note: Provide compatible markings to position keys correctly.

Figure A.13 Cutter motor support brackets

Part 232
Shear Key for Motor Support Bracket

(Porous Bronze)

Note: Provide compatible markings to position keys corectly.

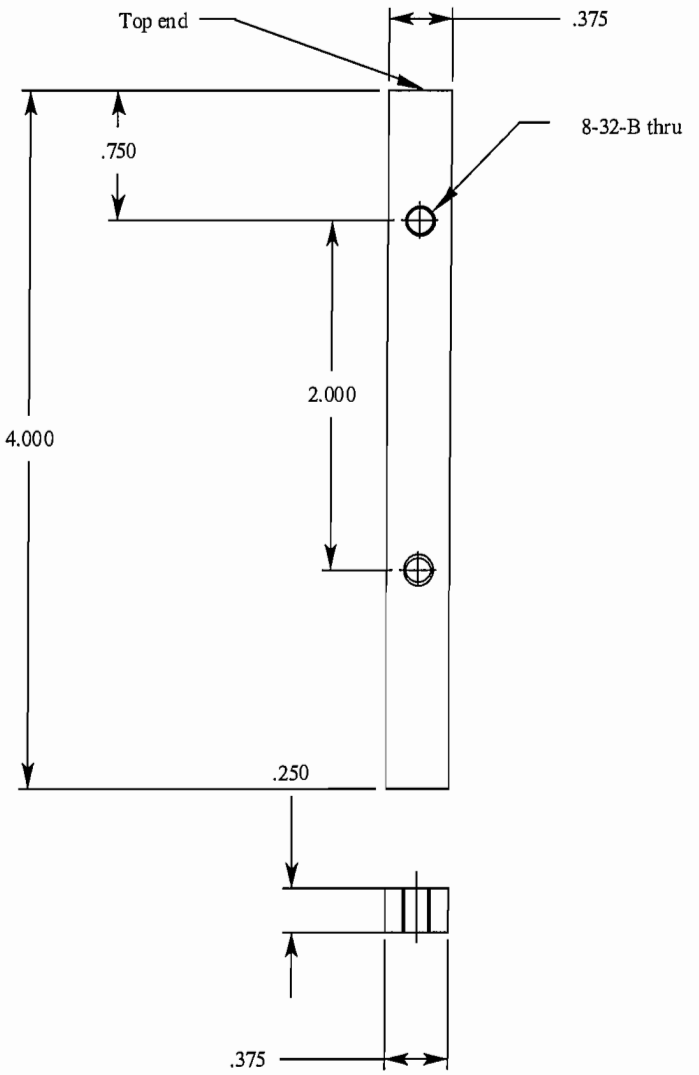

Figure A.14 Motor support bracket's shear key

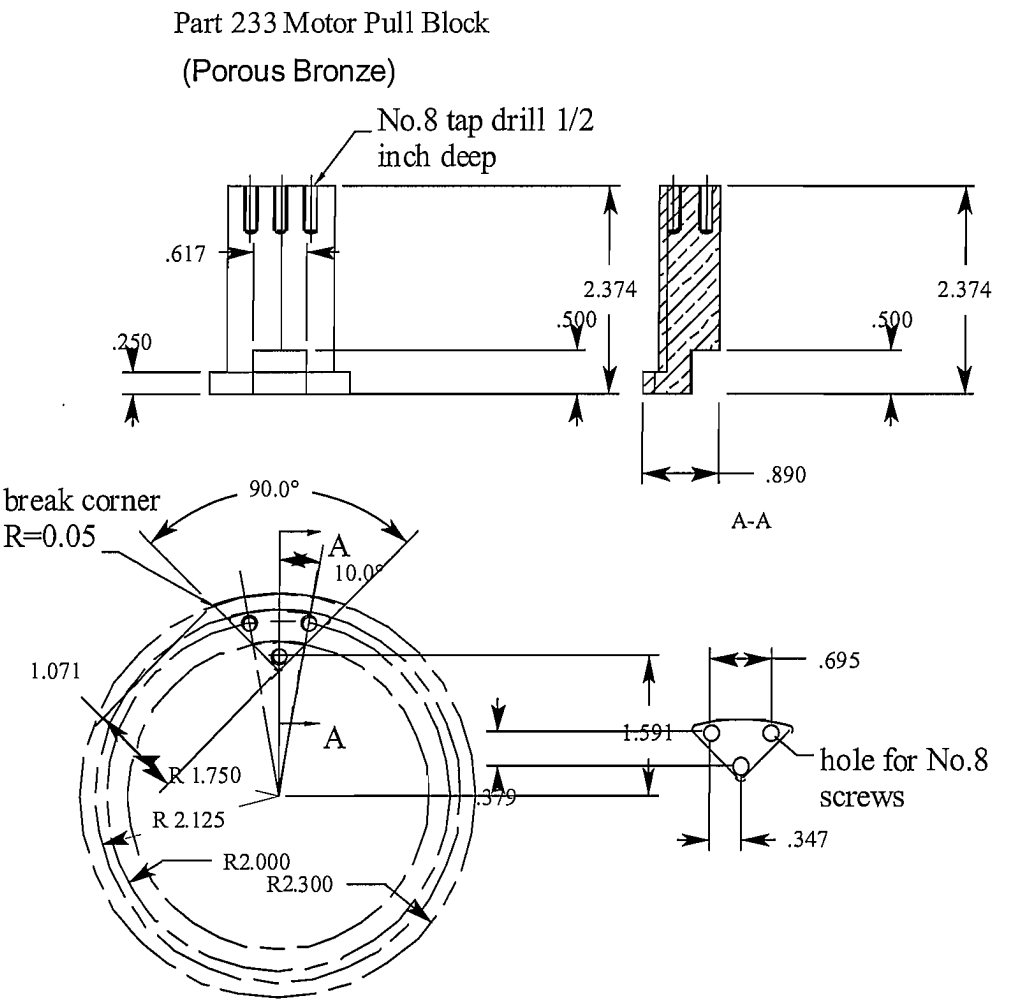

Figure A.15 Motor pull block of the cutter-motor drive system

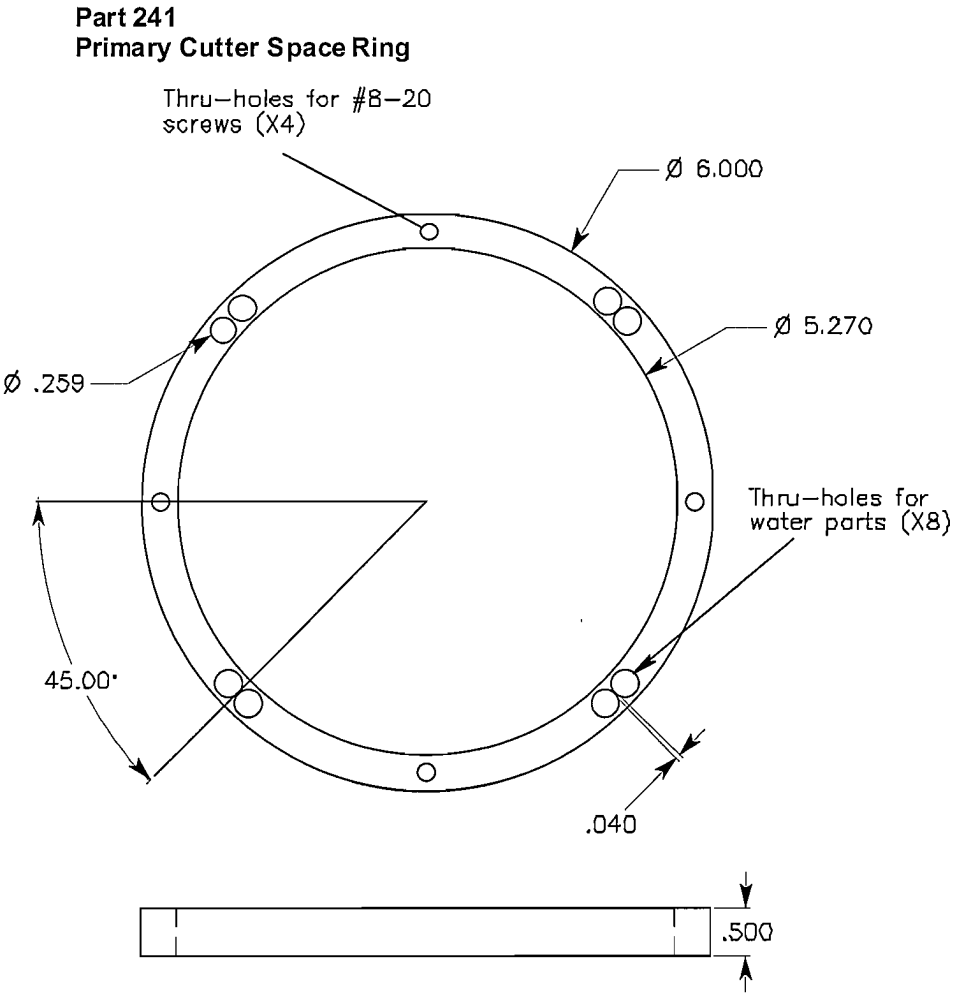

Figure A.16 Primary cutter spacer ring

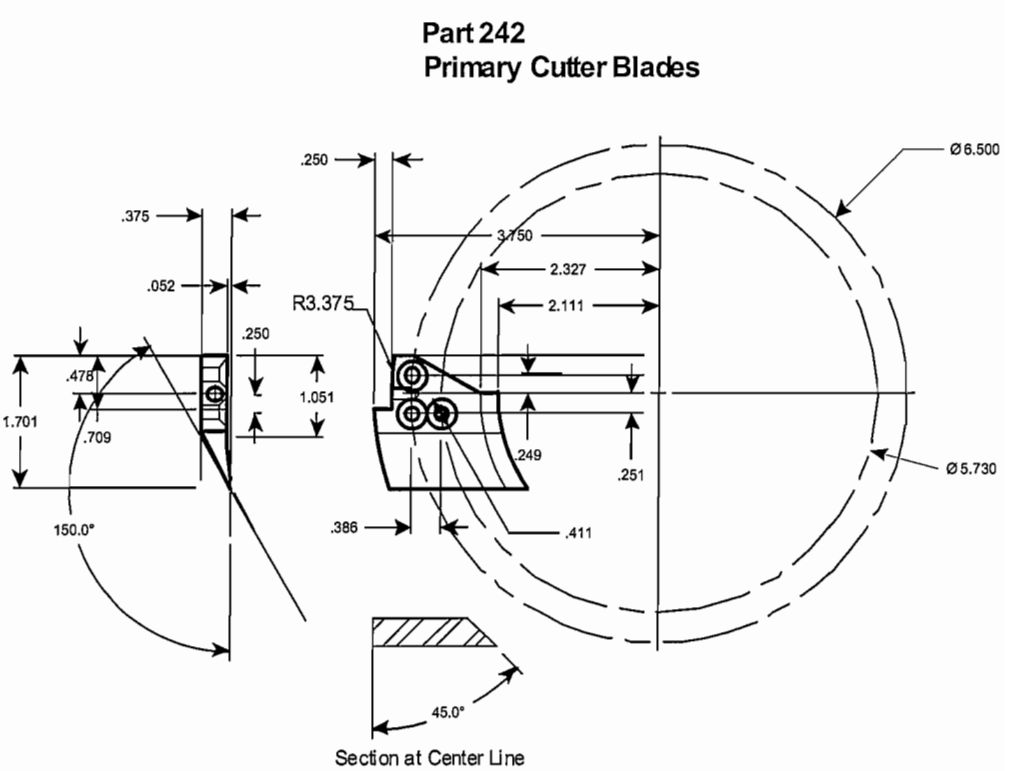

Figure A.17 Primary cutter blades

Part 301Sampler Tube

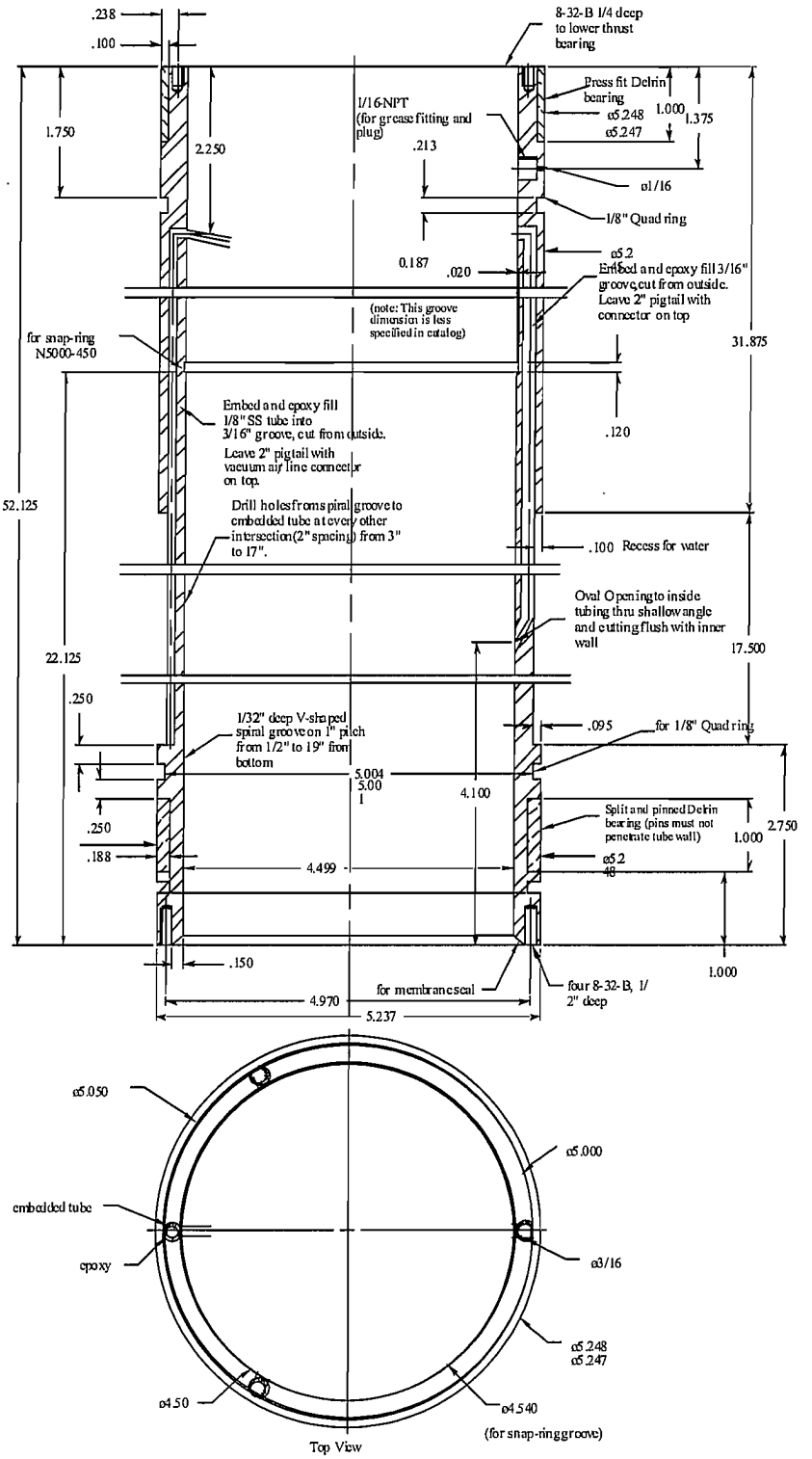

Figure A.18 Design details of sample tube

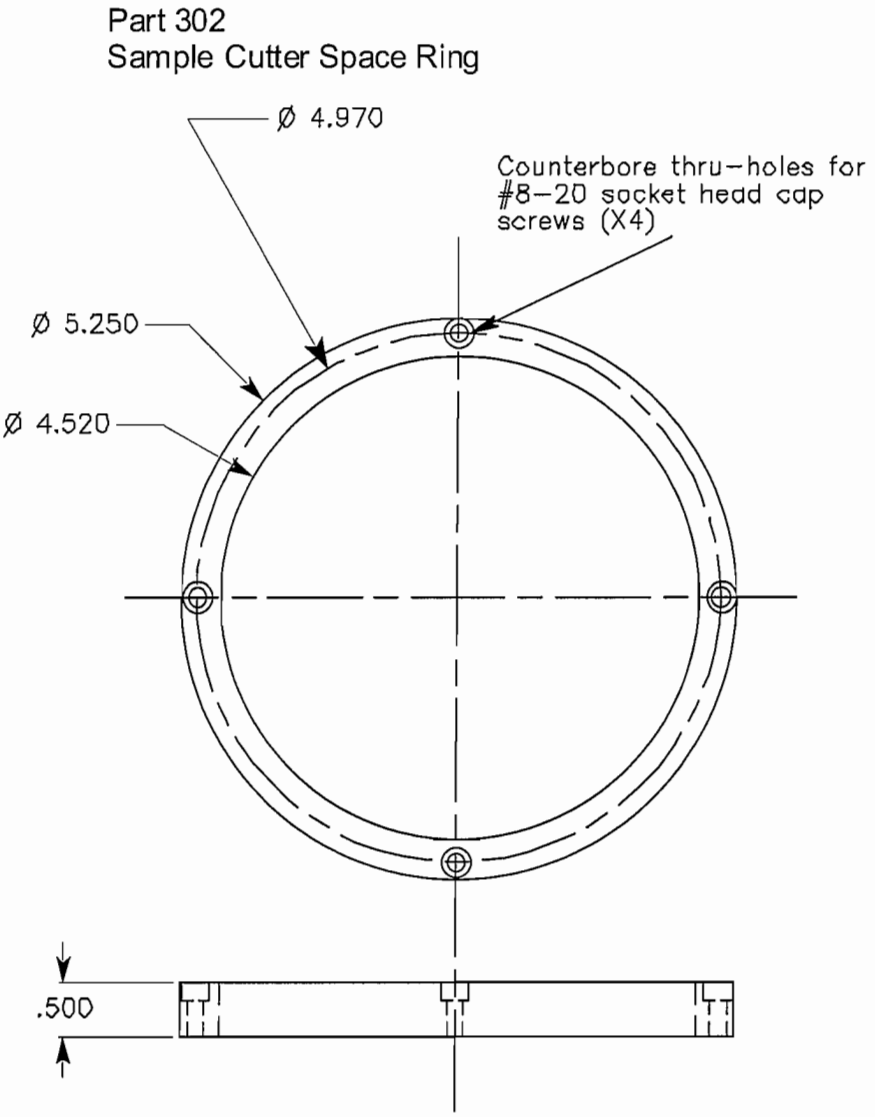

Figure A.19 Sample cutter spacer ring

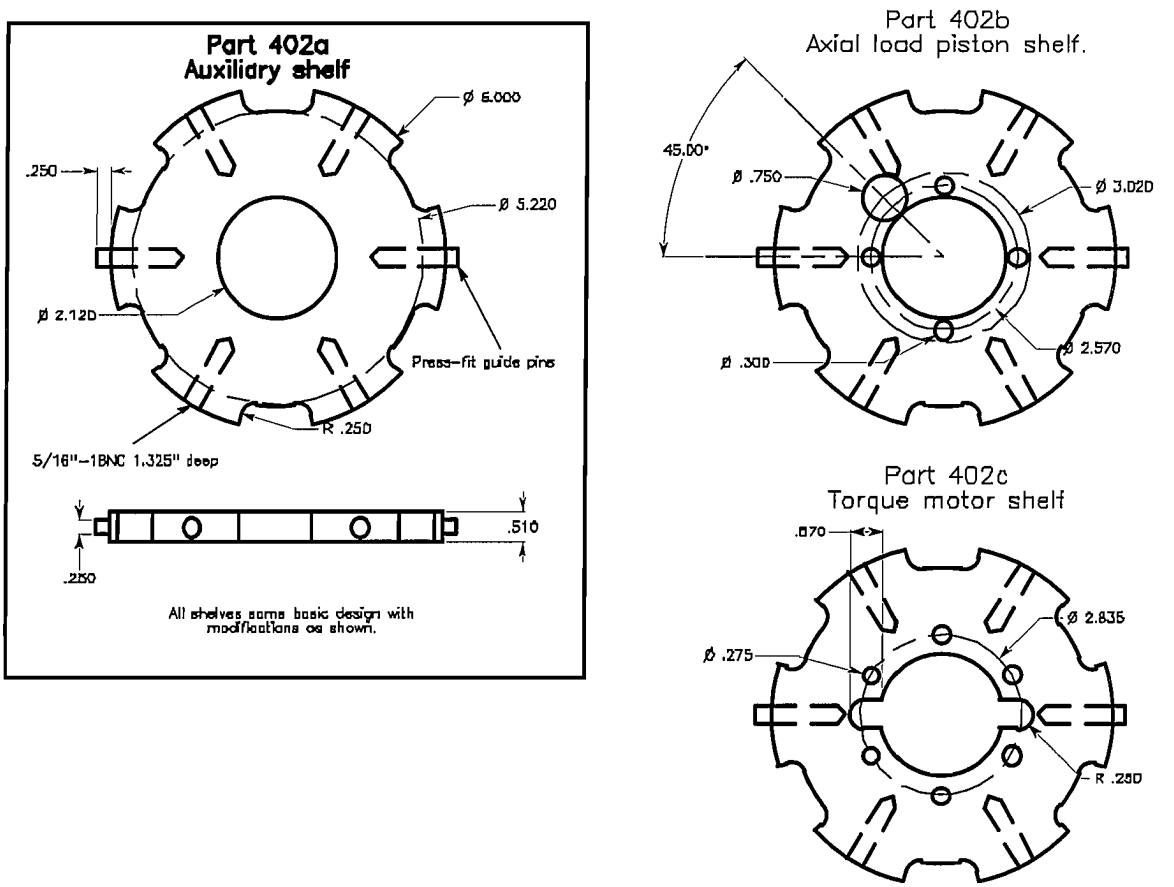

Figure A.20 Load module frame shelves

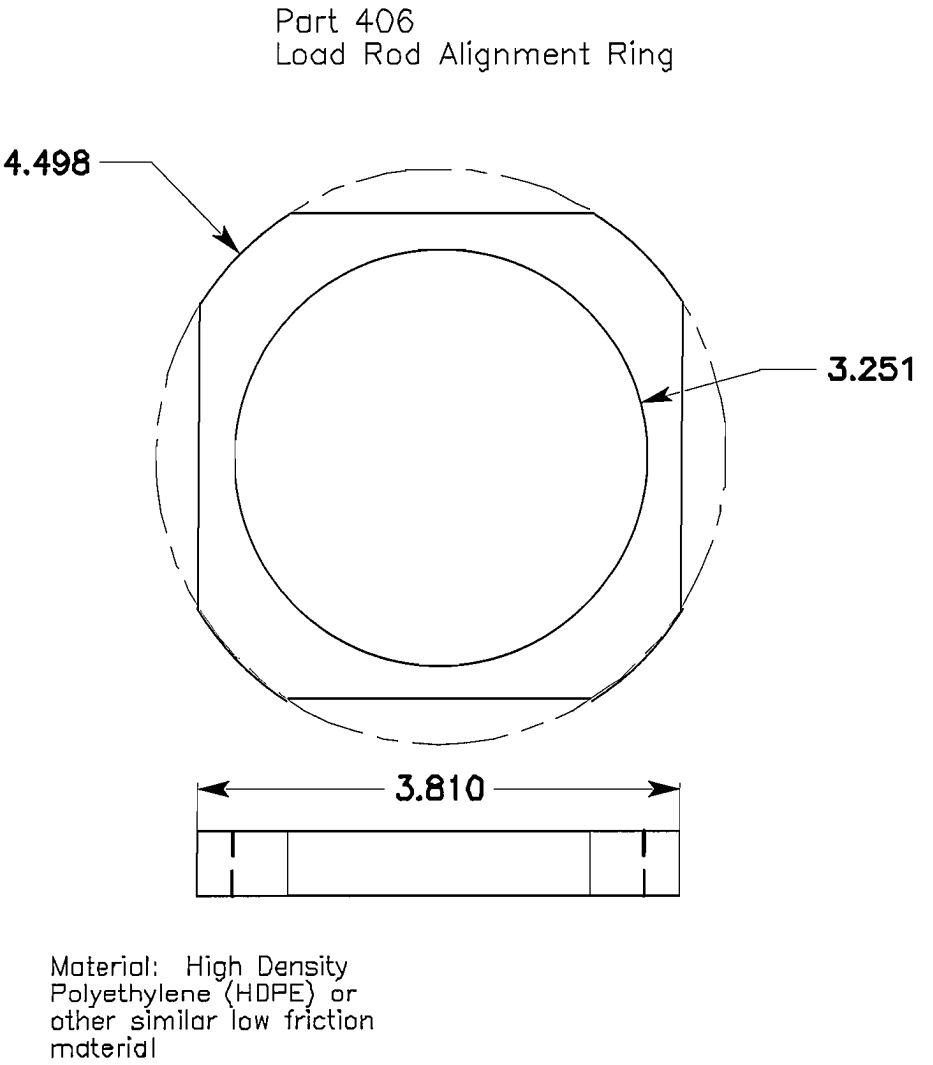

Figure A.21 Load rod alignment ring

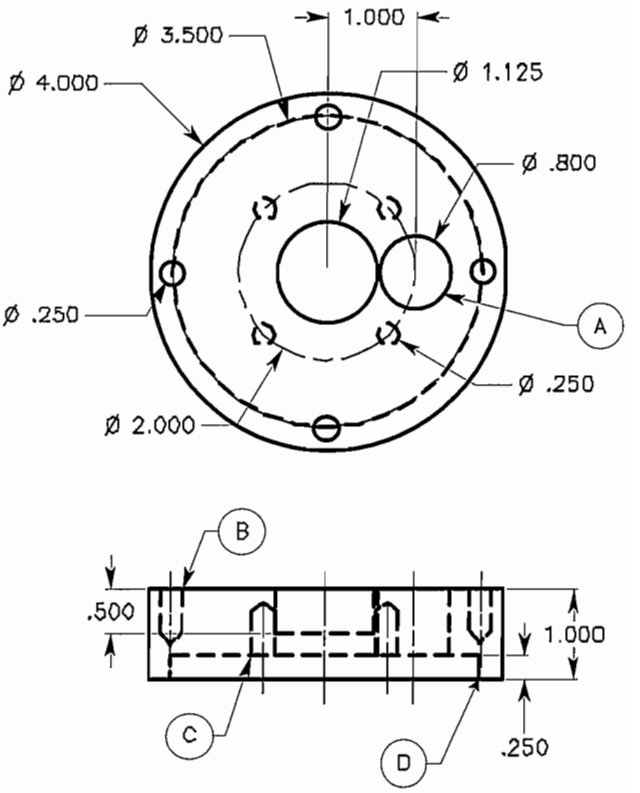

Notes:

A. Through hole.

B. Holes (X4) threaded for standard 1/4" bolts, 1/2" deep.

C. Holes (X4) threaded for standard 1/4" bolts, 1/2" deep.

D. May need to chamfer inside edge for O-ring compression against membrane and top cap.

Figure A.22 Membrane retaining ring

Part 413
2-Axis Load Cell

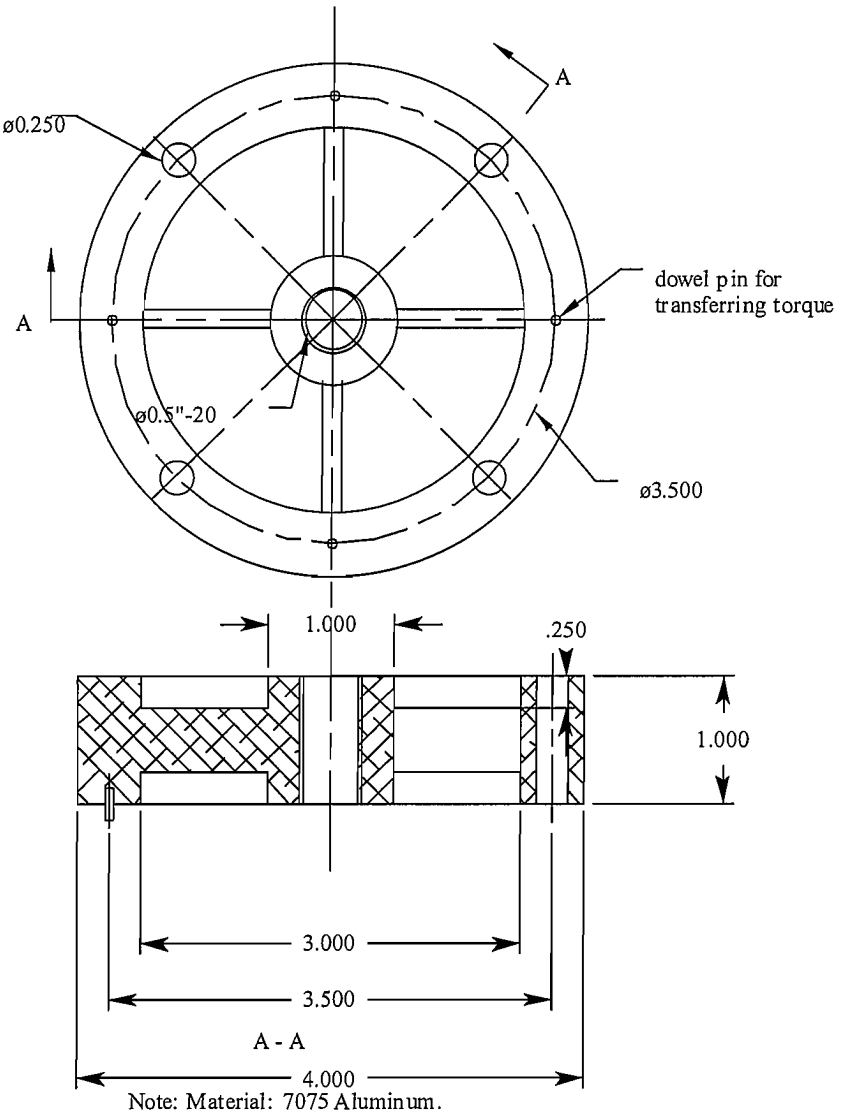

Figure A.23 Tow-axis load cell

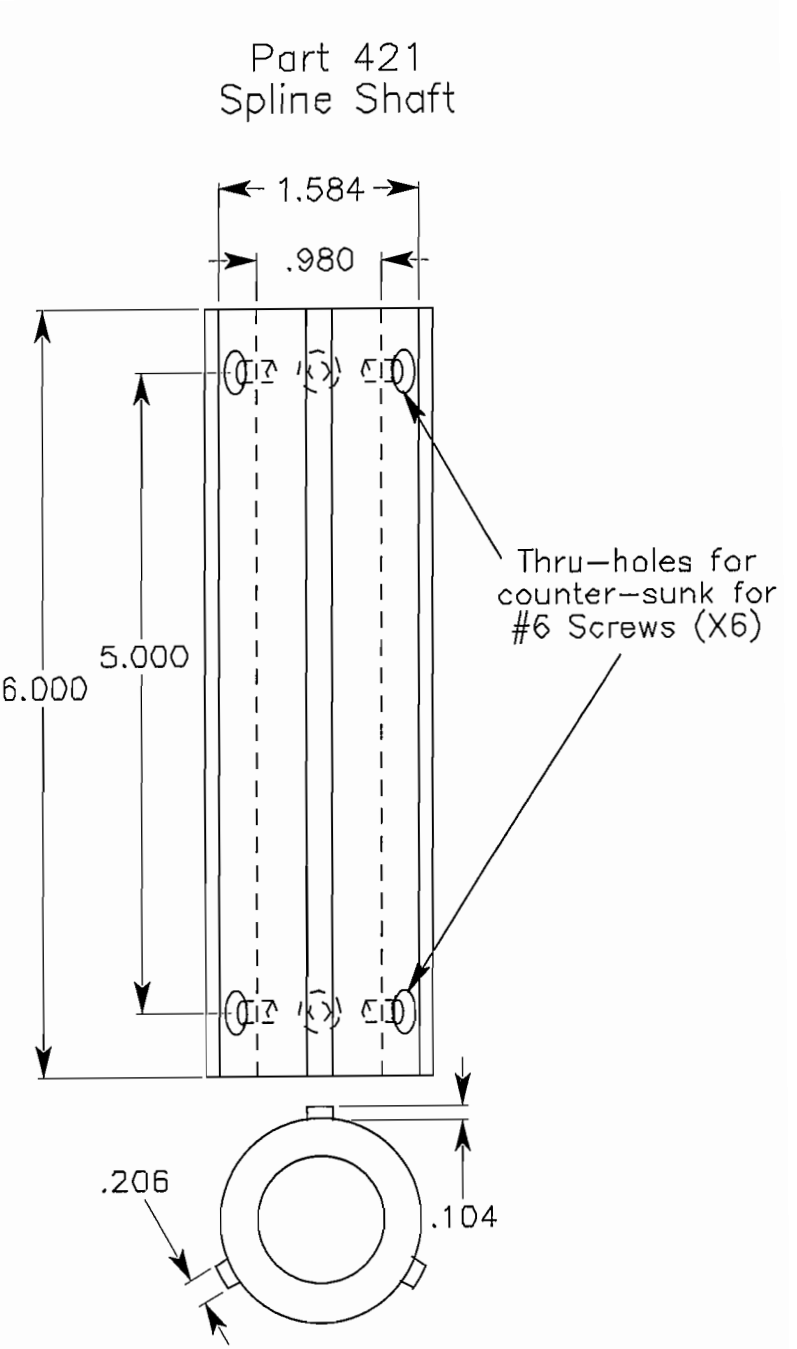

Figure A.24 Torque motor spline shaft

APPENDIX B

METHODS FOR DATA INTERPRETATION OF TORSIONAL SHEAR TESTS ON SOLID CYLINDRICAL SAMPLES

B.1 Introduction

In torsional shear tests, once the linear threshold shear strain is exceeded, the shear stress over a cross-section of a solid cylindrical sample is no longer a linear function of the distance from the center of the sample, and thus the linear assumption does not apply. In order to reduce the stress/strain non-uniformity, many investigators use a hollow cylindrical sample. However, since in this project the test will be performed on a solid cylindrical sample that is carved by the tool, stress/strain non-uniformity is an issue that has to be addressed. This appendix presents an overview of the methods used for determining the shear stress in the non-linear range, for hollow as well as solid samples, if the torque-twist curve is known.

B.2 Overview of Available Methods

B.2.1 Linear Elastic Stress Distribution

A linear elastic stress distribution assumption has been used by many investigators (e.g. Chen and Stokoe (1979) Drenvich (1972), Ishibashi et al (1985), Isenhower et. al. (1987), Vaid et. al. (1990), Wijewickreme and Vaid (1991), Frost and

Drenvich (1994), etc.). For solid cylindrical specimens, shear strains are assumed to vary linearly from zero along the axis of rotation to a maximum at the out side surface of the specimen. This condition occurs at each end of the specimen because of the constraint applied by the platens. For some investigators, since the stresses vary across the wall of the cylinder, it becomes necessary to work in terms of average stresses and strains. Vaid et. al. (1990) and Wijewickreme and Vaid (1991) used the shear stress and strain at 2/3 of the radius along with the linear elastic assumption to represent the average stresses/strains for a hollow cylindrical specimen. The corresponding expressions are:

$$\tau_{z\theta}(ave) = \frac{4T(r_e^3 - r_i^3)}{3\pi(r_e^4 - r_i^e)(r_e^2 - r_i^2)} \qquad \text{(B.1)}$$

$$\gamma_{z\theta}(ave) = \frac{2(r_e^3 - r_i^3)\theta}{3(r_e^2 - r_i^2)H} \qquad \text{(B.2)}$$

where r_e, r_i, H, and θ are the external radius, internal radius, sample height, and rotation angle, respectively. For a solid cylindrical specimen, the corresponding expressions are:

$$\tau_{z\theta}(ave) = \frac{4T}{3\pi r^3} \qquad \text{(B.3)}$$

$$\gamma_{z\theta}(ave) = \frac{2r\theta}{3H} \qquad \text{(B.4)}$$

On the other hand, Chen and Stokoe (1979) and Isenhower et. al. (1987) reported that the results of solid cylinders and hollow cylinders can be correlated by using an *effective* radius for the solid sample equal to 80% of the outside radius. Frost and Drenvich (1994) also recommend, based on Chen and Stokoe (1979) investigation, that for a solid cylindrical specimen, the *average* shear strain is assumed to occur at 80% of the specimen radius. More recently, Prof. Stokoe has used an *effective* radius equal to 82% of the outside radius.

B.2.2 Uniform Stress Distribution:

The assumption of uniform stress distribution across the wall of the specimen was used by many investigators especially for hollow cylindrical specimens (Hight et. al. (1983), Ishibashi et. al. (1985), Tatsuoka et. al. (1986), Miura et. al. (1986), etc.). The corresponding expressions are:

$$\tau_{z\theta}(ave) = \frac{3T}{2\pi(r_e^3 - r_i^3)} \tag{B.5}$$

$$\gamma_{z\theta}(ave) = \frac{2(r_e^3 - r_i^3)\theta}{3(r_e^2 - r_i^2)H} \tag{B.6}$$

For solid cylindrical specimens, using this assumption may lead to reasonable results in case of large-strain tests, however, for small strain tests where the stress is almost linearly distributed, using a uniform stress distribution can result in over predicting the shear modulus value. The corresponding expressions for a solid cylindrical specimen are:

$$\tau_{z\theta}(ave) = \frac{3T}{2\pi r^3} \tag{B.7}$$

$$\gamma_{z\theta}(ave) = \frac{2r\theta}{3H} \tag{B.8}$$

B.2.3 Li (1993) Incremental Procedure:

Li (1993), as part of this project, describes a numerical procedure which may be used to define the shear modulus-shear strain curve based on the torque-twist data from torsional shear test. The numerical procedure treats the soil column as an infinitely long rod so that the parameters of interest vary only in the radial direction, not circumferential or vertical directions. The fundamental assumption of the procedure is that the non-linear

stress strain relationship can be approximated by dividing the applied load into discrete intervals in which the linear stress-strain relationship is still valid. The cross-section of the specimen is divided into annular regions chosen such that shear strain and therefore shear modulus may be considered uniform for each region. The radial increments should also be chosen such that adjacent radii are proportional ($c=r_{n-1}/r_n$). Similarly, the loading increments should be chosen such that succeeding increments are proportional ($c=\theta_j/\theta_{j+1}$). Choosing the same constant of proportionality for both the radial and loading increments permits the following equation: $G_{i-1,j+1}= G_{I,j}$

In other words, the shear modulus of a given ring at the end of a given load increment is equal to the shear modulus of the ring immediately inside of the current one at the end of the next load increment. If a very small θ is chosen for the first loading increment then the material can be considered linearly elastic everywhere which means that the shear modulus is uniform throughout the sample for the first loading increment. The shear modulus for all rings at the end of the first loading increment should, by definition, be equal to G_{max}. The shear modulus of the outermost ring for all subsequent loading increments can be calculated as follows:

$$G_{n,j} = \frac{[2L/\pi(1-c^4)](\Delta T/\Delta\theta)_j - \sum_{i=1}^{n-1} G_{i+1,j-1} r_i^4}{r_n^4} \qquad \text{(B.9)}$$

With known twist angle, θ, the average strain level in the outermost ring may be calculated using the following equation:

$$\gamma_{n,j} = \frac{r_n + r_{n-1}}{2L}\theta_j \qquad \text{(B.10)}$$

Finally, the shear strain and shear modulus derived from equations (B.9) and (B.10) can be used to derive the average shear stress in the outermost ring as follows:

$$\tau_{n,j} = G_{n,j}\gamma \qquad \text{(B.11)}$$

B.2.4 A Closed-Form Solution

A closed-form solution has been developed that allows the calculation of a τ-γ curve from T-θ data obtained during a torsional test. The method is based on the concept first presented by Nadai (1950) to study the high-temperature flow behavior during hot-working conditions of metals and can be applied to digitized torque-twist data. To simplify the analysis, consider the twist angle per unit length θ' ($\theta' = \theta/L$). The shear strain will be:

$$\gamma = r\theta' \qquad \text{(B.12)}$$

The resisting torque in the cross section of the sample can be expressed as follows;

$$T = 2\pi \int_0^R \tau r^2 dr \qquad \text{(B13)}$$

Now the shear stress is related to the shear strain by the stress-strain curve in shear:

$$\tau = f(\gamma) \qquad \text{(B.14)}$$

Introducing equation (B.14) into equation (B.13) and changing the variable from r to γ by means of equation (B.12) gives:

$$T = 2\pi \int_0^{\gamma_a} f(\gamma) \frac{\gamma^2}{(\theta')^2} \frac{d\gamma}{\theta'} \qquad \text{(B.15)}$$

$$T(\theta')^2 = 2\pi \int_0^{\gamma_a} f(\gamma)\gamma^2 d\gamma \qquad \text{(B.16)}$$

$$\gamma_a = R\theta' \tag{B.17}$$

Differentiating equation (B.16) with respect to θ'gives:

$$\frac{d}{d\theta'}(T\theta'^3) = 2\pi Rf(R\theta')R^2(\theta')^2 \tag{B.18}$$

But, the maximum shear stress in the sample at the surface is $\tau_a = f(R\theta')$. Therefore,

$$\frac{d}{d\theta'}(T\theta'^3) = 2\pi R^3(\theta')^2\tau_a \tag{B.19}$$

$$3T(\theta')^2 + (\theta')^3\frac{dT}{d\theta'} = 2\pi R^3(\theta')^2\tau_a \tag{B.20}$$

$$\tau_a = \frac{1}{2\pi R^3}(\theta'\frac{dT}{d\theta'} + 3T) \tag{B.21}$$

If a torque-twist curve is available, the shear stress can be determined with equation (B.21). For digitized torque-twist data the above equation collapses to:

$$\tau_a = \frac{1}{2\pi R^3}(\theta\frac{\Delta T}{\Delta\theta} + 3T) \tag{B.22}$$

The corresponding shear strain at the surface will be:

$$\gamma_a = \frac{R\theta}{L} \tag{B.23}$$

The advantages of this method are:

1. No constitutive law or assumption is used with regard to the non-linearity over the cross-section of the sample.

2. There is compatibility between the shear stress and shear strain since both are determined at the same point, at the surface of the cylinder.

3. The data used in this method is only the measured torque and twist at the surface of the sample and no extrapolation/interpolation is used to predict the torque/twist at the other locations.

4. The method can be applied to cyclic loading and only one formula is needed to determine the shear stress and shear strain from the torque and twist.

B.3 A Comparison Between the Different Methods

In order to compare these methods, a simple exercise was performed. A certain modulus degradation curve was assumed to be the actual reference curve for a solid soil sample. A realistic curve can be obtained using the following formula:

$$G = \frac{G_{max}}{1 + \frac{\gamma}{0.0015}} \qquad \text{(B.24)}$$

The curve defined by this formula is shown in Figure B.1a. Since the modulus degradation curve is known, torque-twist data can be generated numerically. Assuming a hypothetical stain-controlled monotonic torsional shear test, the corresponding shear stress can be determined from the assumed shear strain time history and the real modulus degradation curve. The torque and the twist data can be generated from the shear stress and shear strain, respectively. Figure B.1b shows a torque-twist curve generated using this procedure. From the torque-twist curve, the τ-γ curve and G/G_{max}-γ curve can be back calculated from T-θ curve using each method outlined above and then compared with the reference curve.

Figure B.2 and Figure B.3 show the G/G_{max}-γ curves predicted by the different linear and uniform stress methods. The linear stress method with effective radii at 0.8 and 0.82 was almost the same as the reference curve. Using an effective radius of 0.8R

resulted in a slightly better agreement with the reference curve than when using 0.82R. On the other hand, using an effective radius at 0.67R did not result in a good agreement with the reference curve especially at high shear strain levels. In contrast, using a uniform stress distribution resulted in perfect tracking of the reference curve at high strain levels but largely over predicted the shear modulus at low strain levels. Figure B.4b shows the G/G_{max}-γ predicted by the Li (1993) incremental procedure for different radii ratios, *c*, and number of rings, *n*. The best prediction of the modulus degradation curve is when c=0.2 and n in excess of 200. Because the c value is small, most of the sectors are close to the center of the sample where the strain is small. As a result, the method did not seem to predict the tangent modulus very well at large strain level, perhaps because there are only few points/sectors in the large strain range. As shown in Figure B.4a, the G/G_{max}-γ curve predicted by the closed-form solution (Nadai (1950)) is in good agreement with the reference curve.

In summary, the linear elastic approach with effective radius at 0.8R can reasonably predict both G/G_{max}-γ and τ-γ curves at small to intermediate strain levels. Also, this approach can fairly predict these curves at large strain levels (up to 1-2%). On the other hand, the closed-form approach can be used for all strain levels. However, since in this approach we are basically differentiating the signal, the main disadvantage is that in performing the differentiation of a noisy signal by finite difference, the method can becomes numerically unstable and can give unreasonable results. In order to investigate the effect of noise in the performance of the equivalent linear and the closed-form approaches, white noise was numerically obtained by generating a random number between 0.9-1.1 and multiplying it with the originally generated torque and twist data.

The T-θ curve after adding the noise is shown in Figure B.5a. As shown in Figure B.5b and Figure B.5c, the closed-form approach performed poorly in the presence of high amount of noise. However, since in the DFSD tool the signal will be filtered in the analog mode, the noise will not be as severe as shown in the previous example. However, it will still be difficult to use the method to interpret small-strain tests. This exercise was also implemented using different hyperbolic models by changing the amplitude of the reference curve. The same conclusions were obtained regarding the performance of each method.

The closed-form approach and the equivalent linear approach were also used to process the T-θ data obtained from real torsional shear tests performed with the benchtop version of the tool and using a urethane sample and from a DFSD test on a kaolinite sample. The hysteresis loop obtained by the two approaches is shown in Figure B.6. It should be noticed that the two methods predict the shear modulus at two different strain levels. In the effective radius method, G corresponds to the shear strain at 0.8R while in the closed-from solution the predicted G is at a higher strain level (at R). The effect of this can be clearly seen in Figure B.6. For the urethane sample, the material is linear but inelastic, therefore, G is constant regardless of the strain level. Accordingly, both methods resulted in the same hysteretic loop and therefore, the same G. For the kaolinite sample, the material is non-linear inelastic and, as a result, at large strain levels G is a function of shear strain. Accordingly, the closed-form solution resulted in a smaller measured G than the effective radius method as shown in Figure B.6b.

B.4 Verification by Numerical Modeling of Cyclic Testing

The evidence mentioned above suggests that the effective radius methods can reasonably be used to predict soil non-linearity in monotonic tests. To verify this finding for cyclic tests and to further explore the effects of non-linearity and/or inelasticity on data interpretation, another numerical study has been conducted. The study uses the wave equation and non-linear hysteretic models

B.4.1 Formulation of the Model

A cyclic torsional shear test on a solid cylindrical sample can be modeled as a torsional wave of torque amplitude T traveling along the sample with velocity v_s and causing an angle of twist θ. Development of a wave equation for torsional vibrations follows exactly the same steps as for longitudinal vibration. Torsional waves involve rotation of the sample about its own axis and particle motion is constrained to planes perpendicular to the direction of wave propagation. Dynamic torsional equilibrium requires that the unbalanced external torque is equal to the inertial torque:

$$(T_o + \frac{\partial T}{\partial x} dx) - T_o = \rho J dx \frac{\partial^2 \theta}{\partial t^2} \qquad \text{(B.25)}$$

where J and ρ is the polar moment of inertia of the sample about its axis and the mass density of the sample respectively. This equilibrium equation can be simplified to produce the equation of motion:

$$\frac{\partial T}{\partial x} = \rho J \frac{\partial^2 \theta}{\partial t^2} \qquad \text{(B.26)}$$

Now incorporating the torque-rotation relationship:

$$T = GJ \frac{\partial \theta}{\partial x} \qquad \text{(B.27)}$$

where G is the shear modulus of the sample, the torsional wave equation can be written as:

$$\frac{\partial^2\theta}{\partial t^2} = \frac{G}{\rho}\frac{\partial^2\theta}{\partial x^2} = v_s^2\frac{\partial^2\theta}{\partial x^2} \tag{B.28}$$

Where $v_s{}^2 = G/\rho$ is the velocity of propagation of the torsional wave. The wave propagation velocity depends only on the stiffness and the density of the soil. Equation (B.28) is solved analytically by the separation-of-variable method under a set of initial and boundary conditions that simulates a torsional shear test. First, an input sinusoidal twist-time history with a certain amplitude and frequency is assumed, $\theta(t)$, and then equations (B.27) and (B.28) were used to find the torque-time history. However, since soil is a non-linear material, the shear modulus, G, is also a function of the twist angle, θ. This means that a constitutive law is needed to model the soil non-linearity, and equations (B.27) and (B.28) have to be solved numerically. To model the hysteretic non-linear behavior of the soil, two models have been used. The first model is the Ramberg-Osgood equation to model the backbone curve, and Masing criterion for generation of the hysteretic loop. The Ramberg-Osgood equation empirically describes shear stress versus shear strain as follows:

$$\frac{\gamma}{\gamma_r} = \frac{\tau}{\tau_r}\left(1 + \alpha\left|\frac{\tau}{\tau_r}\right|^{R-1}\right) \tag{B.29}$$

where τ and γ are the shear stress and strain, respectively; α a positive constant and R a constant equal or larger than unity. τ_r and γ_r are the reference stress and strain which can be replaced by τ_{max} and τ_{max}/G_{max}, where τ_{max} is the undrained static shearing strength of

soil. The Masing Criterion for the hysteretic loop can be expressed by the following equation:

$$\frac{\gamma \pm \gamma_o}{2\tau_r} = \frac{\tau \pm \tau_o}{2\tau_r} + \alpha\left(\frac{\tau \pm \tau_o}{2\tau_r}\right) \qquad \text{(B.30)}$$

in which τ_o and γ_o are the coordinates of the tips of the loop. Since in these formulas, shear strain is written as a function of shear stress, the Ramberg-Osgood-Masing Model is used for simulating stress-controlled cyclic tests. Assuming, G_{max}, τ_o, τ_{max} and T(t), equations (B.27) to (B.30) can be used to predict the stress and strain time-histories for a stress-controlled test. Because it is numerically difficult to use equations (B.29) and (B.30) for a strain-controlled test, another hysteretic non-linear model was used. The Hyperbolic Model can be written to describe the stress as a function of the strain. The backbone function $F_b(\gamma)$ can be described by a hyperbola:

$$F_b(\gamma) = \frac{G_{max}\gamma}{1 + (G_{max}/\tau_{max})|\gamma|} \qquad \text{(B.31)}$$

while the stress-strain hysteretic loop follows a path given by:

$$\frac{\tau \pm \tau_r}{2} = F_b\left(\frac{\gamma - \gamma_r}{2}\right) \qquad \text{(B.32)}$$

For a strain-controlled test, γ_o and $\theta(t)$ is assumed and equations; (B.27), (B.28), (B.31) and (B.32) were used to predict the stress and strain time histories.

B.4.2 Application of the Model

In this study G_{max} was assumed to be 1000 ksc and $\tau_{max}=\tau_r$ and equal to 3.5 ksc. For the Ramberg-Osgood-Masing model, α and R were set to 1.0 and 3.0, respectively, while the reference strain in the hyperbolic model was 0.0035. The analyses were

conducted for two cases: (1) a series of strain-controlled cyclic tests on a non-linear inelastic material modeled by the hyperbolic model, (2) a series of stress-controlled cyclic tests on a non-linear inelastic material modeled by the Ramberg-Osgood-Masing model. The data torque-twist curves generated from these models were processed by the effective radius method, the uniform stress distribution method and the closed form solution to back calculate the reference G-γ curve. Similar results were obtained with different models. Figure B.7 shows the modulus reduction curves predicted by the three methods from one of these modeling exercises. Both the effective radius method and the closed-form solution reasonably estimated the G-γ curve while the uniform stress distribution method overestimated the shear modulus especially at small to intermediate strain levels.

In conclusion, the closed-form approach can reasonably predict the τ-γ curve at all strain levels, especially for determining the secant shear modulus, when the data is not noisy. The method can be improved by using a more robust numerical technique to filter and differentiate the data. Li et. al. (1998) presented a technique to differentiate noisy experimental data. He also uses this technique to recover the G/G_{max}-γ curve from T-θ data using a closed-form solution (Taylor (1975)) that is mathematically equivalent to the one used in this study. On the other hand, the linear elastic approach with effective radius at 0.8R is also a fairly accurate approach for the interpretation of T-θ data, especially at strain levels below 1%. The method is very simple to implement and its performance is insensitive to the noise level in the measured signal. Moreover, the method is more widely used than the closed form solution.

B.5 References

Ampadu, S. K. and Tatsuoka, F., (1993), " A Hollow Cylinder Torsional Simple Shear Apparatus Capable of a Wide Range of Shear Strain Measurement", Geotechnical Testing Journal, vol. 16, No. 1, pp.3-17.

Bressani, L. A. (1995), "External Measurement of Axial Strain in the Triaxial Test", Geotechnical Testing Journal, vol. 18, No. 2, pp.226-240.

Cascante, G. and Santamarina, C., (1997), " Low Strain Measurement Using Random Noise Excitation", Geotechnical Testing Journal, vol. 20, No. 1, pp.29-39.

Chen, A. T. and Stokoe, K. H. II, (1979), " Interpretation of Strain-Dependent Modulus and Damping from Torsional Soil Tests" Report No. USGS-GD-79-002, NTIS No. PB-298479, U.S. Geologic Survey, Menlo Park.

Dieter, G., (1961), "Mechanical Metallurgy", MeGraw-Hill Book Company, Inc., New York.

Doroudian, M. and Vucetic, M., (1995), "A Direct Simple Shear Device for Measuring Small-Strain Behavior", Geotechnical Testing Journal, vol. 18, No. 4, pp.69-85.

Frost, J. D. and Drnevich V. P. (1994), " Towards Standardization of Torsional Shaer Testing", Dynamic Geotechnical Testing II, ASTM STP 1213, Ronald J. Ebelhar, Vincent P. Drnevich and Bruce L. Kutter, eds., American Society for Testing and Materials, Philadelphia.

Goto, S., Tatsuoka, F., Shibuya, S., Kim, Y-S. and Sato, T., (1991), " A Simple Gauge For Local Small Strain Measurement in Laboratory", Soils and Foundations, Vol. 31, No.1, pp. 169-180.

Hardin, B.O. and Drnevich, V.P., (1972), " Shear Modulus and Damping in Soils: Measurement and Parameter Effects", Journal of Soil Mechanics and Foundation Division, ASCE, Vol. 98, No. sm6, pp. 603-624.

Hight, D.W., Gens, A., and Symes, M. J., (1983), " The Development of a New Hollow Cylindrical Apparatus for Investigating the Effects of Principle Stress Rotation in Soils", Geotechnique, Vol. 33, No. 4, pp. 355-383.

Hong, W. P, and Lade, P. V., (1989), " Strain Increment and Stress Directions in Torsion Shear Tests", Journal of Geotechnical Engineering Division, ASCE, Vol. 115, No. 10, pp.1388-1401.

Isenhower, W. M., Stokoe, K. H., II, and Allen, J. C., (1987), " Instrumentation for Torsional Shear/Resonant Column Measurements Under Anisotropic Stresses", Geotechnical Testing Journal, vol. 10, No. 4, pp.183-191.

Ishibashi, I., Kawamura, M. and Bahatia, S. K., (1985), " Torsional Simple Shear Apparatus for Drained and Undrained Cyclic Loading", Proceeding, ASCE Special Session, ASCE Convention, Detroit, pp.51-73.

Kim, D.-S. and Stokoe, K. H., II, (1994), "Torsional Motion Monitoring System for Small-Strain Soil Testing", Geotechnical Testing Journal, vol. 17, No. 1, pp.17-26.

Li, X., Yang, J., and Liu, H., (1998), " Differentiation of Noisy Experimental Data For Interpretation of Nonlinear Stress-Strain Behavior", Journal of Engineering Mechanics, ASCE, Vol. 124, No. 7, pp.705-712.

Miura, K., Miura, S., and Toki, S., (1986), " Deformation Behavior of Anisotropic Dense Sand Under Principle Stress Axes Rotation", Soils and Foundations, Vol. 26, No.1, pp. 36-52.

Mohammad, L. N., Puppala, A. J. and Alavilli, P.," Effect of Strain Measurements on Modulus of Sands", Dynamic Geotechnical Testing II, ASTM STP 1213, Ronald J. Ebelhar, Vincent P. Drnevich and Bruce L. Kutter, eds., American Society for Testing and Materials, Philadelphia.

Nadai, A., (1950), " Theory of Flow and Fracture of Solids", 2nd ed., Vol. I, p. 347-349, MeGraw-Hill Book Company, Inc., New York.

Pezo, R. F. and Hudson, W. R. (1994), " Comparisons of Laboratory and Field Measurements of Resilient Modulus of Non-Granular Materials", Dynamic Geotechnical Testing II, ASTM STP 1213, Ronald J. Ebelhar, Vincent P. Drnevich and Bruce L. Kutter, eds., American Society for Testing and Materials, Philadelphia

Saada, A., (1985), "Advances in the Art of Testing Soils under Cyclic Conditions", Proceeding, ASCE Special Session, ASCE Convention, Detroit, pp.1-28.

Scholey, G.K., Frost, J. D., Lo Presti, D. C. F., and Jamiolkowski, M. (1995), " A Review of Instrumentation for Measuring Small Strains During Triaxial Testing of Soil Specimens", Geotechnical Testing Journal, vol. 18, No. 2, pp.137-156.

Shibuya, S., Mitachi, T., Fukuda, F., and Degoshi, T., (1995), "Strain Rate Effect on Shear Modulus and Damping of Normally Consolidated Clay", Geotechnical Testing Journal, vol. 18, No. 4, pp.365-375.

Tatsuoka, F., Sonoda, S., Hara, K., Fukushima, S., and Pradhan, T. B., (1986), " Failure and Deformation of Sand in Torsional Shear", Soils and Foundations, Vol. 26, No.4, pp. 79-97.

Tatsuoka, F., Teachavorasinkun, S., Dong, J., Kohata, Y. and Sato, T., (1994), " Importance of Measuring Local Strains in Cyclic Triaxial Tests on Granular Materials", Dynamic Geotechnical Testing II, ASTM STP 1213, Ronald J. Ebelhar, Vincent P. Drnevich and Bruce L. Kutter, eds., American Society for Testing and Materials, Philadelphia.

Taylor, P. W. (1975), "Interpretation of Dynamic Torsion Tests on Soils", Report No. 120, School of Engineering, University of Auckland, Auckland, New Zealand.

Vaid, Y. P., Sayao, A., Hou, E., and Negussey, D., (1990), "Generalized Stress-Path-Dependent Soil Behavior with a New Hollow Cylinder Torsional Apparatus", Canadian Geotechnical Journal, J. 27, pp. 601-616.

Wijewickreme, D. and Vaid, Y. P. (1991), "Stress Non-uniformities in Hollow Cylinder Torsional Specimens", Geotechnical Testing Journal, vol. 14, No. 4, pp.349-362.

Woods, R. D., (1994), " Laboratory Measurement of Dynamic Soil Properties", Dynamic Geotechnical Testing II, ASTM STP 1213, Ronald J. Ebelhar, Vincent P. Drnevich and Bruce L. Kutter, eds., American Society for Testing and Materials, Philadelphia.

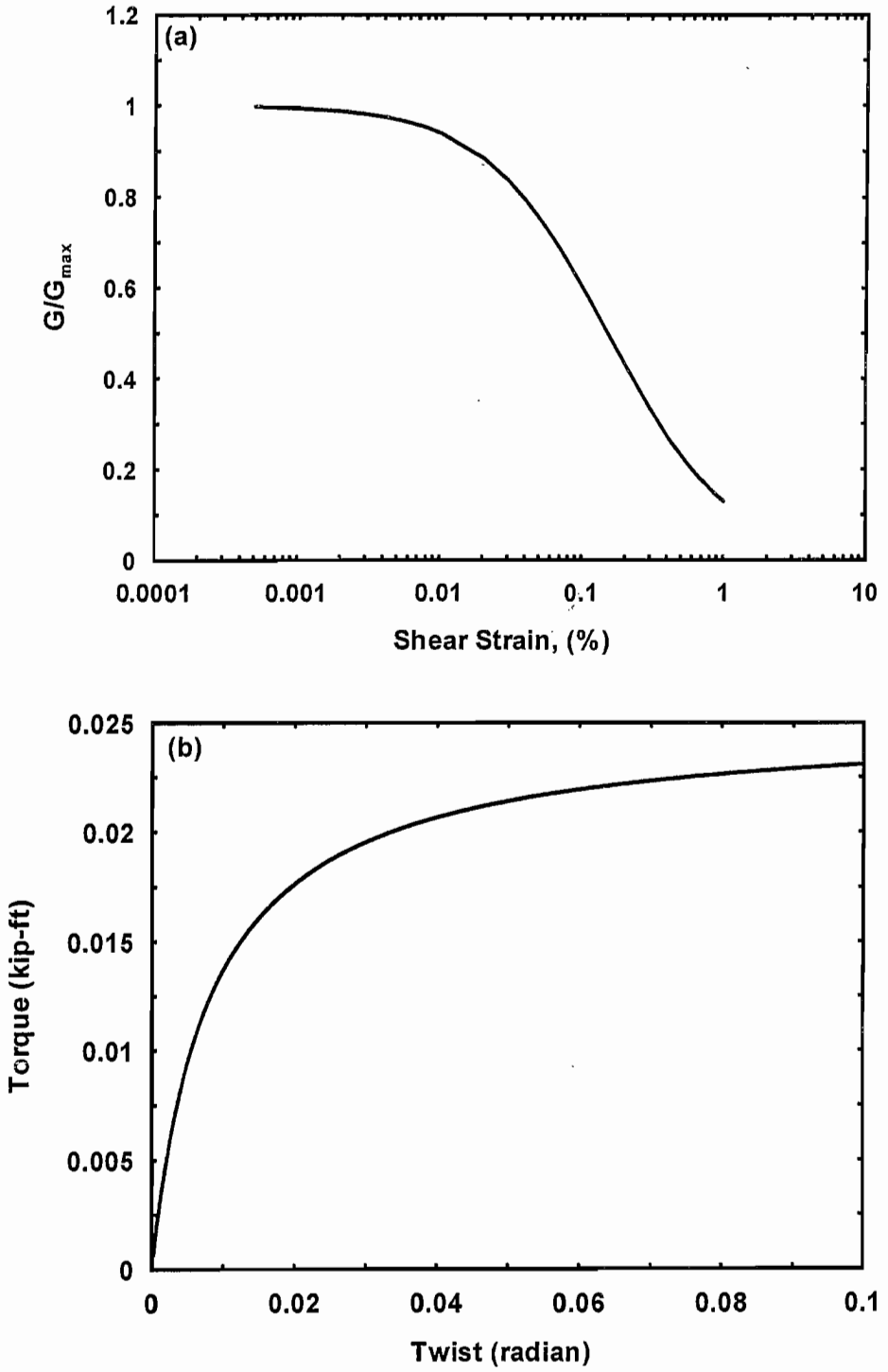

Figure B.1 (a) The reference G/G_{max}-γ curve and (b) the generated torque-twist curve for a hypothetical strain-controlled monotonic shear test

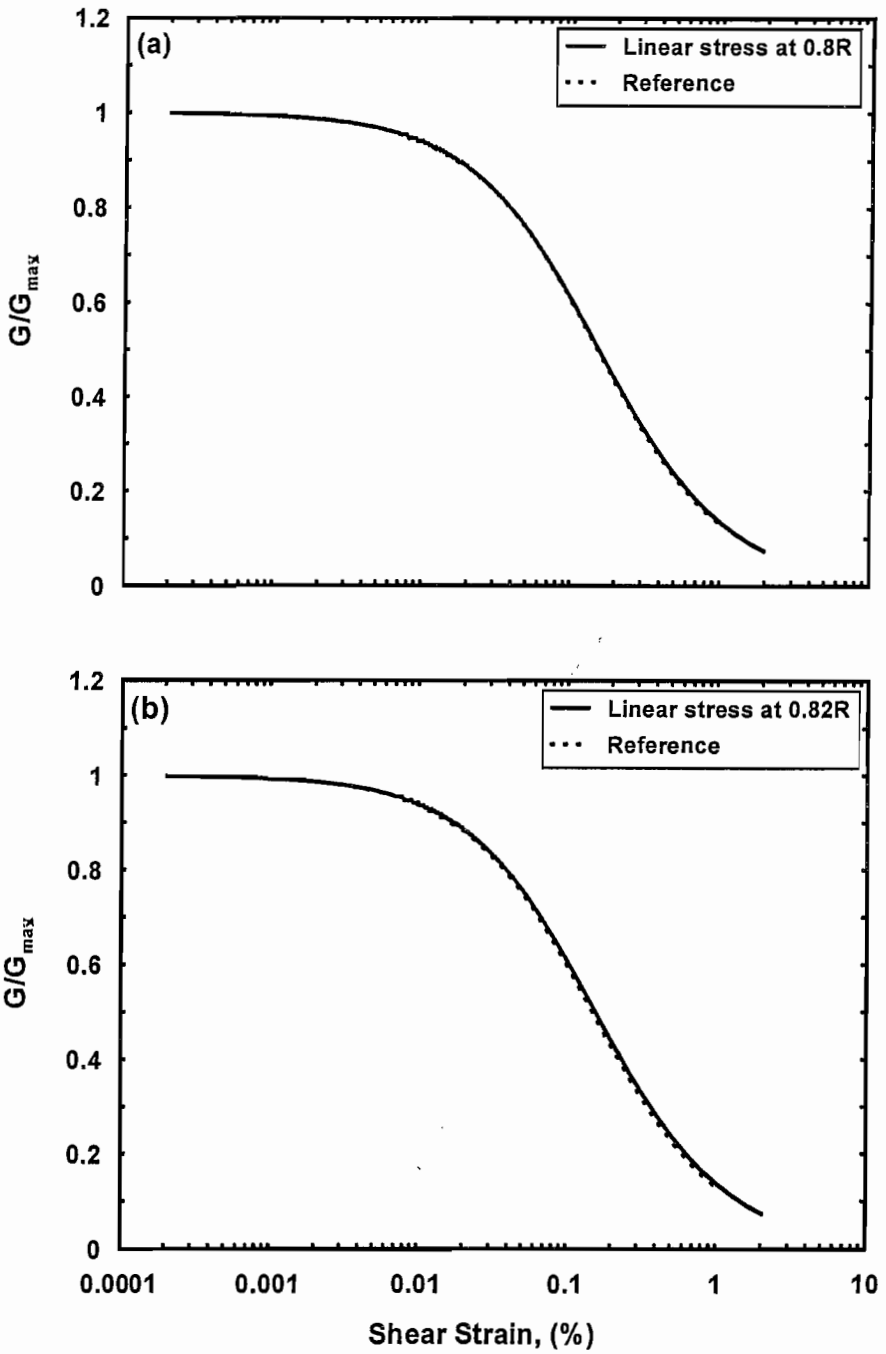

Figure B.2 A comparison between the reference G/G_{max}-γ curve and the one predicted by assuming a linear elastic stress distribution with (a) effective radius at 0.8R and (b) effective radius at 0.82R

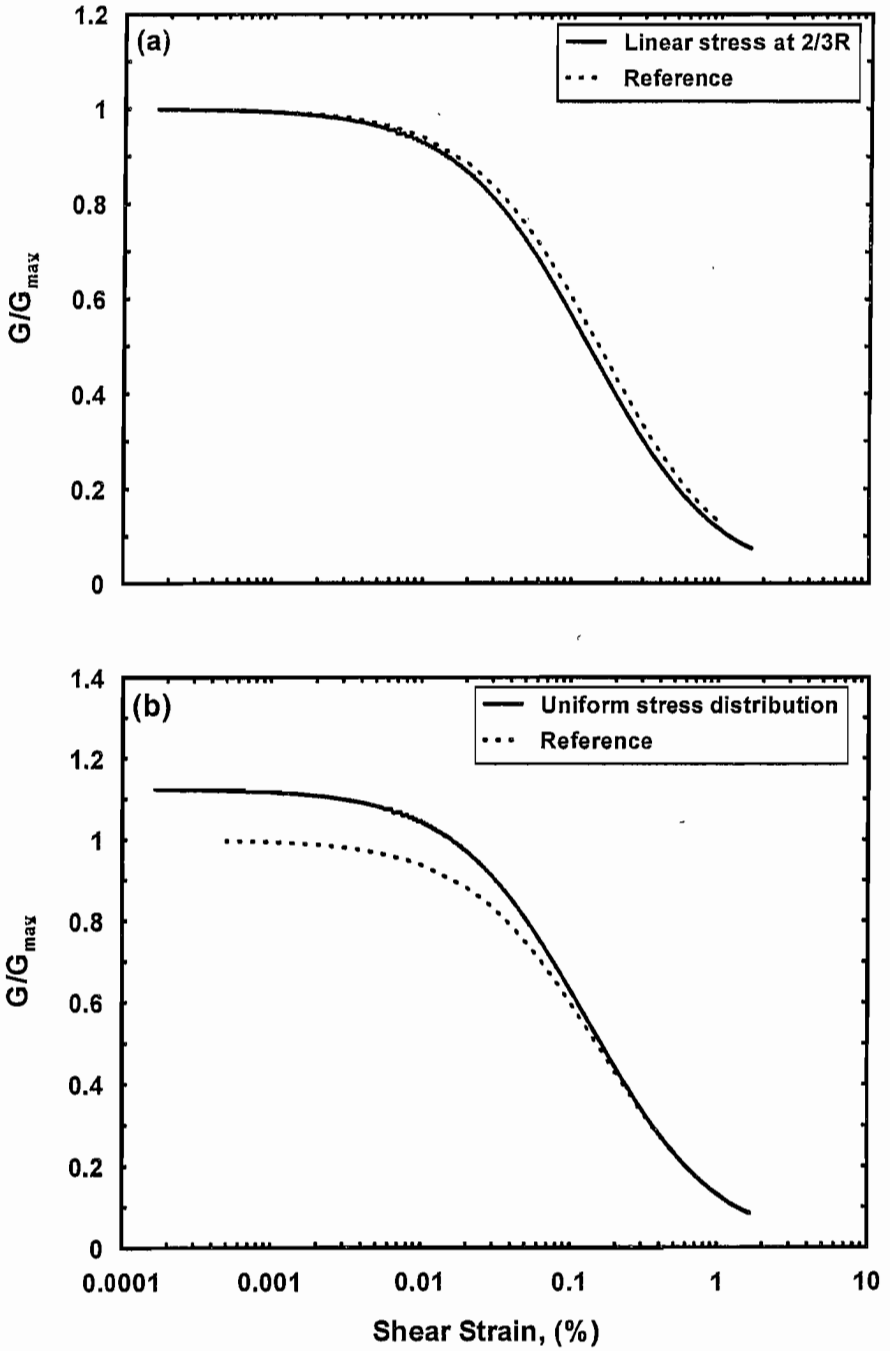

Figure B.3 A comparison between the reference G/G_{max}-γ curve and the one predicted by (a) assuming a linear elastic stress distribution with effective radius at 0.67R and (b) assuming a uniform stress distribution

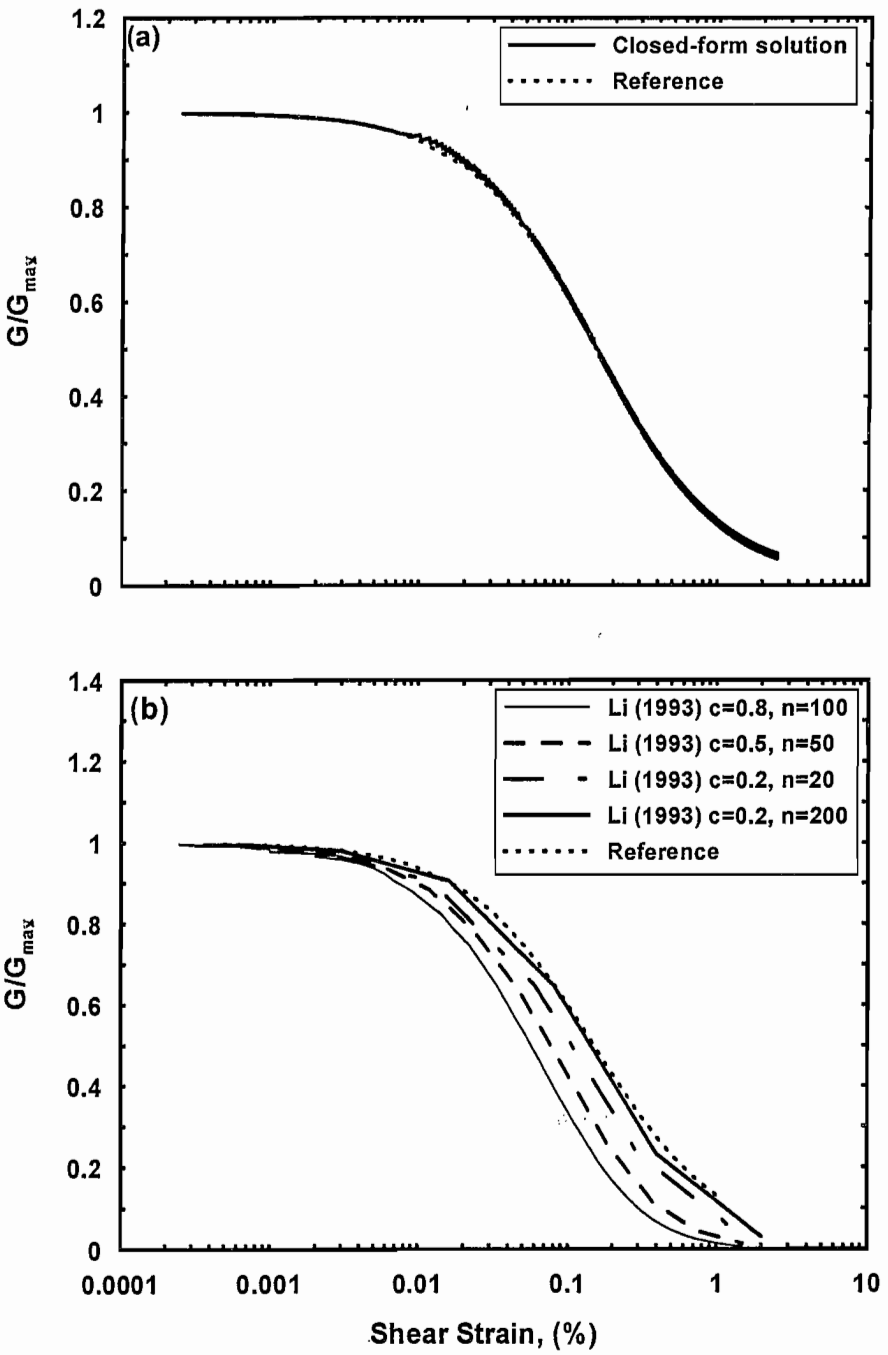

Figure B.4 A comparison between the reference G/G_{max}-γ curve and the one predicted (a) by the closed-form solution and (b) by Li (1993) incremental method

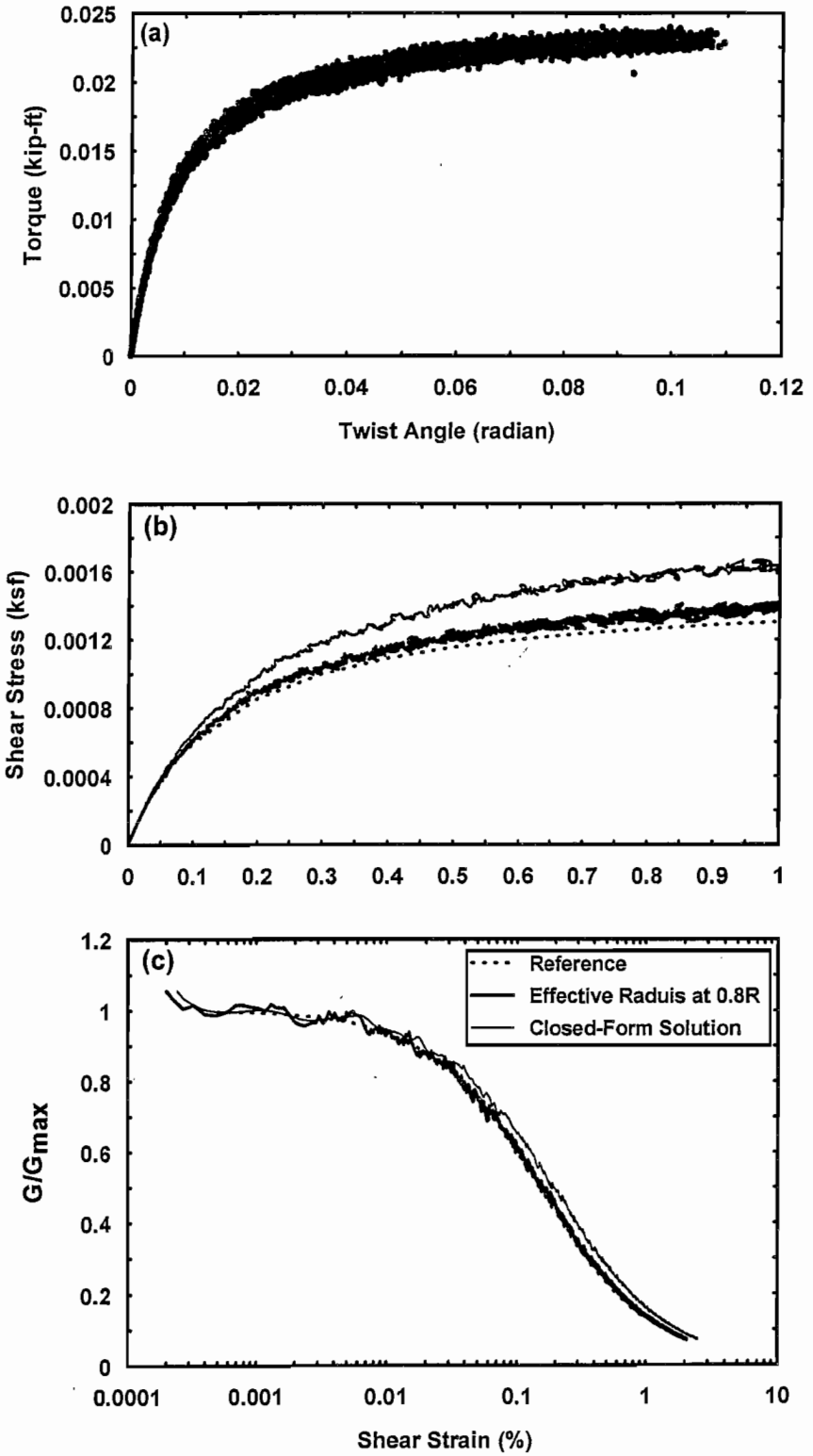

Figure B.5 (a) Effect of a noisy measured T-θ curve on (b) the interpreted stress-strain curve and (c) the interpreted G/G_{max}-γ curve using a closed-form solution and a linear stress assumption with effective radius at 0.8R

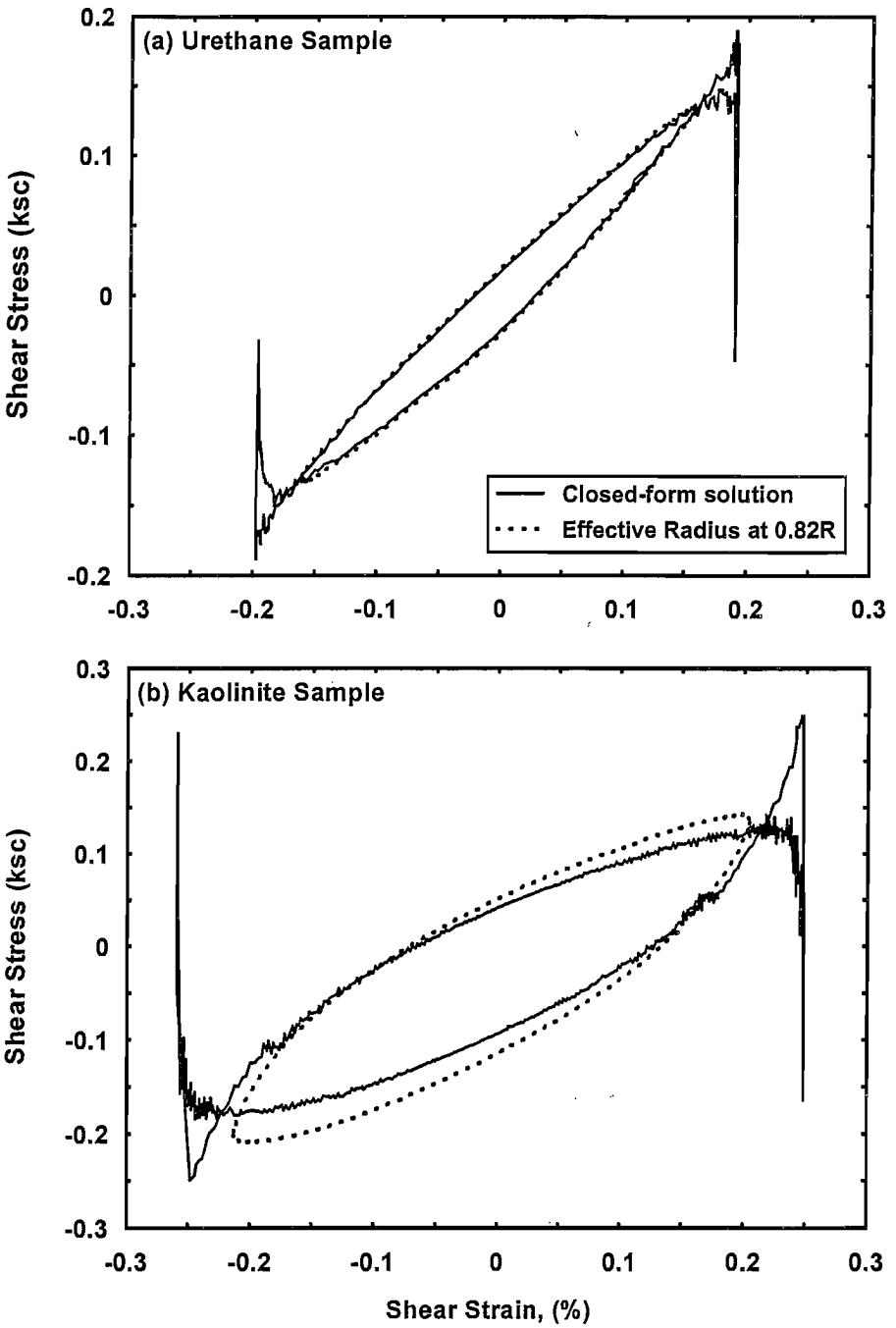

Figure B.6 Applying the closed-form solution and the effective radius at 0.8R methods to interpret the results from a cyclic torsional shear test on (a) a linear but inelastic urethane sample and (b) non-linear inelastic kaolinite sample

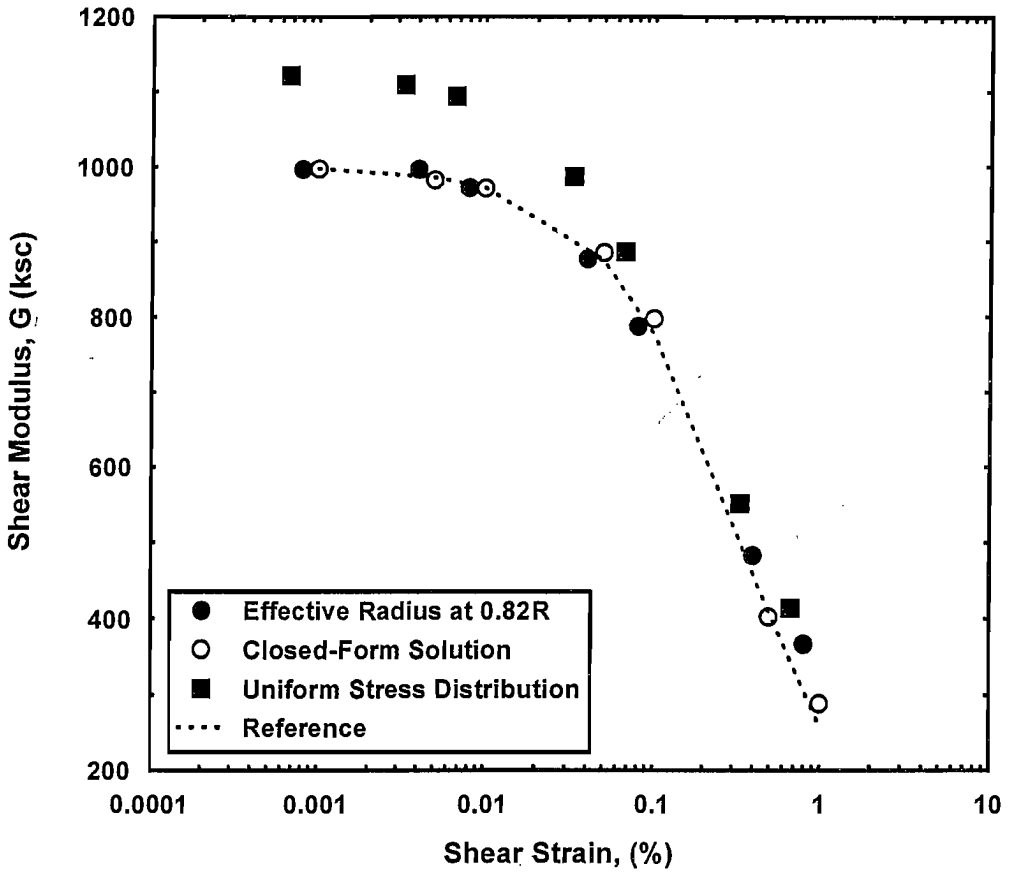

Figure B.7 The G-γ curve as predicted from hypothetical cyclic torsional shear tests using different interpretation methods

Appendix C:

Effect of Drilling and Sampling Disturbance on Dynamic Soil Properties

C.1 Introduction

Laboratory tests on soil samples retrieved from the field usually underestimate the in-situ soil stiffness, when compared with field values determined by shear wave veloicties. This has historically been attributed to disturbance caused by drilling, sampling, transportation, storage, extrusion, and sample preparation. The impact of disturbance on measured soil properties has been recognized for a long time. Hvorslev (1949) suggested that disturbance is caused by five mechanisms; change in stress condition, change in soil structure, change in water content/void ratio distribution, chemical changes, and mixing and segregation of soil constituents. More recent studies suggested that among these mechanisms, changes in the stress condition and soil structure (and their resulting deformations) caused by stress release, and mechanical disturbances are the main two factors affecting the behavior of soil samples obtained by conventional methods.

Mechanical disturbance is caused by the process of drilling, the insertion of a sampling tube, and suction during the retrieval of the sampling tube. Accordingly, one would expect that portions of the soil sample near the top (bottom of borehole) and near the cut surfaces will be disturbed the most. In contrast, stress release has a more uniform "global" effect on the sample. Another difference is that mechanical disturbance can be reduced by using improved procedures and equipment, for example by cleaning the borehole before sampling and by using a more appropriate sampler design. Alternatively, block samples can be obtained but this is generally an

expensive operation and is limited to shallow depths. Stress release, on the other hand, is an inherent consequence of the process of sampling and is unavoidable. Stress change caused by drilling is mainly due to the removal of overburden pressure, and can be reduced by using bentonite slurry while advancing the borehole. Sampling-induced stress change is caused by tube penetration and sample extrusion. Many researchers use the term "perfect sampling disturbance" to refer to a sampling process where disturbance is caused only by stress release, while the term "ideal sampling disturbance" is used when both disturbance mechanisms, i.e. stress release and structural disturbance caused mainly by tube penetration, are considered. Notice that disturbances caused by other processes, e.g. transportation and handling, are not included in either definition because they are very variable and difficult to model. Nevertheless, they are easier to reduce if proper care is taken. Therefore, this chapter will only address disturbance caused by stress release and tube penetration. In addition, since the DFSD is designed to test fine grained soils, only the effect of sampling disturbance on these soils will be discussed here. Cohesionless soils are difficult to sample without a significant change to their structure.

Despite the important impact sampling and drilling disturbance has on measured soil properties, it was not until the last two decades that researchers started to evaluate disturbance quantitatively rather than qualitatively. This trend was especially encouraged by the introduction of the Strain Path Method (Baligh, 1985). However, the phenomenon is still not fully understood and more studies are needed. Moreover, most of the available studies address the impact of disturbance on high-strain soil parameters (e.g., shear strength and failure or peak strain). Relative to dynamic soil properties occur at rather smaller strains and therefore one should be cautious when extrapolating the results of these studies.

The objective of this chapter is to introduce the state-of-the-knowledge regarding the effect of sampling disturbance on soil behavior. Since more than one mechanism is involved, it makes sense to study the effect of each one separately. As pointed out earlier, the focus will be on disturbance caused stress release and tube penetration. Disturbance caused by drilling in clays is addressed through presenting the results of a study done as part of the feasibility of the DFSD project. Before addressing these issues and in order to provide a rational basis for discussion, concepts that help understand the related aspects of soil behavior are presented first.

C.2 Limit State Boundary Concept

The concept of a limit state boundary as related to soil disturbance was presented by Tavenas and Leroueil (1977) and is illustrated in Figure C.a. It is argued that for each soil in its natural condition, there is a limit boundary of stress state beyond which a significant and irreversible deformation may develop. Therefore, an undisturbed soil sample can only be obtained if, in all the stages in the life of a sample, the stress does not go beyond this natural limit boundary. This limit state is established by stress conditions (stress level and history), aging (secondary compression), cementation, and thixotropic hardening. Therefore, normally consolidated soils behave as pseudo-overconsolidated materials, thus, exhibiting an elastic behavior below the limit boundary. As shown in Figure C.a, in the p-q diagram the limit boundary is a continuous line having the shape of an ellipse which represents the "yield" shear stress as a function of effective stress. The intersection of this curve with the K_o-line corresponds approximately to the preconsolidation pressure. The stress condition of natural clays is usually located inside this boundary. The more overconsolidated the natural clay is, the further inside it will be. Leroueil et al. (1979) showed that if a natural clay is consolidated under stresses outside the limit state curve and then rebounded to the same in-situ overconsolidation ratio, the limit

state boundary as well as the mechanical properties of that clay will be modified, as shown in Figure C.b. The study found that the shear strength and the secant shear modulus at peak strain were reduced by 25% and 50%, respectively. It should be noted, however, that this effect varies according to the sensitivity of the clay.

Even though the limit state boundary is defined in the stress field, one could also establish it in the strain field. As discussed in Chapter 2, each soil has a limit strain (i.e. the volumetric threshold shear strain) beyond which significant plastic deformations and irreversible property changes take place. It was also illustrated that the level of this strain is influenced by aging, OCR, plasticity, fabric, and effective confining pressure. Thus, it seems that the factors affecting the limit state boundary in both the stress and strain fields are the same. However, the relationship between the limit state in the stress and in the strain field is not fully understood. Also, it is still not clear in which field the limit state behavior is better described.

C.3 Disturbance Caused by the Release of In-Situ Stresses

In this section the focus will be on changes in soil behavior as a result of the undrained shear stress release from the initial anisotropic in situ stress state to the final isotropic stress condition of the sample after extrusion and before testing. All other disturbance mechanisms are neglected (hence, the name "perfect sampling"). The effect of in situ stress release can be seen in two areas. First, the potential reduction in effective stress inside the sample, which will affect the measured soil properties if the in situ effective stresses are not re-established (which is particularly important for in situ tests on soil samples). Second, whether the stress change will put the soil outside the limit state boundary (either stress- or strain-wise), thus, causing significant changes in the soil structure. To illustrate this point, if the initial in situ anisotropic stresses corresponding to point A in Figure C.a are released due to "perfect sampling", the

deviatoric stress will be monotonically reduced to zero following the path A-A_1. This will decrease the mean effective stress (negative pore water pressure) due to the generated shear stresses. However, since this stress path is within the state boundary, no structural changes are expected and the sample can be referred to as "undisturbed". On the other hand, if the clay is lightly overconsolidated, the initial stress condition may correspond to point B and the stress path may touch the limit state curve before reaching the isotropic stress condition, point B_1, as a result of perfect sampling. In this case, the clay structure is disturbed and its mechanical properties may be significantly changed.

Baligh et al. (1987) showed the effects of perfect sampling on the stress strain behavior and the effective stress path of resedimented K_o-normally consolidated Boston blue clay (BBC) (medium sensitive marine clay with PI of 20%) from triaxial tests reported by Ladd and Varallyay (1965). Curve 1 in Figure C.1 shows the "undisturbed" behavior of the NC clay when shearing from point A which corresponds to anisotropic consolidation (K_o =0.52) under a vertical stress of σ'_{vc}. Curve 2 shows the effect of perfect sampling simulated by the undrained shear stress release from point A to the isotropic state denoted by point B. Even though the mean effective stress was reduced by 8% only, perfect sampling caused a significant change in the stress-strain behavior of the soil especially at axial strains below 0.5%. The secant Young modulus at 50% of the peak strain was reduced by 20% while the undrained shear strength reduced by 15%. It should be noted that since the soil was reconstituted in the laboratory and tested under NC conditions, it is most likely that the stress condition before the test was close to the limit state boundary.

One issue that is not often discussed in the context of sampling disturbance, but which is especially important for dynamic soil properties, is the effect of time under confinement. The

limit state boundary concept suggests that, assuming perfect sampling conditions, if during stress relief the stress/strain state does not exceed the limit state, time effect should still be preserved and reflected in the way soil particles are structured. Therefore, the in situ soil behavior should be retained from the soil sample once the in situ stresses are reapplied. However, if the limit state is exceeded (e.g., with deep tube samples of saturated clay), significant changes in soil structure take place which indicates that the effect of time under confinement is lost (partially at least) and re-applying in situ stresses will not be enough to retain the in situ soil structure. Perfect sampling is practically impossible to achieve because of the mechanical distortion introduced at least by sampling tube insertion. Even with block samples, a thin layer of remolded clay at the surface of the sample is created during the carving process.

C.4 Mechanical Disturbance by Sampling Tube Insertion

In most cases, sampling tube insertion has a larger effect on soil behavior than stress release because of the large mechanical distortions involved. It generates shear stresses and plastic deformations, which will significantly reduce the mean effect stress in the sample (point C in Figure C.a) and affect the inherent soil structure. In Figure C.1, band 4 represents the unconsolidated undrained behavior exhibited by 15 samples of natural BBC soil obtained by pushing thin-walled tube. Disturbance has caused a large reduction in the mean effective stress (maintained as negative pore water pressure) and resulted in a significant modification of the stress-strain behavior of the soil. This implies that the mean effective stress in the soil after sampling is a good indication to its quality. The curves in Figure C.2 clearly suggest, and as pointed out by Baligh et al (1987), that the effect of sampling disturbance can be quite variable signifying the importance of operator-dependent disturbance. Also the data consistently shows that the effect of disturbance on soil stiffness is substantially greater than on undrained shear

strength. Baligh et al (1987) also reported that when natural BBC samples were reconsolidated under K_o-conditions to a vertical stress twice the estimated maximum past pressure and then unloaded to field stresses, their undrained behavior (band 3, Figure C.1) was similar to the behavior of "undisturbed" samples (curve 1, Figure C.1) of resedimented BBC. This conclusion may be an oversimplification of the actual situation, and should be evaluated cautiously. This is because the behavior of resedimented samples may very well be different than the in situ soil behavior because of differences in time and environmental conditions. However, both the process of sedimentation and reconsolidation to a high stress (compared to the maximum past pressure) "erases" the inherent soil structure, and therefore, it is not unexpected that the two processes will result in a similar soil behavior at the same mean effective stress. The question that remains is, how is this related to the actual in situ soil behavior? La Rochelle and Lefebvre (1971) have compared the behavior of a sensitive clay from block and tube samples taken from the same depth at different effective stresses. Some of the block samples were subjected to large strain before their undrained shear strength was determined. As shown in Figure C.2, the shear strength of tube samples was about 30% smaller than those of block samples. The reported tangent Young modulus was also smaller, by 50%, for the tube samples. On the other hand, after subjected to large strains, block samples had similar strength characteristics as tube samples, which imply that the latter were subjected to large strains during sampling.

It is clear that sampling tube insertion causes large changes in the stress condition in the soil, which may exceed its limit state boundary, therefore causing significant changes to its structure. Those changes are difficult to track or represent by a stress path. Baligh (1985) has argued that the undrained penetration of rigid objects into deep saturated clay is strain-controlled and independent of the shearing resistance of the soil due to kinematic constraints. In another

words, the process of sampling is reduced to a flow problem where soil particles move along streamlines around a fixed rigid body. Baligh (1985) proposed what he called the Stain Path Method, SPM, in which it is assumed that soil deformations can be estimated with a reasonable accuracy without the need to consider constitutive relations but by estimating the velocity field satisfying the conservation of volume and boundary conditions. The velocity field describes the velocity of the soil particles as they move around the penetrating object and from which soil deformation can be obtained by integration. Baligh's analyses showed that the strain levels are much greater than normally encountered in laboratory tests and can be up to 50% near the sampler tube itself. In addition, initial failure of the soil located near the sample axis takes place a head of the tube. As shown in Figure C.3, in the radial direction the soil is monotonically pushed outward to a position that is imposed by conservation of volume. On the other hand, in the vertical direction, the movement is not monotonic but the soil is initially pushed downward in the direction of penetration and then pushed upward after the passage of the sampling edge. Moreover, sampling disturbance depends on the soil type and tube geometry. Normally consolidated soils have a brittle behavior compared to overconsolidated soils and therefore will be more disturbed. Tube geometry as reflected in the diameter-to-thickness ratio (B/t) or area ratio and shoe-geometry which is characterized by the inside and outside cutting angels (ICA and OCA, respectively), have a large influence on the degree of disturbance experienced by the soil. A tube with a larger B/t and sharper cutting edge will result in less disturbance. Figure C.4 shows the theoretical strain history at the centerline of the sample obtained using tubes with different B/t ratios. For a typical thin-walled Shelby tube with B/t of 40 to 47 (area ratio of about 10%), the process of sampling is roughly equivalent to one axial strain cycle with peak strain of 1%. The results indicate that the soil is subjected to three phases of triaxial shearing, (1) an initial

compression phase ahead of the sampler where the axial strain increases from zero to a maximum, (2) an extension phase in the vicinity of the cutting edge, and (3) a second compression phase during which the axial strain goes back to zero. For normally consolidated soils an axial strain of 1% may be beyond the strain at failure. Baligh et al. (1987) suggested the following formula to estimate the maximum axial strain, ε_{max}, during sampling as a function of the t/B ratio of the tube:

$$\varepsilon_{max} = 0.385\frac{t}{B} \qquad \text{K (5.1)}$$

Clayton et al (1998) implemented the SPM in a finite element code using an analytical solution based on Bessel functions, and found similar results to Baligh (1985). In an effort to simulate and evaluate the effect of "ideal sampling disturbance" which involves the effects of stress release and tube penetration but neglects all other types of disturbances, Baligh et al. (1987) conducted a laboratory testing program on block samples of resedimented Boston Blue clay by K_o-consolidation from slurry. Specimens for triaxial testing were cut from block samples and reconsolidated in the triaxial cell under K_o-conditions to an initial vertical stress three to four times the preconsolidation stress in order to obtain K_o-normally consolidated samples. Then six types of tests were conducted. In test 1, some of the samples were subjected to monotonic undrained shearing to determine the reference "undisturbed" NC behavior of the soil before disturbance. In test 2, ideal sampling disturbance was simulated by subjecting some of the NC samples to (1) the undrained strain path predicted by SPM for soil elements along the center line of a sampling tube with B/t=40 and inside clearance ratio ($(D_{inside}-D_{min})/ D_{min}$ x 100) of 1% and (2) the undrained stress relief to an isotopic stress state to model sample retrieval and extrusion. In test 3, the soil was subjected to the same disturbance as in test 2 but without stress relief. In tests 4, 5, and 6 the samples were K_o-reconsolidated, after applying ideal sampling disturbance

and before shearing, to a vertical stress of σ'_{vm}, 1.5 σ'_{vm}, and 2 σ'_{vm} (maximum past pressure), to reduce the effect of disturbance as proposed by the Recompression and SHANSEP techniques. Figure C.5a and b present the stress path and the soil stress-strain behavior during ideal disturbance which involves compression to 1% axial strain (ab), extension to -1% (bc), recompression to 0% strain, and finally undrained stress relief (de). The results show that as a consequence of ideal sampling disturbance, the mean effective stress was reduced by 62% compared to perfect sampling disturbance which involved only 8% reduction. Figure C.5c shows a comparison between the stress paths obtained from "undisturbed" samples (test 1), samples subjected to ideal (test2) and perfect disturbance, and from a UU test on a good quality tube sample taken from natural BBC soil. The results indicate that much of the disturbance is due to tube penetration, which seems to account for most of the disturbance effects observed in UU tests on good-quality samples. The remaining difference is probably due to operator-dependent other types of disturbance. Figure C.6 shows the stress-strain and stress path behavior from all tests described above. The results indicate that tube penetration disturbance significantly change soil behavior. Samples from tests 2 and 3 have similar stress paths and stress-strain behavior at strain levels above 0.5% but at smaller strain levels the rebounded sample (test 2) has a higher stiffness. On the other hand, most aspects of ideal sampling disturbance effects were reduced by re-establishing the initial mean effective stress with SHANSEP method (consolidation to a stress beyond σ'_{vm} and then rebound to in situ stresses) giving better results than the Recompression method (reconsolidation to in situ stresses). It should be noted, however, that resedimented clays, such as those used in Baligh's study, are devoid of soil structure gained during aging of soil, therefore, much of the disturbance effect in the above study is merely due to the reduction in

mean effective stress. Therefore, the concept of limit state boundary may not apply here. Also this means that the study overestimated the effect of reconsolidation in "erasing" disturbance.

C.5 Effect of Disturbance on Dynamic Soil Properties

The discussion presented above forms the basis for evaluating the effect of disturbance on dynamic soil properties. The concept of a limit state boundary is especially important because it is supported by many experimental observations. This concept indicates the presence of a yield stress/strain after which the soil behavior is significantly changed. Below this limit state, the in situ soil behavior is largely preserved and reflects the effect of stress history, aging, and other environmental conditions that are manifested in void ratio, chemical bonds, and structure. For some situations, these processes affect mainly the void ratio (pseudo-consolidation), which explains why a technique like SHANSEP (which involves rebound) is successful in retaining the in situ behavior. If disturbance induces stress/strain conditions that exceed this limit state, the inherent in situ soil behavior is changed. The degree of this modification depends on the degree of disturbance and the degree of initial structuring of the soil, which is usually a function of its age and depositional environment. This is evident from the observation that the difference between G_{max} obtained from field and laboratory tests is usually smaller in young soils (e.g. Holocene deposits) than old soils (e.g., Pleistocene deposits). There is also evidence, as will be shown later, that even with a moderate degree of disturbance part of the in situ behavior is retained. The above observations are also supported by the fact that disturbance affects the shape of the e-log(P) curve obtained from consolidation testing. The larger the degree of disturbance, the less clearly defined the maximum past pressure (sometimes referred to as yield stress) will be, and the closer the slope of the recompression curve to the virgin curve. This observation is

closely related to the limit state boundary concept since the maximum past pressure also reflects in situ conditions.

Despite the wide recognition of the effect of sampling disturbance on dynamic soil properties, few studies have directly addressed the issue. Lohani et al. (1999) studied the effect of sampling disturbance on the dynamic behavior of Holocene clay deposits by comparing the value of G_{max} of samples of natural clays with different degrees of disturbance, and with reconstituted samples. Samples from three natural clay deposits were tested; Bangkok clay (Thailand), Ariake clay (Japan), and Louiseville clay (Canada). Bangkok clay is a soft marine clay (S_u around 15 kPa) with PI of 60-70% and is believed to have been deposited around 4000 years ago. Samples from two sites were obtained, one where the clay deposit is 4-5 m thick (AIT series, samples A1 and A2), and the other where it is 12m thick (AIT series, samples N1 and N2). The Ariake clay is located on the Kyushu Island of Japan and has a PI of 50%, but the natural water content is high and close to the liquid limit, suggesting a higher degree of sensitivity. The samples (YNU series, samples ak3 and ak4) were obtained from a site where the clay deposit is about 15 m thick. The Louiseville clay is a medium stiff marine clay (series YNU, samples lv1 and lv2) with a PI of 49%, OCR between 1.4 and 4, and an estimated age of 10,000 years. Samples at all sites were obtained using a thin-walled fixed-piston sampler (FP) driven mechanically at a constant rate and were handled with great care, and therefore high-quality samples were obtained. For the Bangkok clay deposit, additional samples were also obtained using a commonly-used floating-piston sampler with manual driving (ST). Also, for all soils, reconstituted samples (RC) were prepared from slurries and consolidated at pressures of 49 and 98 kPa. G_{max} Measurements were obtained from bender element tests with 50 Hz square-shaped waveform. Figure C.8 and Figure C.9 show the e-log(σ'_{vc}), log(G_{max})-log(σ'_{vc}), and the e-

log(G_{max}) curves for all samples. As expected, the data consistently shows that the consolidation curves of FP samples are better defined (around the maximum past pressure or yield stress) than ST samples, thus, indicating better-quality and less-disturbed samples. The data clearly shows a two-phase log(G_{max})-log(σ'_{vc}) relationship separated by the yield stress (i.e., a limit state boundary). At effective stresses above the yield stress, i.e. virgin loading, values of G_{max} from all samples including RC samples fall close to each other and show a large dependence on the level of stress/void ratio. This behavior clearly suggests less dependency on the degree of disturbance because the inherent in-situ soil structure (or what is left of it after sampling) has been "erased" after consolidation under a stress higher than the yield stress (i.e., exceeding the limit state boundary). At "pre-yield" stresses, another trend is observed where measured values of G_{max} show less dependency on stress level but more dependency on the degree of disturbance. The less-disturbed FP samples have higher G_{max} values than the ST samples. Values of G_{max} for RC samples represent a lower bound. The larger the degree of disturbance, the larger the slope, m, of the log(G_{max})-log(σ'_{vc}) curve. This is because at this stress range, samples are consolidated to a stress state below the limit state, therefore, soil behavior depends on how much of the inherent in situ soil structure is preserved after disturbance. RC samples are devoid of soil structure, hence, they have no yield stress and show the same dependency on stress and the same slope m regardless of the stress level. Therefore, they represent a complete disturbance and destructuring of the inherent in situ soil fabric. The only exception to this behavior was observed from tests on Araike clay, in which the G_{max} of RC samples were higher, mainly because in remolding this sensitive clay the density at a given stress is substantially higher. Since the yield stress separates elastic from plastic behavior, one would expect that soil stiffness (i.e., G_{max}) at any pre-yield stress to be less dependent on the stress level. Accordingly, the log(G_{max})-log(σ'_{vc}) curve should

be close to a horizontal line at this stress range. This behavior is clearly observed from tests on Louiseville clay, perhaps because it is a relatively old, overconsolidated clay which means that its in situ state is far from its limit state, making it more tolerant to disturbance. The results also suggest that this pre-yield stress behavior is not necessarily a consequence of a smaller level of void ratio resulting from stress rebound or pseudo-consolidation, but something else, perhaps the particle arrangement, chemical bonding, or cementation. This observation is obvious from the tests on Bangkok clay, where the void ratios of FP samples were higher than all other samples, but their G_{max} were also the largest.

The above observations and conclusions are summarized in the conceptual sketch presented in Figure C.10 which shows the field $\log(G_{max})$-$\log(\sigma'_{vc})$ relation and the effect of the degree of disturbance on it. As discussed before, two phases are identified and separated by the yield stress, which is right on the limit state boundary and is a function of the soil's age, stress history, and other in situ environmental conditions. At an effective stress level below the yield stress, the inherent soil structure is preserved, the soil exhibits an elastic behavior, and the stiffness is independent of stress level. Beyond the yield stress, the current limit state boundary corresponding to the in situ conditions is exceeded, therefore, the current soil structure is altered and the soil behaves plastically as its stiffness becomes dependent on the stress level. Young and normally consolidated soils have their in situ stress state close to the yield stress, while old and overconsolidated soils have their in situ stress state farther to the left. Figure C.11 illustrates, schematically, how aging (reflected in secondary compression, structuring, etc.) affects the $\log(G_{max})$-$\log(\sigma'_{vc})$ relation of the soil by increasing the yield stress and stiffness.

During sampling, disturbance alters part of the inherent soil structure causing an apparent decrease in the yield stress and soil stiffness. The apparent behavior will be somewhere between

the truly "undisturbed" (field) behavior and the completely remolded "destructured" behavior, which is equivalent to re-sedimentation. The larger the degree of disturbance, the more the destructuring of the soil and the closer its behavior to the remolded soil. Lohani et al. (1999) suggested the following parameter, $(SD)_{Gmax}$, to quantify the effect of disturbance on dynamic soil properties:

$$(SD)_{G_{max}} = \frac{(m - m_{field})}{(m_{RC} - m_{field})} \qquad \text{K (5.2)}$$

where m, m_{field}, and m_{RC} are the slopes of the $\log(G_{max})$-$\log(\sigma'_{vc})$ curve for the disturbed, "undisturbed" and reconstituted samples, respectively. Since, theoretically, the $\log(G_{max})$-$\log(\sigma'_{vc})$ curve of truly undisturbed sample is a horizontal line, m_{field} is zero and the formula reduces to:

$$(SD)_{G_{max}} = \frac{m}{m_{RC}} \qquad \text{K (5.3)}$$

For example, the $(SD)_{Gmax}$ value for the FP and ST samples of Bangkok clay is 23 and 52%, respectively, while for the FP samples of Louiseville clay it is 0.05%. When compared to results from field tests, Lohani (1999) reported that $G_{max,lab}$ is at least 20% smaller than $G_{max,field}$.

Similar behavior was found by Kalinski (1998) and Kalinski et al. (1999) in a study to measure the in situ $\log(G_{max})$-$\log(\sigma'_{vc})$ using the newly developed borehole SASW tool. The method involves the measurement of axially propagated surface waves inside an uncased borehole using the SASW approach and an inflatable tool. Inflation pressures applied by the tool are used to vary radial stresses in the surrounding soil and the dispersion curve is measured for each pressure. Based on these measurements, the variation in V_s (and hence G_{max}) with distance from the wall of the borehole is determined. These tests made it possible to determine the in situ $\log(G_{max})$-$\log(\sigma'_{vc})$ relation for the first time. Kalinski et al. (1999) conducted an in situ borehole

SASW test on a poorly-graded silty sand. The estimated σ'_h and K_o is around 10 kPa and 0.5. Another cross-hole test was also conducted on the same material, and resonant column testing was performed in the laboratory on "undisturbed" specimens obtained using a thin-wall sampling tube. Figure C.11a shows the measured V_s as a function of distance from the borehole wall at each inflation pressure. The $\log(G_{max})$-$\log(\sigma'_{vc})$ relation from in situ and laboratory tests as well as the range of G_{max} from cross-hole tests are shown in Figure C.11b. It is interesting to notice the similarity between Figure C.9 and Figure C.11. At a stress range close to the in situ stresses, the results show that resonant column tests underestimate G_{max} and predict more sensitivity (larger slope) to stress level than in in-situ tests because of disturbance, a behavior similar to that in the previous study. As the stress level increases well beyond the in situ level (which is close to the yield stress), G_{max} predicted by laboratory and field tests start to converge indicating increased destructuring of the soil. Also the slope of the $\log(G_{max})$-$\log(\sigma'_{vc})$ relation determined at different distances from the borehole wall decreases as the distance increases. This observation is in agreement with previous observations because the degree of disturbance of the surrounding soil (from drilling the borehole) decreases as the distance from the borehole wall increase.

Lo Presti et al. (1999a) conducted bender element tests in vertical and horizontal directions inside a triaxial apparatus to study the anisotropy of G_{max} of "undisturbed" and reconstituted samples and the effect of disturbance simulated by axial straining. The results show that the process of straining modified the inherent anisotropy by increasing the difference between $G_{max,v}$ and $G_{max,h}$. The study also found that a monotonic axial strain of 4% caused 20% reduction in G_{max}. Similarly, Viggiani and Atkinson (1995) found that G_{max} of reconstituted kaolinite samples were reduced by 5% after 1% shear strain. It should be noted, however, that these specimens were already affected by sampling disturbance or resedimentation, and so may

not accurately reflect in situ soil behavior. Lo Presti et al. (1999b) suggested that the change in void ratio during reconsolidation of natural soil samples be used as an indication of sample quality. More disturbed samples undergo larger volume change when reconsolidated to in situ stresses than less disturbed soil, an observation which is consistent with the discussion above and Figure C.9.

Many studies have also investigated the effects of laboratory testing conditions on the dynamic properties of soil samples. Tatsuoka et al. (1997) reported that aging after reconsolidation has more effect on the G_{max} of a soil sample than the re-consolidation stress path, while Athanapoulous and Richart (1984) showed that the effect of different reconsolidation stress paths on G_{max} increases with increasing degree of disturbance. Mukabi et al. (1994) and Jardine (1994) reported that overconsolidation with swelling in the reconsolidation procedure may be employed to compensate for disturbance and aging effects but noticed that this method has more effect on the non-linear range. Jamiolkowski et al. (1994), however, reported that this effect vanishes when correction is made for volume change during overconsolidation. On the other hand, Tatsuoka et al. (1997) suggested that for high quality undisturbed samples of stiff natural clays, $G_{max,lab}$ should be very close to $G_{max,field}$. Mukabi and Tatsuoka (1999) conducted a series of tests on high quality samples of stiff overconsolidated natural clay (either using a fixed-piston thin-walled tube or block samples) reconsolidated to in situ stresses using different stress paths and under different aging periods. The results showed little difference in initial stiffness between different samples, but rebounded samples and samples aged to longer periods showed a more linear behavior at larger strains. The study also included tests on reconstituted samples consolidated to the same yield stress and rebounded to the in situ stress conditions. Even though the void ratio of reconstituted samples was smaller than natural samples, their initial moduli were

much smaller and they showed a more non-linear behavior. This clearly indicates the importance of soil structure. The same results were obtained by d'Onofrio et al. (1999), who also found that small-strain damping ratio was higher in reconstituted samples than in intact samples.

C.7 Summary and Implications for Tool development

The concept of the limit state boundary as related to the sampling process seems to be an effective approach to evaluate the effect of disturbance on dynamic soil properties. If disturbance induces conditions that exceed the limit state, significant changes to soil structure are likely to occur. The degree of those changes depends on the degree of disturbance and soil type. For a moderate degree of disturbance, stiff and overconsolidated soils seem to suffer less than soft and lightly overconsolidated soils, perhaps because their limit state boundary and yield locus are farther from their in situ condition. Less-disturbed samples show smaller volume change after reconsolidation to in situ stresses and their stiffness is less dependent on effective stress. On the other hand, more-disturbed samples are more sensitive to reconsolidation stress path and aging. The effect of disturbance can also be examined in the strain domain by utilizing the concept of the volumetric threshold strain, which separate the elastic from the plastic behavior of the soil. A sampling process which results in strains beyond this threshold will cause a large amount of permanent plastic deformation and damage to the soil structure. The estimated lower bound of the volumetric threshold strain is in the range 0.01 to 0.1%. However, these values are based on laboratory tests on soil samples, which may underestimate the extent of the linear zone exhibited by the in situ soil. Also, these values are based on one direction of strains, while other straining conditions (e.g., unloading vs. simple shear) may imply larger volumetric threshold strains. Experimental results show that moderate disturbance seems to affect G_{max} by 20-40%.

Disturbance also seems to decrease the initial linear zone, or put in other words, it increases the non-linear behavior of the soil. However, the observed reduction in G_{max} seems very moderate given the high amplitude of sampling-generated strains predicted by Baligh's work. This is especially true when one realizes that laboratory tests on soil samples are also affected by many other processes like transportation, storage, handling, extrusion, and preparation, which might have more adverse effects on the specimen than sampling tube insertion. This leads one to believe that a downhole in-situ test that circumvents many disturbance-generating processes, minimizes sampling disturbance by cutting through the soil instead of displacing it and by optimizing the sampler design and minimizing the stress release, and one that targets the least-disturbed material, will result in high-quality samples with properties that fairly accurately represent the in situ soil behavior. Moreover, such a device will be particularly valuable for testing deep clay deposits, where samples obtained by conventional sampling techniques are likely to have a large degree of disturbance due to the large amount of unloading and cavitation of pore water.

References

ABAQUS, (1994). "ABAQUS 5.3 Theory manual and User's manual I and II," Hibbitt, Karlsson, & Sorensen, Inc., Pawtucket, R.I.

Athanasopoulos, G.A., and Richart, F.E. (1984). "Effect of stress release on shear modulus of clays," Journal of Geotechnical Engineering Division, ASCE, Vol. 109, No. 10, pp. 1233-1245.

Baligh, M.M. (1985). "Strain path method," Journal of Geotechnical Engineering, ASCE, Vol. 111, No. 9, pp. 487-501.

Baligh, M.M., Azzouz, A.S., and Chin, C-T. (1987). "Disturbance due to ideal tube sampling," Journal of Geotech. Eng. Div., ASCE, Vol. 113, No. 7, pp. 739-757

Clayton, C.R.I., Siddique, A., and Hopper, R.J. (1998). "Effects of sampler design on tube sampling disturbance-numerical and analytical investigation," Geotechnique, Vol. 48, No. 6, pp.847-867.

Dafalias, Y.F. (1986). "Bounding surface plasticity. I: Mathematical foundation and the concept of hydroplasticity," Journal of Engineering Mechanics Division., ASCE, Vol. 112, No. 9, pp. 966-987.

d'Onofrio, A., Vinale, F., and Silvestri, F. (1999). "Effects of micro-structure on the stress-strain behavior of two natural clays," Proceedings of the 2nd International Symposium on Pre-Failure Deformation Characteristics of Geomaterials-IS Torino, M. Jamiolkowski, R. Lancellotta, and D. Lo Presti (eds.), A.A. Balkema, Rotterdam, Vol. 1, pp. 257-264.

Herrmann, L.R., and Kaliakin, V.N. (1987). "User's manual for SAC2, a two-dimensional nonlinear, time dependent soil analysis code using bounding surface elastoplasticity-viscoplasticity model," Report, Department of Civil Engineering, University of California, Davis.

Herrmann, L.R., and Mish, K.D. (1983). "Finite element analysis for cohesive soil, stress and consolidation problems using bounding surface plasticity theory," Report, Department of Civil Engineering, University of California, Davis, October 1983.

Hvorslev, J.M. (1949). "Subsurface exploration of and sampling of soils for civil engineering purposes," Waterways Experiment Station, Vicksburg, Miss., 521 pp.

Jamiolkowski, M., Lancellota, R., and Lo Presti, D.C.F. (1994). "Remarks on the stiffness at small strains of six Italian clays", Proc., International Symp. on Pre-Failure Deformation Characteristics of Geomaterials, IS-Hokkaid '94', Balkema, Vol. 2, pp. 817-836.

Jardine, R.J. (1994). "One perspective of the pre-failure deformation characteristics of some geomaterials," Proc., International Symp. on Pre-Failure Deformation Characteristics of Geomaterials, IS-Hokkaid '94', Balkema, Vol. 2, pp. 855-885.

Kaliakin, V.N. (1985). "Bounding surface elastoplasticity-viscoplasticity for clays," Ph.D. Dissertation, University of California at Davis.

Kalinski, M.E. (1998). "Determination of in situ material properties using surface wave measurements in cased and uncased holes," Ph.D. Dissertation, University of Texas at Austin.

Kalinski, M.E., Stokoe, K.H., Young, Y.L., and Roesset, J.M. (1999). "In situ $\log(G_{max})$-$\log(\sigma')$ relationships using a borehole SASW tool," Proceedings of the 2nd

International Symposium on Pre-Failure Deformation Characteristics of Geomaterials-IS Torino, M. Jamiolkowski, R. Lancellotta, and D. Lo Presti (eds.), A.A. Balkema, Rotterdam, Vol. 1, pp. 371-378.

Ladd, C.C., and Varallyay, J. (1965). "The influence of stress system on the behavior of saturated clays during undrained shear," Research Report R65-11, No. 177, Dept. of Civil Engineering, M.I.T., Cambridge, Mass., 263 pp.

La Rochelle, P., and Lefebvre, G. (1971). "Sampling disturbance in Champlain clays," In Sampling of Soil and Rock, American Society of Testing and Materials, Special Technical Publication 483, pp. 143-163.

La Rochelle, P., Sarrailh, J., Tavenas, F., Roy, M., and Leroueil, S. (1981), "Causes of sampling disturbance and design of a new sampler for sensitive soils," Canadian Geotechnical Journal, Vol. 18, pp. 52-66.

Leroueil, S., Tavenas, F., Brucy, F., La Rochelle, P., and Roy, M. (1979). "Behavior of destructured natural clays," Journal of Geotechnical Engineering Division, ASCE, Vol. 105, No. GT6, pp. 759-778.

Li, X.S., Holland, J., Wang, G., and Roblee, C.J. (1997). "Analysis of stress-change disturbance caused by ideal drilling in clay," Journal of Geotech. and Geo-environmental Eng. Division, ASCE, Vol. 123, No. 7, pp. 626-634.

Li, X.S., Roblee, C.J., and Wang, G. (1993). "Development and evaluation of a prototype tool for in situ determination of high-strain properties of soft to medium-stiff clays," Report No. FHWA/CA/TL-94/05, Research Project F92TL05, Caltrans, Division of New Technology, Materials and Research, Office of Geotechnical Engineering.

Lohani, T.N., Imai, G., and, Shibuya, S. (1999). "Effect of sample disturbance on G_{max} of Holocene clay deposits," Proceedings of the 2nd International Symposium on Pre-Failure Deformation Characteristics of Geomaterials-IS Torino, M. Jamiolkowski, R. Lancellotta, and D. Lo Presti (eds.), A.A. Balkema, Rotterdam, Vol. 1, pp. 115-122.

Lo Presti, D.C.F., Pallara, O., and Jamiolkowski, M. (1999a). " Anisotropy of small strain stiffness of undisturbed and reconstituted clays," Proceedings of the 2nd International Symposium on Pre-Failure Deformation Characteristics of Geomaterials-IS Torino, M. Jamiolkowski, R. Lancellotta, and D. Lo Presti (eds.), A.A. Balkema, Rotterdam, Vol. 1, pp. 3-10.

Lo Presti, D.C.F., Jamiolkowski, M., Pallara, O., and Tordella, M.L. (1999b). "Assessment of sample disturbance in the Laboratory ," Proceedings of the 2nd International Symposium on Pre-Failure Deformation Characteristics of Geomaterials-IS Torino, M. Jamiolkowski, R. Lancellotta, and D. Lo Presti (eds.), A.A. Balkema, Rotterdam, Vol. 1, pp. 11-18.

Mukabi, J.N., Tatsuoka, F. (1999). "Effects of stress path and aging in reconsolidation on deformation characteristics of stiff natural clays," Proceedings of the 2nd International Symposium on Pre-Failure Deformation Characteristics of Geomaterials-IS Torino, M. Jamiolkowski, R. Lancellotta, and D. Lo Presti (eds.), A.A. Balkema, Rotterdam, Vol. 1, pp. 131-140.

Mukabi, J.N., Tatsuoka, F., Kohata, Y., and Akino, N. (1994). "Small strain stiffness pf Pleistocene clays," Proc., International Symp. on Pre-Failure Deformation Characteristics of Geomaterials, IS-Hokkaid '94', Balkema, Vol. 1, pp. 189-195.

Tatsuoka, F., Jardine, R.J., Lo Presti, D., Benedetto, D.H., and Kodaka, T. (1997). "Characterizing the pre-failure deformation properties of geomaterials," Theme Lecture, ICSMFE, Hamburg, Vol. 4, pp. 2129-2164.

Tavenas, F., and Leroueil, S. (1977). "Effects of stresses and time on yielding of clays," Proceedings, 9th International Conference on Soil Mechanics and Foundation Engineering, Tokyo, Vol. 1, pp. 319-326.

Viggiani, G., and Atkinson, J.H. (1995). "Stiffness of fine-grained soils at very small strains," Geotechnique, Vol. 45, No. 2, pp. 249-255.

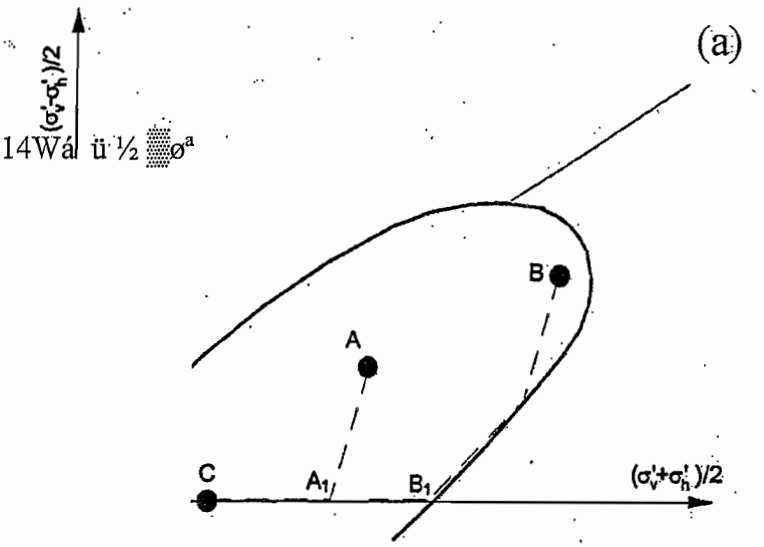

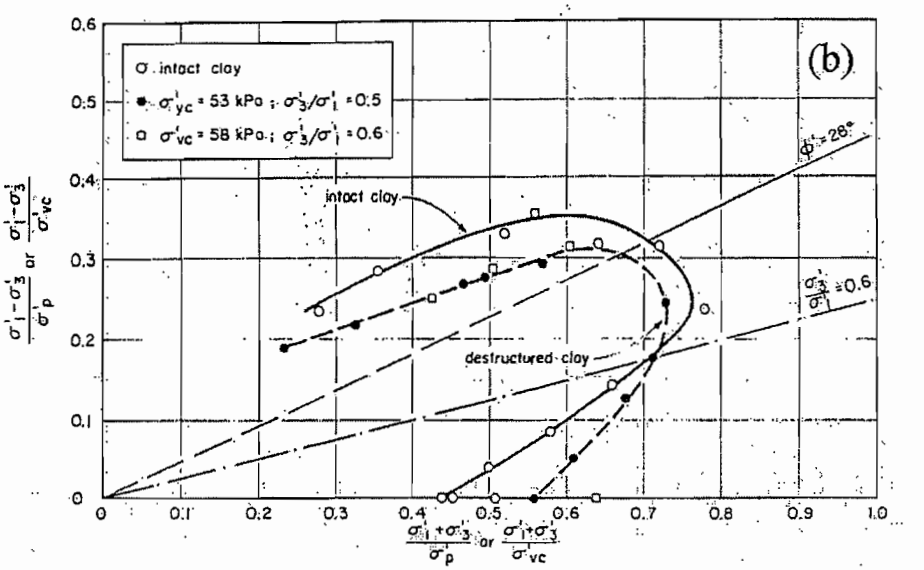

Figure C.1: (a) Limit state curve for natural clays and stress change caused by sampling (Tavenas and Leroueil, 1977), and (b) limit state curves of intact and destructured clay (Leroueil et al., 1979)

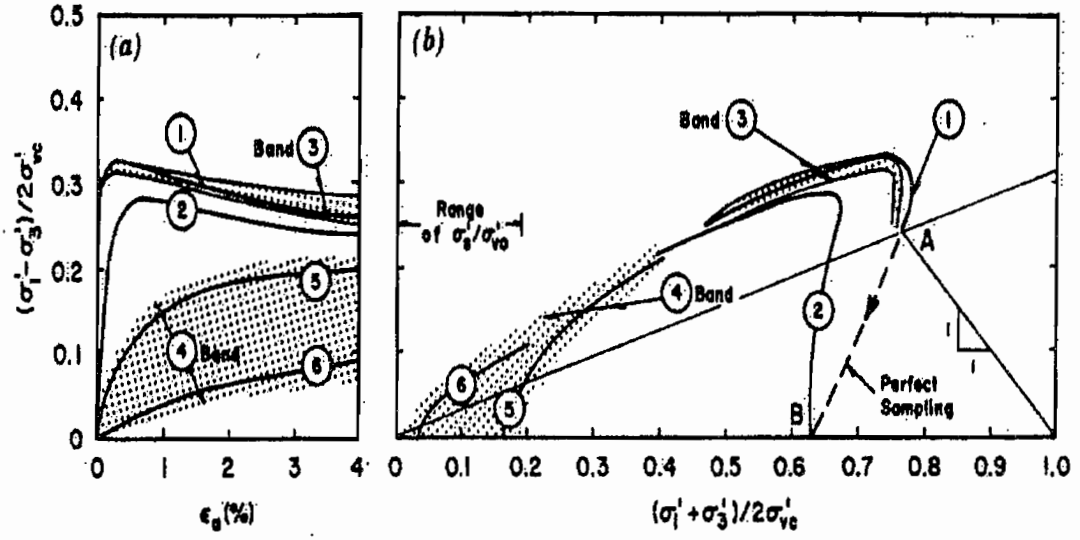

Figure C.1: Undrained behavior of BBC in triaxial compression tests: (a) stress-strain; and (b) effective stress paths (Baligh et al., 1987)

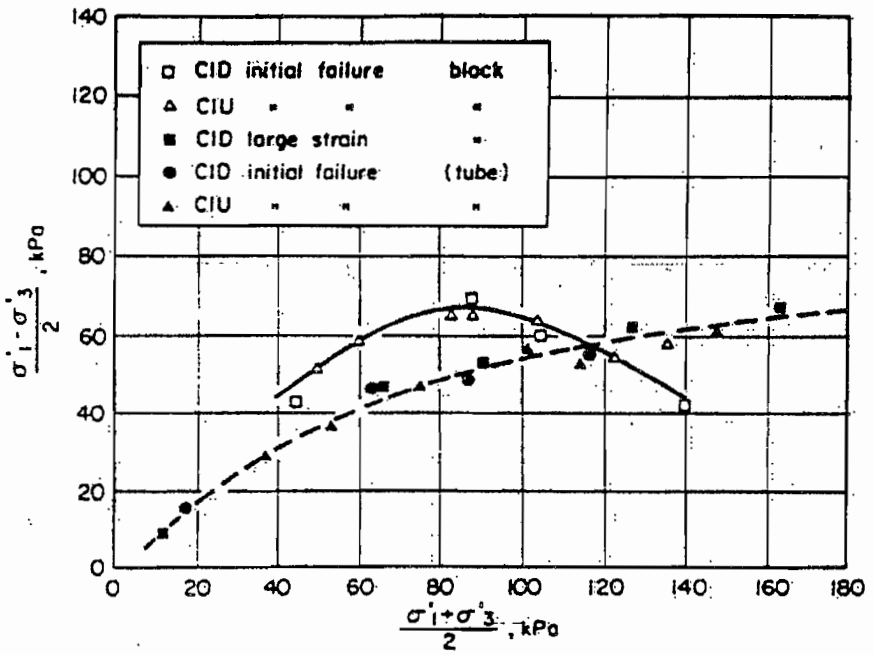

Figure C.2: Effective strength envelopes of tube and block samples of Champlain clay (La Rochelle and Lefebvre, 1971)

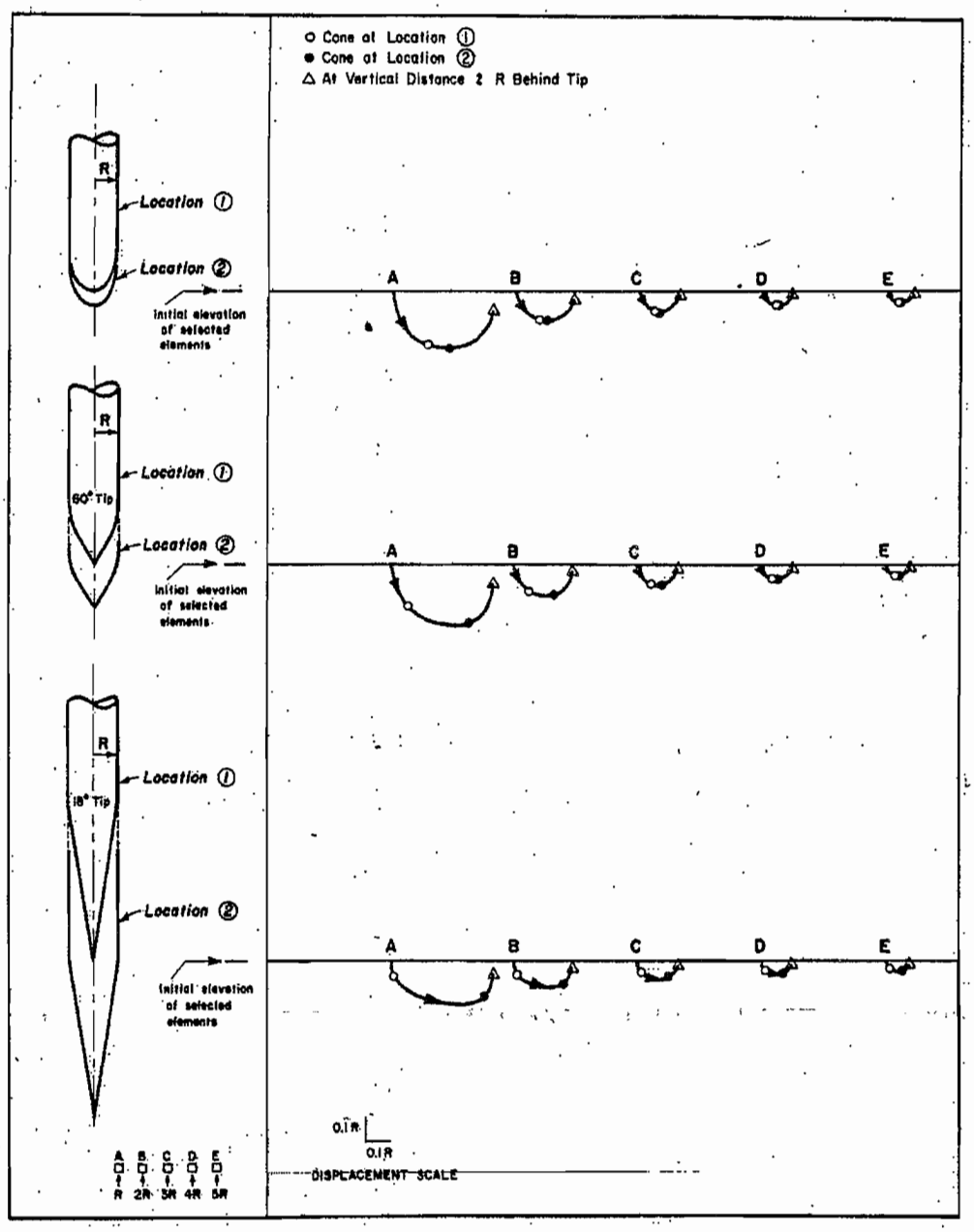

Figure C.3: Soil deformation paths during tube penetration (Baligh, 1985)

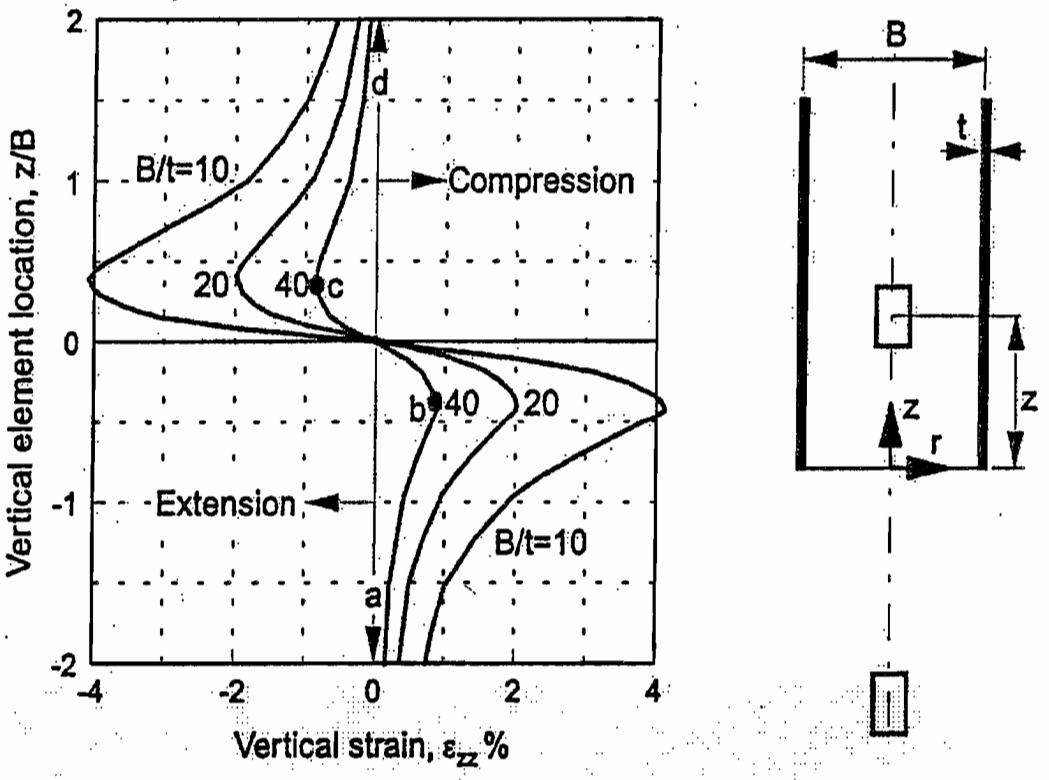

Figure C.4: Strain history at sampler centerline (Baligh, 1985)

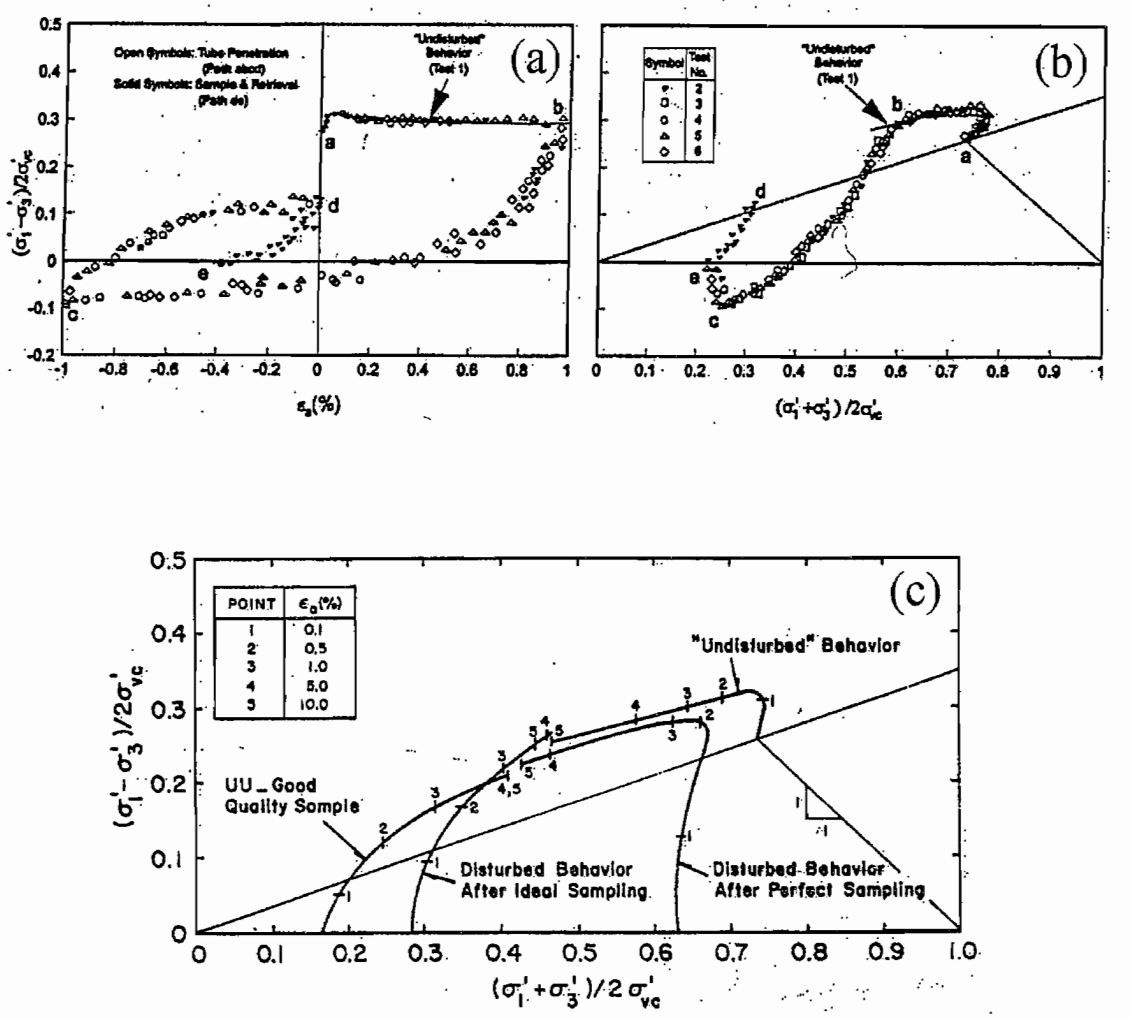

Figure C.5: (a) stress-strain and (b) stress path of the simulation of ideal sampling disturbance; (c) comparison of ideal versus perfect sampling (Baligh et al., 1987)

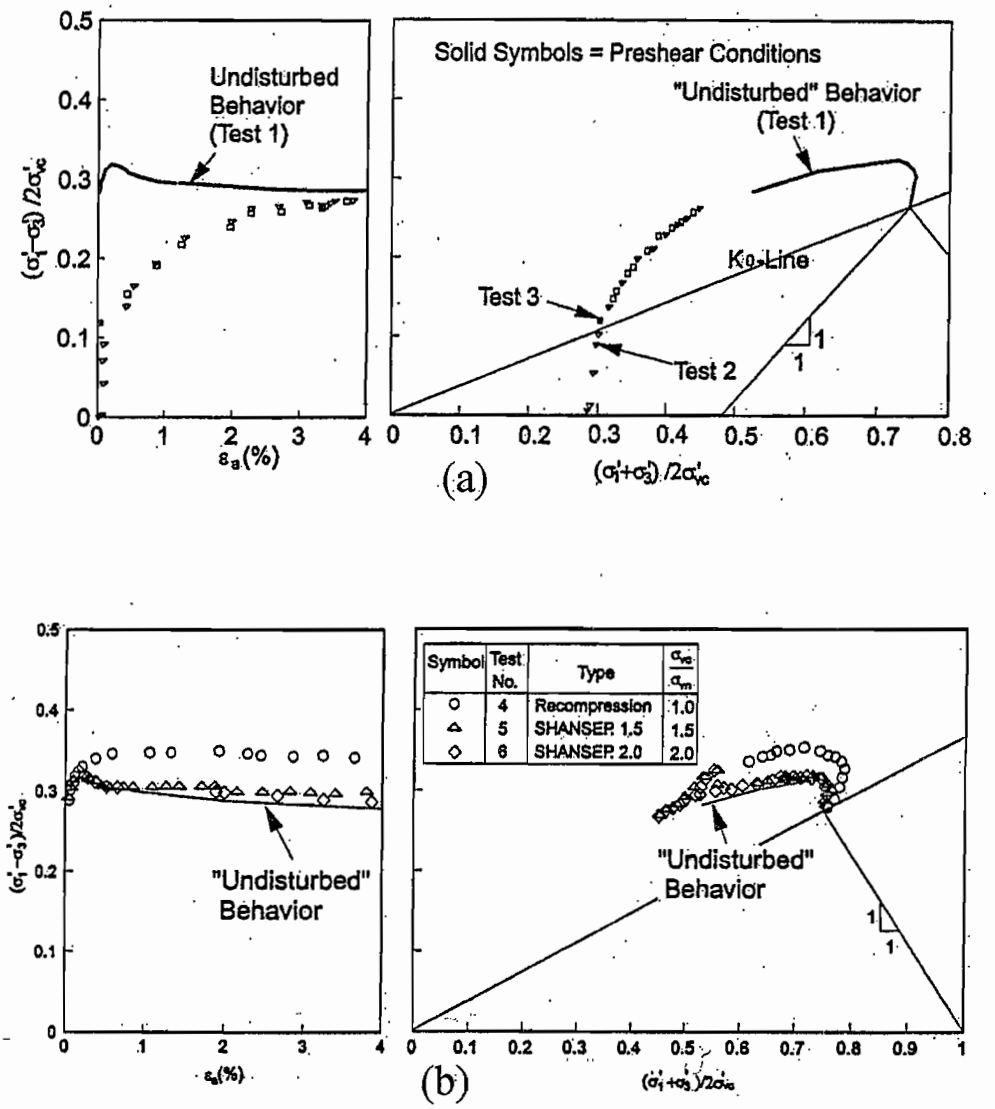

Figure C.6: (a) Tube penetration effects in ideal sampling disturbance and (b) effect of reconsolidation (Baligh et al., 1987)

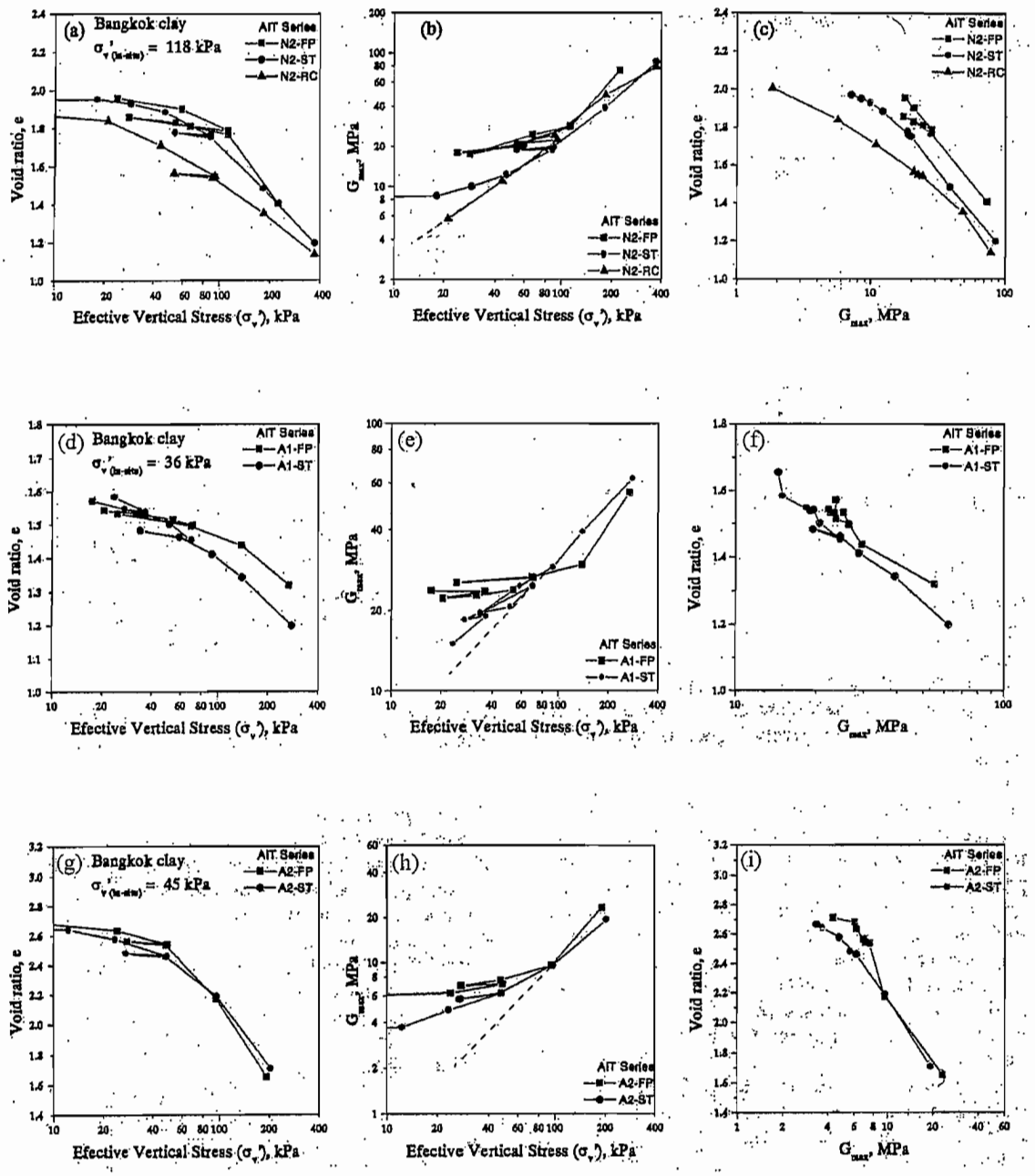

Figure C.7 Relationship between e, σ'_{vc}, and G_{max} in FP and ST samples of Bangkok clay series AIT-N2 (a-c), series AIT-A1 (d-f), and series AIT-A2 (g-i) (Lohani et al., 1999)

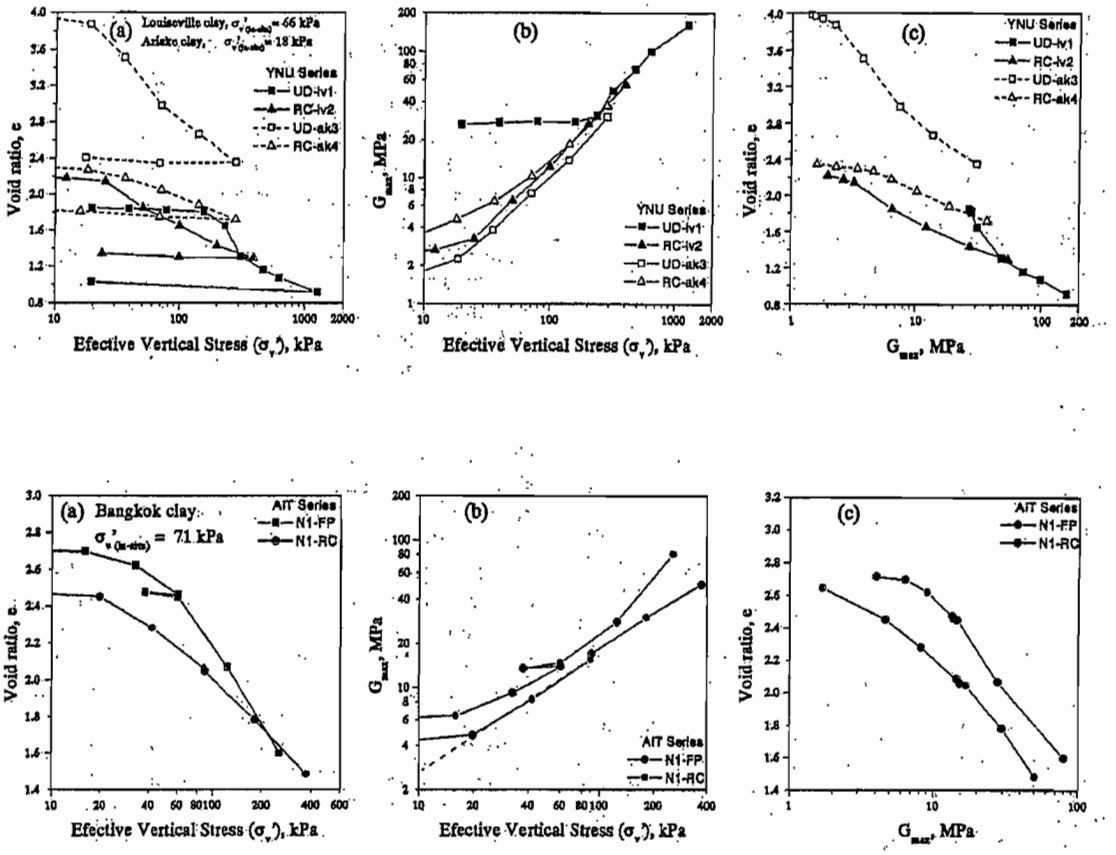

Figure C.8: Relationship between e, σ'_{vc}, and G_{max} in FP and RC samples of Louiseville clay (lv) and Ariake clay (ak) series YNU (a-c), and Bangkok clay series AIT-N1 (d-f) (Lohani et al., 1999)

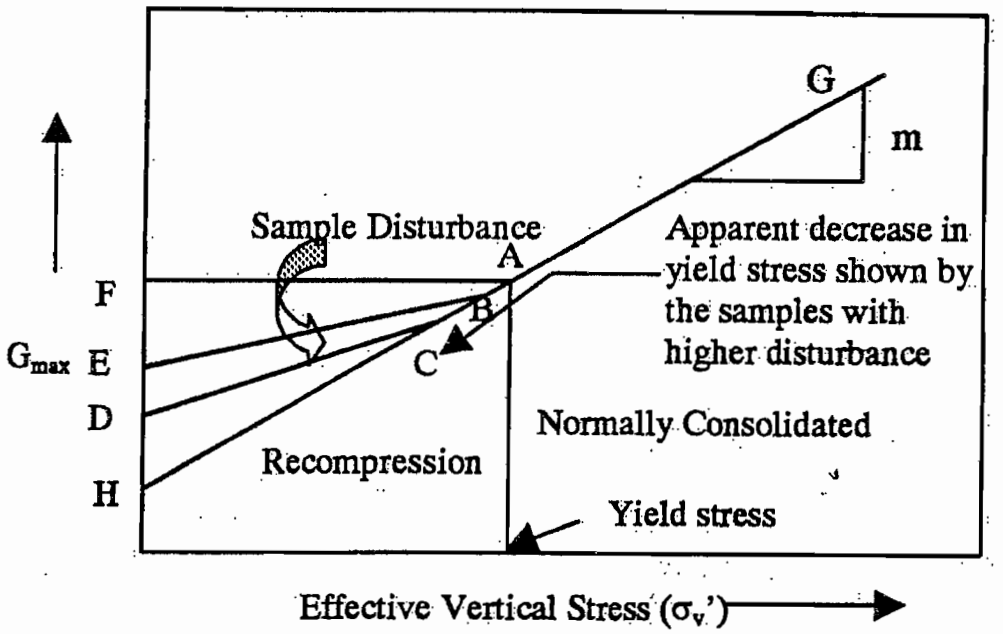

Figure C.9 Schematic diagram showing the change in G_{max}-σ'_{vc} curve slope (m) with the extent of sample disturbance (Lohani et al., 1999)

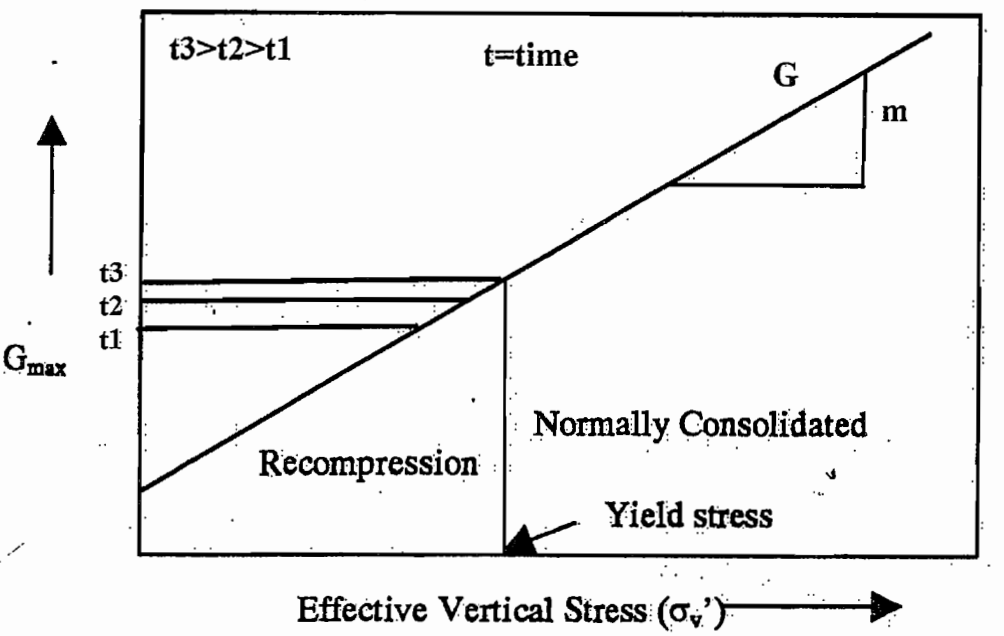

Figure C.10: Schematic diagram showing the effect of time on the in situ G_{max}- σ'_{vc} relationship

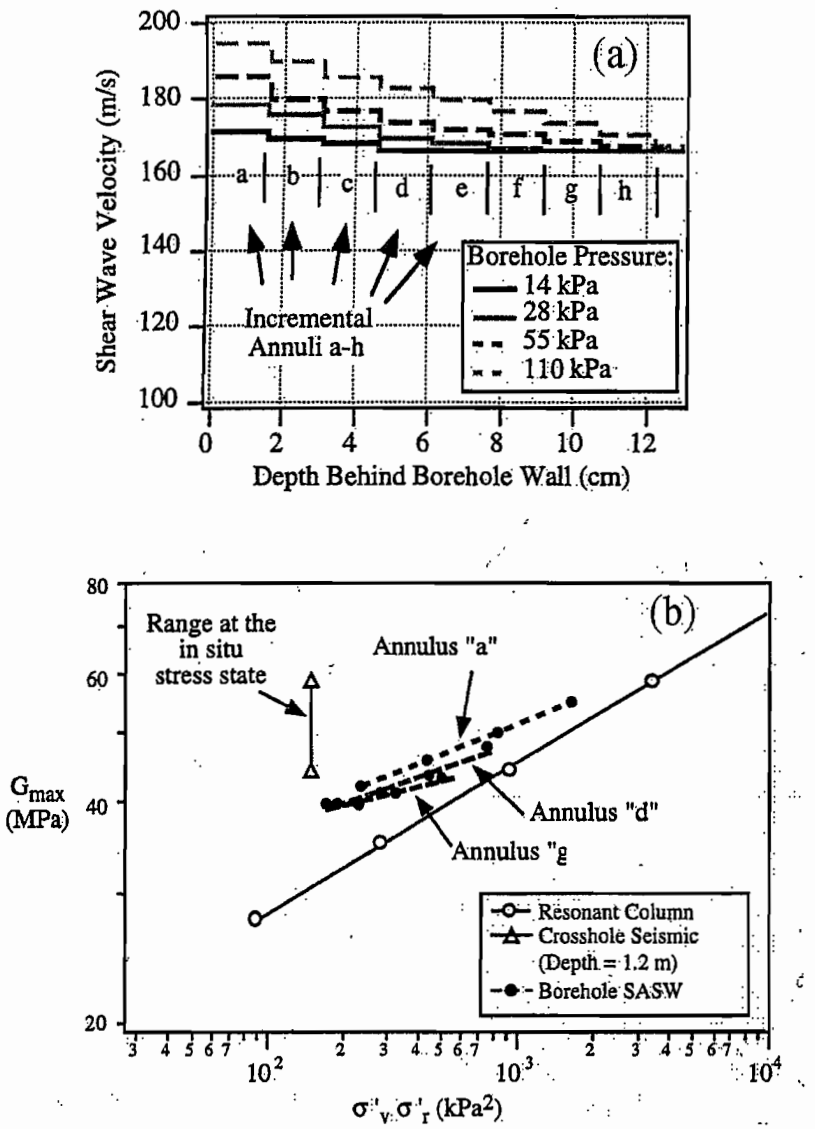

Figure C.11: (a) Variation in V_s with distance behind the borehole wall and (b) $\log(G_{max})$-$\log(\sigma'_v \sigma'_r)$ relationship measured in situ using SASW tool and cross-hole tests, and from laboratory RC tests on intact samples (Kalinski et al., 1999)

Appendix D: FACTORS AFFECTING THE DYNAMIC PROPERTIES OF SOILS

D.1 Introduction

In recognition of the importance of accurate predictions of the soil dynamic properties for site response analyses, researchers have spent considerable effort over the past two to three decades trying to develop the modulus reduction and damping curves for various soils. They have noted that these curves vary widely among different soils. Therefore, in order to gain an understanding of the dynamic behavior of soils, one must investigate the important factors that affect this behavior. Hardin and Drnevich (1972) were among the first to study the effect of different parameters on the shear modulus and damping of cohesionless and cohesive soils using their torsional shear device and resonant column apparatus. Their tests have shown that strain amplitude, mean effective stress, and void ratio are among the most important parameters to impact the measured values of modulus and damping in all soils. They also emphasized that the degree of saturation is very important to the dynamic behavior of cohesive soils. In a more recent study, Dobry and Vucetic (1987) studied the factors affecting the dynamic properties of clays. They concluded that the level of shear strain and the number of cycles are the main loading parameters, while plasticity index and overconsolidation ratio are the main soil parameters needed to characterize soil response to cyclic loading. Their findings are summarized in Table D.1. Other studies have addressed the effect of a single parameter such as frequency, aging, etc. In this chapter a more detailed and comprehensive revision

of the factors affecting the dynamic properties of soils is introduced. As mentioned in the previous chapter, the dynamic properties commonly reported are the maximum shear modulus, G_{max}, the normalized modulus reduction curve, G/G_{max} vs.γ, and the damping ratio curve, D vs. γ. Therefore, the factors affecting each one are discussed separately.

D.2 Cyclic Threshold Shear Strains

Depending on the level of shear strains, three categories of soil behavior can be identified. At very small strains, the soil behaves essentially as a linearly elastic material with practically constant shear modulus, G_{max}. This behavior continues until a threshold shear strain, called the linear cyclic threshold shear strain, γ_{tl}, is reached above which the soil becomes non-linear but largely elastic. At this stage, the soil's shear modulus is no longer constant (G_{max}), but a function of shear strain. However, since the behavior is still elastic, soil stiffness, including G_{max}, is not permanently degraded and can be re-obtained at the corresponding level of shear strain. If the shear strains are large enough to exceed a second threshold strain, called the volumetric cyclic threshold shear strain, γ_{tv}, significant permanent plastic deformations will take place. At this phase, dry or partially saturated soils will experience permanent volume changes, while residual cyclic pore-water pressure will develop in fully saturated soils. This means that this phase is also marked by permanent degradation of soil stiffness where initial soil moduli at smaller strain levels cannot be fully recovered under the current conditions. Figure D.1 shows the different zones of soil behavior according to the amplitude of cyclic shear stain. The amplitude of threshold shear strains depends on the soil type and can be correlated to plasticity index (Vucetic and Dobry, 1991, and Vucetic, 1994). Soils with high PI have larger levels of elastic and volumetric cyclic threshold strains, meaning that they deform linearly and

elastically to higher levels of shear strain. On the other hand, cohesionless soils and soils with low PI exhibit nonlinear behavior at lower strains. Different researchers have proposed different interpretations and ranges of what they defined as a threshold strain (e.g., Hardin and Black, 1968; Drnevich and Richart, 1970; Anderson and Richart, 1976; Stoll and Kald, 1977; Stokoe and Lodde, 1978; Ishihara, 1981; Dobry et al., 1981, 1982; Kim et al., 1991; and Vucetic and Dobry, 1991). Vucetic (1994) performed a comprehensive study on the subject and summarized his findings in the charts shown in Figure D.2. The study indicates that the average amplitude of γ_{tl} and γ_{tv} ranges between $5x10^{-4}$ % to about $5x10^{-3}$ % and 10^{-2} % to 10^{-1} %, respectively

D.3 Low-Strain Shear Modulus (G_{max})

The low-strain shear modulus, G_{max}, is an important parameter for a variety of geotechnical design applications which involve small-strain dynamic analyses such as machine or traffic vibrations and wind or wave loading. G_{max} is also important for large-strain situations, e.g. earthquakes, where non-linear analysis is to be performed. First, because it is the starting point, i.e. initial soil stiffness, in any site response or soil-structure interaction analyses (e.g. G_{max} is one of the inputs for SHAKE). Second, by normalizing the mid-to-high-strain modulus reduction curve (G vs. γ) by G_{max} so that they can be predicted or measured separately, the value of G_{max} not only affects the soil stiffness at small strains but at mid and high strains too. Third, G_{max} correlates well to other soil properties such as density, fabric, sample disturbance, and liquefaction potential, hence, it may be used as an indirect indicator of these soil parameters.

D.3.1 General Correlations

One of the most widely used empirical relationships which incorporate the major factors affecting the magnitude of G_{max} is the one presented by Hardin (1978):

$$G_{\max} = A\frac{(OCR)^k}{0.3+0.7e^2}\bar{\sigma}_o^{n} p_a^{1-n} \qquad \text{K (3.1)}$$

where $\bar{\sigma}_o$ is mean effective confining pressure, P_a is the atmospheric pressure, and e and OCR are void ratio and overconsolidation ratio, respectively. A, k, and n are material constants. This equation can be used for cohesive and cohesionless soils and is good for any unit system. For cohesive soils, the parameters A and n are usually assigned a value of 625 and 0.5, respectively, while k is a function of the plasticity index (PI) as shown in the following equation:

$$k = \frac{PI^{0.72}}{50} \le 0.5 \qquad \text{K (3.2)}$$

It should be emphasized that the relationship in 3.1 is based on laboratory test results. Studies have shown that field values may be 20% to 100% higher than laboratory values mainly due to sample disturbance and aging effects. Thus, this should be taken into consideration before using equation 3.1 to predict G_{max} for design purposes. Another general relationship similar to (3.1) was suggested by Jamiolkowski et al. (1991):

$$G_{\max} = \frac{625}{e_o^{1.3}}(P_a.\sigma_m')^{0.5} OCR^k \qquad \text{K (3.3)}$$

where G_{max} is in units of lb/ft^2. Seed et al. (1984) proposed the following relationship for cohesionless soils:

$$G_{\max} = 1000(K_2)_{\max}(\sigma_m')^{0.5} \qquad \text{K (3.4)}$$

where σ'_m is the mean effective stress and $(K_2)_{max}$ is a function of soil density (void ratio) and is also correlated with the Standard Penetration Test (SPT) results. Other formulas (e.g. Imai and Tonouchi, 1982; Sykora and Stokoe, 1983; Mayne and Rix, 1993) were also introduced to correlate G_{max} (or shear wave velocity, V_s) with field tests like SPT and CPT (Cone Penetration Test). However, since G_{max} is a small-strain parameter while penetration tests produce large strains, these formulas should be used with caution. Examining Equations (3.1) to (3.4) it is clear that the effective confining pressure, and void ratio (or relative density) are the primary factors influencing the magnitude of G_{max} for all normally consolidated soils. G_{max} also increases with increasing overconsolidation ratio (OCR). For cohesive soils, plasticity index by itself (i.e. at constant void ratio) does not seem to have a significant impact on G_{max} for normally consolidated soils (OCR=1), but it does amplify the effect of OCR as suggested by equation (3.2) and noted by Dobry and Vucetic (1987). However, there are other important factors that could significantly affect the magnitude of G_{max} and yet are not captured by the relationships mentioned above. These include the geologic age (or time under confinement), strain rate (or frequency of cyclic loading), and degradation under repeated cyclic loading. The effects of these factors are discussed in more detail in the following paragraphs.

D.3.2 Time-Under-Confinement (Aging Effects)

The aging effect is one of the main reasons for the often observed discrepancy between $G_{max,field}$ and $G_{max,lab}$, especially for old soil deposits. It is very well known now that G_{max} increases with time (Marcuson and Wahls, 1972; Afifi and Richard, 1973; Anderson and Woods, 1975, 1976; and Anderson and Stokoe, 1978). Time effects also

apply for all strain levels and was observed in laboratory tests for stresses as low as 5 psi and as high as 100 psi (Anderson and Stokoe, 1978). As shown in

Figure D.3, the increase in G_{max} has two phases; an initial phase from primary consolidation (short-term effect), and a second phase from secondary consolidation (long-term effect). The rate of increase in the two phases depends on the soil type, initial void ratio, and stress conditions. The shape of G_{max} vs. time curve depends on whether the soil is fine- or coarse-grained. In the initial phase, G_{max} increases rapidly and non-linearly with the logarithm of time because of the change in void ratio due to water dissipation. In the second phase G_{max} increases linearly with the logarithm of time and can be expressed in an absolute since as a coefficient of shear modulus increase with time, I_G (Anderson and Stokoe, 1978):

$$I_G = \frac{\Delta G}{\log_{10}(\frac{t_2}{t_1})} \qquad \text{K (3.5)}$$

where t_1 and t_2 are the times after primary consolidation and ΔG is the change in G_{max} from t_1 to t_2 as shown in

Figure D.3. To remove the effect of confining pressure, this effect can be expressed by the normalized shear modulus increase with time, N_G:

$$N_G = \frac{I_G}{G_{1000}} \qquad \text{K (3.6)}$$

where G_{1000} is the shear modulus (or G_{max}) after 1000 minutes of constant application of the confining pressure (i.e., primary consolidation must be completed). Values of N_G can be used to correct G_{max} obtained form laboratory tests or from the relationships mentioned earlier to estimate $G_{max,field}$. For example, Anderson and Woods (1975) found

that their $G_{max,lab}$ extrapolated to 20 years is in good agreement with $G_{max,field}$ obtained from a cross-hole test. Anderson and Stokoe (1978) proposed the following formulas to correct for time effects so that $G_{max,field}$ can be estimated:

$$G_{max,\,field} = G_{max-primary,lab} + F_A * I_G \qquad \text{K (3.7)}$$

$$F_A = \log_{10}\left(\frac{t_c}{t_p}\right) \qquad \text{K (3.8)}$$

where F_A is the age factor, while t_c and t_p are the geologic time or the time since the start of the most recent significant change in stress history at the site, and the time to complete primary consolidation at the site as a result of stress change, respectively. The value of t_p will vary with soil type, thickness of deposits, drainage conditions, etc. For sand deposits, t_p is usually small, whereas for clays it may be on the order of years. For site ages of 20 to 200,000 years, typical values of F_A will be in the range from 4 to 8.

The effect of time on the G_{max} value of soils seems to be influenced by several factors. Figure D.4 shows the G_{max} versus time curves for three soils; a normally consolidated clay, an overconsolidated clay, and a sand. What is obvious from the plot is that time effect is more significant for predominantly fine-grained cohesive soils than for coarse-grained cohesionless soils and for normally consolidated cohesive soils than for overconsolidated cohesive soils. Also for clean sands, there is no initial phase since the time for primary consolidation is very short. However, at high stresses, a non-linear initial phase □ay be noticed due to grains' crushing and viscoelastic adjust□ents in the crystalline structure. Generally, the value of I_G increases with increasing confining pressures and decreasing overconsolidation ratios. On the other hand, the value of N_G increases with increasing void ratio and plasticity index and decreases with increasing

values of undrained shear strength, overconsolidation ratio, and mean grain diameter. Note that some of these factors are related. Typical ranges for N_G value for NC clays, OC clays and sands are 5-20%, 3-10%, and 1-3%, respectively.

Kokusho et al. (1982) proposed the following, commonly-used, correlation between the effect of time on normally consolidated clays and plasticity index PI:

$$\frac{\Delta G}{G_{1000}} = 0.027\sqrt{PI} \qquad \text{K (3.9)}$$

Time effect on G_{max} is also present when the confining pressure is decreased, which is a case relevant to the effect of sampling and the effect of an in situ tool that might temporarily release the confining pressure. Unfortunately, few studies have addressed this issue. However, one would predict that there will also be two phases of change in the value of G_{max}. An initial phase in which G_{max} decreases with time due to the change in void ratio (swelling) and a second phase in which G_{max} rebounds due to secondary compression under the new stress conditions. For the initial phase, the decrease in G_{max} due to unloading will be much smaller than the increase in G_{max} due to loading if the absolute change in confining pressure in the two directions is the same. This is because the swelling index is much smaller than the compression index (the ratio is about 1:10). However, the average rate of this change may be about the same in both cases because swelling happens faster than virgin compression (the ratio is about 1:10 to 1:15). On the other hand, the rate of increase in G_{max} in the second phase will be smaller after unloading than after "virgin" loading because in the first case the soil will be overconsolidated (secondary compression index for overconsolidated clays is smaller than for normally consolidated clays). In their attempt to study the effect of stress history on G_{max}–time relationship, Anderson and Stokoe (1978) incrementally consolidated a

Detroit Clay sample to three stress levels and then incrementally unloaded the sample back to the same stress level. The G_{max}–time curve was established for each loading and unloading step and is shown in Figure D.5. The results of their experiment are consistent with the discussion above. Also, Athanosopoulos and Richart (1983) showed that temporary release of confinement of cohesive soil caused a reduction of shear modulus. However, the initial value was regained when the confinement was reapplied over an interval of time. This modulus-regain time increased with the age of the cohesive soil.

D.3.3 Strain Rate Effects

The shear modulus of soil including G_{max} is also affected by the strain rate of the applied load. This effect has been studied by many researchers mostly by varying the frequency at which G_{max} is measured in the laboratory. The test results (e.g. Aggour et al., 1987) clearly indicate that G_{max} increases with increasing the loading frequency and that this effect increases with increasing plasticity index. For cohesionless soils, it is generally believed that G_{max} is not influenced by the frequency of loading. Frequency effect on cohesive soils is obvious from the difference in G_{max} value between a resonant column (RC) test (20-30 Hz) and a torsional shear (TS) test (0.1-1 Hz). Kim et al. (1991) reported that the shear modulus increases linearly with the logarithm of loading frequency and that the range of this effect is between 2% and 9% per log cycle of loading frequency. Hara and Kiyota (1977) noted, however, that G of undisturbed clays in the range of γ between 0.001-0.01% was not affected using frequencies between 0.1-10 Hz. Similarly, Zavoral and Campanella (1994) reported that frequency effect on shear modulus is insignificant in the range 0.01-1.0 Hz for marine clay samples with plasticity indexes between 20-40%. Shibuya et al. (1995) also reported that for shear strains below 0.002%, the shear

modulus of normally consolidated clays was hardly influenced by the shear strain rate when the loading frequency was changed between 0.005 and 0.1 Hz. Stokoe et al. (1999) tested three soils with different plasticity indexes on a RS/TS device and found that the effect of frequency on G_{max} is small and averages about 10% as frequency changes from 1 to 50 Hz. The study also indicated that the influence of plasticity index on frequency effect is only significant at frequencies higher than 10 Hz.

D.3.4 Number of loading Cycles

As mentioned above, G_{max} starts to degrade when the shear strain level exceeds the volumetric threshold strain, γ_{tv}, which ranges between 0.01 to 0.1%. Thus, one could say that G_{max} is independent on the number of loading cycles (N) below this strain level. On the other hand, G_{max} decreases after N cycles of shear strain larger than γ_{tv} and this decrease increases with increasing N and cyclic shear strain level. However, G_{max} recovers later with time. Anderson and Richart (1976) studied the regain in G_{max} after high amplitude cycling of a clay sample and found that the time for 100% regain depends on the cyclic strain level, number of cycles, and the soil type.

D.3.5 Fabric Anisotropy

Fabric anisotropy in soils, characterized by a preferred orientation of soil particles, is mainly the result of one dimensional consolidation which results in natural soils having cross anisotropic mechanical properties, with the axis of symmetry along the direction of consolidation. Experimental investigations have shown the important influence fabric anisotropy can have on the dynamic behavior of soils. Saada et al. (1978) found that there is a substantial difference in the moduli obtained from vertical and

horizontal samples of anisotropic clays and that fabric anisotropy cannot be erased even under the most severe cyclic strains. The study also found that the behavior under axial compression and torsional loadings are also different for anisotropic clay. Fabric anisotropy is particularly relevant to in-situ measurement of G_{max} based on shear wave velocity because it is usually assumed that waves travel through isotropic media at the same speed in all directions. Macari and Ko (1994) conducted a study on anisotropically consolidated silt and found that the difference in G_{max} of horizontal and vertical samples decreases with increasing isotropic confining pressure and decreasing OCR.

D.3.7 Summary

From the previous discussion, the most important factors affecting G_{max} are the effective confining stress, void ratio, overconsolidation ratio, time-under-confinement, and strain rate (frequency) effects. G_{max} increases with increasing confining pressure, OCR, time-under-confinement, and frequency but decreases with increasing void ratio. The effects of these factors are more pronounced at higher soil plasticity. The effect of frequency seems to be more significant at higher frequencies (more than 10 Hz) than at lower frequencies and should be taken into considerat p2910Xe difference between the testing and the design frequency exceeds one log cycle. G_{max} is also sensitive to prior high –strain cycles, but not influenced by the number of low-strain cycles.

D.4 Normalized Shear Modulus Reduction Curve (G/G_{max}-γ)

Normalized shear modulus curves, G/G_{max}-γ, are used by engineers to characterize the shear modulus, G, of soils in the non-linear range. The normalization by G_{max} is useful for many reasons. First, it makes it possible to categorize the modulus reduction

curve, G-γ, for different soils based on some material and loading factors. Second, this allows the introduction of generic G/G_{max} - γ curves which are useful as a starting point in the esti□ation of the soil's dyna□ic properties. Third, it allows the s□all-strain linear G and the high-strain non-linear G to be measured/predicted separately. This is especially useful since G_{max} is usually measured in the field while G in the non-linear range is measured in the laboratory or predicted by a generic curve. Accurate measurement of G in the non-linear range is very important because the shear strains in the soil generated by large earthquakes are in the range 0.01-0.1% which is well within the non-linear range for most soils. Understanding the factors affecting the shape of the G/G_{max}-γ curve is very important to accurately predict the non-linear soil behavior for site response analyses.

D.4.1 Empirical Analytical Representations

As discussed in the previous chapter, soil non-linearity can be modeled using empirical or elastoplastic models. The most commonly used empirical formulas to describe the stress-strain backbone curve of any soil are the hyperbolic equation and the Ramberg and Osgood (1943) equation. The hyperbolic function can be written as:

$$\tau = \frac{G_{max}\gamma}{1+\frac{\gamma}{\gamma_r}} \qquad \text{K (3.10)}$$

where τ and γ are the shear stress and strain, respectively; and γ_r is the reference strain and is defined as the ratio of τ_{max}/G_{max}, where τ_{max} is the soil's shear strength. Notice that you can easily obtain the modulus reduction curve from equation (3.10). The hyperbolic model is not flexible to represent the variations observed from experimental results since variations in the reference strain (the only variable in the equation if G/G_{max}-γ is to be

modeled) produces small variations in shape of G/G_{max}-γ curve. However, it can easily model shear modulus (or shear stress) as a function of shear strain. A more flexible equation used to model the backbone curve is the Ramberg-Osgood model which describes empirical shear stress as a function of shear strain as follows:

$$\gamma = \gamma_r \left[\frac{\tau}{G_{\max}\gamma_r} \right] \left[1 + \alpha \left| \frac{\tau}{G_{\max}\gamma_r} \right|^{R-1} \right] \qquad \text{K (3.11)}$$

in which α and R are positive constants (R should be equal to or greater than unity) and other parameters are as defined in (3.10). The parameters α and R can be estimated according to soil type or can be deduced from laboratory tests. Equation 3.11 can be re-written as:

$$\frac{G}{G_{\max}} = \frac{1}{1 + \alpha(\frac{\gamma}{\gamma_r}\frac{G}{G_{\max}})^{R-1}} \qquad \text{K (3.12)}$$

The above equations, as useful as they are, do not show the soil or loading parameters that affect the shape of the G/G_{max} - γ curve and are mainly used to fit experimental results. However, since the reference strain is a function of G_{max} and τ_{max}, which are functions of confining pressure, these formulas suggests that the shape of the normalized curve is also a function of the confining pressure. This assumption is not valid for all soils as will be illustrated later. Ishibashi and Zhang (1993) proposed a formula that describes G/G_{max} as a function of mean effective stress, σ'_m, and plasticity index, PI, as shown in the following equation:

$$\frac{G}{G_{\max}} = K(\gamma, PI)(\sigma'_m)^{m(\gamma,PI)-m_o} \qquad \text{K (3.13)}$$

They also give expressions for the parameters K(γ,PI) and m(γ,PI). What is obvious from this formula is that the effective stress and plasticity index are the main state and soil parameters affecting the shape of the G/G_{max}-γ curve and that the effect of confining pressure is also influenced by plasticity. A more detailed discussion on the effects of these two parameters and others is presented in the following sections.

D.4.2 Soil Plasticity (PI)

Recent research and the expansion of the database of measured dynamic soil properties have brought about a new understanding of the relationship between the shape of G/G_{max}-γ curve and soil plasticity. Zen et al. (1978) and Kokushu et al. (1982) were the first to notice this influence. The new thinking today is of a gradual transition of the modulus reduction behavior between non-plastic, low-plastic and high-plastic soils. Zen et al. (1978) introduced a set of G/G_{max}-γ curves for laboratory-prepared samples with different plasticity indexes and noticed that the shear modulus of high-plasticity soils degrades more slowly than low-plasticity soils. Therefore, with increasing plasticity the normalized curve moves up and to the right. Later, Sun et al. (1988), and Vucetic and Dobry (1991) introduced a set of generic G/G_{max}-γ curves, mainly for cohesive soils, based only on soil's plasticity index as shown in Figure D.6 and Figure D.7. The similarity of the G/G_{max}-γ curves between the two studies suggests a strong correlation between the normalized curve and plasticity index. In their explanation of the influence of plasticity on shear modulus, Dobry and Vucetic (1987) argued that soils with higher plasticity have a more open structure, smaller particle size, and stronger physico-chemical bonds between particles, thus they have more flexible and elastic behavior than low or non-plastic soils.

D.4.3 Void Ratio

The effect of void ratio is difficult to assess because it is usually tied with other factors like plasticity index, confining pressure, and stress history. For cohesive soils, studies show that with increasing void ratio, G/G_{max} increases, i.e., the G/G_{max}-γ curve drops more slowly (Dobry and Vucetic, 1987; Lodde and Stokoe, 1981; etc.). However, most of these studies involved soils with different plasticities, thus the observed trend could be attributed to a plasticity effect. For cohesionless soils, the opposite trend is reported when comparing the normalized curve at different void ratios for the same soil, but again these curves are obtained at different confining pressures. In summary, void ratio is not an independent factor and hence its effect should not be looked at apart from other factors.

D.4.4 Confining Pressure

The effect of confining pressure is especially important for cohesionless soils and one can say that it is the main factor affecting the shape of the normalized modulus curve of these soils. As the confining pressure increases, the G/G_{max}-γ curve moves up and to the right indicating slower modulus degradation with shear strains (Iwasaki, et al. 1976; Stokoe et al. 1999). This also means that the elastic and the volumetric threshold strains increase with increasing confining pressure. For cohesive soils, the same trend is observed but the influence of confining pressure on G/G_{max}-γ curve diminishes as plasticity index increases. Sun et al. (1988) reported that this influence is small for clays with PI exceeding 25% and for shear strains less than 1%. This observation is supported by other studies (e.g., Dobry and Vucetic, 1987; and Ishibashi, 1992). Therefore, many generic G/G_{max}-γ curves do not take the effect of confining pressure into consideration.

However, recent studies (e.g. Lanzo et al., 1997, and Stokoe et al. 1999) show that the effect of confining pressure on G/G_{max}-γ curve of cohesive soils (especially with PI < 40%), even though smaller than on cohesionless soils, is still significant enough to be taken into account, especially at high confining pressures.

D.4.5. Overconsolidation Ratio

The effect of overconsolidation ratio on the G/G_{max}-γ curve is thought to be insignificant because it influences both the small-strain and the large-strain modulus at about the same rate, thus their ratio remains unchanged. Kokusho et al. (1982) showed that the G/G_{max}-γ curves for clays with PI<40% and with various OCR (from 1-15) fall within a narrow band. The same conclusion was reached by Sun et al. (1988) and Vucetic and Dobry (1988) and is reflected in the generic curves proposed by them. However, in a more recent study, Lanzo et al. (1997) have shown that the effect of OCR on G/G_{max}-γ curve can be significant for sands and clays having small PI (say below 30%) and is a function of plasticity index.

D.4.6 Strain Rate

The effect of strain rate on static soil stiffness under monotonic loading has been widely investigated. The experimental results clearly show that soil stiffness increases with increasing strain rate. In a previous section, the effect of strain rate on G_{max} was discussed and it was pointed out that G in the linear range increases with increasing strain rate (frequency) and that the rate of this increase depends on soil plasticity. The effect of strain rate on G in the non-linear range is expected to be the same. Idriss et al. (1978) and Vucetic and Dobry (1988) studied the effect of strain rate on the backbone curve of San

Francisco Bay Mud and Venezuelan North of Paria (VNP) clay, respectively. Their results showed the backbone curve is higher at larger strain rates. In the Vucetic and Dobry (1988) study, the backbone curve was approximately 1.5 times higher for dynamic loading at a strain rate of between 0.4 and 4% per second than that obtained by static loading at a strain rate of 0.00013% per second for NC clay, as shown in Figure D.8a. Under cyclic loading, studies show that non-linear G increases with increasing frequency (Isenhower and Stokoe, 1981; Aggour et al., 1987). However, the magnitude of this increase may be a function of strain level. This is especially obvious from comparing the modulus reduction (G-γ) curve from RC tests and TS tests for the same soil. Using the RC/TS combined device, Stokoe et al. (1999) conducted cyclic tests on three soils at two loading frequencies; 50 Hz and 1 Hz. The tested soils include silty sand, sandy clay, and fat clay. As shown in Figure D.9a, the results show that the effect of frequency on G decreases as cyclic strain increases above the elastic threshold strain, γ_{tl}, and as the plasticity of the soil decreases. The shear modulus increases slightly with increasing frequency once the volumetric threshold strain, γ_{tv}, is exceeded perhaps because of cyclic stiffening which becomes important at higher strains. Zavoral and Campanella (1994) found that for a marine clay at shear strains higher than γ_{tv}, the generated residual pore water pressure decreases as the frequency increases. As with G_{max}, the effect of frequency on G in the non-linear range is a function of plasticity. Also the effect of frequency on G seems to be level-dependent, i.e., more significant at higher frequency levels than at lower levels (e.g. Shibuya et al. (1995)).

The normalized shear modulus does not seem to be affected by the strain rate for both monotonic and cyclic loading. Li et al. (1993) presented the results from Vucetic

and Dobry (1998) in a normalized format as shown in FigureD.8b. The normalized modulus shows no evidence of strain rate effects. The same applies for the normalized curve, G/G_{max}-γ, obtained from cyclic loading if both G_{max} and G are measured at same strain rate (Vucetic and Dobry, 1987).

Finally, one should emphasize that measuring the modulus reduction curve using a constant loading frequency means that at each strain level, G is measured at a different strain rate. Isenhower and Stokoe (1981) pointed out that if G-γ curve is measured a constant strain rate, as shown in FigureD.10, small-strain G will continue to increase with decreasing strain level and it is difficult to define a linear elastic threshold strain. This suggests that, at constant frequency, the plateau of the G-γ curve at small strain may be merely apparent due to the effect of shear strain rate, which increases as γ increases (Shibuya et al. (1995)).

D.4.7 Cyclic Degradation

As pointed out earlier, once the volumetric threshold shear strain is exceeded, repeated cyclic loads will degrade the shear modulus of the sample. In a strain-controlled test, it will be manifested as a gradual decrease in the measured shear stress as the number of cycles increases. In saturated, normally consolidated and slightly overconsolidated clays, the degradation may be attributed mainly to the decrease in the mean effective stress because of the generation of positive pore water pressure. However, since the degradation is also observed in heavily overconsolidated clay, other reasons such as structural changes may also cause this phenomenon. Idriss et al. (1978) tried to quantify this effect by introducing a parameter called the degradation index, δ, which

relates the shear modulus after N cycles, G_N, to the shear modulus in the fist cycle, G_1, as shown in the following equations:

$$G_N = \delta * G_1 \qquad \text{K (3.14)}$$

$$\delta = N^{-t} \qquad \text{K (3.15)}$$

where t is the degradation parameter, which decreases with increasing PI and overconsolidation ratio, and increases with increasing cyclic strain amplitude as shown in Figure D.11 (Idriss et al., 1978, and 1980; Vucetic and Dobry, 1988). Because cyclic degradation affects only high-strain G, the normalized curve, G/G_{max}-γ , will degrade as the number of cycles, N, increases especially in the high-strain range as shown in Figure D.7b.

D.4.8 Consolidation Stress Path and K_o Effects

Unfortunately, there are few studies that have investigated the effect of applied effective stress anisotropy on "undisturbed" soil sa□ples on the □agnitude of G_{max}. The formulas presented above suggest that G_{max} is a function of the mean effective stress, implying that soil samples under isotropic and anisotropic effective confining pressures should have the same G_{max} if they are subjected to the same mean effective confining pressure. However, the limited available experimental results show that this is not the case. Macky and Saada (1984) conducted an experimental investigation on the cyclic behavior of both artificially prepared and natural cross anisotropic clays and concluded that shear modulus is affected by the inclination of principle stresses. The study by Saada et al. (1978) found that for the same clay the value of G_{max} differs depending on whether the clay was K_o- or isotropically consolidated. The study shows that at the same mean effective stress, G_{max} of isotropically consolidated clay is about 15% higher than K_o-

consolidated sample of the same clay. This is mainly due to a lower void ratio. In another study on reconstituted kaolinite (PI=4 3%) samples tested in a triaxial device, Mukabi (1991) found that at small strains the difference in shear modulus between K_o – consolidated (K_o=0.64) and isotropically consolidated samples is insignificant. However, as the level of shear strain increases the difference starts to show up with a higher G for isotropically consolidated samples. Roesler (1979) and Stokoe et al. (1985) have shown that body wave velocities in sands depend mainly on the void ratio and on the normal effective stresses acting in the direction of wave propagation. Roesler (1979) suggested the following empirical formulas for the vertical and horizontal small-strain shear modulus, G_{vh} and G_{hh}, which account for the inherent and stress-induced anisotropy:

$$G_{vh} = C_{vh}F(e)\sigma_v^{'n}\sigma_h^{'n}P_a^{(1-2n)} \qquad \text{K (3.16)}$$

$$G_{hh} = C_{hh}F(e)\sigma_h^{'2n}P_a^{(1-2n)} \qquad \text{K (3.17)}$$

where C_{vh} and C_{hh} are dimensionless material constants which incorporate the effect of inherent anisotropy, F(e) is the void ratio function, n is the modulus exponent, and P_a is the atmospheric pressure. Yu and Richart (1984), proposed that the dependence of G_{max} on the effective consolidation stresses should be expressed by $S'=(\sigma'_v+\sigma'_h)/2$ rather than by $\sigma'_m=(\sigma'_v+2\sigma'_h)/3$. Overall, despite the limited available data, consolidation path does seem to affect the magnitude of measured shear modulus and one should try to replicate the state of stress present in the field.

D.5 Damping Ratio

Damping is a dynamic soil property that characterizes energy dissipation during cyclic loading. In general, less is known about damping than modulus. First because the mechanisms that cause damping are not fully understood, and second, damping is more

difficult to accurately measure than shear modulus. Damping ratio could be the controlling parameter in site response analyses in some cases, such as deep stiff soil layers subjected to motions with relatively small peak strains (EPRI, 1991).

D.5.1 Viscous and Frictional Damping

The state-of-knowledge today identifies two mechanisms through which energy dissipation *within* the soil takes place; viscous and frictional damping. The so called radiational or geometric damping will not be discussed here since it is a function of geometric transmission, rather than dissipation, of energy away from an energy source. Viscous damping is the result of the delayed response of the soil to the applied loading, while frictional damping is the result of energy dissipation in the form of plastic work (permanent deformation) done on the soil. Frictional damping is usually referred to as hysteretic damping despite the fact that a hysteretic loop in the stress-strain curve can be generated by either or both damping mechanisms. In this study, the word damping will be used to refer to the total damping regardless of the mechanism(s) that caused it. Two approaches have been used to model damping in analytical procedures; the viscous damping theory, and the hysteretic damping model. One should make the distinction between viscous and hysteretic damping as mechanisms and as models.

In the viscous damping model, material damping (including the frictional part) is considered as viscous and is modeled as such in mathematical representation. This is so because of mathematical convenience and because it is the model employed in the commonly used equivalent-linear approach for site response analyses. In this approach, soil is modeled as a Kelvin-Voight solid where the total shear stress is the sum of an elastic part and a viscous part as shown in the following equation.

$$\tau = G\gamma + \eta\dot{\gamma} \qquad \text{K (3.16)}$$

where η is the viscous damping coefficient. One can show through mathematical derivation that the so called damping ratio, D, can be expressed as:

$$D = \frac{\eta\omega}{2G} \qquad \text{K (3.18)}$$

where ω is the angular frequency. Equation (3.18) indicates that D is frequency dependent and that the hysteretic loop is elliptical in shape. Another, more practical way, to express the damping ratio (in the viscous damping model) is by the following expression:

$$D = \frac{1}{4\pi}\frac{\Delta W}{W} \qquad \text{K (3.19)}$$

$$W = \frac{1}{2}G\gamma_o^2 \qquad \text{K (3.20)}$$

where W and ΔW is the stored and dissipated energy in one load cycle, respectively, and γ_o is the peak shear strain. The expression in (3.19) is the most widely used approach to mathematically quantify damping in soils.

In the hysteretic model, material damping is assumed to be frictional and loading rate independent. Damping is accounted for by point-to-point tracking of the stress-strain path during loading. As discussed in the hysteretic loop can be created either by an empirical formula (e.g. Masing Criteria) or by a constitutive elasto-plastic model. At small strains this model predicts zero damping (because the material is in the linear elastic range), thus, a small amount of viscous damping is added to simulate the observed data.

Finally, as will be discussed later, the contribution of viscous and frictional damping to the total measured damping depends on the soil type and strain level. There is

no available technique that can allow the measurement of each type separately. However, one could argue that viscous damping is most significant at small strains and with plastic soils.

D.5.2 Strain Dependency

As shown in Figure D.1, damping ratio is strain-level dependent. Experimental investigations have shown that even at small shear strains, where soil behavior can be described as linear elastic (no hysteretic energy dissipation), damping still exists. The damping ratio at this strain level is usually referred to as minimum damping ratio, D_{min}. At shear strains below the elastic threshold strain, γ_{tl}, D is assumed constant and equal to D_{min}. As the shear strain level increases above γ_{tl}, so does the damping ratio, such that D has an opposite trend with shear strain compared to shear modulus. However, there is compatibility between the G/G_{max}-γ and D-γ relationships, meaning that the more linear the soil is, the slower the degradation in G vs.γ, and the slower the increase in D vs. γ. Stokoe et al. (1999) reported that while the elastic threshold strain, γ_{tl}, is nominally the same for both D and G, the volumetric threshold strain, γ_{tv}, is somewhat smaller for D than found for G. As mentioned before, damping is difficult to measure accurately because of the many factors in the testing procedure that can affect it. Therefore, it was not until recently that researchers begin to understand the effects of the different material, state and loading parameters on the D-γ relationship. Moreover, as will be discussed later, recent research suggests the effect of some of these parameters on D-γ is more complex than on G/G_{max}-γ. In general, one can say that D is better defined at intermediate-to-large strains than at small strains.

D.5.3 Correlations to Index Parameters

Because of the observed "inverse" co□patibility between D and G, one would expect that the factors affecting G should also affect D. Kokusho (1982) was among the first to suggest a relation between da□ping and soil's plasticity index. Dobry and Vucetic (1987) studied the effects of a number of factors on D as well as G of clayey soils. The results of their study are summarized in Table D.1. Their study concluded that an increase in PI will cause a decrease in D as well as an increase in G/G_{max} for a given shear strain level, as shown in Figure (D.12a). They also suggested that, compared to PI, the effect of other parameters such as OCR, confining pressure, and number of loading cycles is insignificant. Later, Vucetic and Dobry (1991) presented a set of generic damping curves as a function of plasticity index which is shown in Figure D.12b. Ishibashi and Zhang (1993) suggested the following empirical formula for damping ratio of plastic and non-plastic soils:

$$D = 0.333\frac{1+\exp(-0.0145PI^{1.3})}{2}\left[0.586\left(\frac{G}{G_{max}}\right)^2 - 1.547\frac{G}{G_{max}} + 1\right] \qquad \text{K (3.21)}$$

where G/G_{max} can be estimated from equation (3.13). The expression in (3.21) suggests that D is a function of PI and the confining pressure, because G/G_{max} in (3.13) is a function of confining pressure.

Stokoe et al. (1999) proposed the following expression for estimating D_{min}:

$$D_{min} = BP_a^{m}\sigma_a^{'-m} \qquad \text{K (3.22)}$$

where B and m are constants and function of soil type (plasticity) and OCR. σ'_a and P_a are the effective confining pressure and atmospheric pressure, respectively. This formula suggests that factors such as confining pressure and OCR as well as PI should be taken

into consideration when estimating D_{min}. The effect of these factors is discussed in more details in the coming paragraphs.

D.5.4 Confining Pressure

The effect of confining pressure, σ'_c, on D is smaller than on G. In their study, Dobry and Vucetic (1987) reported that D decreases with increasing effective confining pressure, but concluded that its effect is not significant enough to be a factor in estimating D for clays and therefore did not include it in their generic curves. Vucetic et al. (1998a) reported that generally D decreases with increasing confining stress for both sands and clays. However, for non-plastic soils and soils with low plasticity the effect of σ'_c on D is significant but decreases and may eventually disappear as PI increases. Accordingly, their conclusion was that σ'_c has a much smaller influence on D of plastic clays than on sands and that this explains why the experimental data for sands are more scattered than clays. Stokoe et al. (1999) also reported the same trend between σ'_c and D and that a larger effect is observed in non-plastic soils. However, their study shows a significant effect even for a fat clay sample. Interestingly, in this study the effect of σ'_c is larger in resonant column (RC) tests that in torsional shear (TS) tests. This is especially obvious from the reported values of the constant m in equation (3.22). For a silty sand and a fat clay (PI of clay from 36-79%) the value of m from RC tests are 0.2 and 0.06, respectively, but from TS tests the reported values are 0.07 and 0.05. It should also be noticed that the effect of σ'_c on the non-plastic soil from Vuectic et al. (1998a) study was much larger than in Stokoe et al. (1999) study, perhaps because the first study tested remolded samples while in the second study intact samples from the field were tested. This may signify the influence of inherent fabric on the way σ'_c affects damping.

D.5.5. Overconsolidation Ratio

Even though some studies (e.g. Dobry and Vucetic (1987)) reported that D is not affected by OCR, recent research suggests that the effect of OCR on D is similar to the effect of σ'_c. As OCR increases, D decreases. Also the effect of OCR is influenced by the plasticity index. The effect of OCR increases as the plasticity index decreases (Vucetic et al., 1998a). Thus for non-plastic soils and soils with low plasticity (say PI less than 20%) the effect of OCR on D is significant and should be taken into consideration. This is obvious from the bi-linear relation between σ'_c and D when increasing σ'_c changes OCR from above one to one.

D.5.6 Strain Rate (Frequency)

The effect of strain rate (or frequency) on D is not fully understood despite the fact that many studies have been conducted on the subject. However some of these studies covered a small range of frequencies and/or materials, therefore their conclusions should not be extrapolated to a wider range of frequencies. The results of a study on cohesive soils by Aggour et al. (1987), in which random vibrations with different cutoff frequencies were used, indicated a decrease in damping with increasing frequency. Dobry and Vucetic (1987), however, reported that for cohesive soils D may increase or stays the same with increasing strain rate. Kim (1991) used a RC/TS combined device to study the effect of loading frequency on damping ratio. For dry sand, the study found no difference between D from RC and TS tests at the same strain level and the same number of cycles. For compacted clay, damping ratios from RC and TS tests were different over the complete strain range (from 0.0004 to 0.05%). However, when tested in TS, the effect of frequency on D of the compacted clay does not begin until the frequency exceeded about

2-5 Hz. Zavoral and Campanella (1994) also used a RC/TS device to study the effect of frequency on D of undisturbed clay samples with PI ranges between 20-40%. To the contrary of the Kim (1991) study, damping ratios from RC tests and from TS tests with a frequency range from 0.01 to 1.0 Hz are approximately the same, thus, suggesting no significant effect of frequency on damping. As well, Vucetic et al. (1998a) did not observe the effect of frequency on D in the range between 0.01-0.1 Hz for both sand and clay samples. The same was observed by Hara and Kiyota (1977) for undisturbed clay samples and for frequencies in the range between 0.1-10 Hz.

Interestingly, Stokoe et al. (1999) reported a very significant increase (about 100%) in D_{min} of a sandy clay (CL) sample when frequency was increased from 1 to 50 Hz (compared to 10% increase in G_{max}) also using a RC/TS device. The study also reported an increase in D_{min}, though less than sandy clay, of silty sand and fat clay (CH) samples but no trend with PI could be established. Moreover, the results indicated that the effect of frequency on D_{min} is more noticeable after 10Hz.

Examining the results of the studies presented above, one would certainly be confused about how strain rate or frequency affects damping. Shibuya et al (1995) presented what seems to be the explanation for the contradictions in the results of different studies. Shibuya et al. (1995) suggested that the effect of frequency on D has three phases, as shown in FigureD.13. In the first phase, for frequencies smaller than 0.1 Hz, D decreases as f increases. This may be attributed to the strain-rate dependent nature, or creep, of the stress-strain relationship. The second phase, for f between 0.1-10 Hz, D remains unchanged irrespective of strain rate. The third phase, for f larger than 10 Hz, D increases with increasing f and D is governed by the shear strain rate. This is because of

the increase in the contribution of viscous damping, which is strain-rate dependent, at these relatively high frequencies. This analysis seems to fit very well with the observed experimental data.

D.5.7 Number of Loading Cycles

The effect of the number of loading cycles, N, on D is the same as on G. For shear strains below the volumetric threshold strain, γ_{tv}, N has no effect on D because the soil is still behaving elastically. For shear strain above, γ_{tv}, D decreases as N increases. The effect of N increases as the shear strain increases further above γ_{tv}. The effect of N is more significant for non-plastic unsaturated soils (Kim, 1991 and Stokoe et al., 1999). For plastic soils, the effect is insignificant at moderate N and shear strain (Dobry and Vucetic, 1987).

D.5.8 Shape of Cyclic Loading

Vucetic et al (1998b) studied the effect of the shape of the cyclic strain-time history on the damping ratio for reconstituted sands and clays. The results showed that D can be significantly affected by the shape of cyclic loading because of the viscous nature of soil and the associated effect of creep and relaxation. Damping ratio gets larger as the shape changes from triangular to sinusoidal and further from trapezoidal to square. The shape of the tip of the cycle is important because it is where the shear strain reaches its maximum value. For a shape other than triangular, the strain rate at the tip of the cycle reaches zero. As the tip of the loading cycle become flatter, the soil will have more time to relax and creep. The study found that as the cycle shape changes from triangular to trapezoidal, D doubled in value at a shear strain at 0.01%. Moreover, the effect is much

larger at small strains than at large strains, perhaps because D at large strains is already large. The effect of cycle shape on D increases as PI increases, obviously, because of the increase in the soil's viscosity. Therefore, clean sands are not susceptible to this effect, but with increase in silt content, the effect of shape becomes more noticeable. This explains why, during straining with sinusoidal shape, the tips of the loops of clays are typically rounded, whereas those of clean sands are pointed (Dobry and Vucetic, 1987).

D.5.9 Time under Confinement

Marcuson and Wahls (1978) used a RC device to study this effect on kaolinite (which exhibits very little secondary compression) and calcium bentonite (which exhibits relatively large secondary compression). Their study shows, as expected, that damping ratio decreases with increasing time at constant effective stress after completion of primary consolidation. The change in D was as low as 7.5% for the low-PI soil and as high as 25% for high-PI soil per log cycle of time. The results also show that the decrease in D was larger in drained rather than undrained tests, perhaps because of changes in the void ratio. Other studies reported the same trend between time and D (e.g. Dobry and Vucetic, 1987). Due to this time effect, laboratory testing will always tend to overestimate the damping ratio in field.

D.5.10 Plasticity Index

With recent advances in cyclic testing apparatuses and the introduction of very sensitive transducers, experimental results are showing a more complex effect of PI on the D-γ relationship not shown in the generic curves. The results show that D has two opposing trends with respect to PI (EPRI, 1993; Vucetic et al., 1998a; Lanzo and Vucetic,

1999; and Stokoe et al., 1999). At small strains (below about 0.005%) D for clays is larger than for sands, and increases with increasing PI. At larger strains (say above 0.01%), the trend is reversed and D for sands is larger than for clays and decreases with increasing PI. The effect of PI on D-γ is shown in a general sense in Figure D.14 and from experimental results in Figure D.15. Vucetic et al. (1998a) explained this reversal in trend by the relative contributions of soil nonlinearity (hysteretic damping) and soil viscosity (viscous damping) at small versus large strains. At small strains, the soil deforms linearly and elastically, thus, D depends predominantly on viscous damping which increases with increasing PI. At larger strains, however, soil behavior becomes nonlinear and inelastic, hence, D depends predominantly on frictional damping. Soils with lower PI have more nonlinearity than soils with high PI, therefore, they experience more damping at large strains. However, the trend between PI and D at small strains may not be obvious as PI decreases because of the increase of scatter of the data points. This may indicate that D in low-plasticity clays and sands is more sensitive to factors such as confining stress and OCR than in high-plasticity clays (Lanzo and Vucetic, 1999).

D.5.11 Consolidation Stress Path

The influence of consolidation stress path on damping has not been sufficiently studied, and test data which quantify this effect are rare. Theoretically, the hysteretic loop induced by earthquake loading will be centered on the origin of the stress-strain coordinates, where the magnitude of the shear stress can be characterized by the value of the second invariant of the deviatoric stress tensor, J2D (Li et al., 1993):

$$J_{2D} = \left(\frac{q}{3}\right)^3 + \tau^2 \qquad \text{K (3.23)}$$

in which $q=\sigma_v-\sigma_h$, the difference between vertical and horizontal normal stresses. This is because the soil in the field is usually K_o-consolidated, therefore, q is unlikely to be zero and contributes with τ to J_{2D}. As shown in Figure D.16, the shape of the hysteretic loop can be affected by q due to soil nonlinearity (Li et al., 1993). This means that D for a anistropically consolidated soil may be larger than if the soil is isotropically consolidated. However, there is not, yet, sufficient experimental results that quantify this effect.

References

Afifi, S.E.A., and Richart, F.E. (1973). "Stress history effects on shear □odulus of soils," Soils and Foundations (Japan), Vol. 13, No. 1, pp.77-95

Aggour, M.S., Tawfiq, K.S., and A□ini, F. (1987). "Effects of frequency content on dynamic properties for cohesive soils," Proceedings. 3rd International Conference on Earthquake Engineering and Soil Dynamics, Princeton, June, pp. 31-39.

Anderson, D.G., and Richart, F.E. (1976), "Effect of straining on shear □odulus of clays," Journal of Geotechnical Engineering, ASCE, Vol. 102, No. 9, pp. 975-987

Anderson, D.G., and Stokoe, K.H. (1978), "Shear Modulus: A ti□e dependent soil property," Dyna□ic Geotechnical Testing, ASTM STP 654, A□erican Society for Testing and Materials, pp. 66-90.

Anderson, D.G., and Woods, R.D. (1975). "Co□parison of field and laboratory shear □odulus," Proceedings of the ASCE Conference on In-Situ Measurement of Soil Properties, Vol. 1, pp.69-92.

Anderson, D.G., and Woods, R.D. (1976). "Ti□e-dependent increase in shear modulus of clays," Journal of Geotechnical Eng. Div., ASCE, Vol. 102, No. GT5, pp.525-537

Athanasopoulos, G.A., and Richart, F.E. (1983). "Effect of stress release on shear □odulus of clays," Journal of Geotechnical Eng. Division, ASCE, Vol. 109, No. 10, pp. 1217-1232.

Drnevich, V.P., and Richart, F.E. (1970), "Dyna□ic prestraining of dry sand." Journal of Soil Mechanics and Foundations Div., ASCE, Vol. 96, No. 2, pp. 453-469.

Dobry, R. (1991). "Low and high-strain cyclic □aterial properties," Proceedings: NSF/EPRI Workshop on Dynamic Soil Properties and Site Characterization, Chapter 3, CH2M HILL, Bellevue, Washington, Volume 1.

Dobry, R., Ladd, R.S., Yokel, F.Y., Chung, R.M., and Powell, D. (1982). "Prediction of pore water pressure buildup and liquefaction of sands during earthquakes by the cyclic strain □ethod." Nat. Bureau of Standards Build. Science Series 138, Washington, DC.

Dobry, R., Yokel, F.Y., and Ladd, R.S. (1981). "Liquefaction potential of overconsolidated sands in □oderately seis□ic areas." Proc., Conf. on Earthquakes and Earthquake Eng. in Eastern U.S., Knoxville, Tenn., Ann Arbor Science Publishers, Inc., Ann Arbor, Mich., Vol. 2, 643-664.

Dobry, R., and Vucetic, M. (1987), "State-of-the-art report: dynamic properties and response of soft clay deposits." Proc., Int. Sy□p. on Geotechnical Eng. of Soft Soils, Sociedad Mexicana de Mecanica de Suelos, Mexico, Vol. 2, pp. 51-87.

EPRI (1991). "Low- and high-strain cyclic □aterial properties," Proc., NSF/EPRI Workshop on Dynamic Soil Properties and Site Characterization, Report NP-7337, Vol. 1, Electric Power Research Institute, Project 810-14, June.

Hara, A., and Kiyota, Y. (1977). "Dyna□ic Shear Tests of soils for seis□ic analysis," Proceedings, 9th International Conference on Soil Mechanics and Foundation Engineering, Vol. 3, pp. 247-250.

Hardin, B.O., and Black, W.L. (1968), "Vibration □odulus of nor□ally consolidated clay," Journal of Soil Mechanics and Foundations Div., ASCE, Vol. 94, No. 2, pp. 353-369.

Hardin, B.O., and Drnevich, V. (1972), "Shear □odulus and damping in soils: Design equations and curves," Journal of Soil Mechanics and Foundations Div., ASCE, Vol. 98, No. 7, pp. 667-691.

Hardin, B.O. (1978), "The nature of stress-strain behavior of soils," Earthquake Engineering and Soil Dynamics, ASCE, Vol. 1, pp. 3-90.

Idriss, I.M., Dobry, R., and Singh, R.D. (1978). "Nonlinear behavior of soft clays during cyclic loading," Journal of Geotechnical Engineering Division, ASCE, Vol. 104, No. GT12, pp. 1427-1447.

Idriss, I.M., Moriwaki, Y., Wright, S.G., Doyle, E.H., and Ladd, R.S. (1980). "Behavior of normally consolidated clay under simulated earthquake and ocean loading conditions," Proceedings, International Sy□posiu□ on Soils under Cyclic and Transient, Swansea, United Kingdom, Vol. 1, pp. 437-445.

Imai, T., and Tonouchi, K. (1982), "Correlation of N-value with S-wave velocity and shear □odulus," Proceedings of the 2nd European Symposium on Penetration Testing, Amsterdam, The Netherlands, pp. 67-72.

Isenhower, W.M., and Stokoe, K.M. (1981), "Strain rate dependent shear modulus of San Francisco Bay Mud," Proceedings, International Conference on Recent Advances in Geotechnical Earthquake Engineering and Soil Dynamics, University of Missouri-Rolla, Vol. 2, pp. 597-602

Ishibashi, I. (1992). Discussion to "Effect of soil plasticity on cyclic response," by M. Vucetic and R. Dobry, Journal of Geotechnical Engineering, ASCE, Vol. 118, No. 5, pp. 830-832

Ishibashi, I., and Zhang, X. (1993). "Unified dyna□ic shear □oduli and da□ping ratios of sand and clay," Soils and Foundations, Vol. 33, No. 1, pp. 182-191.

Ishihara, K. (1981). "Strength of cohesive soils under transient and cyclic loading conditions." State-of-the-Art in earthquake Eng., Proc., 7th World Conf. on Earthquake Eng., Istanbul, Turkey, 154-169.

Iwasaki, T., Tatsuoka, F., and Takagi, Y. (1978). "Shear □odulus of sands under torsional loading," Soils and Foundations, Vol. 18, No. 1, pp. 39-56.

Ja□iolkowski, M., Leroueil, S. and LoPresti, D.C.F. (1991), "The□e lecture: Design parameters from theory to practice," Proceedings, Geo-Coast '91, Yokoha□a, Japan, pp. 1-14.

Kim, D.-S (1991). "Defor□ational characteristics of soils at s□all to inter□ediate strains fro□ cyclic tests," Ph.D. dissertation, University of Texas at Austin.

Kim, D.-S, Stokoe, K.H., and Hudson, W.R. (1991). "Defor□ational characteristics of soils at s□all to inter□ediate strains fro□ cyclic tests." Research Report No. 1173-3, Ctr. Trans. Res., Bureau of Eng. Res., Univ. of Texas, Austin.

Kokusho, T., Yoshida, V., and Esashi, Y. (1982). "Dyna□ic properties of soft clay for wide strain range," Soils and Foundations, Vol. 22, No. 4, pp. 1-18.

Lanzo, G., Vucetic, M., and Doroudian, M. (1997). "Reduction of shear □odulus at s□all strains in si□ple shear," Journal of Geotechnical Engineering Division, ASCE, Vol. 123, No. 11, pp. 1035-1042.

Lanzo, G., Vucetic, M. (1999). "Effect of soil plasticity on da□ping ratio at s□all cyclic strains," Soils and Foundations, Vol. 39, No. 4, pp. 131-141.

Li, X.S., Roblee, C.J., and Wang, G. (1993). "Develop□ent and evaluation of a prototype tool for in situ determination of high-strain properties of soft to medium-stiff

clays," Report No. FHWA/CA/TL-94/05, Research Project F92TL05, Caltrans, Division of New Tech., Materials and Research, Office of Geotechnical Eng.

Lodde, P.F., and Stokoe, K.H. (1981). "Dyna□ic response of San Francisco Bay Mud," Geotechnical Engineering Report, The University of Texas at Austin.

Macari, E.J., and Ko, H.-Y. (1994). "A study of an anisotropically overconsolidated silt by the resonant colu□n □ethod," Geotechnical Testing Journal, GTJODJ, Vol. 17, No. 3, pp. 315-324.

Macky, T.A., and Saada, A.S. (1984). "Dyna□ics of anisotropic clays under large strains," Journal of Geot. Eng. Div., ASCE, Vol. 110, No. 4, pp. 487-504.

Marcuson, W.F., and Wahls, H.E. (1972). "Ti□e effects on the dyna□ic shear □odulus of clays," Journal of Soil Mechanics and Foundation Engineering Division, ASCE, Vol. 98, No. SM12, pp.1359-1972.

Marcuson, W.F., and Wahls, H.E. (1978). "Effect of ti□e on da□ping ratio of clays," Dynamic Geotechnical Testing, ASTM STP 654, American Society for Testing and Materials, pp. 126-147.

Mayne, P.W., and Rix, G.J. (1993), "G_{max}-q_c relationships for clays," Geotechnical Testing Journal, ASTM, Vol. 16, No.1, pp. 54-60.

Mukabi, J.N., A□padu, S.K., Tatsuoka, F., Sato, T., and Hirose, K. (1991). "S□all strain stiffness and elasticity of clays in □onotonic loading triaxial co□pression," Proc. Of 46th Annual Conf. of the JSCE, Vol. 111, pp. 498-499.

Ramberg, W., and Osgood, W.T. (1943). "Description of stress-strain curves by three para□eters," Technical Note 902, National Advisory Co□□ittee for Aeronautics.

Roesler, S.K. (1979)." Anisotropic shear □odulus due stress anisotropy," Journal of Geotechnical Engineering Div., ASCE, Vol. 105, No. GT7, pp. 871-880.

Saada, A.S., Bianchini, G.F., and Shook, L.P. (1978). " The dyna□ic response of anisotropic clay," Proceedings, Geotechnical Eng. Div. Specialty Conf. on Earthquake Eng. and Soil Dynamics, Vol. 11, ASCE, Pasadena, CA.

Seed, H.B., Wong, R.T., Idriss, I.M. and Toki□atsu, K. (1984), "Moduli and da□ping factors for dyna□ic analyses of cohesionless soils," Earthquake Engineering Research Center, Report No, UCB/EERC-84/14, Univ. of California, Berkeley.

Shibuya, S., Mitachi, T., Fukuda, T., and Degoshi, T. (1995). "Strain rate effect on shear □odulus and da□ping of nor□ally consolidated clay," Geotechnical Testing Journal, GTJODJ, Vol.18, No. 3, pp. 365-375.

Stokoe, K.H., Darendeli, M.B., Andrus, R.D., and Brown, L.T. (1999). "Dyna□ic soil properties: Laboratory, field, and correlation studies," 2nd International Conference on Earthquake Engineering, Vol. 3, Lisbon, Portugal.

Stokoe, K.H., Lee, S.H., and Knox, D.P. (1985). "Shear □odulus □easure□ent under true triaxial stresses," Proceedings, Advances in the Art of Testing Soils Under Cyclic Conditions, ASCE.

Stokoe, K.H., and Lodde, P.F. (1978). "Dyna□ic response of San Francisco Bay Mud ." Proc., ASCE Earthquake Eng. and Soil Dynamics Conf., Pasadena, California, Vol. 2, 940-959.

Stoll, R.D., and Kald, L. (1977). "Threshold of dilation under cyclic loading," Journal of Geotechnical Engineering, Vol. 103, No. 10, pp. 1174-1178.

Sun, J.I., Golesorkhi, R., and Seed, H.B. (1988). "Dyna□ic □oduli and da□ping ratios for cohesive soils," Report No. EERC-88/15, Earthquake Engineering Research Center, University of California, Berkeley.

Sykora, J.I., and Stokoe, K.H. (1983), "Correlations of in situ □easure□ents in sands with shear wave velocity," Geotechnical Engineering Report GR83-33, University of Texas, Austin.

Vucetic, M., and Dobry, R. (1988). "Degradation of □arine clays under cyclic loading," Journal of Geotech. Eng. Div., ASCE, Vol. 114, No. 2, pp. 133-149

Vucetic, M., and Dobry, R. (1991). "Effect of soil plasticity on cyclic response," ASCE, Journal of Geotechnical Engineering, Vol. 117, No. 1, pp. 89-107.

Vucetic, M. (1994). "Cyclic threshold shear strains in soils," Journal of Geotechnical Eng. Div., ASCE, Vol. 120, No.12, pp. 2208-2227.

Vucetic, M., Lanzo, G., and Doroudian, M. (1998a). "Da□ping at s□all strains in cyclic si□ple shear test," Jourl. of Geo. Eng. Div., ASCE, Vol. 124, No.7, pp. 585-593

Vucetic, M., Lanzo, G., and Doroudian, M. (1998b). "Effect of the shape of cyclic loading on damping ratio at small strains," Soils and Foundations, Vol. 38. No.1, pp.111-120.

Yu, P., and Richart, F.E. (1984). "Stress-ratio effects on shear □odulus of dry sands," Journal of Geotechnical Eng. Div., Vol. 110, No. 3, pp. 331-345.

Zavoral, D.Z., and Ca□panella, R.G. (1994). "Frequency effects on Damping/modulus of cohesive soil," Dyna□ic Geotechnical Testing II, ASTM STP 1213, Ronald J. Ebelhar, Vincent P. Drnevich, and Bruce L. Kutter, Eds., American Society for Testing and Materials, Philadelphia.

Zen, K., Umehara, Y., and Ha□ada, K. (1978). "Laboratory tests and in-situ seismic survey on vibratory shear □odulus of clayey soils with different plasticities," Proceedings, 5th Japan Earthquake Engineering Symposium, Tokyo, pp. 721-728.

TableD.1 Effect of increase of various factors on Gmax, G/ Gmax, and damping ratio of normally consolidated and moderately overconsolidated clays (Dobry and Vucetic, 1987)

Increasing Factor	G_{max}	G/G_{max}	λ
Confining Pressure $\bar{\sigma}_0$	Increases with $\bar{\sigma}_0$	Stays constant or Increases with $\bar{\sigma}_0$	Stays constant or decreases with $\bar{\sigma}_0$
Void Ratio e	Decreases with e	Increases with e	Decreases with e
Geologic Age t	Increases with t	May increase with t	Decreases with t
Cementation c	Increases with c	May increase with c	May decrease with c
Overconsolidation OCR	Increases with OCR	Not affected	Not affected
Plasticity Index P.I.	• Increases with P.I. if OCR>1 • Stays about constant if OCR=1	Increases with P.I.	Decreases with P.I.
Cyclic Strain γ_c	----	Decreases with γ_c	Increases with γ_c
Strain Rate $\dot{\gamma}$ (Frequency of Cyclic Loading)	Increases with $\dot{\gamma}$	• G increases with $\dot{\gamma}$ • G/G_{max} probably not affected if G and G_{max} are measured at same $\dot{\gamma}$	Stays constant or may increase with $\dot{\gamma}$
Number of Loading Cycles N	Decreases after N cycles of large γ_c but recovers later with time	Decreases after N cycles of large γ_c (G_{max}, measured before N cycles)	Not significant for moderate γ_c and N

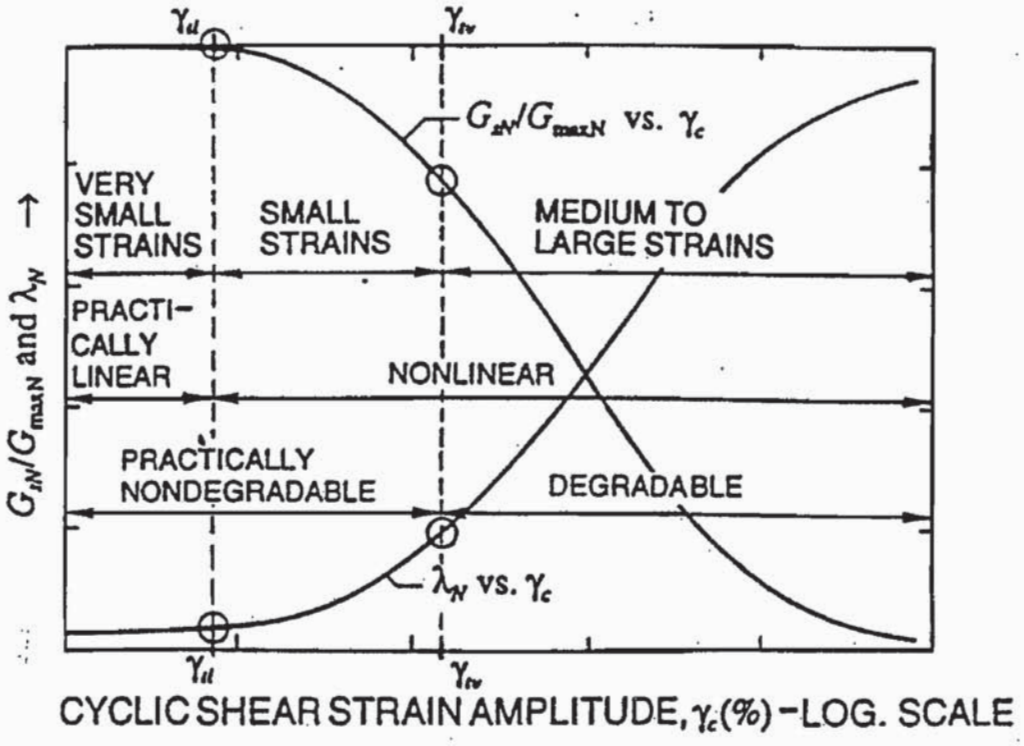

FigureD.1 Shear modulus reduction curve with different zones of cyclic shear strain amplitude (After Vucetic, 1994)

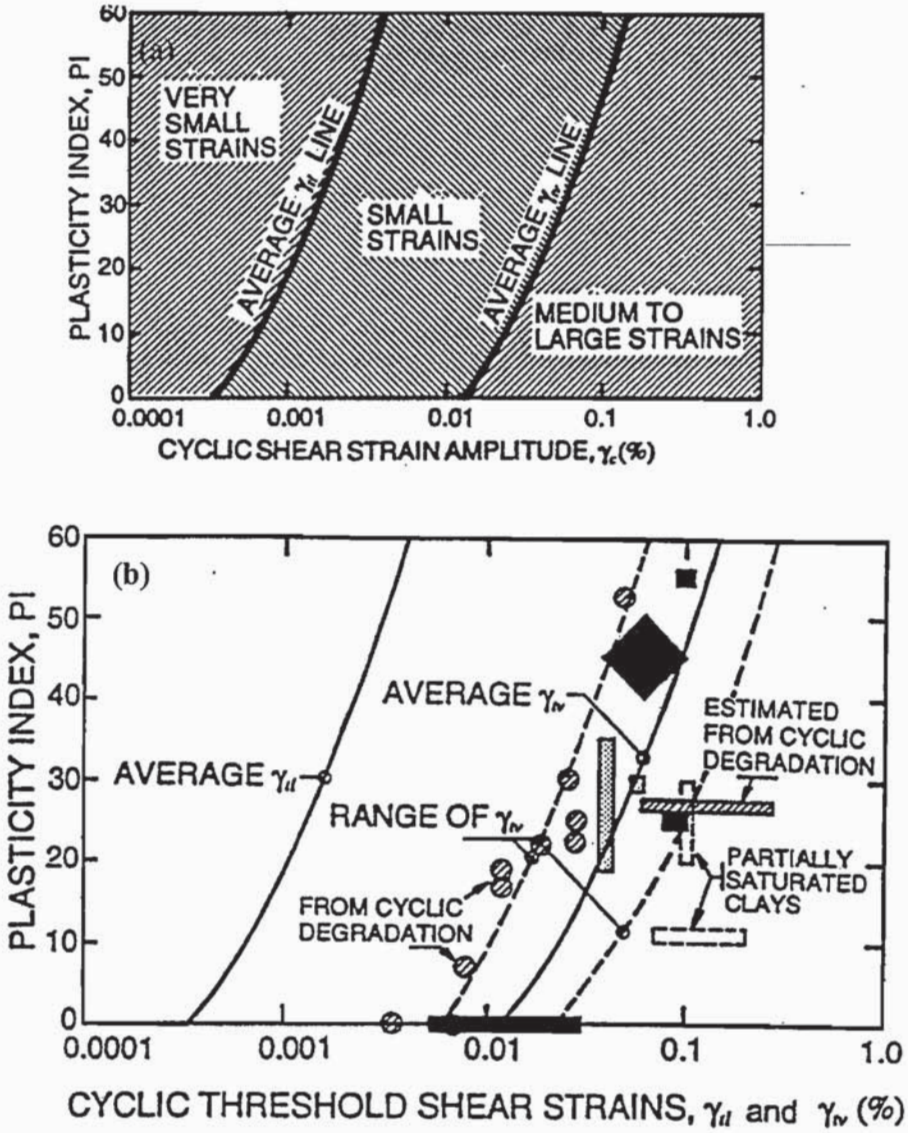

FigureD .2 Categorization of cyclic shear strain (a), and (b) effect of plasticity index on the cyclic threshold shear strains (After Vucetic, 1994)

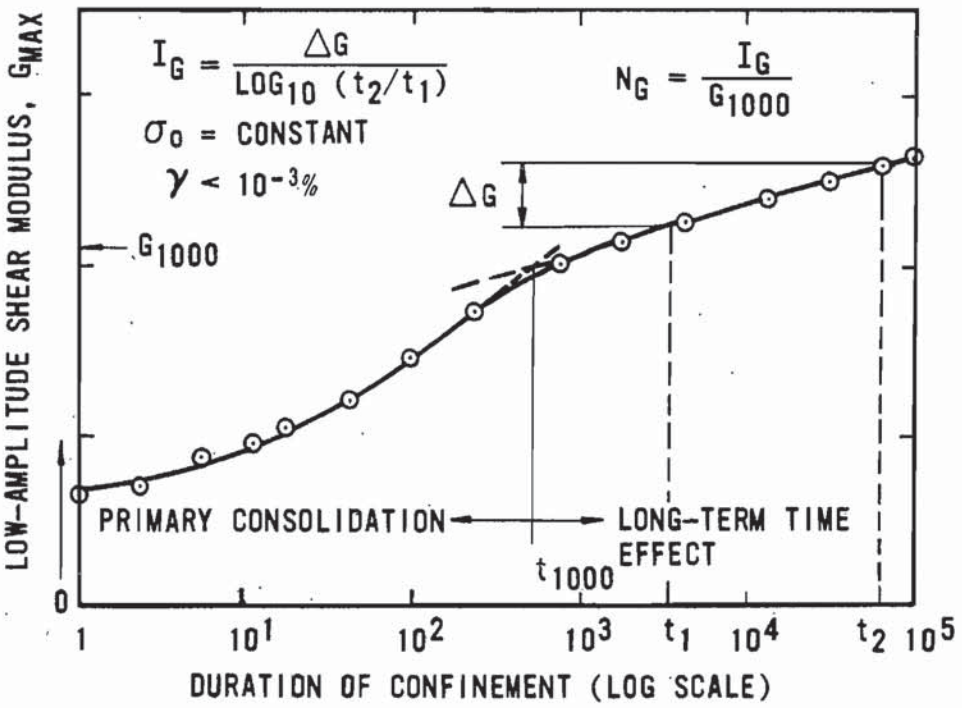

Figure D.3 Phases of modulus-time response (After Anderson and Stokoe, 1978)

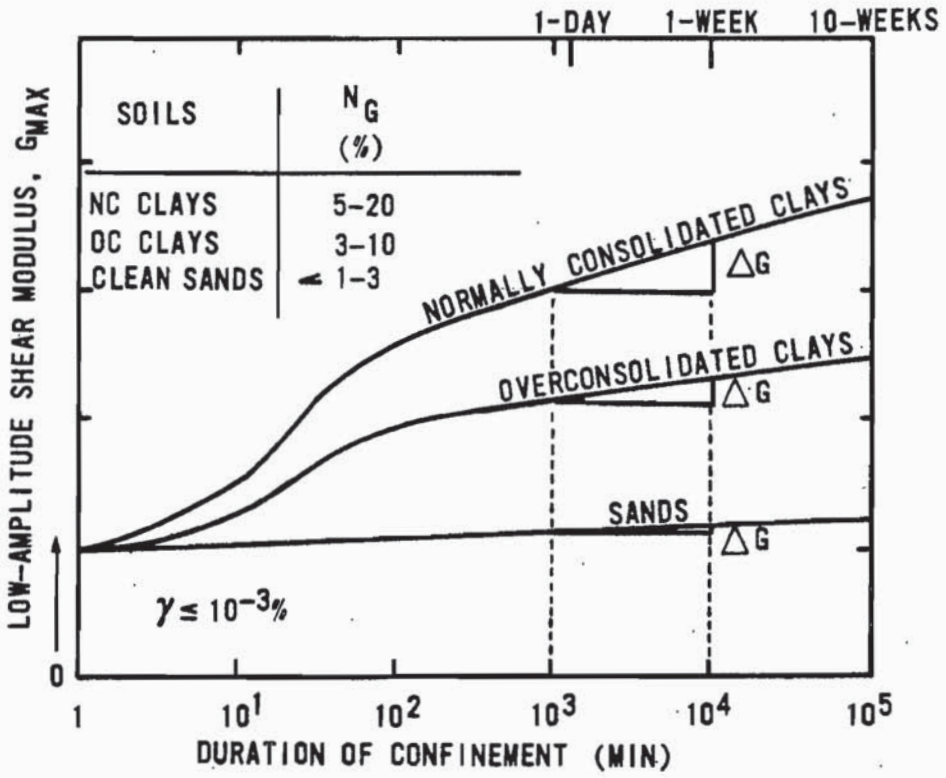

Figure D.4 Effect of confinement time on shear modulus of different soils (After Anderson and Stokoe, 1978)

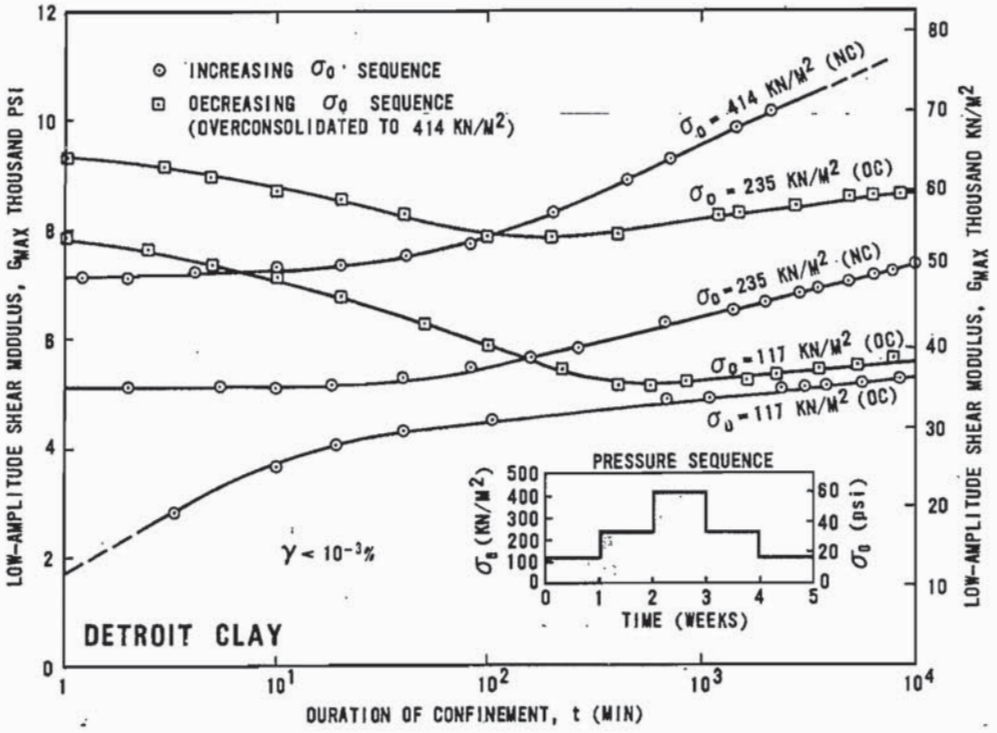

FigureD.5 Effect of stress history on shear modulus-time relationship (After Anderson and Stokoe, 1978)

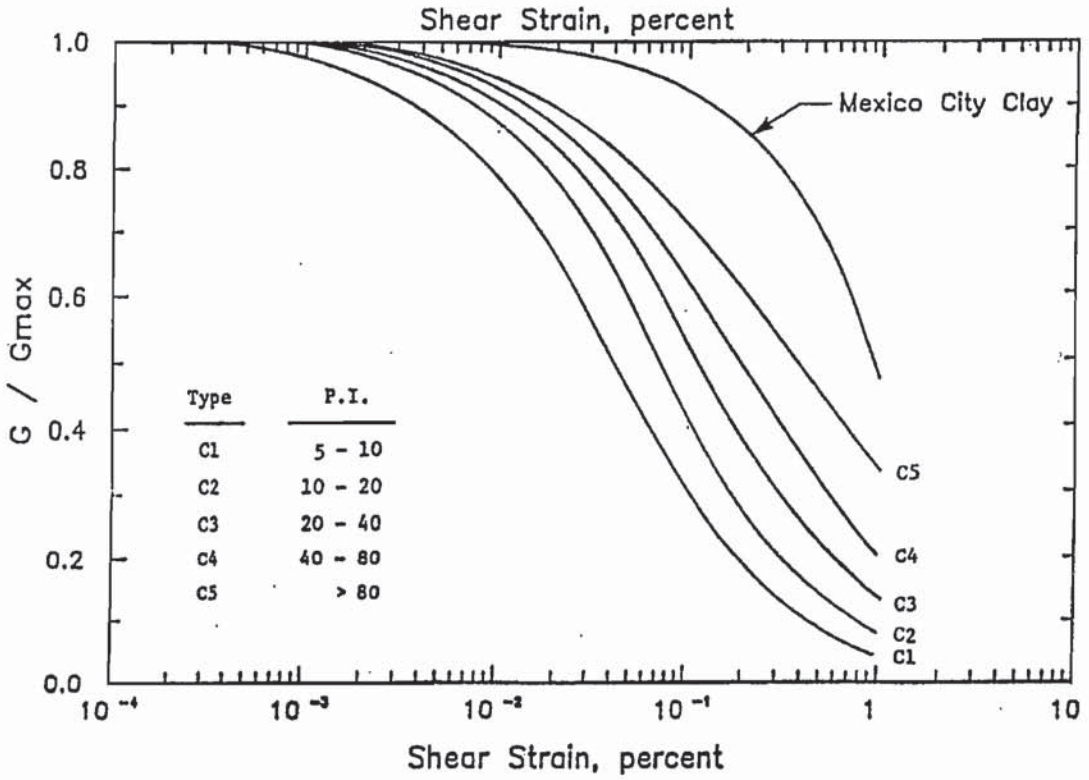

Figure D.6 Normalized modulus reduction curve for clays with different plasticity indices (After Sun et al., 1988)

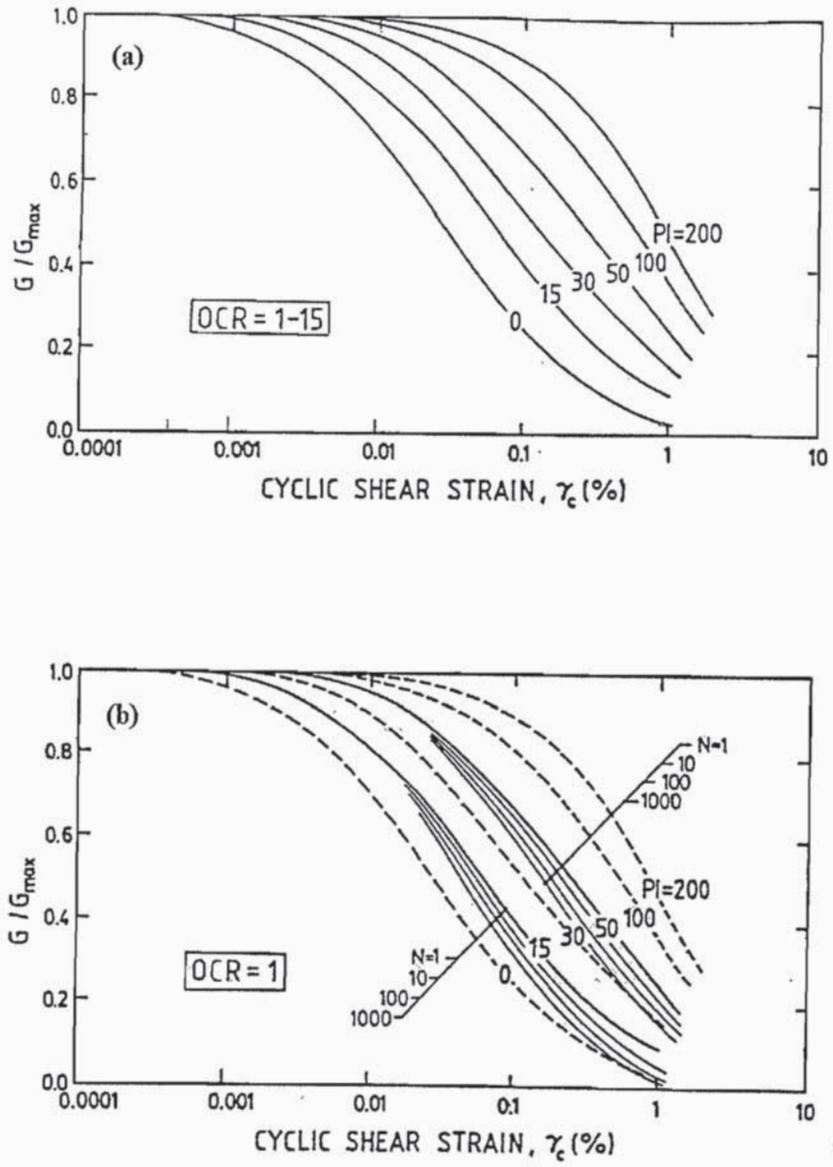

FigureD.7 Normalized modulus reduction curves for clays (a) influence of plasticity index (b) number of loading cycles (after Vucetic and Dobry, 1991)

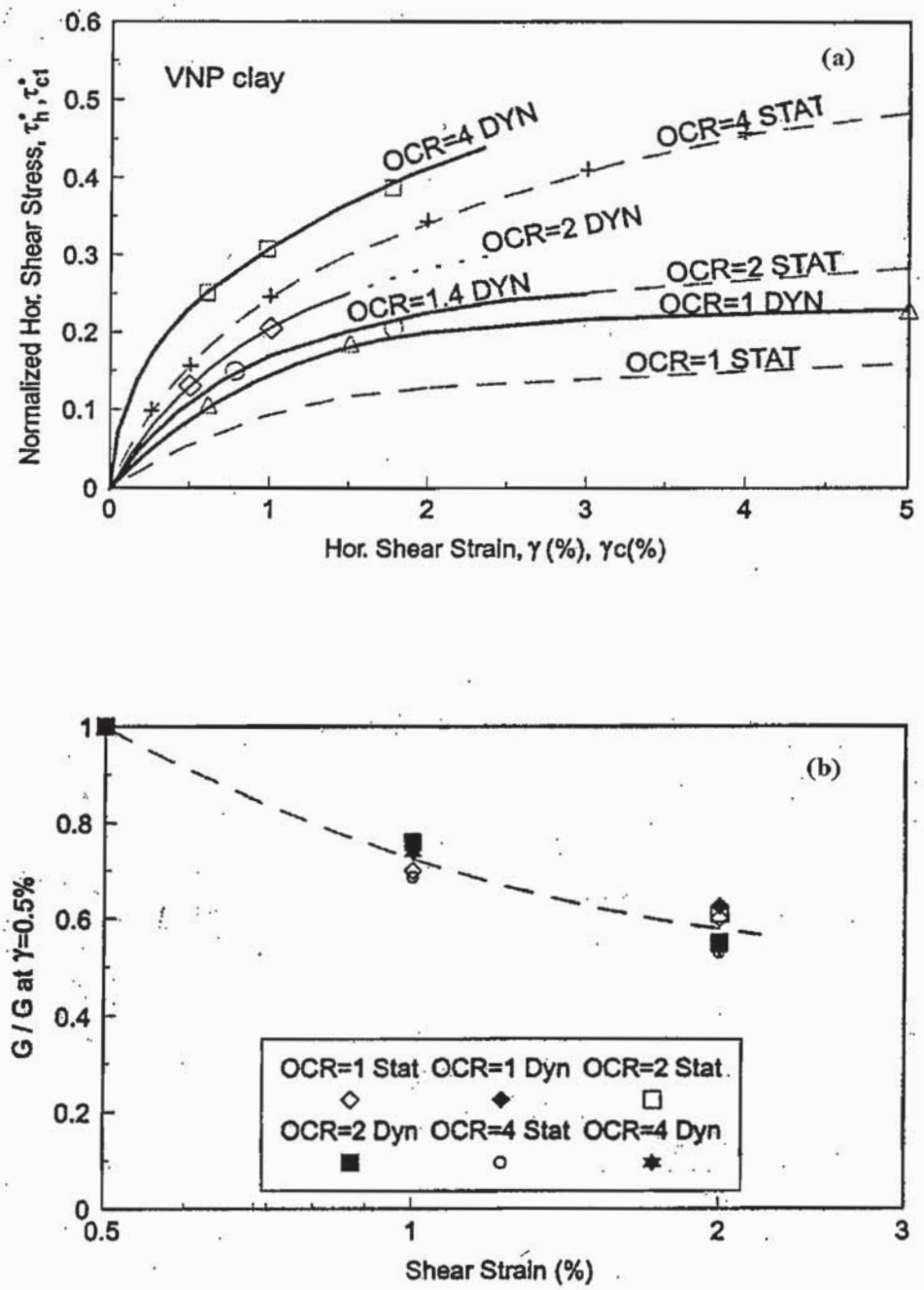

Figure D.8 (a) Comparison of static and dynamic test results on VNP clay (Dobry and Vucetic, 1988) and (b) modulus reduction curve normalized at γ=0.5% (after Li et al., 1993; and Dobry and Vucetic, 1988)

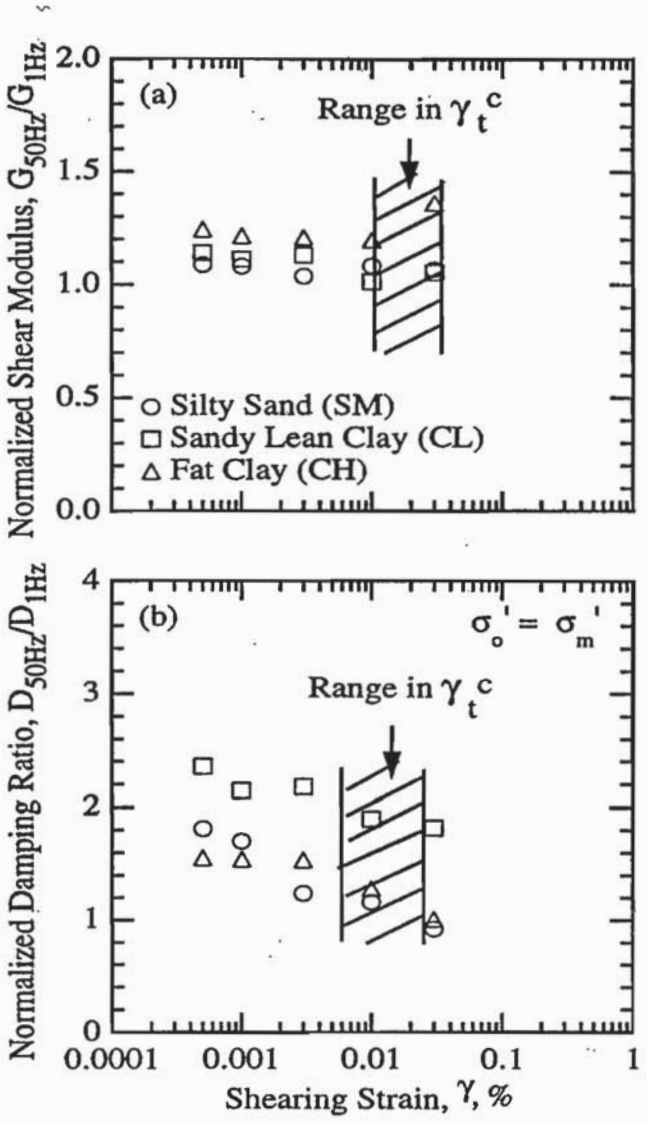

Figure D.9 Variation in G (a) and D (b) with frequency over a range of shear strains for three different soils (after Stokoe et al., 1999)

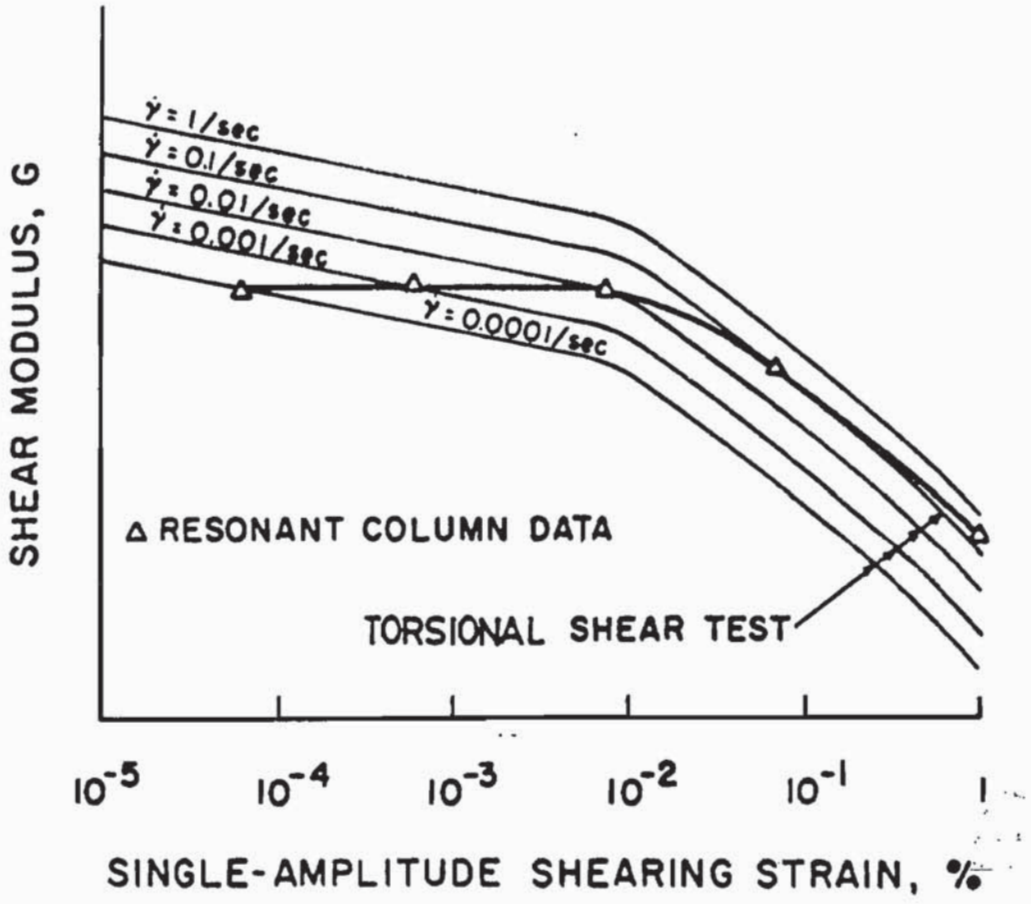

FigureD.10 Combined strain amplitude and strain rate effects on shear modulus (After Isenhower and Stokoe, 1981)

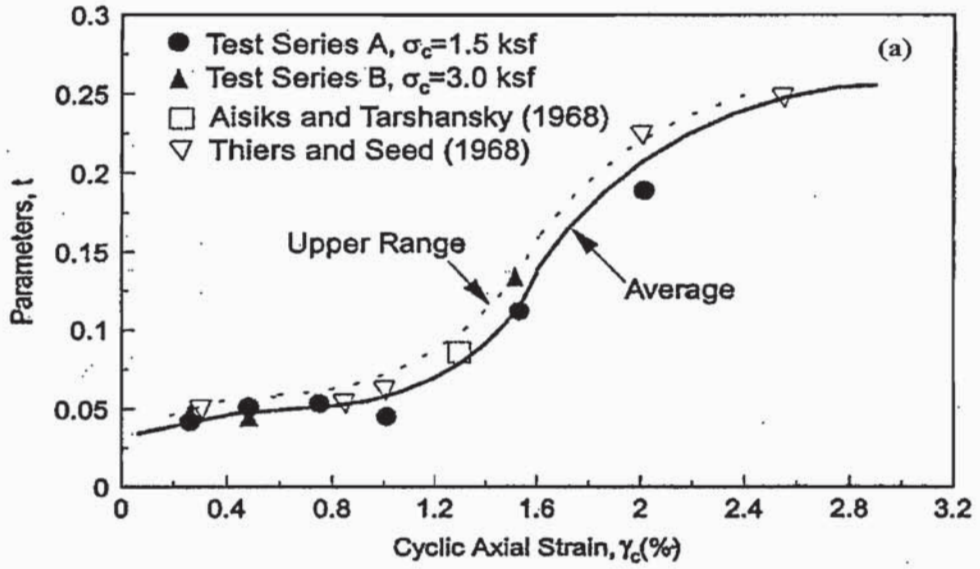

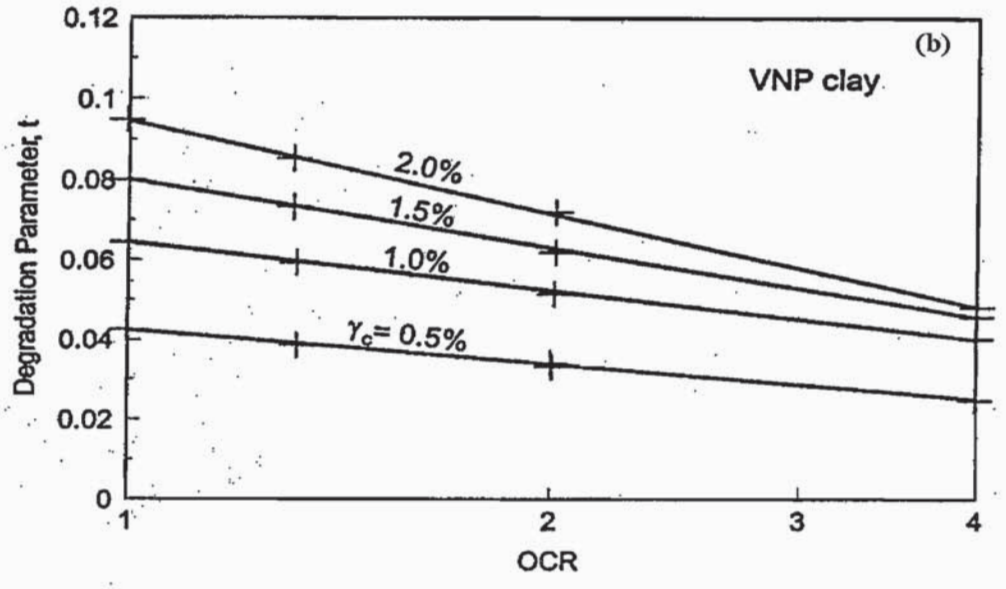

Figure D.11 Variation of degradation parameter t with (a) cyclic strain (After Idriss et al., 1978) and (b) OCR (After Vucetic, 1988)

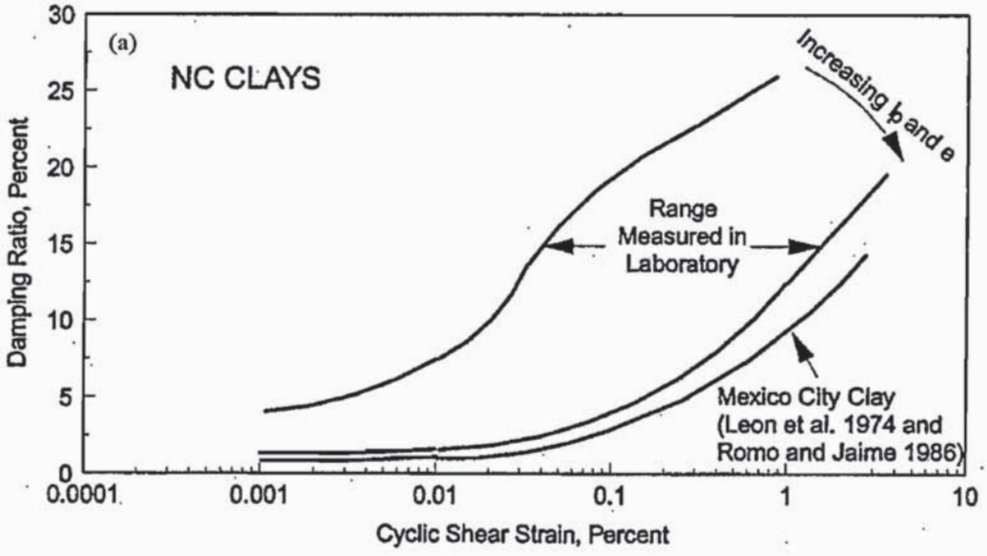

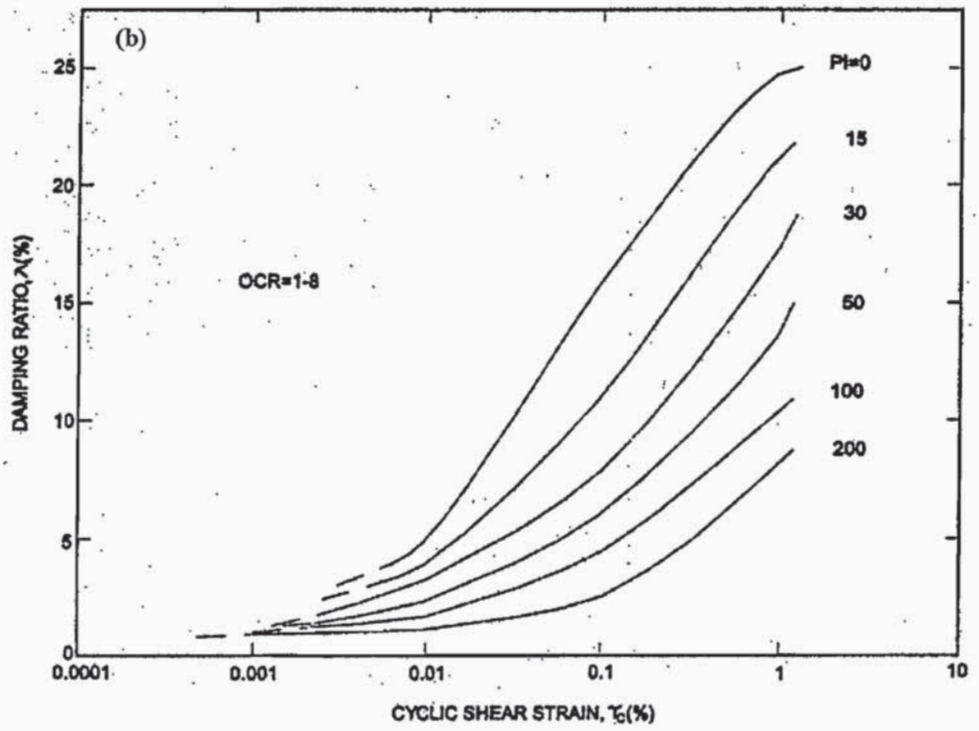

FigureD.12 (a) Damping ratio and trends of clays measured in the laboratory (After Dobry and Vucetic, 1987) and (b) generic curves as a function of plasticity index (After Vucetic and Dobry, 1991)

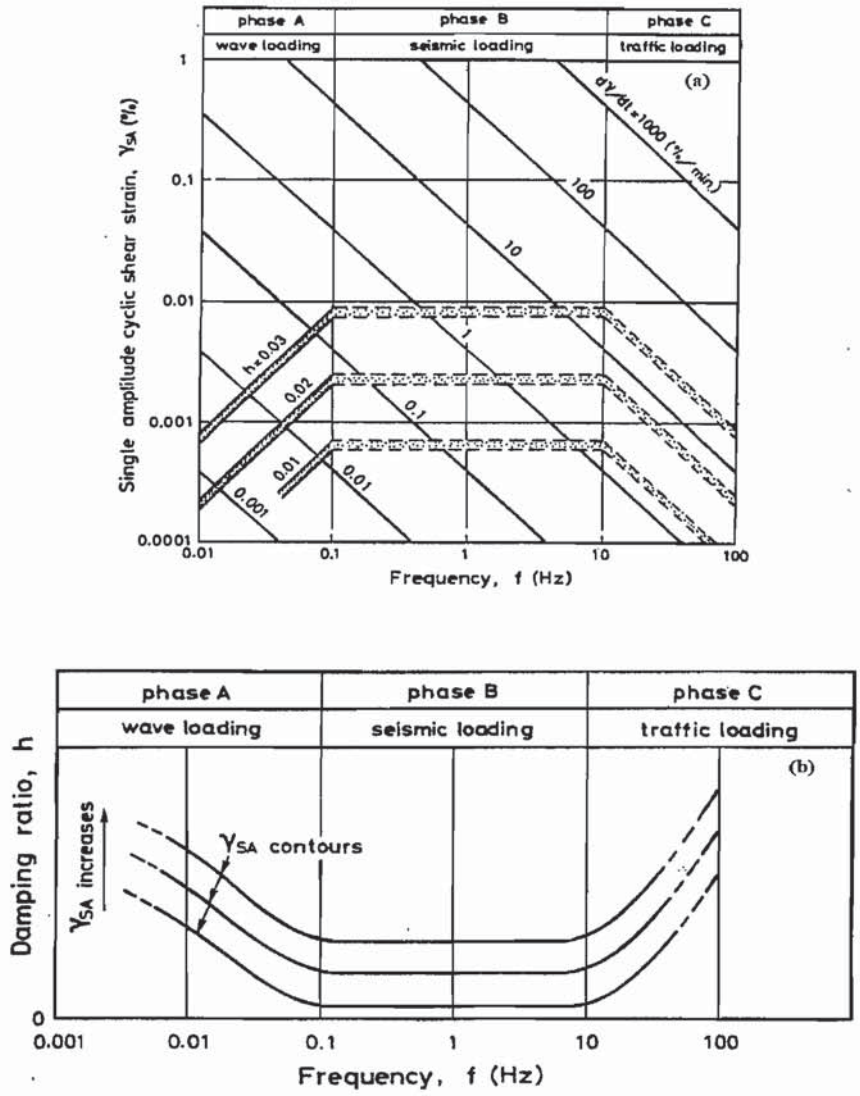

Figure D.13: (a) Contours of shear strains and damping ratio, h, and (b) a conceptual diagram depicting the effect of frequency on damping of cohesive soils (after Shibuya et al., 1995)

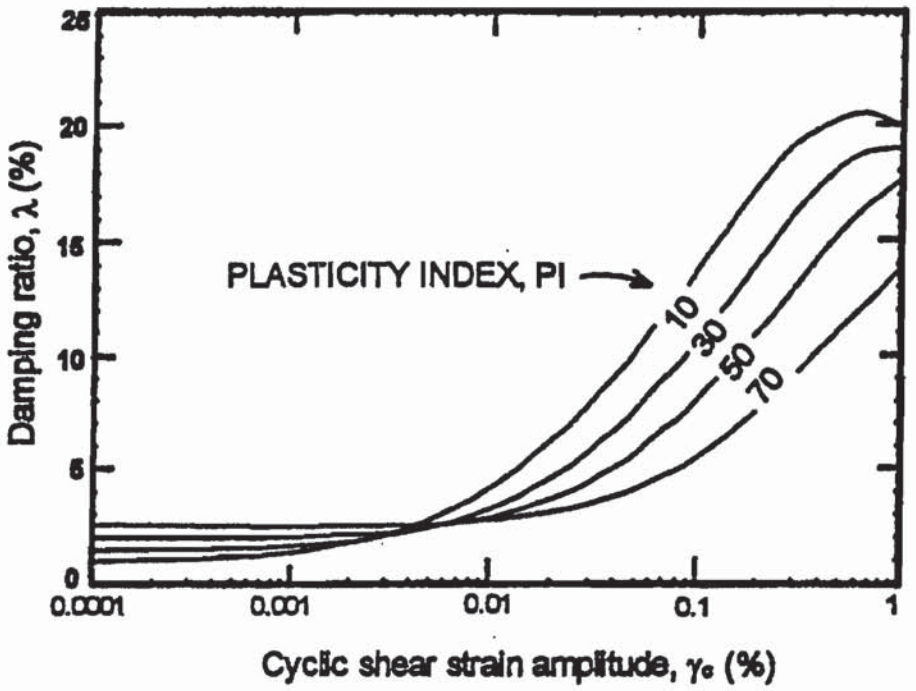

Figure D.14 Effect of plasticity index on damping ratio curves derived analytically for clays by Pyke (After EPRI, 1993)

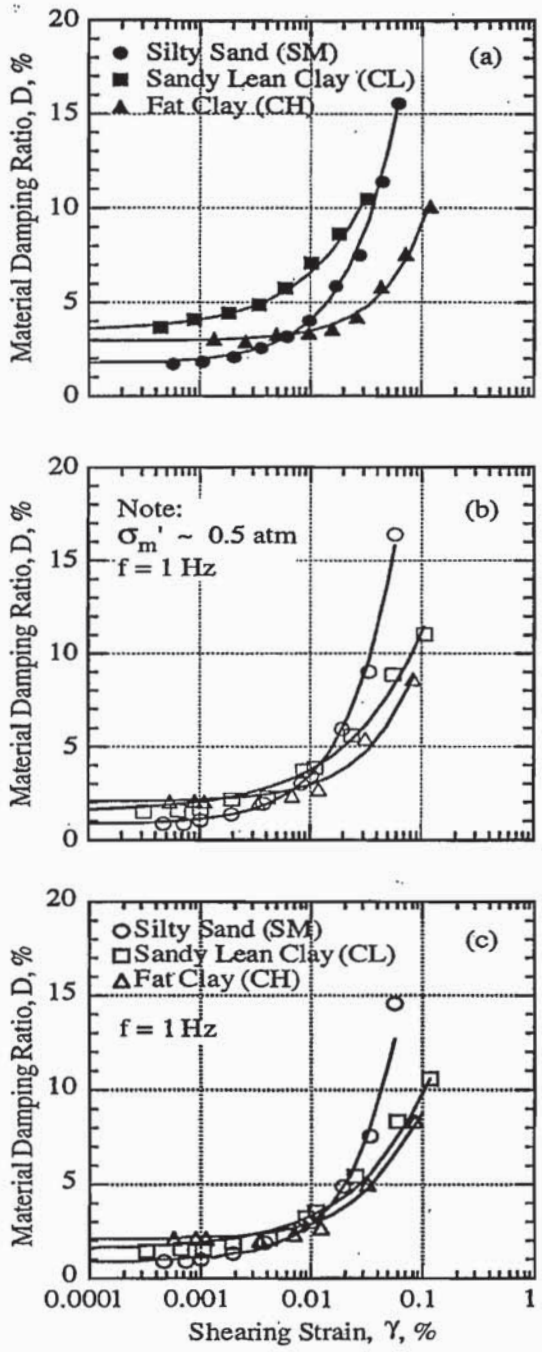

Figure D.15 Effect of soil type on damping ratio curve as determined by RC test (a), 1st cycle of TS test (b), and 10th cycle of TS test (c) (after Stokoe et al., 1999)

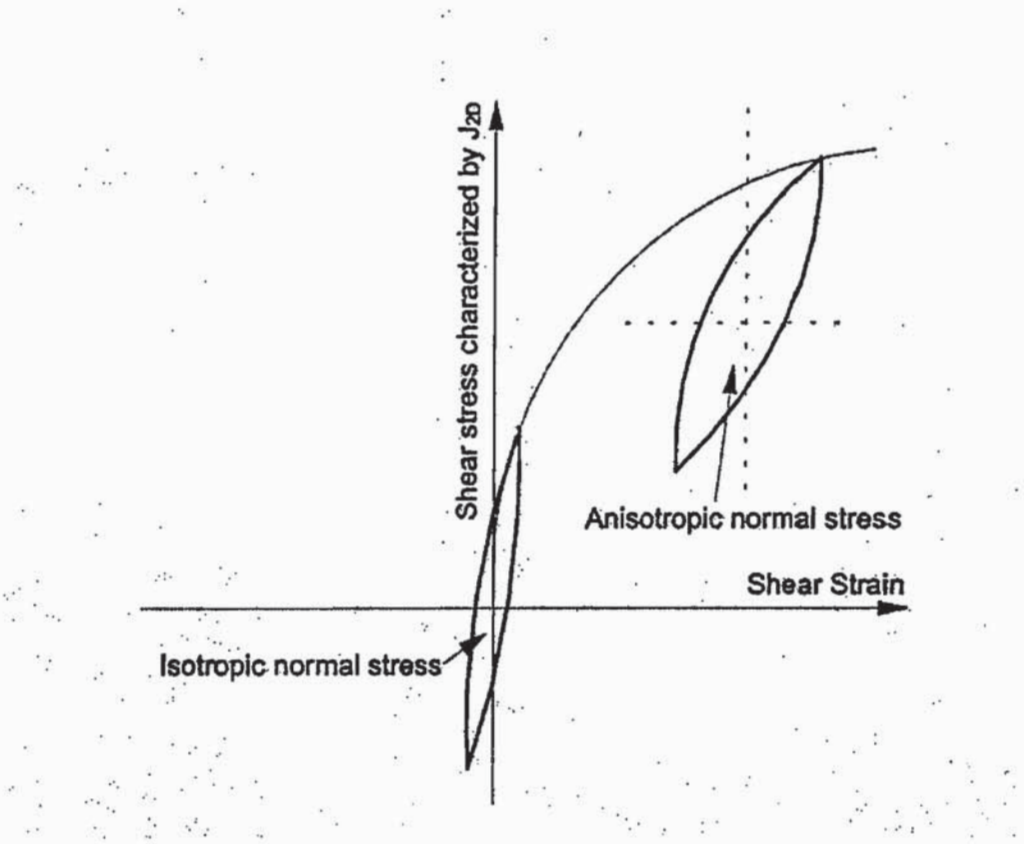

FigureD.16: Influence of initial normal stress state on damping (after Li et al., 1993)

Appendix E:

Development and Validation of the Elastomer Gauge

E.1 Introduction

This chapter introduces a new type of local strain gauge for soil testing called the Elastomer Gauge. It is the first on-sample full-contacting local strain gauge that is flexible enough to be attached to the inside of a conventional latex membrane so that the gauge is in full contact with the soil specimen's surface. The gauge has very versatile design characteristics including variable length, sensitivity and hardness, which enable measurement over a wide range of static and cyclic strains from about 0.0005% to 10%. The gauge can be used in many testing systems including triaxial, torsional shear, and simple shear devices to directly measure axial, circumferential, and shear strains. The gauge has been validated in triaxial and torsional testing systems using a "calibration sample" made of urethane with known stiffness characteristics. The tests' results show that the gauge can be reliably used in monotonic and cyclic testing systems to measure local strains and to accommodate coupled axial and radial deformations without loss of accuracy. The gauge flexibility suits the needs of the DFSD so well. With the ability to attach the gauges to the inside of a flexible membrane, it is possible to remotely deploy the gauges after sample preparation. The gauges can also handle large amount of pre-stretching during tool assemblage and carving process and still remain functional.

E.2 Local Strain Measurement in Soil testing

Accurate measurement of the small strains required for determining soil stiffness has been one of the challenging tasks in soil testing. The importance of using the appropriate small

strain stiffness of soils has been widely recognized both under static and dynamic loading conditions. For example, Burland (1989) has shown that the strain levels in the ground under working loading conditions are less than about 0.1%. Conventionally, triaxial tests are usually used to characterize the stress-strain behavior of soil specimens. However, because of the effects of the compliance in the loading system and the bedding/seating errors at both ends of the specimen, small-strain stiffness can only be achieved if the strains are measured internally within the triaxial cell. Moreover, because of the end-restraint effects, the stress distribution within the soil specimen is likely to be more non-uniform near the top cap and the base pedestal. These conditions dictate that small strains should be measured locally, typically within the central one third of the specimen (Rowe and Braden (1964), Kirkpatrik et al. (1968, 1970), etc.). It has been shown by many researchers that there is a significant difference in the stiffness of soil specimens, sheared monotonically or cyclically, when strains are measured locally rather than over the whole sample (e.g., Jardine et al. (1984, 1985a), Tatsuoka et. al. (1994), etc.). Usually, local strain measurement results in stiffer soil response because of end-restraint effects and bedding/seating errors, an observation that is in agreement with the long-recognized fact that laboratory measurements of soil stiffness are typically far smaller than the apparent in-situ values when conventional strain-measuring techniques are used (Jardine et al. (1984)). Hight et al. (1983) also recommended using local strain measurement at mid-height of the specimen in torsional shear tests because of stress non-uniformity introduced by end-restraint effects.

In recognition of the aforementioned observations, a number of local-strain measuring devices have been developed. The list includes: the electrolevel gauge or inclinometer (Burland and Symes (1982) and Jardine et al. (1984)), the Hall effect transducer (Clayton et al. (1986,1989)), the non-contact proximity transducer (El-Hosri et al. (1981) and Hird and Yung

(1987, 1989)) and the local deformation transducer (LDT) (Goto et al. (1991)). Recently, Li (1996) described and developed the "Flexible Gauge", which is a high-frequency resonating coil that senses deformation through changes in inductance. Linear-variable-differential-transformers, (LVDTs), have also been used by many investigators for local strain measurement. However, the majority of these devices have complex set-up procedure and other limitations and deficiencies. For example, tilting and barreling of the specimen during testing will lead to non-coaxiality between the core and the body of the LVDT which will affect its measurements, in addition to its possible interference with radial deformation. On the other hand, the positioning and alignment of the sensor and the target in a proximity transducer system is a delicate operation that needs skill and care, beside the possible potential errors that could occur if the deformation is non-uniform or if there are bedding errors between sample and target. In addition, such devices need a non-conducting cell fluid unless the electrical system is completely sealed and the method of attaching the instruments to the outside if the specimen introduce additional compliance source. Moreover, most of these gauges have a limited strain range, which means that multiple devices with different sensitivities are needed to measure strains over a wide range.

Scholey et al. (1995) reviewed the instrumentation used for measuring small local strains and pointed out the complexities associated with these devices. They also pointed out that an ideal system should have the following characteristics: (1) Strains should be measured to an accuracy of at least 10^{-3} % (2) Measuring systems should be able to accommodate coupled axial and radial deformation without loss of accuracy (3) Instrumentation should not interfere with the soil behavior (4) Axial strain measurement must ideally be made locally, over the central one third of the specimen so that end-restraint effects are eliminated (5) Instruments must be capable of operating under different stress paths (6) Instruments must be submersible and capable of

operating under typical ranges of triaxial cell pressures (7) Instruments must be capable of operating on specimens of any dimension typically used throughout the world, and (8) For cyclic systems, instruments must have low hysteresis and rapid response.

The elastomer gauge is a totally new type of local strain gauge that meets most if not all the requirements mentioned above. It is an on-sample local strain gauge that can be attached to a membrane so that the gauge is in direct contact with the soil specimen surface and deforms in the same way as the soil. Some of the advantages of this gauge include: (1) it can be used to measure a wide range of strains from at least 0.0005% to over 10%, (2) it has flexible design characteristics including different lengths, sensitivities and resolutions and even adjustable hardness to fit the stiffness of the material being tested, (3) it can be used to measure axial as well as radial deformations and (4) it has a simpler set-up, calibration procedures and acquisition system than most other local transducers.

E.3 Development of the Elastomer Gauge:

The original version of the elastomer gauge was first introduced during 1975 as a new type of gauge designed to measure strains in soft flexible materials such as rubber, plastic, and living tissue. The device made it possible to employ a gauge which uses the same electrical resistance principles as does a conventional foil strain gauge, but can function on structures composed of rigid or flexible materials. A key feature was also their ability to survive much larger deformations of the flexible material without being damaged. The original purpose was to measure relatively large strains in excess of 1% and up to 50%, which are larger than most applications in soil testing. However, the idea of having an on-sample local strain gauge that is in full contact with the soil surface was appealing. In 1998, researchers in the geotechnical laboratories at University of California at Berkeley started experimenting with this gauge to

improve its performance. The goal was to be able to manufacture this gauge "in-house", since it is no longer available commercially, and to make the gauge capable of measuring small strains. Today, the new generation of elastomer gauges can be fabricated with a workable strain range from at least 0.0005% to over 10% with excellent resolution.

E.4 Structure of the Elastomer Gauge

As shown in Figures E.1 and E.2, the sensing element of the gauge is a 0.051, 0.038, 0.025, or 0.019 mm (2, 1.5, 1.0, or 0.75 mil) diameter capillary filled with an electrically conductive liquid metal alloy and encapsulated in a supple polyurethane gauge body. At each end of the capillary there is a spherical reservoir approximately 10 mil in diameter, which is also filled with the liquid alloy, to maintain the continuity of the capillary while the gauge body is deforming. The cross-sectional area and length of the capillary change as the gauge body deforms, producing a predictable variation in electrical resistance. For a gauge with 1.5 mil capillary and 12.5 mm gauge length, the nominal resistance is approximately 5 ohms. All gauges have been made to be 5 mm wide, and 1 mm thick, but with variable lengths. To date, gauges with 6, 12.5, 25, 50 and 65-mm nominal lengths have been manufactured at Berkeley. In order to be able to measure the changes in the resistance of the capillary, two 5-mil platinum wires, one at each end, is attached to the gauge body such that it is in contact with the reservoir. The elastomer gauge is essentially an extension gauge, but has a variety of uses depending on the orientation and the pre-stretching of the gauge.

E.5 Materials for the Elastomer Gauge

As mentioned before, a thin capillary filled with liquid alloy is the sensing element in this gauge. Therefore, for optimal performance, the alloy should have low surface tension, good wetting capability, good electrical conductivity, and remain in the liquid state at the working

temperature range. Two types of alloys have been found to fulfill these requirements. The first alloy is the one used with the original design, which was called Viking LS 232. This metal alloy is a ternary eutectic of the mercury-indium-thallium system. It has the unique ability to "wet" virtually all materials to form contacts of very low electrical and thermal resistance. This results in a thin film which forms a protective envelope and prevents further wetting. At room temperature, the alloy is silver-gray liquid with high surface reflectance, a density of about 10 gm/cm^3, a thermal conductivity of 0.1 watts/ °C-cm, and a viscosity similar to mercury. The operating temperature range of this alloy is from -20 to 90 °C. The second alloy is called Indalloy® 46L, which is an indium alloy composed of gallium, indium, tin and zinc. It is a low-melting point indium alloy that is liquid at room temperature. The density of this alloy at room temperature is 6.5 gm/cm^3 and it solidifies at 6.5 °C. Both alloys have been used to manufacture gauges with acceptable performance. The mercury alloy has higher resistivity, and a lower melting point while the indium alloy seems to produce gauges which are more electrically stable. For example, for a 50-mm gauge (2-inches) the resistance of a 1.5-mil capillary filled with the mercury alloy is around 18.0 ohms while the one with the indium alloy has a resistance of about 14.0 ohms.

The gauge body is composed of polyurethane that can be made with different hardness. The materials used to make the polyurethane include; Adiprene, castor oil, butanediol, and MOCA. The proportions and the choices of the materials used to make the polyurethane mix, control the resulting hardness of the gauge body. The materials are mixed in a liquid state at a certain temperature, poured into a mold to form the gauge-body shape, subjected to vacuum to get rid of entrapped air, and then left to cure in the oven at a certain temperature. The electrical

connections are made with two 5-mil platinum wires that are later connected with 300 mm of 28 gage PVC coated strain gauge wire.

E.6 Working Principle of the Elastomer Gauge

As mentioned earlier, the operating principle of the elastomer gauge is similar to that of metallic wire or foil strain gauges. As the capillary deforms, element resistance is expressed by the equation:

$$R = \rho \frac{l}{a} \qquad \text{(E.1)}$$

Where R is the resistance of the element, ρ is the resistivity of the alloy, which is a material property, and l and a are the length and the cross-sectional area of the capillary, respectively. Since the alloy is an incompressible fluid, capillary volume is constant during gauge deformation and therefore gauge strain can be related to its resistance. However, since it is much easier to measure and monitor voltage instead of resistance, a Wheatstone bridge circuit is used to convert changes in resistance to changes in voltage as shown in Figure E.3. It can easily be shown that the relationship between the voltage difference across the bridge and the gauge deformation is fairly linear up to 20% strain. In most cases, the elastomer gauge constitutes one arm of the bridge while the other three arms have constant resistors, usually equal to the gauge resistance at a particular reference condition. Theoretically, the voltage difference across the bridge is related to the gauge resistance in the following formulas:

$$V_b = \frac{V_{exc}}{2}\left[\frac{R_b - R_g}{R_b + R_g}\right] \qquad \text{(E.2)}$$

$$if \qquad R_g = R_b + \Delta R$$

$$V_b = \frac{V_{exc}\Delta R}{4R_b} \qquad (E.3)$$

where, V_b is the voltage across the bridge, V_{exc} is the bridge excitation voltage, R_b is the bridge completion resistance and R_g is the resistance of the gauge. As shown in the previous formulas, the voltage across the bridge is a function of the change in gauge resistance and the excitation voltage of the bridge.

E.7 Data Acquisition System

Figure E.3 shows the block diagram of the basic elements of the data acquisition system for the elastomer gauge. As mentioned above, a Wheatstone bridge is used to convert changes in resistance to changes in voltage. The Wheatstone bridge consists of four resistors and a voltage source. When the bridge is balanced, the voltage across the bridge is zero. To balance the bridge, a potentiometer is used at one arm so that the voltage difference across the bridge can be adjusted before conducting the test. Because of the relatively small resistance of the gauge, the electrical excitation of the gauge should not produce more than 10 milliamperes of current to remain stable, though the gauges can sustain currents of 30 milliampere without damage. The bridge completion resistors should be close to the resistance of the gauge, thus, their values range between 6 to 50 ohms according to the gauge being used. Given these resistances and current values, the excitation voltage of the bridge will range from 0.125 to 1.0 volts according to the gauge resistance and the required gauge sensitivity as will be discussed later. The difference in voltage across the bridge is measured by a differential amplifier as shown in Figure E.3. The differential amplifier receives a continuous signal through the two bridge terminals, measures the difference in voltage between the terminals, and amplifies the signal. The amplification ratio, or the gain, is controlled by changing the ratio between certain resistors. The gain should be set to

obtain the optimum resolution depending on the level of the strains being measured and the required sensitivity of the gauge. A gain up to 4000 has been used to measure very small strains. In that case, the output of the circuit should be adjusted or zeroed before conducting the test, to maximize the use of the measurable voltage range. In order to increase the signal-to-noise ratio and eliminate unwanted high-frequency noise, a low-pass analog filter can also be used. For this project, a compact and robust configuration of signal conditioning was developed to house eight gauge-circuits at a time Each gauge circuit has a Wheatstone bridge, a differential amplifier with controllable gain, a voltage divider and a low-pass filter with 30 Hz cutoff frequency.

E.8 Sensitivity and Resolution of the Elastomer Gauge

The primary factors affecting the sensitivity of the elastomer gauge are the diameter and the length of the gauge capillary and the excitation voltage. Another factor is the circuit gain, but this is not an inherent property of the gauge. As indicated by equation E.3, there is a direct relationship between the excitation voltage of the bridge and the output voltage of the circuit (and thus the sensitivity of the gauge). In order to be able to measure small strains it is favorable to increase the excitation voltage so that the output voltage of the circuit is increased. However, there is a limit to how high the excitation voltage can be raised, which is governed by the maximum current the gauge can handle without damage or signal dri 32bit X6 over heating. It is also worth mentioning that from Ohm's Law, the larger the resistance of the gauge, the smaller the current passing through it at a given excitation voltage. In other words, the larger the resistance of the gauge, the higher the excitation voltage that could be applied and hence the more sensitive the gauge is. Therefore, the sensitivity of the gauge can be increased by increasing the length of the gauge or decreasing its diameter since in both situations the

resistance of the gauge is increased. Moreover, the longer the gauge, the larger the deformation at a given strain and thus the larger the gauge output and signal-to-noise ratio.

Theoretically, the gauge should have an infinite resolution. Practically, since the analog signal is prone to noise and digitized by means of A/D converter, the resolution of the measured signal will depend on the number of bits in the A/D card (i.e. the resolution of the A/D card), and the range of input voltage of this card. For a 16-bit A/D converter with a capacity of ±10 volts of input voltage, the resolution of the logging system is $\pm 3.05 \times 10^{-4}$ volts. For a gauge with a sensitivity of 40 volts/mm, this corresponds to a resolution of $\pm 1.5 \times 10^{-5}$ % or 0.76μm (50-mm gauge). However, this resolution can be jeopardized by noise and the actual resolution can be coarser by an order of magnitude.

In summary, the elastomer gauge has a variable sensitivity that is a function of the length and diameter of its capillary and the excitation voltage. The gauge potential sensitivity increases with increasing the capillary length, decreasing the capillary diameter, and increasing the excitation voltage. Gauges with lengths of 12.5, 25, 50 and 65 mm and capillary diameters of 0.75, 1.0, 1.5, and 2.0-mil have been manufactured and used successfully to test soil samples with different dimensions. The choice of a gauge length and sensitivity depends on the application and the strain level of interest. So far, gauges with sensitivity as high as 60 volts/mm have been manufactured and used to measure strains as low as 5×10^{-4} %.

E.9 Calibration and Attachment of the Elastomer Gauge

The elastomer gauge has a relatively simple calibration and setup procedure. The calibration starts with clamping the gauge between the jaws of a stainless steel caliper so that the interior edge of each jaw is just outside the reservoir. The gauge is then connected to a channel of signal processing (Figure E3). After that, the gauge is incrementally stretched and the length

of the gauge as measured by the caliper is related to its output voltage. Figure E.4 shows a typical calibration curve for a 50-mm long 1.0-mil capillary gauge at two different excitation voltages showing the variation of sensitivity.

After calibration, the gauge can be attached to a latex membrane, but first the membrane has to be expanded to a diameter that is slightly smaller than the diameter of the sample to be tested to pre-stretch the gauge. This is especially important for gauges to be used in compression tests. The use of a pre-stretched elastomer gauge in compression has proven to be valid, as will be shown later. The gauge is then glued onto the inside of the membrane at a vertical, horizontal or inclined orientations according to the type of strain to be measured. Two materials have been used to attach the gauges to the membrane. Liquid polyurethane, which is the same material used to make the gauges, was used for a more durable attachment of the gauge, but it takes at least two days for the material to cure and solidify at room temperature. Liquid latex was also used for the same purpose and it has the advantage of a short curing time, though the gauge attachment is less durable than the first material.

E.10 Implementation and Validation of the Elastomer Gauge

One means of evaluating the performance of the elastomer gauge is to use it to test specimens with known stiffness characteristics (i.e. calibration specimens). The values of the stiffness determined with the elastomer gauge can be compared with the stiffness of the specimen that has been established by independent tests. Stokoe et. al. (1990) pointed out the advantages of using synthetic specimens in equipment calibration, especially because they have stiffness properties that can be determined by independent tests and can be repeatedly tested as desired. In this study, a two-component urethane elastomer resin specimen (Stokoe et. al. (1990)) was used. Urethane can be modeled as a linear, viscoelastic material with stiffness characteristics

essentially independent of confining pressure, strain amplitude, and stress history. Urethane stiffness is, however, dependent on loading frequency and temperature. Therefore, the value of the modulus has to be compared at the appropriate frequency and temperature. A common index test used when selecting urethane is durometer hardness. In this study, the urethane specimens used have a hardness of A75 and were obtained from University of Texas-Austin. Tests conducted at UT (1994) indicated that the material has a static Young's modulus of 2250 psi and a Poisson's ratio of around 0.49-0.5 for strains up to 0.5%. To examine the capability and performance of the elastomer gauges, three types of tests have been conducted: (1) monotonic triaxial tests, (2) cyclic triaxial tests and (3) cyclic torsional shear tests.

E.10.1 Monotonic and Cyclic Triaxial Tests

An advanced triaxial testing system (Gookin et.al. 1996) has been used to monotonically and cyclically test a 22-cm long and 10-cm diameter urethane sample over a wide range of strains. The system has the capability of internal and external measurements of load and displacement using load cells and LVDTs with varying sensitivities. The system uses four internal LVDTs and can measure strains as low as 0.0001%. Figure E.5 shows the basic elements of the system. An instrumented membrane was used with two pairs of elastomer gauges. Each pair included a vertical and a horizontal gauge. One pair consisted of gauges with 1-mil diameter and 50-mm long capillary to measure small-to-intermediate strains while the other pair has 1.5-mil diameter and 50-mm long capillary for intermediate-to-large strain measurements. With the appropriate excitation voltage, these elastomer gauges could measure strains from 0.0005 % to over 1%. Vacuum was used to confine the membrane and the attached gauges against the sample.

E.10.1.1 Monotonic Triaxial Tests

Figure E.6 and Figure E.7 show the stress-strain curves obtained from two monotonic triaxial tests on urethane at small and large strain levels. The results show a good agreement between the averaged local, and averaged internal strains measured by the elastomer gauges and the internal LVDT's, respectively. The average Young's modulus value measured by the elastomer gauge is 2290 psi, which is the value expected for urethane. Moreover, the quality and resolution of measurements made by the elastomer gauge is as good as a very sensitive LVDT. These results indicate a successful use of the elastomer gauge and the concept of on-surface strain measurement in static compression tests.

E.10.1.2 Cyclic Triaxial Tests

To evaluate the performance of the elastomer gauge under cyclic axial loads, another series of triaxial tests were conducted. Figure E.8 shows the axial strain-time histories as measured by the elastomer gauge and the internal LVDT's from tests at different strain levels. The results clearly show that the elastomer gauge can be used to measure cyclic strains without undergoing any significant hysteretic behavior under a wide range of strains, and as low as 10^{-3}%.

Another important finding from the results of the triaxial tests is that the linearity of the output voltage of the gauge with the deformation over a wide strain range. This is evident from the fact that a calibration factor obtained at intermediate-to-large strains was used in tests with small strain levels and the results agree well with those of the LVDTs and the known value of Young's modulus.

E.10.1.3 Radial Strain Measurements

Measurement of radial strains has also been a challenging task in soil testing because of the non-uniform radial deformation and bulging in soil specimens, and the difficulties in using the available transducers to accurately measure the radial strain without interfering with the sample deformations. Therefore, one important application of the elastomer gauge is its capability to measure radial as well as vertical strains. Figure E.9 shows the radial strain-time history obtained from the horizontal elastomer gauges as compared to the axial strain-time history from a cyclic triaxial test on urethane, and the radial strain versus axial strain for the same test. The Poisson's Ratio predicted by the elastomer gauges' measurement is 0.49, which is the value expected for urethane. This shows that the elastomer gauge can accurately be used to measure radial deformation locally at any section of the sample.

E.10.2 Cyclic Torsional Shear Tests

The use of the elastomer gauges is not limited to triaxial devices but can also be used to measure radial deformations in simple shear tests and shear strains in torsional shear tests. To evaluate the performance of the elastomer gauge in torsion, a series of cyclic torsional shear tests have been conducted on urethane. The device used is the benchtop version of the DFSD. The device is described in more details in Chapter 4. The device applies a harmonic angular displacement (strain-controlled) to the top of the solid cylindrical sample of urethane. The bottom of the specimen is fixed against rotation and translation. The device measures the torque exerted on the top of the sample, the twist at the top, and the local strain on the surface of the sample. The torque and twist can then be converted into stress-strain hysteresis loops from which the shear modulus and damping ratio can be determined. As in triaxial tests, vacuum was also used to confine the membrane and the attached gauges against the sample. The axial and torque loads are coupled and carried to the sample through a load rod and measured by

means of a 2-axis wheel-shaped load cell assembly Shear strains were measured globally by proximity transducers and locally by four elastomer gauges.

The proximity transducer used in the tests is model KD2400 from Kaman Instrumentation with a sensitivity of about 1.5 volts/mm. The target was mounted on the side of the load cell while the probe was mounted on a metal base that is fixed to the top cover of the cell. The gap between the center of the proximity probe and the center of the target is about 0.4 mm. The relation between the shear strain and the twist measured by the proximity transducer is given by the formula:

$$\gamma = \frac{R\theta}{L} \qquad \text{(E.4)}$$

Where R and L are the radius and length of the sample and θ is the twist angle measured by the proximity transducer. Four elastomer gauges were used to measure the local shear strains at the surface of the sample. The gauges were attached to a latex membrane at an angle of 45° from horizontal. At this orientation, it can easily be shown that the shear strain is twice the gauge strain. The four gauges were distributed around the middle third of the sample, one in each quadrant, so that bending errors were minimized.

A series of cyclic torsional shear tests have been conducted at different strain levels. Figure E.10 shows the stress-strain hysteresis loop from one of these cyclic tests with shear strains obtained by averaging the four elastomer gauges measurements. Figure E.11 shows a comparison between the elastomer gauges and the proximity transducers strain measurements. The proximity transducers slightly over-predict the shear strain and thus under predict the shear modulus mainly because of the alignment errors and end-restraint effects, an observation that has also been noted by Hight et al. (1983). The shear modulus of urethane as measured by the

elastomer gauge is 73 ksc compared with 67 ksc using the proximity transducer and 63 ksc from by the University of Texas tests (1994) (using internal proximity transducers).

E.11 Summary

The importance of local strain measurement in soil testing is now widely recognized, particularly if the small strain stiffness of the soil is being investigated. Although many devices have been introduced for this purpose, most of them have complex setup and installation procedures, high cost, and can interfere with the soil behavior. Hence, local strain measurement is still rarely conducted in everyday practice in geotechnical laboratories and is currently limited to research. There is a need for a new type of a local strain gauge that has a simple setup procedure, yet is accurate enough to resolve small strains. The elastomer gauge introduced in this study is believed to fulfill most if not all of these requirements. It is flexible enough to be attached to the inside of a membrane before the test is conducted, thus bypassing the many steps of setup required by other devices. The gauge can be used to measure axial, radial and shear strains over a wide range, and to values as low as 0.0005% without interfering with the soil behavior. The gauge has flexible design characteristics including variable lengths, sensitivities and hardness. The gauge can be used in different testing devices including triaxial, torsional shear, simple shear (and perhaps the pressuremeter) to measure static as well as cyclic local strains. The gauge is particularly valuable for the DFSD field measurement where the instrumented membrane is remotely deployed downhole.

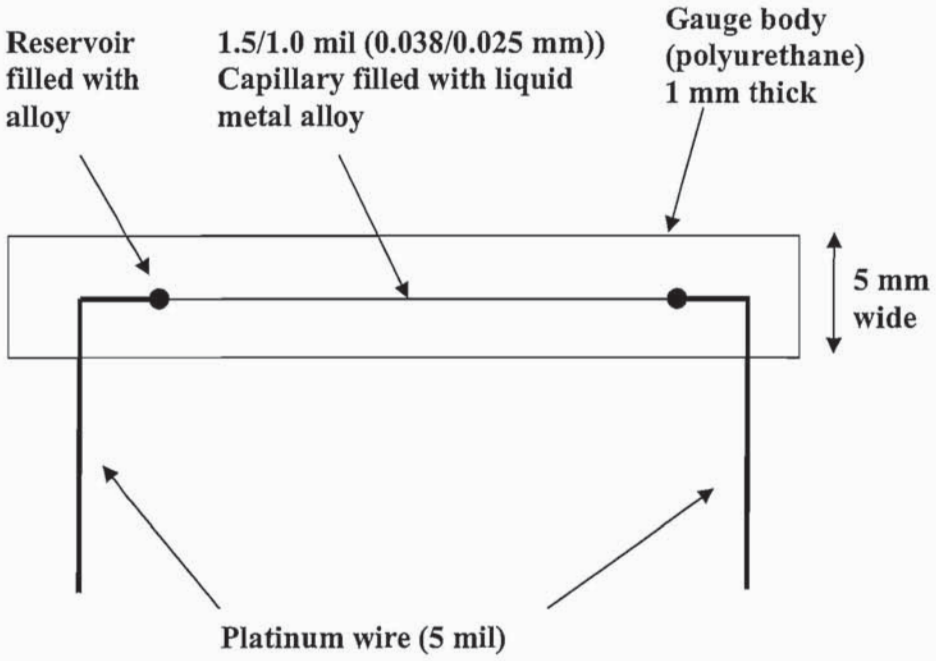

Figure E.1 Structure of the elastomer gauge

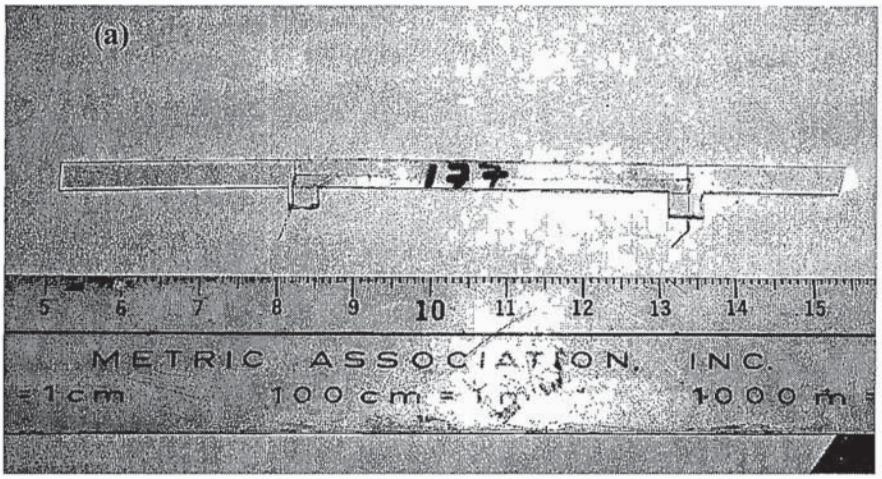

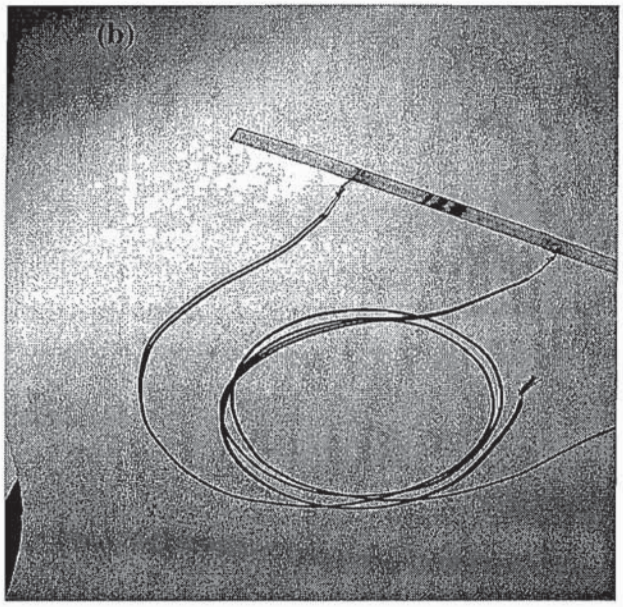

FigureE.2 Pictures showing the elastomer gauge with and without leads

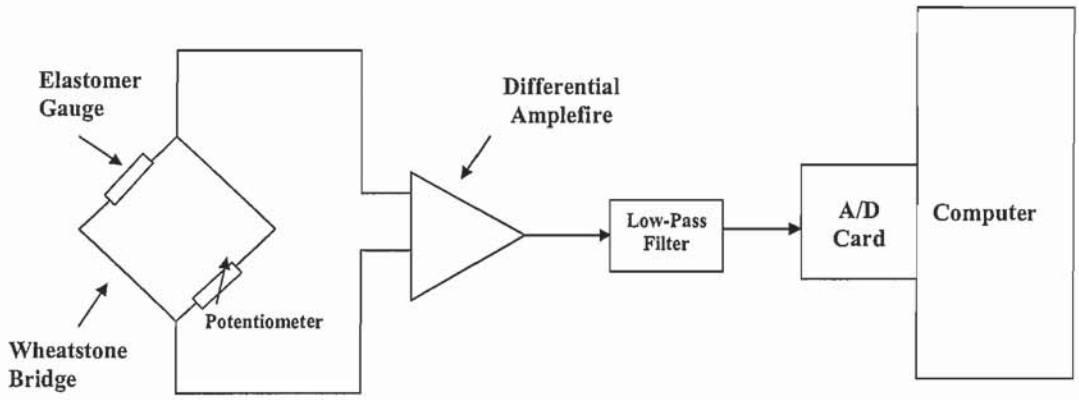

Figure E.3 A schematic diagram showing the signal processing and data acquisition circuit of the elastomer gauge

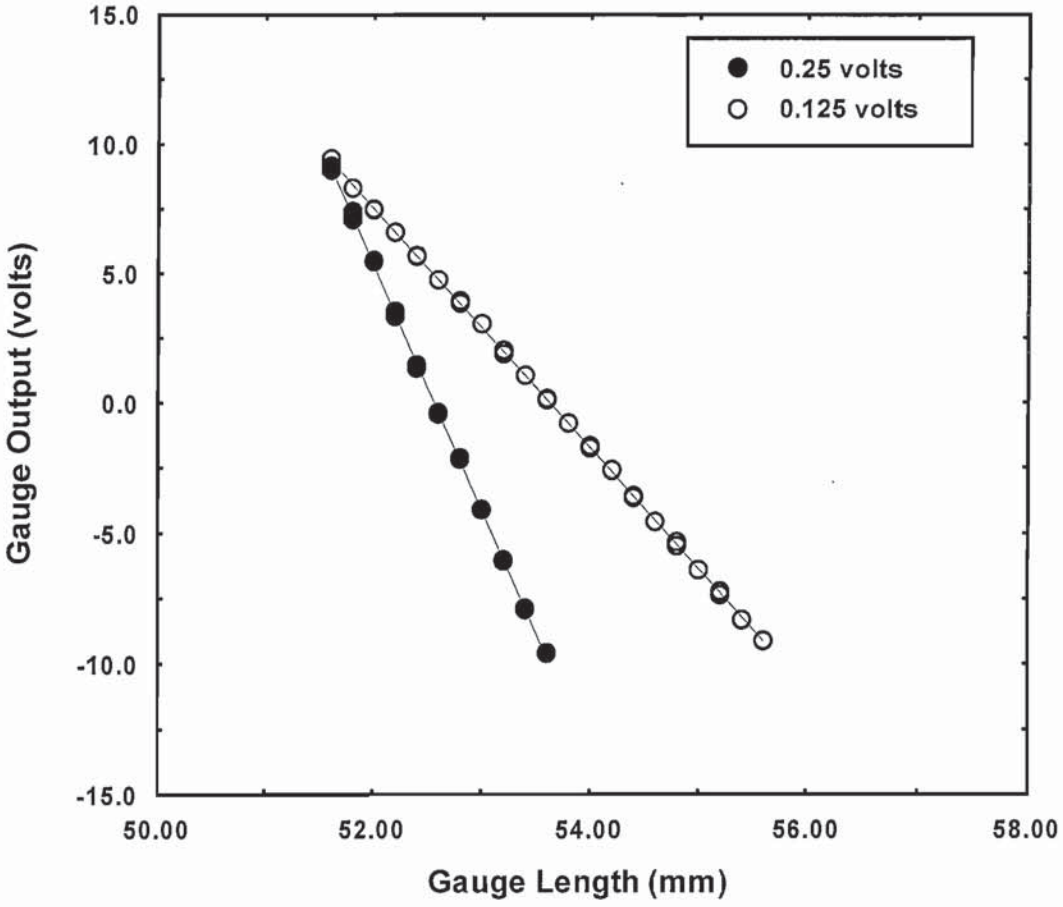

Figure E.4 Calibration curve for a 50-mm long a-mil diameter elastomer gauge at two excitation voltages 0.125 and 0.25 volts

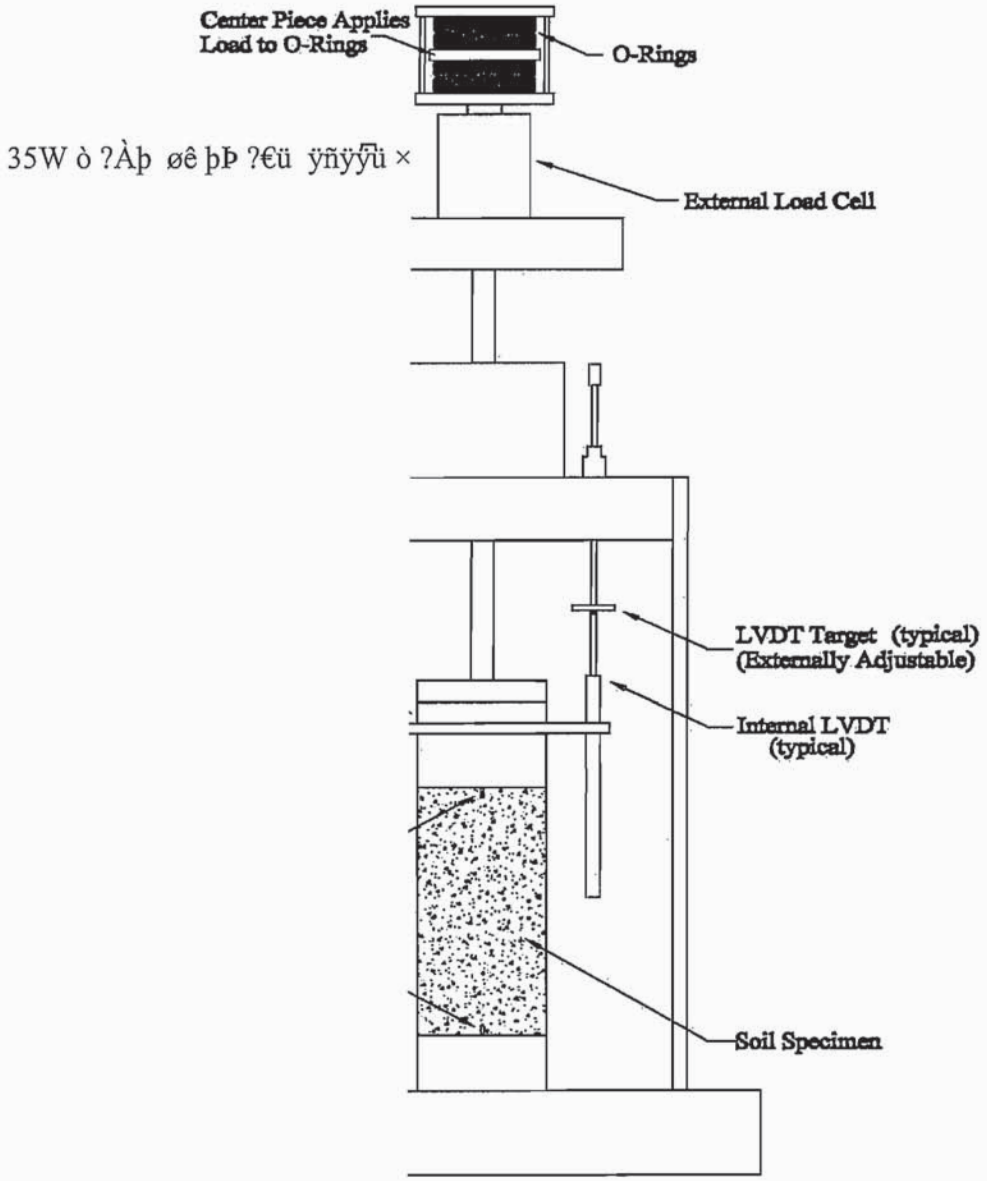

Figure E.5 A schematic diagram of the cyclic triaxial shear device (after Gookin, 1998)

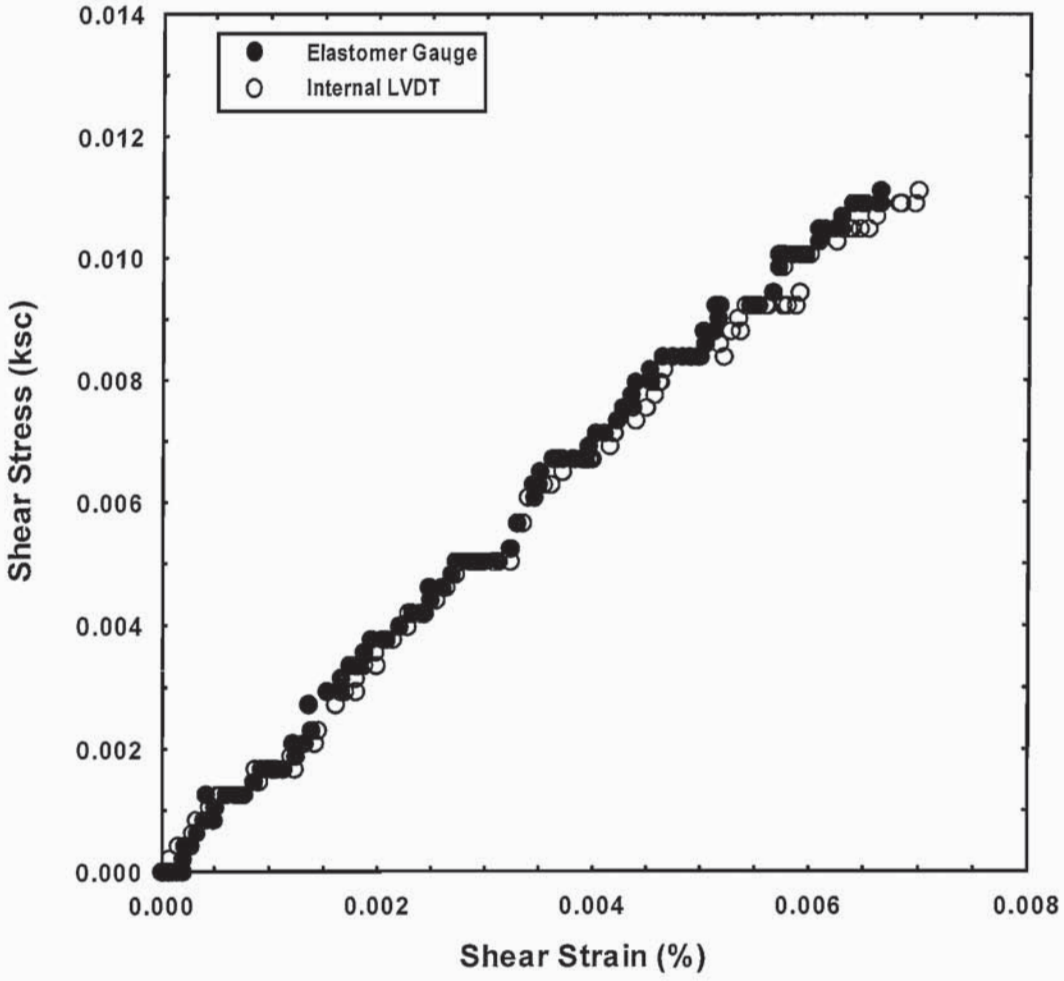

Figure E.6 Small-strain triaxial test on urethane using the elastomer gauge and internal LVDT

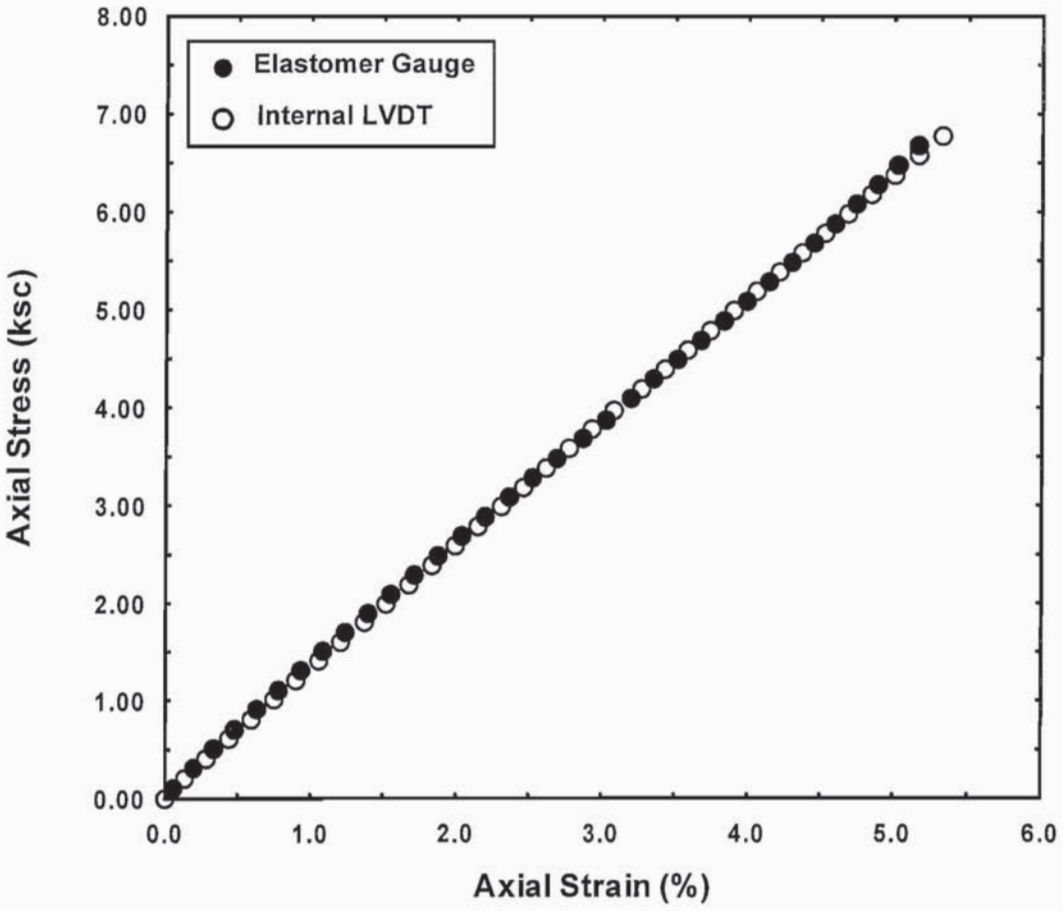

Figure E.7 Large-strain triaxial test on urethane using the elastomer gauge and internal LVDT

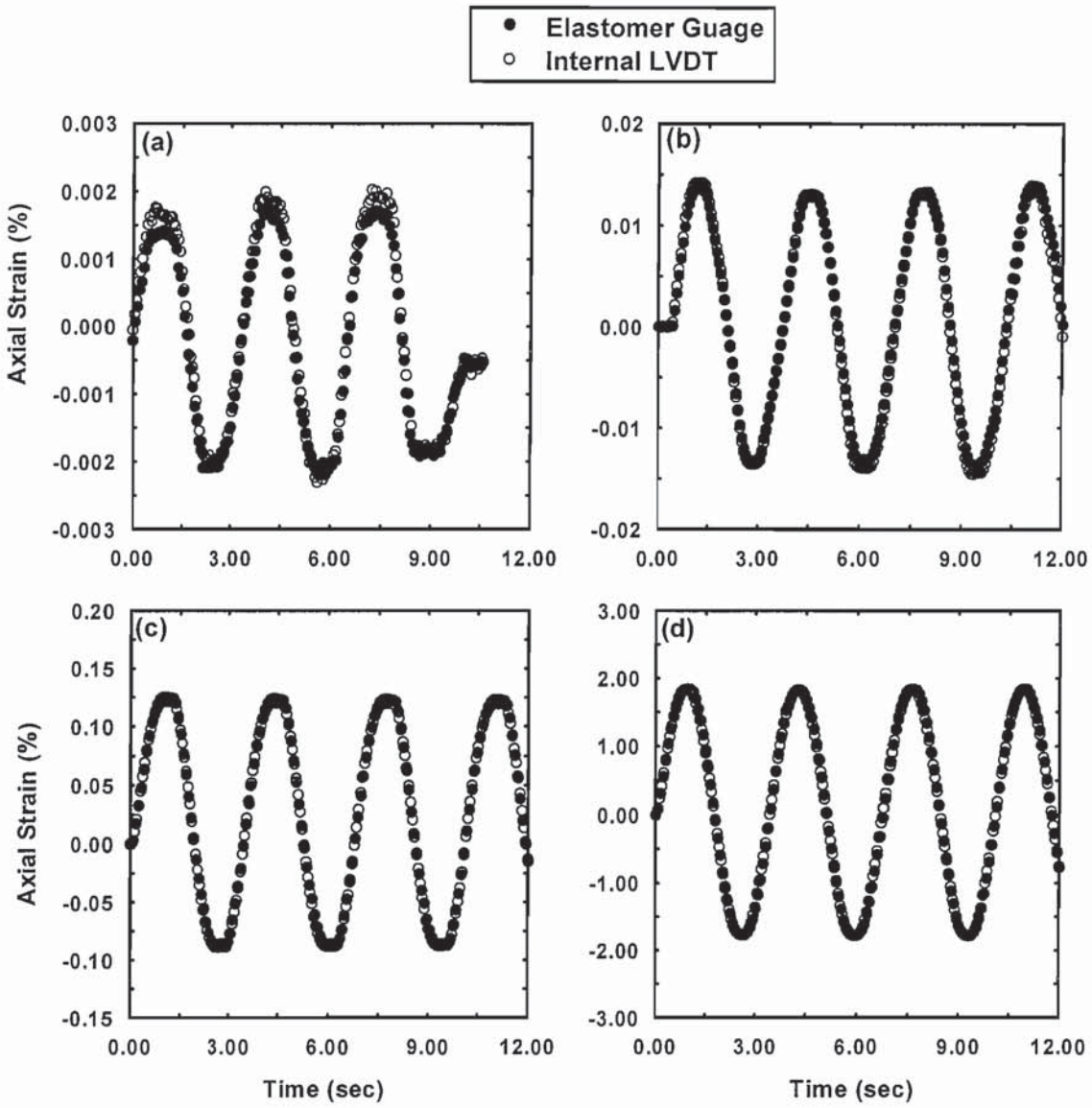

Figure E.8 Axial strain-time histories from four cyclic tests on urethane with maximum strain of (a) 0.002%, (b) 0.013%, (c) 0.13%, and (d) 1.8%

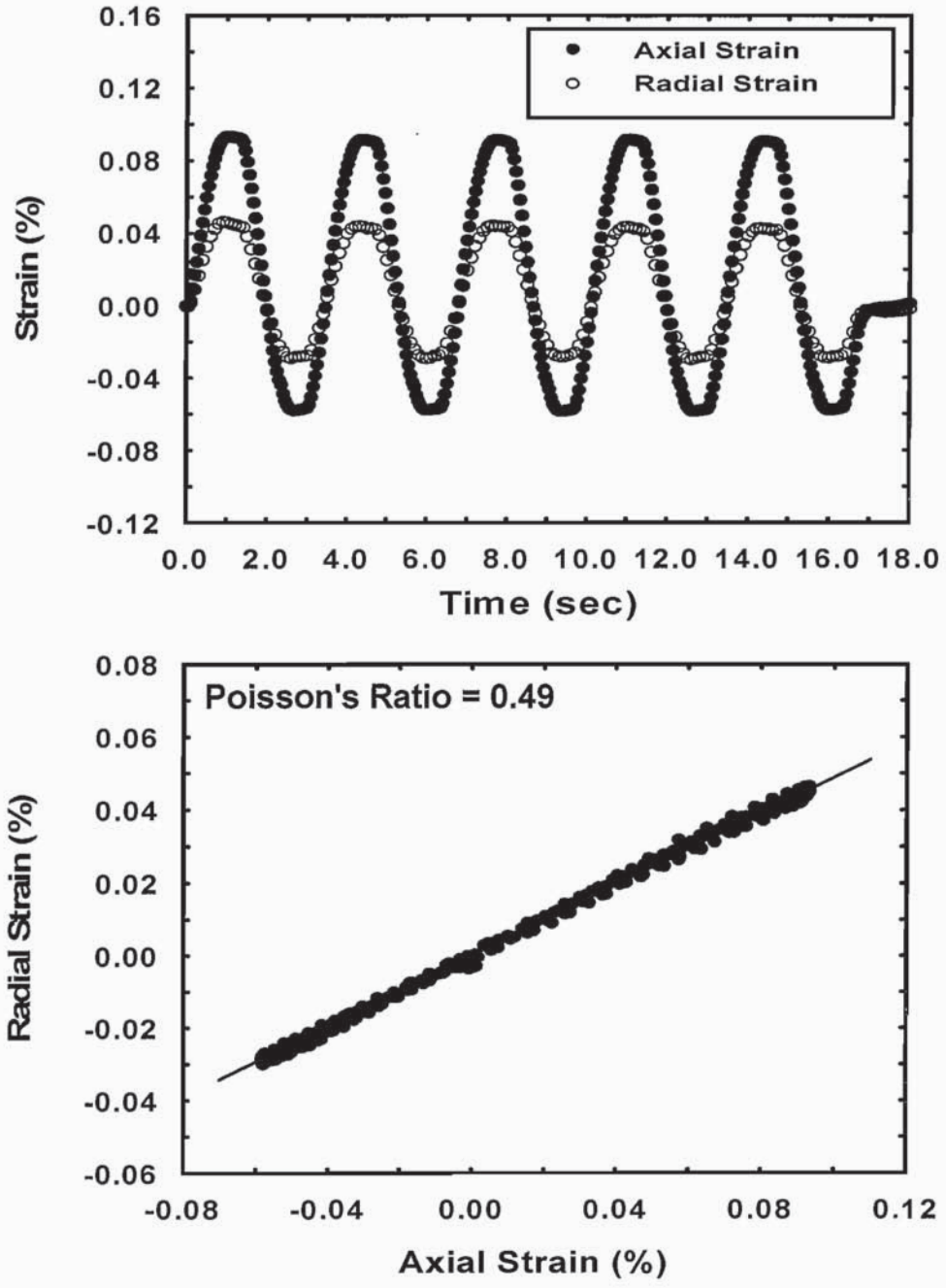

Figure E.9 Radial strain measurements by the elastomer gauge from a cyclic triaxial test on urethane

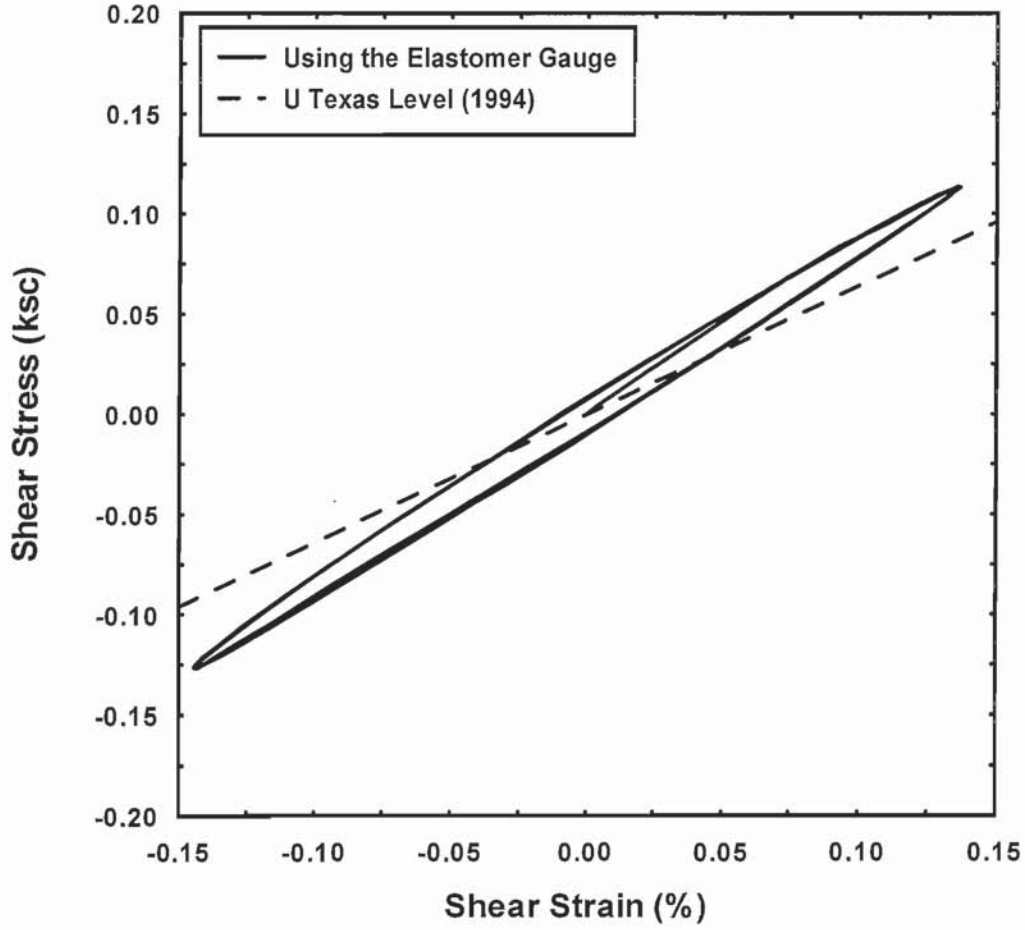

FigureE'.10 A hysteresis loop from a cyclic torsional shear test on urethane

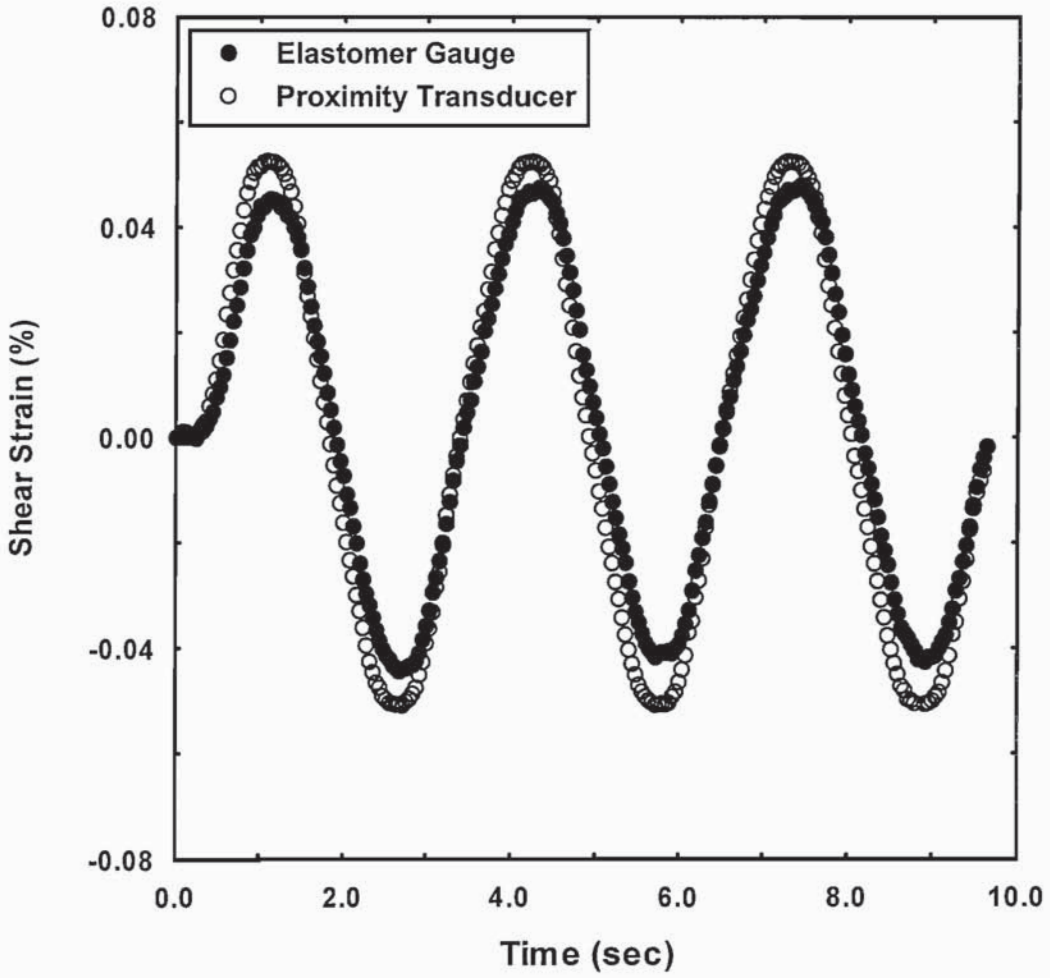

Figure E.11 A comparison between the shear strain-time history measured by the elastomer gauge and the proximity transducer from a cyclic torsional test on urethane